

**TRIGLYCERIDE-RICH LIPOPROTEINS INFLUENCE MONOCYTE AND
MACROPHAGE HOMEOSTASIS AND EXACERBATE EXPERIMENTAL
KIDNEY INJURY**

Maha Fahad Saja

A thesis submitted to Imperial College for the degree of Doctor of Philosophy

**Centre for Complement and Inflammation Research
Imperial College
London**

DECLARATION OF ORIGINALITY

I certify that the work in this thesis is my own and that all else is appropriately referenced.

COPYRIGHT DECLARATION

The copyright of this thesis rests with the author and is made available under a Creative Commons Attribution Non-Commercial No Derivatives licence. Researchers are free to copy, distribute or transmit the thesis on the condition that they attribute it, that they do not use it for commercial purposes and that they do not alter, transform or build upon it. For any reuse or redistribution, researchers must make clear to others the licence terms of this work.

ABSTRACT

Hypertriglyceridemia and its associated increase in triglyceride-rich lipoproteins (TGRLs) is a great threat to today's modern society. Sedentary life style and western type diet subject our bodies to repetitive influx of TGRLs following each meal which is being increasingly recognised as a risk factor for coronary artery disease (CAD). Moreover, a hyper-TGRL state complicates the course of various immunological and non-immunological conditions contributing to both morbidity and mortality. How TGRLs mediate their harmful effects is unclear. In view of their ideal location, monocytes (MOs) are at the front line against fluctuating levels of TGRLs, yet the influence of such an environment on their behaviour remain obscure. With the growing recognition of MO heterogeneity, the impact of this diversity on MO functions deserves more attention. In the mouse, two MO subsets are recognized; Gr1^{high} or "inflammatory" MOs, known to populate inflamed tissue giving rise to macrophages (MØs) and the Gr1^{low} or "patrolling" MOs, shown to crawl along the endothelial surface under steady-state conditions and rarely extravasate.

To explore whether changes in TGRLs could alter MO behaviour, I used a compound, P-407, that induces a dose-dependent increase in TGRLs in C57BL/6 (B6) mice. The increase in plasma TGRLs led to a sharp drop in blood Gr1^{low} MOs subsets while levels of Gr1^{high} MOs remained unchanged. The drop in Gr1^{low} MOs was associated with accumulation of CD68⁺ MØs in the liver, heart, and kidney. In the absence of an inflammatory insult, CD68⁺ MØs did not trigger kidney injury. However, with an inflammatory insult (accelerated nephrotoxic nephritis), the kidneys of P-407 injected mice exhibited more renal damage. Collectively my findings demonstrate that an

environment loaded with TGRLs influences the steady state behaviour of MOs and MØs, and primes the kidney for injury during inflammation.

ACKNOWLEDGEMENTS

I would first like to thank my supervisors, Professors Marina Botto and Matthew Pickering whose continued support, encouragement and expertise has been instrumental in the completion of this project. I am also indebted to Dr. Kevin Woollard for his invaluable collaboration which helped take the project to where it is. I also gratefully acknowledge the help of Professor Terry Cook with renal histopathology. This work could not have been possible without the invaluable advice and teaching from; Dr. Marieta Ruseva who guided me through my first steps in the lab and continued to help throughout the project, to Dr. Liliane Fossati-Jimack and Dr. Lucie Baudino for their invaluable guidance and teaching in flow cytometry, and to Dr. Marta Szajna whom without her help and support my kids would not have seen much of myself. I would like to extend my thanks to Dr. Talat Malik for his help in lipid measurements, and to Miss Lorraine Lawrence for her help in processing the renal histology. I would also like to thank every member of the Centre for Complement and Inflammation Research for their support throughout my PhD and for making it such a wonderful journey.

My thanks go to my magnificent parents, Fahad Saja and Nouriah Al-Hamdan, without whom I would not have been the person I am today. I am also grateful to my wonderful husband, Tariq Abalkhail, whom without his support I may not have had this wonderful opportunity, and to my Lovely kids, Mohammed and Fahad Abalkhail, whose presence lighted up my days here in London. My thanks go to my cousin Manahil Al-Hamdan, for her generosity and support in looking after the kids during my studies here in London. I am also indebted to Mr. Nasir Ahmad and Miss. Abeba Haile Derar whose trust-worthy and reliable help in looking after my kids gave me the peace of mind to focus on my

studies. Last but not least, I thank God who has given me the strength to pursue my dreams and surrounded me with all those lovely people to help make the journey a wonderful one.

This work was funded by a studentship from King Saud University in Saudi Arabia.

Contents

List of Figures	12
List of Tables.....	16
List of Abbreviations	17
CHAPTER 1- INTRODUCTION	23
1.1. Overview	23
1.2. Triglycerides (TGs) and TGRLs: their pathogenic potential	25
1.2.1. Plasma lipids.....	28
1.2.2. TGRL metabolism	34
1.2.3. RCT and the CETP-mediated lipid exchange	40
1.2.4. Hypertriglyceridemia; definition, causes and atherogenicity.....	48
1.2.5. Hyperlipidemic animal models.....	53
1.2.6. Poloxamer 407 (P-407) model	57
1.2.7. Conclusion	61
1.3. The Mononuclear Phagocytic System (MPS)	63
1.3.1. MO heterogeneity	64
1.3.2. MØ heterogeneity.....	80
1.3.3. The role of MOs and MQs in hyperlipidemia	87
1.3.4. Conclusion	90
1.4. The atherogenic lipid profile and kidney disease	91
1.4.1. The role of lipid in renal disease	93
1.4.2. Accelerated nephrotoxic nephritis (aNTN)	94
1.5. Summary	100
1.6. Aims of my project.....	101

1.6.1. My specific aims	101
CHAPTER 2- Material and Methods	102
2.1. Mice	102
2.2. Preparation of P407	102
2.3. Experimental design.....	103
2.4. Lipid levels and lipoprotein profiles.....	106
2.5. Renal functional analysis	107
2.5.1. Proteinuria and hematuria	107
2.5.2. Albuminuria	107
2.5.3. Plasma urea	108
2.6. Hematocrit measurement	109
2.7. Flow cytometry studies.....	109
2.7.1. Peripheral blood flow cytometry	109
2.7.2. Bone marrow flow cytometry	110
2.7.3. Organ flow cytometry	111
2.8. Histologic studies	114
2.8.1. Light microscopy	114
2.8.2. Immunohistochemistry (IHC) staining	115
2.9. Cytokine/chemokine levels.....	119
2.10. Enzyme linked immunoassays (ELISA)	119
2.10.1. Plasma C3 levels	119
2.10.2. Immune response measurement	120
2.11. BrdU pulsing and staining	121
2.12. Intravital microscopy and image analysis of the ear	122

2.13.	Bone Marrow Transplantation (BMT):.....	123
2.14.	Adoptive transfer experiment	123
2.15.	Serum nephrotoxic nephritis	123
2.16.	Statistical analysis	124
CHAPTER 3- P-407-INDUCED MODEL OF HYPERLIPIDEMIA.....		125
3.1.	Introduction	125
3.2.	Establishing the dosage of P-407	125
3.3.	P-407-induced lipoprotein profile	132
3.4.	Side-effects of P-407	134
3.5.	Conclusion.....	142
3.6.	Summary	142
3.7.	Discussion.....	142
CHAPTER 4- THE EFFECTS OF P-407-INDUCED HYPER-TGRL ENVIRONMENT ON PERIPHERAL BLOOD MONOCYTES AND TISSUE MACROPHAGES		148
4.1.	Introduction:	148
4.2.	The effect of P-407-induced hyper-TGRL environment on PB MOs.....	149
4.3.	The effect of P-407 on the BM production of MO subsets	161
4.4.	The effect of P-407 on the peripheral conversion of MO subsets	171
4.5.	The effect of P-407-induced hyper-TGRL environment on the behaviour of Gr1 ^{low} MOs	175
4.6.	The effect of P-407-induced hyper-TGRL environment on the extravasation of Gr1 ^{low} MOs	186
4.7.	Conclusion.....	194
4.8.	Discussion.....	194

CHAPTER 5- THE EFFECT OF P-407-INDUCED HYPER-TGRL ENVIRONMENT IN PRIMING THE KIDNEY FOR RENAL INJURY	199
5.1. Introduction:	199
5.2. The effect of 10mg P-407 induced hyper-TGRL environment on IC-mediated renal disease 200	
5.2.1. Renal functional parameters.....	203
5.2.2. Renal histology	206
5.2.3. Glomerular C3 and IgG deposition.....	209
5.3. The effect of a milder hyper-TGRL environment on IC-mediated renal injury.....	217
5.4. Conclusion.....	226
5.5. Discussion.....	226
CHAPTER 6- EFFECTS OF DIET-INDUCED HYPERLIPIDEMIA IN LDLR-DEFICIENT MICE ON MONOCYTES AND RENAL DAMAGE.....	231
6.1. Introduction:	231
6.2. The effect of Ldlr ^{-/-} diet-induced hyperlipidemia on peripheral blood MOs and tissue MØs	232
6.2.1. Changes in peripheral blood MOs and tissue MØs in Ldlr ^{-/-} mice following diet modification	235
6.3. The effect of Ldlr ^{-/-} diet-induced hyperlipidemia on renal damage following aNTN 239	
6.3.1. Lipid levels	240
6.3.2. Renal functional parameters.....	242
6.3.3. Renal histology	244
6.4. Conclusions	252
6.5. Discussion.....	252

CHAPTER 7-	DISCUSSION	255
CHAPTER 8-	CONCLUSION	263
CHAPTER 9-	FUTURE WORK.....	264

List of Figures

Figure 1.1. Chemical structure of major plasma lipids.	30
Figure 1.2. Lipoprotein structure.	32
Figure 1.3. Metabolism of TGRLs.	39
Figure 1.4. HDL metabolism.	44
Figure 1.5. CETP-mediated lipoprotein modification.	47
Figure 1.6. MO subsets in humans and mice.	73
Figure 1.7. MO development.	79
Figure 1.8. The origin of tissue resident MØs.	84
Figure 2.1. Experimental design for time course PB and lipid data.	105
Figure 3.1. Dose-dependent effect of P-407 on plasma lipid levels.	127
Figure 3.2. P-407 trough levels.	130
Figure 3.3. P-407-induced lipoprotein profile.	133
Figure 3.4. Effect of P-407 on body weight, spleen and hematocrit.	136
Figure 3.5. Histological examination of tissues following 28 days of P-407 induced hyper-TGRL state.	138
Figure 3.6. Hematuria and proteinuria following 28 days of P-407-induced hyper-TGRL state.	139
Figure 3.7. Plasma levels of different inflammatory cytokine/chemokines following 28 days of P-407-induced hyper-TGRL state.	141
Figure 4.1. Time course of lipid levels upon 10 and 5mg P-407 injection over a period of 28 days.	151
Figure 4.2. Time course of peripheral blood MOs upon 10 and 5mg P-407 injections.	153
Figure 4.3. The effect of 10mg P-407 injections on the total number of WBCs over a period of 28 days.	154
Figure 4.4. The effect of 10mg P-407 injection on MO subsets in the blood.	157
Figure 4.5. The effect of 5mg P-407 injection on MO subsets in the blood.	158

Figure 4.6. The effect of 10mg P-407 injection on the different peripheral blood cells.	159
Figure 4.7. The effect of 5mg P-407 injection on the different peripheral blood cells.	160
Figure 4.8. Gating strategy used to identify MDPs, mature MOs and their subsets in the BM.	163
Figure 4.9. The effect of P-407-induced hyper-TGRL environment on the percentages of mature MOs, their subsets, and their precursors in the BM.	165
Figure 4.10. The effect of P-407-induced hyper-TGRL environment on the number of MDPs, MOs and their subsets in the BM.	166
Figure 4.11. Gating strategy for the flow cytometry analysis of early BM progenitors.	168
Figure 4.12. Numbers of early BM progenitors after 28 days of P-407 injection.	170
Figure 4.13. The effect of P-407 induced hyper-TGRL environment on BrdU incorporation into the different MO subsets.	174
Figure 4.14. The <i>in vivo</i> effect of P-407-induced hyper-TGRL on GFP ^{high} MO behaviour.	176
Figure 4.15. CD11b expression on MO subsets after 28 days of P-407 administration.	178
Figure 4.16. CD68-stained sections of liver, heart, and kidney following P-407 injections.	181
Figure 4.17. Quantitative representation of CD68 staining in the liver, heart, and kidney following P-407 injections.	182
Figure 4.18. Tissue Ki-67 staining after 4 weeks of P-407 injections.	184
Figure 4.19. BMT experimental plan and PB analysis to check reconstitution.	187
Figure 4.20. Gating and BM reconstitution for MO subsets in BMT mice.	188
Figure 4.21. Flow cytometric analysis of organs from B6 mice following 2 months of BMT with BM cells from Cx3cr1 ^{gfp/+}	190
Figure 4.22. Adoptive transfer experiment.	192
Figure 4.23. Quantitative analysis of the adoptively transferred cells.	193

Figure 5.1. The aNTN model under P-407-induced hyper-TGRL conditions.	202
Figure 5.2. Percentages of mice developing hematuria and proteinuria following aNTN.	204
Figure 5.3. Renal functional parameters after aNTN.	205
Figure 5.4. Histological evaluation of renal tissue after aNTN.	207
Figure 5.5. Comparison of CD68 staining in the absence or presence of aNTN.	208
Figure 5.6. Glomerular C3 and IgG deposition.	211
Figure 5.7. Plasma C3 levels along the course of aNTN.	212
Figure 5.8. Plasma lipid levels of the 2nd NTN experiment using 10mg P-407.	215
Figure 5.9. Renal parameters of the 2nd aNTN experiment using 10mg P-407.	216
Figure 5.10. Plasma lipid levels in response to 5mg P-407 injection over the aNTN experimental period.	219
Figure 5.11. Renal parameters following aNTN induction in mice receiving 5mg P-407 against a PBS control.	220
Figure 5.12. CD68 staining of kidney sections following aNTN induction in mice receiving 5mg P-407.	222
Figure 5.13. Glomerular C3 and IgG staining following the induction of aNTN in mice receiving 5mg P-407.	223
Figure 5.14. Immune response determined at the end point of the aNTN experiment.	225
Figure 6.1. Changes in plasma lipid levels in Ldlr ^{-/-} mice in response to HF or LF diets.	234
Figure 6.2. Numbers of peripheral blood MOs and their subsets in Ldlr ^{-/-} mice fed either HF or LF diets.	236
Figure 6.3. CD68-stained kidney tissue of Ldlr ^{-/-} mice after 50 days of feeding either HF or LF diet.	237
Figure 6.4. Experimental design and lipid levels of the aNTN experiment induced in Ldlr ^{-/-} and B6 mice fed either HF or LF diets.	241
Figure 6.5. Renal functional parameters following the induction of the aNTN model in Ldlr ^{-/-} and B6 mice fed either HF or LF diets.	243

Figure 6.6. Glomerular cellularity score in Ldlr ^{-/-} and B6 fed either HF or LF diets following the induction of the aNTN model.	245
Figure 6.7. CD68-stained kidney tissue following the induction of aNTN in Ldlr ^{-/-} and B6 mice fed either HF or LF diets.	246
Figure 6.8. Plasma lipid levels in Ldlr ^{-/-} mice fed either HF or LF diets over the course of the 2 nd aNTN experiment.	248
Figure 6.9. Renal functional parameters of HF and LF-fed Ldlr ^{-/-} mice following the induction of the 2 nd aNTN experiment.	250
Figure 6.10. CD68 staining of kidney tissue from Ldlr ^{-/-} mice fed either HF or LF diet following the induction of aNTN.	251

List of Tables

Table 1.1. Apolipoprotein distribution and function.....	33
Table 1.2. Summary of classical hyperlipoproteinemia phenotypes.....	51
Table 2.1. List of antibodies used in flow cytometry studies.	113
Table 3.1. Comparison of mean lipid level elevation over the experimental period between the different groups.....	128

List of Abbreviations

Ab	Antibody
Ab	Antibody
ABCA1	ATP-binding cassette transporter A1
ABCG1	ATP-binding cassette transporter G1
Ag	Antigen
AGM	Aorto-gonado-mesonephros
ALT	Alanine transaminase
aNTN	Accelerated nephrotoxic nephritis
APC	Allophycocyanin
APC-Cy7	Allophycocyanin-Cyanine 7
apo	Apolipoprotein
apoE ^{-/-}	Apolipoprotein E knockout mice
AST	Aspartate transaminase
B6	C57BL/6
BM	Bone marrow
BMT	Bone marrow transplant
BrdU	Bromodeoxyuridine
C/EBP α	CCAAT/enhancer-binding protein alpha
C3	Complement component 3
CAD	Coronary artery disease
CARB	Carbohydrate
CCR2	C-C chemokine receptor type 2
CCR2 ^{-/-}	CCR2 knockout
CD	Cluster of differentiation
cDC	Classical DC
cDNA	Complementary DNA
CDP	Common DC precursor
CETP	Cholesterol ester transfer protein
CFA	Complete Freund's adjuvant

CFH	Combined familial hyperlipidemia
CHOL	Cholesterol
CLP	Common lymphoid progenitors
CM	Chylomicron
cMoP	Common monocyte precursor
CMP	Common myeloid progenitors
CMr	Chylomicron remnant
CO ₂	Carbon dioxide
CVD	Cardiovascular disease
CX ₃ CR1	CX3C chemokine receptor 1
CXCL1	chemokine (C-X-C motif) ligand 1
D/L	Dead/live
DAB	3,3'-Diaminobenzidine
DC	Dendritic cells
ddH ₂ O	Double-distilled water
Dil	(1,1'-dioctadecyl-3,3,3',3'-tetramethylindocarbocyanine perchlorate
ds-DNA	Double stranded DNA
E8	Embryonic day 8
EGFP	Enhanced green fluorescent protein
ELISA	Enzyme-linked immunoassay
ESRD	End stage renal disease
FC	Free cholesterol
FcγR	Fcγ receptor
FFA	Free fatty acid
FITC	Fluorescein isothiocyanate
FPLC	Fast-performance liquid chromatography
GATA-1	GATA-binding factor 1
GBM	Glomerular basement membrane
GFP	Green fluorescent protein
GIDH	Glutamate dehydrogenase
GM-CSF	Granulocyte-monocyte colony stimulating factor

GMP	Granulocyte macrophage progenitor
GPI	Glycosylphosphatidylinositol
Gr1	Myeloid differentiation antigen
GWAS	Genome wide association study
H & E	Hematoxylin & eosin
H ₂ O ₂	Hydrogen peroxide
HAEC	Human aortic endothelial cells
Hct	Hematocrit
HDL	High-density lipoprotein
HF	High fat
HIV	Human immunodeficiency virus
HL	Hepatic lipase
HLA-DR	Human leukocyte antigen-DR
HMG-CoA	3-hydroxy-3-methylglutaryl-coenzyme A
HPA	Hypothalamic pituitary axis
HSCs	Hematopoietic stem cells
HSPG	Heparan sulphate proteoglycan
HUVEC	Human umbilical vein endothelial cells
i.p.	Intraperitoneally
i.v.	Intravenous
IC	Immune complex
ICAM	Intercellular adhesion molecules
IDL	Intermediate density lipoprotein
IFN- γ	Interferon- γ
IgG	Immunoglobulin G
IHC	Immunohistochemistry
IL-10	Interleukin-10
IL-6	Interleukin-6
IL-7R α	Interleukin-7 receptor α
IR	Insulin resistance
Ki-67	Proliferation marker

LC	Langerhan's cell
LCAT	Lecithin:cholesterol acyltransferase
LDL	Low density lipoprotein
LDLR	Low density lipoprotein receptor
Ldlr ^{-/-}	LDL receptor knock-out
Lep ^{ob/ob}	Leptin deficient mice
LepR ^{db/db}	Leptin receptor deficient mice
LF	Low fat
LFA-1	Lymphocyte function-associated antigen 1
Lin	Lineage
Lo-SSC	Low side scatter
LP	Lamina propria
LpL	Lipoprotein lipase
LPS	Lipopolysaccharide
LRP	LDL receptor-related protein
LSK	Lineage negative Sca1 ⁺ c-Kit ⁺
LT-HSC	Long-term hematopoietic stem cells
Ly6C	Lymphocyte antigen 6 complex, locus C
Ly6G	Lymphocyte antigen 6 complex, locus G
M1	Classically-activated MØs
M2	Alternatively-activated MØs
mAb	Monoclonal antibody
Mac-1	Macrophage-1 antigen
MC3-R ^{-/-}	Melanocortin 3 receptor knock-out
MC4-R ^{-/-}	Melanocortin 4 receptor knock-out
MCP-1	Monocyte chemoattractant protein-1
M-CSF	Macrophage colony-stimulating factor
MDP	Macrophage/DC progenitor
MEP	Megakaryocyte erythrocyte progenitor
MHC	Major histocompatibility complex
MI	Myocardial infarction

MIP-1 α	Macrophage inflammatory protein 1- α
MO	Monocyte
M \emptyset	Macrophage
MPPs	Multipotent progenitors
MPS	Mononuclear phagocytic system
MS	Metabolic syndrome
MUFA	Monounsaturated fatty acids
NADH	Nicotinamide adenine dinucleotide
NK	Natural killer
NMS	Normal mouse serum
NO	Nitric oxide
NTN	Nephrotoxic nephritis
NTS	Nephrotoxic serum
NZBxW	New Zealand black and white
P-407	Poloxamer 407
PAS	Periodic acid Schiff
PAS-D	Periodic acid Schiff-Diastase
PB	Peripheral blood
PBS	Phosphate buffered solution
pDC	Plasmacytoid DC
PE	Phycoerythrin
PE-Cy7	Phycoerythrin-Cyanine 7
PerCP-Cy5.5	Peridinin Chlorophyll Protein-Cyanine 5.5
PL	Phospholipid
PLP	Periodate-lysine-paraformaldehyde
PMNs	Polymorphonuclear cells
pp	Postprandial
PPAR- γ	Peroxisome proliferator-activated receptor- γ
PPL	Postprandial lipemia
PUFA	Polyunsaturated fatty acids
RBC	Red blood cell

RCT	Reverse cholesterol transport
RLP	Remnant lipoprotein particle
ROS	Reactive oxygen species
RT	Room temperature
Sca-1	Stem cell antigen-1
sd-LDL	Small dense LDL
SFA	Saturated fatty acids
SLE	Systemic lupus erythematosus
SR-B1	Scavenger receptor B1
ss-DNA	Single stranded DNA
ST-HSCs	Short-term hematopoietic stem cells
T2D	Type-2 diabetes
TF	Transcription factor
TG	Triglyceride
TGRL	Triglyceride-rich lipoprotein
Th1	Type-1 helper T cell
Th2	Type 2 helper T cells
Thy1.2	Thymocyte antigen
TLR	Toll-like receptor
TNF- α	Tumor necrosis factor- α
VCAM-1	Vascular cell adhesion molecule 1
VLA-4	Very late antigen-4
VLDL	Very low density lipoprotein
VLDLr	VLDL remnant
WBCs	White blood cells
WT	Wild type
YS	Yolk sac

CHAPTER 1- INTRODUCTION

1.1. Overview

Hypercholesterolemia and post-prandial hypertriglyceridemia are risk factors for cardiovascular disease (CVD). Abnormalities in triglyceride-rich lipoprotein (TGRL) metabolism are frequently encountered in chronic inflammatory conditions such as systemic lupus erythematosus (SLE) and contribute to end organ damage under such circumstances. Monocytes (MO) and macrophages (MØ) are sensitive to changes in circulating lipids and contribute to both the initiation and progression of atherosclerosis. With the growing recognition of MO heterogeneity, the distinct functional role of each subset deserves more attention. In the mouse, two MO subsets are recognized; Gr1^{high} or “inflammatory” MOs and Gr1^{low} or “patrolling” MOs. Inflammatory MOs populate inflamed tissue giving rise to MØs, whereas Gr1^{low} MOs appear to crawl along the endothelial surface under steady-state conditions and rarely extravasate. Hypercholesterolemia was reported to cause a progressive increase in circulating Gr1^{high} MOs favouring their recruitment into atherosclerotic lesions with minimal effect on Gr1^{low} MOs. However, the effect of hypertriglyceridemia on these elegant cells has not been addressed with such detail. Current sedentary life style along with the advent of quick fatty meals subjects our bodies to a repetitive influx of TGRLs on daily basis. Understanding the effects of such an environment on normal homeostasis is deemed necessary. In view of their intravascular location, MOs are at the front line against the daily fluctuations of TGRLs. With their documented role in hypercholesterolemia-mediated vascular damage, it becomes reasonable to hypothesize a central role for these cells in mediating the injurious effects of a hyper-TGRL state. The aim of the

present study is to delineate the effect of a hyper-TGRL state and hypertriglyceridemia on the behaviour of MOs under steady state conditions and the impact of such an environment on end organ damage in the presence of secondary inflammatory condition.

This introduction will thus present an overview on TGRL metabolism and their atherogenic potential. This will be followed by a brief account on MOs and MØs with special emphasis on the current literature supporting their heterogeneity and their behaviour in a hyperlipidemic state. The introduction will be concluded by a short report on the evidence supporting the detrimental role of a hyper-TGRL environment on end organ damage in the presence of an inflammatory disease using kidney inflammation as an example.

1.2. Triglycerides (TGs) and TGRLs: their pathogenic potential

Lipids comprise a heterogeneous group of organic compounds with diverse structural as well as metabolic functions. They constitute a major energy source for the body and serve as building blocks for synthesis of cellular membranes (Champe et al., 2005; Murray et al., 2003). Lipids are also precursors for a variety of vital regulatory compounds and hormones including; steroid hormones, prostaglandins and leukotrienes (Champe et al., 2005). Of the various classes of biologically important lipids, plasma lipids and lipoproteins received the greatest attention in the literature. Abnormal plasma lipid levels is a leading risk factor for atherosclerosis and CAD worldwide (Yusuf et al., 2004). Despite the recognition of atherosclerosis as a multifactorial disease, disturbances in lipid metabolism remain at the root of the problem and one of the driving forces behind its pathology. Elevated levels of plasma cholesterol (CHOL) and CHOL-rich low density lipoproteins (LDL) are generally accepted as the major culprits. The isolation of CHOL and modified-LDL from atherosclerotic plaques along with the observed reduction in the incidence of ischemic heart disease that accompanied the use of LDL cholesterol lowering agents (Grundy, 1998; Ramasamy, 2013), have emphasized the role played by CHOL in the pathogenesis of atherosclerosis causing it to take centre stage in atherosclerosis research and management.

The role of TGs, however, is less clear. Despite various studies reporting elevated TG levels as an independent risk factor in CAD (Boren et al., 2014; Stavenow and Kjellstrom, 1999; Stensvold et al., 1993), this association has been viewed with scepticism leading to a controversial debate on their role in CAD (Boren et al., 2014; Goldberg et al., 2011; Kannel and Vasan, 2009). The uncertainty behind such an

association stems from several factors; firstly, the level of TGs in plasma is closely linked and inversely related to that of the cardio-protective high density lipoprotein (HDL), and as such, HDL levels need to be considered whenever a link between hypertriglyceridemia and CAD is being entertained. Some of the earlier studies that demonstrated an independent risk factor for TGs in CAD did not measure HDL and thus were unable to correct for it (Stavenow and Kjellstrom, 1999; Stensvold et al., 1993). Whereas other studies have failed to detect an association between hypertriglyceridemia and CAD once HDL levels were taken into account (Assmann and Schulte, 1992; Castelli, 1986). Secondly, hypertriglyceridemia seldom occurs as a solitary abnormality in the clinical setting, rather it is usually associated with hypercholesterolemia or more commonly with an array of metabolic derangements as occurs in the context of diabetes and the metabolic syndrome (MS), making it difficult to dissect its isolated role in disease development and progression (Goldberg et al., 2011). The above along with the fact that atherosclerotic plaques contain CHOL rather than TGs, have undermined the impact of abnormal TG levels in atherosclerosis and CAD (Goldberg et al., 2011).

Nonetheless, a growing appreciation of the importance of TG metabolic derangement on CAD risk is emerging. The recognition of the intricate relationship between HDL and TG metabolism have raised questions on the efficacy of multivariate analysis in assessing the independent CAD risk of such interlinked variables (Patsch et al., 1992). In fact, and regardless of the results of multivariate analysis, the concomitant presence of hypertriglyceridemia with low HDL levels is associated with marked increase in CAD risk when compared to the sole presence of low HDL levels (Assmann and Schulte,

1992; Castelli, 1986). The use of non-fasting TG levels has also contributed to the enhancement of the role of TGs in CAD by providing consistent evidence supporting its CAD risk prediction (Kannel and Vasan, 2009). Given that humans spend most of their time in a postprandial (pp) state, the superiority of non-fasting TG levels over their fasting counterparts as predictors for CAD risk, carry great implications. The current western life-style dominated by quick fatty meals and lack of physical exercise, subjects our bodies to repetitive transient elevations in plasma lipids following each meal (Napolitano et al., 2013). This massive pp influx of lipids is mainly caused by a surge in TGs and TGRLs and has come to be known as “pp lipemia” (Napolitano et al., 2013; Zilversmit, 1995). There is mounting evidence supporting the atherogenic potential of pp lipemia (Zilversmit, 1995). Furthermore, changes in plasma lipid profile similar to those observed postprandially occur in various disease conditions, such as SLE and the nephrotic syndrome, and are thought to contribute to enhanced morbidity and mortality (Bobulescu, 2010; Bruce, 2005). Overall disturbances in TG metabolism, whether due to primary abnormalities in TG handling machinery or arising as secondary complications of other diseases, carry significant repercussions on the general well-being as well as the course of the concomitant disease. An understanding of how such disturbances influence the homeostatic balance of the body and its eventual response to injury is deemed necessary. However, and before discussing the pathogenic role of TGs and their carrier lipoprotein particles, it is necessary have a general understanding of the pathways involved in TG metabolism and their interactions. This part of the introduction aims to paint a broad picture of lipoprotein metabolism starting with a brief overview on major plasma lipids and their carrier lipoproteins, followed by a more

extensive description of TG metabolism emphasising the interactions between TGRLs and other particles. This is followed by a short account on causes of hypertriglyceridemia and its pathogenicity, followed by a description of the available hypertriglyceridemic animal models used in lipid research along with a more detailed account of the model used in the current study: the P-407 model.

1.2.1. Plasma lipids

Plasma lipids exist in four major forms; TGs (16%), phospholipids (PL) (30%), CHOL (14%), cholesterol esters (CE) (36%), and a small fraction of unesterified (free) fatty acids (FFA) (4%) (Murray et al., 2003).

Fatty acids are essential molecules characterised by the presence of a hydrophobic hydrocarbon chain of varying length with one end attached to a hydrophilic hydroxyl group (Coffee, 1998). They serve as efficient energy substrates and as precursors for the majority of other lipid classes (Coffee, 1998; Young and Zechner, 2013). In plasma, fatty acids can occur in one of two forms; the free “un-esterified” form, known as free fatty acids (FFA), or the “esterified” form, which represents fatty acids incorporated into more complex structures such as, TGs, PLs, and CEs. Only a minority of fatty acids are found in their free “un-esterified” form in plasma where they circulate bound to albumin, whereas the majority are in their esterified forms (Champe et al., 2005). The esterification of three fatty acids to glycerol, a trivalent alcohol, forms **TGs** (Young and Zechner, 2013) (Fig-1.1). TGs represent the major storage form of lipids in the body and can be found as lipid droplets in the cytoplasm of adipocytes. They are extremely hydrophobic and are transported in plasma packaged in particles known as “lipoproteins”. Hydrolysis of TGs releases energy by removing one or two fatty acids,

the energy substrates, from the TG molecule yielding diacylglycerol and monoacylglycerol, respectively (Champe et al., 2005; Coffee, 1998). **CHOL**, on the other hand, is composed of four fused hydrocarbon rings attached on one end to a hydrocarbon tail and to a hydroxyl group at the other end (Champe et al., 2005) (Fig-1.1). As with fatty acids, most of the CHOL in plasma is in its esterified form, i.e. attached to a fatty acid (Champe et al., 2005). Esterified CHOL, CEs, are extremely hydrophobic and thus are carried in the core of the lipoprotein particle. The less hydrophobic un-esterified “free” cholesterol (FC) forms part of the amphipathic shell surrounding the hydrophobic core with its polar end oriented towards the outer surface of the lipoprotein (Champe et al., 2005; Murray et al., 2003). CHOL performs many important biological functions in the body being a major structural component of plasma membranes as well as a precursor of several key biological compounds including; steroid hormones, bile acids, and vitamin D (Champe et al., 2005). In addition to FC, the outer shell of the lipoprotein particle is largely made of **PLs** (Murray et al., 2003). PLs are amphipathic lipid molecules that constitute the main structural component of cellular membranes (Coffee, 1998). Their amphipathic nature is attributed to their structure which is characterised by a hydrophilic head made of two alcohols linked together through a phosphodiester bridge, and a hydrophobic tail of fatty acids or fatty acid-derived hydrocarbon (Champe et al., 2005; Coffee, 1998) (Fig-1.1).

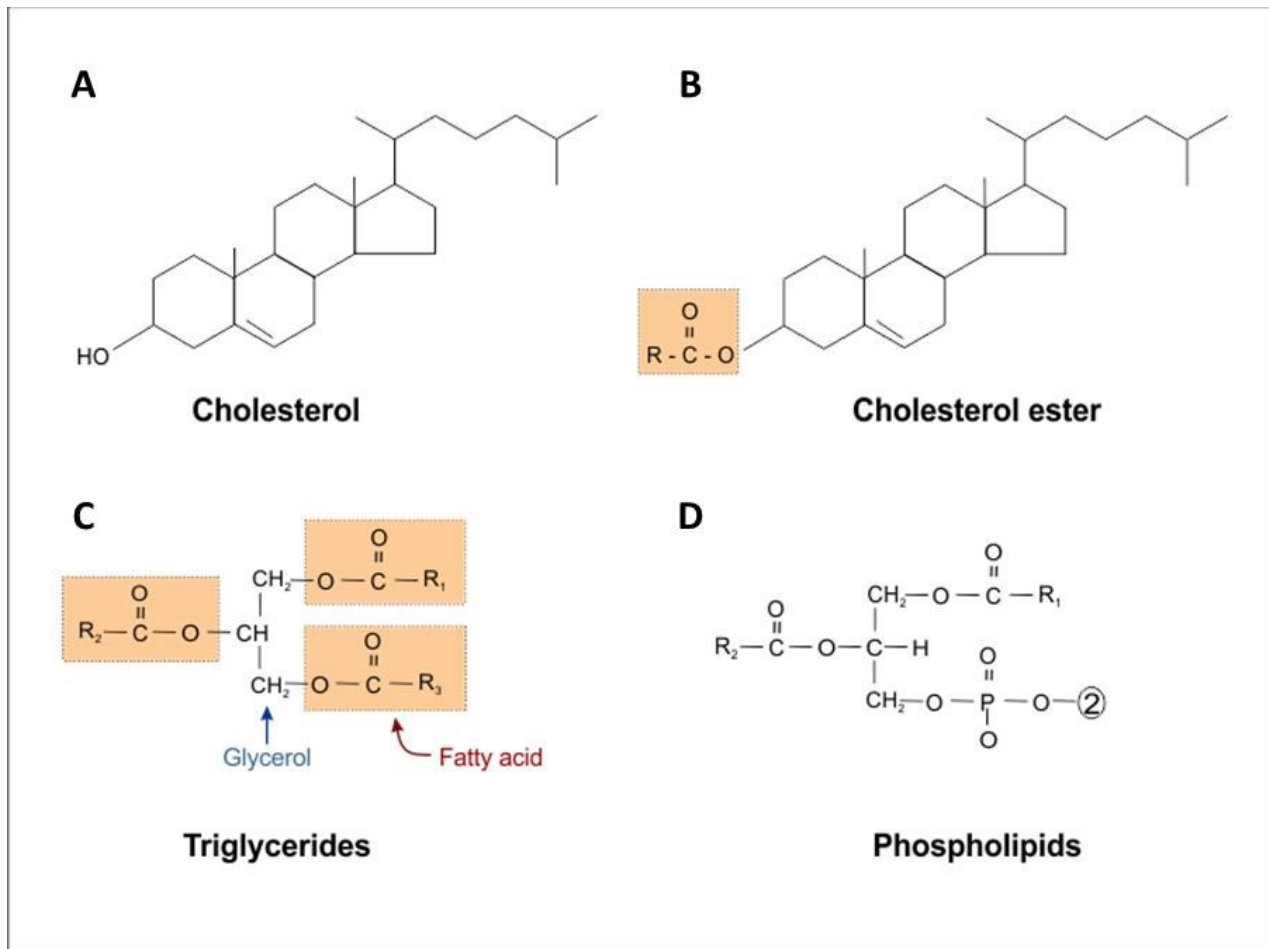


Figure 1.1. Chemical structure of major plasma lipids.

Chemical structure of (A) CHOL and (B) CE. The latter is formed by the esterification and replacement of the hydroxyl group in CHOL with a fatty acid. TGs (C) are formed by esterification of three fatty acids to glycerol. (D) PLs are two alcohols linked together by a phosphodiester bridge, the first alcohol is diacylglycerol and the second, denoted by ②, can be choline or ethanolamine or serine or inositol. Figure modified from (Coffee, 1998).

Due to their hydrophobic nature, plasma lipids are generally transported packaged into lipoproteins. Lipoproteins are a heterogeneous group of particles that share a common basic structure consisting of a hydrophobic TGs and CEs-rich lipid core shielded from the surrounding aqueous plasma by a single layer of amphipathic lipids, PLs and FC, along with specialised proteins known as apolipoproteins or “apoproteins” (Fig-1.2) (Champe et al., 2005; Murray et al., 2003). Apolipoproteins are fundamental components of lipoproteins and serve structural as well as metabolic functions. Several classes of apolipoproteins exist and are designated as apo A to E. The primary function of each class is shown in Table-1.1. With the exception of the structural apo B, most of these apoproteins are constantly being exchanged between the different lipoprotein particles.

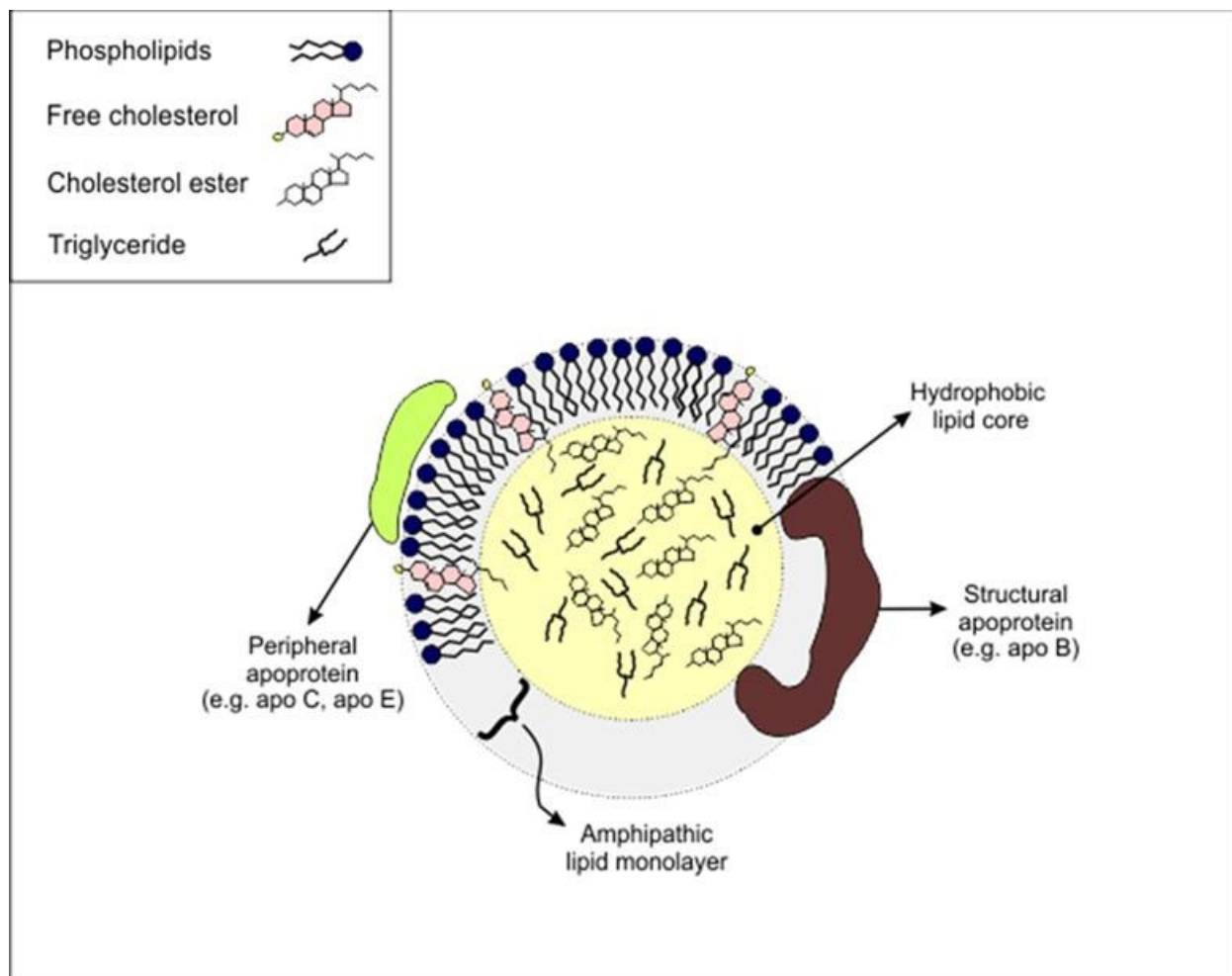


Figure 1.2. Lipoprotein structure.

Graphic representation of the general structure of a lipoprotein particle showing the TG and CE-rich hydrophobic lipid core surrounded by a single layer of amphipathic lipids, mainly PLs and FC. The amphipathic lipid shell contains different apolipoproteins that may serve as structural or peripheral proteins. Adopted with modification from (Murray et al., 2003).

Table 1.1. Apolipoprotein distribution and function.

Apolipoprotein	Major function	Lipoprotein association
Apo A		
Apo A-I	<ul style="list-style-type: none"> - Important for reverse cholesterol cycle - Co-factor for LCAT 	HDL
Apo A-II	HDL structure	HDL
Apo A-IV	? Role in CM synthesis and dietary fat absorption	TGRL and HDL
Apo A-V	Promotes LpL-mediated lipolysis by enhancing attachment of lipoproteins	
Apo B		
Apo B-48	Important for CM synthesis and secretion	CM, CMr
Apo B-100	<ul style="list-style-type: none"> - Important for VLDL synthesis and secretion - LDL receptor ligand-mediates clearance of the particles from circulation 	VLDL, IDL, LDL
Apo C		
Apo C-I	<ul style="list-style-type: none"> - Inhibits LpL - ? Inhibits CETP 	HDL, VLDL, CM
Apo C-II	Co-factor for LpL	HDL, VLDL, CM
Apo C-III	Inhibits LpL	HDL, VLDL, and CM
Apo E	Ligand for LDL and LDL-like receptors-mediates the clearance of TGRL and their remnants from the circulation	HDL, VLDL, IDL, CM, and CMr

(Li et al., 2014; Murray et al., 2003; Ribalta et al., 2003; Sotos-Prieto and Penalvo, 2013; Tulenko and Sumner, 2002)

Lipoproteins differ in their size and density. The density of lipoproteins decreases as the proportion of lipid to protein within the particle increases, and are accordingly divided into five major classes; chylomicrons (CM), very low density lipoproteins (VLDL), intermediate density lipoproteins (IDL), LDL, and HDL. TGs and CEs are carried by all plasma lipoproteins, though in different proportions. TGs constitute the major lipid carried by CMs and VLDL, and hence these two lipoprotein classes along with their remnant products of degradation are collectively referred to as “TGRLs”. CHOL, on the other hand, is the major constituent of LDL and HDL (Murray et al., 2003).

The primary role of lipoproteins is to transport lipids from sites of production to sites of usage in the body (CM and VLDL). This forward movement is paralleled by an opposite movement of excess cholesterol from peripheral tissue to the liver for its eventual elimination known as, “Reverse Cholesterol Transport (RCT)” mediated primarily by HDL.

An understanding of the role of TGRLs in human diseases mandates an understanding of the pathways governing lipoprotein metabolism as well as their interactions.

1.2.2. TGRL metabolism

TGs account for 90-95% of ingested dietary fat with the remainder being composed of PLs, CHOL and fat soluble vitamins (Champe et al., 2005; Ramasamy, 2013). Under the influence of a variety of lipases located in the digestive system, dietary TGs are sequentially broken down to diacylglycerol and 2-monoacylglycerols yielding FFAs (Champe et al., 2005; Ramasamy, 2013). In the intestine the primary products of dietary lipid degradation (FFAs, 2-monoacylglycerol, and CHOL) are absorbed into enterocytes, where they are re-esterified forming TGs and CEs and packaged along with intestinally

synthesized apo B-48 into “nascent” CMs (Champe et al., 2005). Following their synthesis, nascent CMs are secreted into surrounding lymphatics and enter the blood stream via the thoracic duct. The liver is also capable of synthesising TGRLs and secreting them in the form of VLDLs. TGs incorporated into VLDL come from several sources including; TGs arriving at the liver via remnant lipoprotein particle uptake as well as newly synthesized TGs by hepatic re-esterification of FAs (Tulenکو and Sumner, 2002). FAs used in hepatic TG synthesis arise either from “de novo” hepatic synthesis of FAs secondary to excess carbohydrate intake and/or the uptake of FFAs liberated into circulation following adipose tissue lipolysis, as occurs during fasting (Berglund et al., 2012; Murray et al., 2003; Ramasamy, 2013). Hence, VLDL production by the liver is largely driven by FFA availability, which, in turn, is subject to insulin control (Adiels et al., 2008). Endogenously-derived TGs along with substantial amounts of CEs are incorporated into newly synthesized apo B-100 in the liver and secreted into the circulation as the “nascent” VLDL particle (Ramasamy, 2013).

Apo B is synthesized by both the intestine and the liver and is a structural pre-requisite for the synthesis and secretion of apo B-containing lipoproteins, i.e. CM and VLDL, by these organs. Intestinal apo B-48 is a truncated form of liver-derived apo B (B-100) that lacks the LDL-receptor (LDLR) binding domain (Murray et al., 2003; Ramasamy, 2013). Each apo B-containing lipoprotein contains one apo B molecule (Ramasamy, 2013).

Upon entering the circulation, both nascent particles mature by acquiring apo C-II and apo E from circulating HDL (Murray et al., 2003). Apo C-II serves as a co-factor for lipoprotein lipase (LpL), whereas apo E is a ligand for lipoprotein receptors (Murray et

al., 2003). As mature CMs and VLDL circulate, their TG content is hydrolysed by the action of the LpL enzyme located on the endothelial surface yielding FFA and glycerol. LpL is a member of the lipase family of enzymes that play crucial roles in lipid metabolism (Von Eckardstein et al., 2001). LpL functions mainly as a TG lipase facilitating the uptake of TGs that are otherwise unable to cross cellular membranes. This is achieved by LpL-mediated intravascular lipolysis of TGs releasing FFAs and glycerol that can easily be taken up into surrounding parenchymal cells (Young and Zechner, 2013). LpL is a glycoprotein with two structurally distinct domains; the N-terminal domain containing the apo C-II binding site along with the catalytic site, and a C-terminal domain containing lipoprotein-binding site (Li et al., 2014; Wong et al., 1994). The active enzyme is a homodimer arranged in a head-to-tail orientation with the lipid-binding domain of one monomer facing the catalytic domain of the second monomer, providing it with its substrate (Young and Zechner, 2013). Synthesis of LpL occurs primarily in parenchymal cells of adipose, skeletal and cardiac tissues. Following its synthesis, the enzyme is trans-located to the luminal surface of the endothelium where it gets anchored to the endothelium via heparan sulphate proteoglycans (HSPG) and exerts its lipolytic function (Li et al., 2014; Young and Zechner, 2013). MØs have also been shown to secrete LpL (Khoo et al., 1981; Stray et al., 1985). The function of LpL differs according to its location; in the heart and skeletal muscle, the LpL-mediated lipolysis of TGRL releases FFAs that are mainly used for oxidation and energy production by these tissues, whereas in adipose tissue, FFAs released by the lipolytic action of LpL are channelled for lipid storage. The activity of LpL can be modified, as

presented earlier, by several proteins such as apo C-II as well as hormones such as insulin, steroid hormones and catecholamines (Li et al., 2014).

The shedding of the TG content of both CMs and VLDLs along with their surface apo C-II results in the generation of smaller TG-depleted remnant lipoprotein particles (TGRL remnants), i.e. CM remnant (CMr) and VLDL remnant (VLDLr or IDL) (Berglund et al., 2012; Ramasamy, 2013). In the hepatic bed, the contents of CMr undergo further processing by hepatic lipase (HL), another lipase located in hepatic peri-sinusoidal space, and are rapidly cleared up by the liver (Ramasamy, 2013; Tulenko and Sumner, 2002). VLDLr/IDL may be taken up directly by the liver or their remaining TG content may undergo further degradation yielding the smaller CHOL-rich LDL (Murray et al., 2003). The resultant LDL particle is responsible for providing CHOL to peripheral tissues or returning it to the liver (Champe et al., 2005). The uptake of the TGRL remnant particles by the liver is mediated by both the LDLR and the LDL receptor-related protein (LRP). The LDLR recognizes apo B-100 and apo E, but not apo B-48, and is mainly concerned with the clearance of apo B-100 containing lipoproteins (i.e. IDL and LDL). However, due to its recognition of apo E, LDLR may also contribute to the clearance of CMr. The LRP, on the other hand, cannot bind apo B but recognises apo E and is thought to be the primary receptor for TGRL remnant particles, specifically CMr (Karpe, 1999; Murray et al., 2003; Ramasamy, 2013). Apo E is thus crucial for the liver-mediated uptake of TGRL remnant lipoproteins, and its deficiency or the presence of less efficient isoforms of the protein such as apo E-2 results in the accumulation of these remnant particles in the blood and subsequent development of hypertriglyceridemia (Ribalta et al., 2003). Following their uptake by the liver, the

particles are degraded and their content re-used. A summary of TGRL metabolism is shown in Fig-1.3.

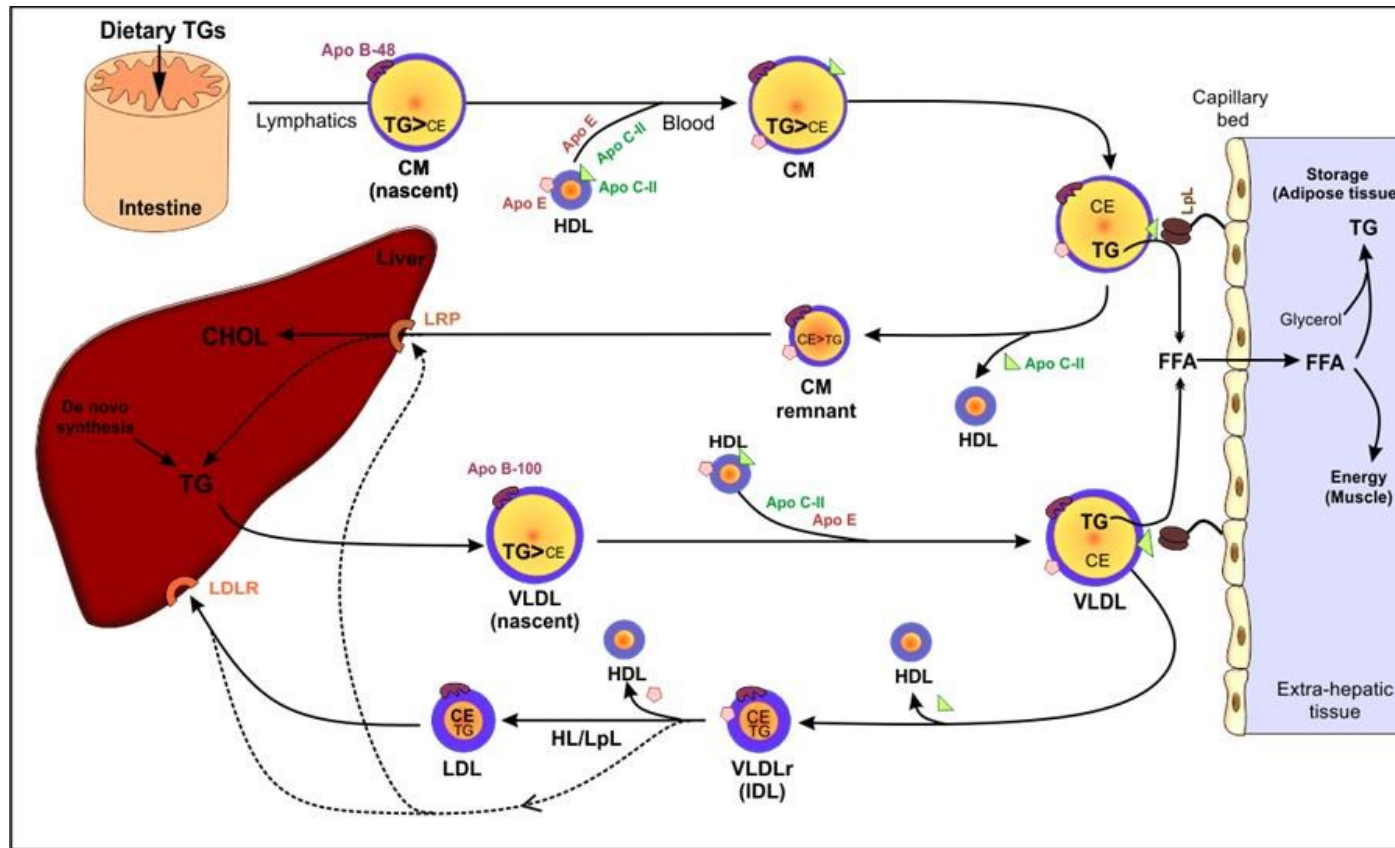


Figure 1.3. Metabolism of TGRLs.

A diagrammatic representation of TGRL metabolism. Dietary TGs are packaged into nascent CMs and secreted into lymphatics. They acquire apo C-II and apo E from HDL as they enter the circulation forming mature CMs. In the capillary bed, their TG content is hydrolysed by LpL forming remnant particles (CMr) which are taken up and recycled by the liver. Endogenous TGs are packaged and secreted by the liver as nascent VLDL. In the circulation they acquire apo C-II and apo E from HDL forming the mature VLDL, which is eventually hydrolysed by LpL forming the remnant particle, VLDLr (IDL). IDL is either taken up directly by the liver or may undergo further hydrolysis forming LDL that is cleared by the liver via the LDLR. Adopted with modification from (Champe et al., 2005).

It becomes clear that CMs and VLDLs are concerned with the delivery of dietary and endogenous TGs, respectively, from sites of production to peripheral tissues where they are used either for energy production or storage. The delivery of their TG content as well as the eventual uptake of their remnant particles by the liver is dependent upon the presence of certain surface apoproteins such as apo C-II and apo E, which they acquire from circulating HDL. However, apoproteins are not the only thing being exchanged between HDL and TGRLs. These lipoproteins exchange their core lipids as well. As a result, the composition of lipoprotein particles is very dynamic and undergoes many modifications during its journey between the liver and peripheral tissues. HDL is a central element in this dynamic remodelling of lipoproteins by being both a repository for apoproteins, as well as the main vehicle by which excess tissue CHOL gets eliminated from the body (Rosenson et al., 2012; Von Eckardstein et al., 2001). The disposal of CHOL from the body is achieved by a series of changes in the composition of HDL particle resulting in the net movement of CHOL from peripheral tissues to the liver or intestine for its ultimate biliary excretion (Rosenson et al., 2012). While performing its function, HDL does not only acquire free cholesterol (FC) from peripheral tissues, it also donates some of its CE content to VLDL and LDL in exchange for their TG content. This heterogeneous lipid exchange between the different lipoprotein particles is mediated by cholesterol ester transfer protein (CETP) and forms the basis for the pathogenicity of TGRLs in hypertriglyceridemic states.

1.2.3. RCT and the CETP-mediated lipid exchange

HDL is synthesized by the liver and intestinal cells from which it gets released into the circulation as “nascent” or pre- β -HDL (Tulenکو and Sumner, 2002). The pre- β -HDL is a

small discoidal particle containing apo A-I either as a lipid-free apolipoprotein (lipid-poor apo A-I) or in association with phospholipids and represents the progenitor form for all other HDL classes (Tulenکو and Sumner, 2002; Von Eckardstein et al., 2001). As these lipid-poor pre- β -HDL particles circulate, they avidly acquire FC from peripheral tissues. CHOL efflux from peripheral cells into nascent HDL is achieved by simple aqueous diffusion and/or through more active mechanisms involving ATP-binding cassette transporters A1 and G1 (ABCA1 and ABCG1) and scavenger receptor B1 (SR-B1). The latter plays a role in CHOL efflux mainly from M ϕ (Fu, 2010; Rosenson et al., 2012). The initial efflux of FC into the lipid-poor pre- β -HDL is thought to be facilitated by binding to ABCA1 (Rosenson et al., 2012; Tall et al., 2012; Tulenko and Sumner, 2002). Apo A-I on the surface of pre- β -HDL interacts with the ABCA1 transporter resulting in the hydrolysis of cellular CE to FC, which is then adsorbed onto the surface of the pre- β -HDL particle (Ramasamy, 2013; Tulenko and Sumner, 2002). On the surface of HDL, the newly acquired FC is then re-esterified forming the fully hydrophobic CE that moves into the lipophilic core of the particle creating more space for further FC uptake (Tulenko and Sumner, 2002). This re-esterification process is mediated by the action of lecithin:cholesterol acyltransferase enzyme (LCAT) with apo A-I acting as its co-factor. Because FC adsorbed on the surface of the lipoproteins equilibrates rapidly with that of the cell membranes, the re-esterification reaction by LCAT and movement of CE into the core of the particle serves to maintain a concentration gradient favouring further efflux of FC from cell membranes into the HDL particle (Barter et al., 1982; Murray et al., 2003; Rosenson et al., 2012). As the discoidal pre- β -HDL accumulates CE into its core, it gradually expands forming the more mature HDL₃ particle. Further acquisition of

FC from peripheral cells into the HDL₃ particle is thought to occur by simple aqueous diffusion and/or through ABCG1, and results in the formation of the larger, more spherical HDL₂ particles (Von Eckardstein et al., 2001). The mature CHOL-rich HDL₃ and HDL₂ particles are collectively known as α -HDL, and constitute the majority of circulating HDL in humans (Ramasamy, 2013; Tulenko and Sumner, 2002). Apart from FC, these particles acquire several apoproteins such as apo A-II, apo E, and apo C from circulating apo B-containing lipoproteins (Tulenko and Sumner, 2002).

Harvested CE in mature α -HDL particles gets eliminated either directly or indirectly by the liver (Tulenko and Sumner, 2002; Von Eckardstein et al., 2001). Direct elimination involves either the hepatic SR-B1-mediated selective uptake of cholesterol from cholesterol-rich α -HDL without particle internalisation or whole particle uptake mediated by apo E receptors (Von Eckardstein et al., 2001). The SR-B1 uptake involves the interaction of hepatic SR-B1 with HDL via apoA-I that acts as a ligand for SR-B1 (Murray et al., 2003; Ribalta et al., 2003; Tulenko and Sumner, 2002). Upon binding to SR-B1, the CE content of α -HDL is taken up by the liver without internalizing the HDL particle, leaving behind a lipid-depleted HDL particle that dissociates and re-enters the circulation (Rosenson et al., 2012; Von Eckardstein et al., 2001). The uptake of lipids by SR-B1 is thought to be facilitated by the hydrolytic action of HL located on the sinusoidal endothelium (Von Eckardstein et al., 2001). Conversely, uptake via apo E receptors such as LDL receptor involves internalization of the whole particle and its eventual degradation (Von Eckardstein et al., 2001). The indirect disposal of HDL-cholesterol involves an exchange mechanism mediated by CETP which transfers CE from α -HDL into apo B-containing lipoproteins (i.e. VLDL and LDL) in exchange for TGs

(Ramasamy, 2013; Tulenko and Sumner, 2002). This reciprocal exchange generates a large TG-enriched HDL as well as CE-enriched VLDL and LDL. The CE-enriched apo B-containing lipoproteins are cleared by the liver via LDLR- and LRP-mediated mechanisms (Ramasamy, 2013). While the TG content of the TG-enriched HDL undergoes hydrolysis via HL re-generating the smaller HDL₃ particle and releasing lipid-poor apo A-I ready for another round of CHOL uptake (Masson et al., 2009). A schematic representation of HDL metabolism is shown in Fig-1.4.

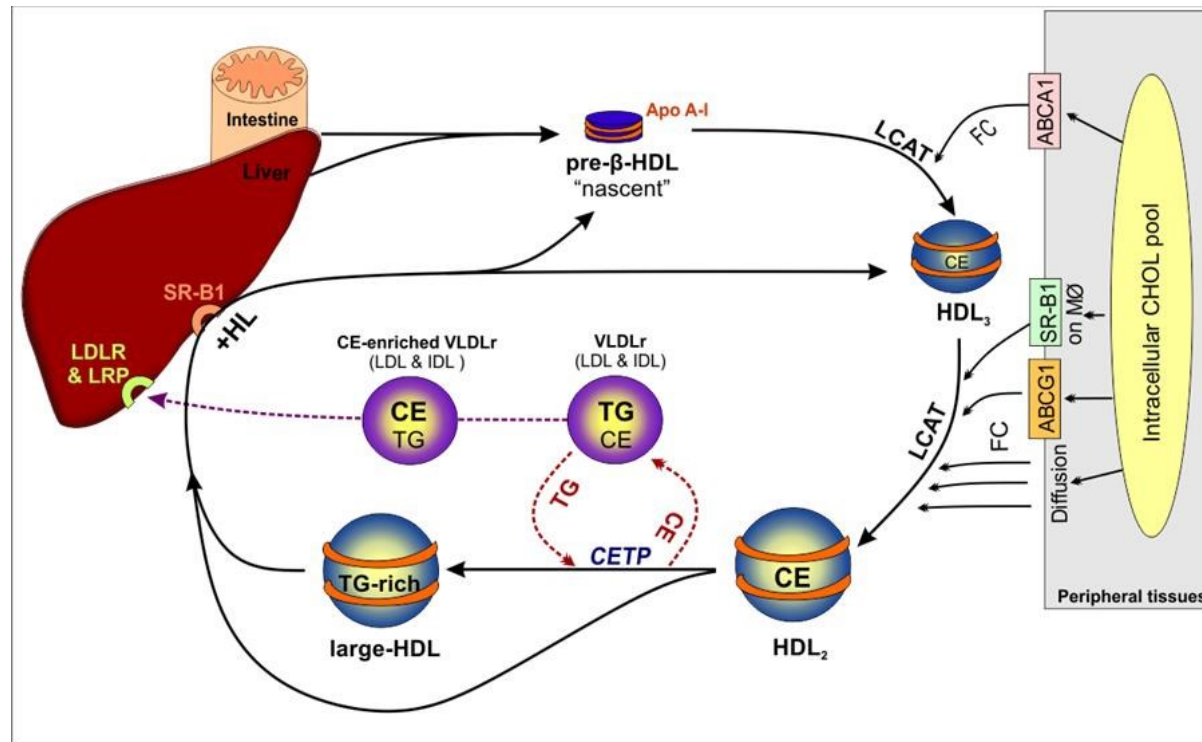


Figure 1.4. HDL metabolism

A graphic representation of HDL metabolism. The liver and intestine secrete the progenitor lipid-poor apo A-I particle “pre-β-HDL” or “nascent HDL” into the circulation. The pre-β-HDL acquires FC from peripheral cells through aqueous diffusion, ABCA1 and ABCG1-mediated transport or, in MØ, SR-B1-mediated efflux. Acquired FC is then re-esterified by LCAT forming CE that moves into the core of the particle. The accumulation of CE into the HDL particle generates HDL₃ and HDL₂, sequentially. The combined action of HL and SR-B1 results in the selective uptake of CE content of HDL₂ into the liver, releasing HDL₃ and lipid-poor HDL particles. HDL₂ may undergo further modification in plasma mediated by CETP resulting in the acquisition of TGs from VLDLr and LDL in exchange for CE. The TG-enriched HDL is a favourable substrate for HL, while CE-enriched VLDLr is eliminated by apo E receptors (LDLR and LRP). Adopted with modification from (Ohashi et al., 2005; Von Eckardstein et al., 2001).

CETP plays an important role in lipoprotein remodelling by promoting lipid exchange between lipoprotein particles with different CE/TG ratios (Masson et al., 2009). CETP-mediated lipid exchange is not restricted to the transfer of CEs and TGs between HDL and apo B-containing lipoproteins, but also includes a similar exchange between apo B-containing lipoproteins themselves, namely between VLDL and LDL. The action of CETP appears to promote a net transfer of TG from VLDL to both LDL and HDL, while promoting the transfer of CE from HDL into both VLDL and LDL. In this context, LDL accepts TGs from VLDL and donates them to HDL with CE flowing in the opposite direction, HDL→LDL→VLDL (Fig-1.5). Under steady state conditions, CETP plays in favour of RCT by providing additional means for CHOL disposal through LDL (Masson et al., 2009). However, in the presence of hypertriglyceridemia, its action may take an unfavourable course. Elevated levels of circulating TGRLs, specifically VLDLs and their remnant particles, promote an exaggerated transfer of their TG content into both HDL and LDL in exchange for their CE contents. Thus this diverts newly acquired CE from its path for hepatic disposal via LDL and allows it to linger in the circulation in association with VLDLr, contributing to their atherogenic nature (Patsch et al., 1992; Zilversmit, 1995). Not only are the CE-enriched VLDLrs atherogenic, but also are the TG-enriched HDL and LDL. TG-enrichment of CE-depleted HDL and LDL makes them more vulnerable for lipolytic modification by HL at the hepatic bed generating small dense LDL (sd-LDL) and HDL (sd-HDL) particles. The presence of sd-LDL in circulation has been associated with increased risk for CVD, whereas sd-HDL undergoes rapid clearance from the body leading to a drop in circulating HDL levels (Fig-1.5) (Adiels et al., 2008; Lamarche et al., 1999). Therefore, an increase in TGRLs in circulation drives

a series of changes in the composition and size of lipoproteins that are mediated mainly by CETP and HL. These changes result in the accumulation of CE-enriched VLDLr and sd-LDL in plasma along with the enhanced loss of HDL from circulation (Grundy, 1998). The co-existence of these three abnormalities is known as the “atherogenic lipid triad” and have been reported to be extremely atherogenic (Grundy, 1998).

From the above it can be appreciated that each class of lipoprotein represents a heterogeneous group of particles. Heterogeneity arises from differences in size as well as in composition determined by the interplay of several factors, enzymes, and receptors. The fate of these particles and the body’s ability to metabolize them is also a function of their composition. Hypertriglyceridemia, arising from various causes, drives a series of changes in lipoprotein composition culminating in the generation of a pathogenic phenotype that have detrimental consequences on the individual’s well-being (Fig-1.5).

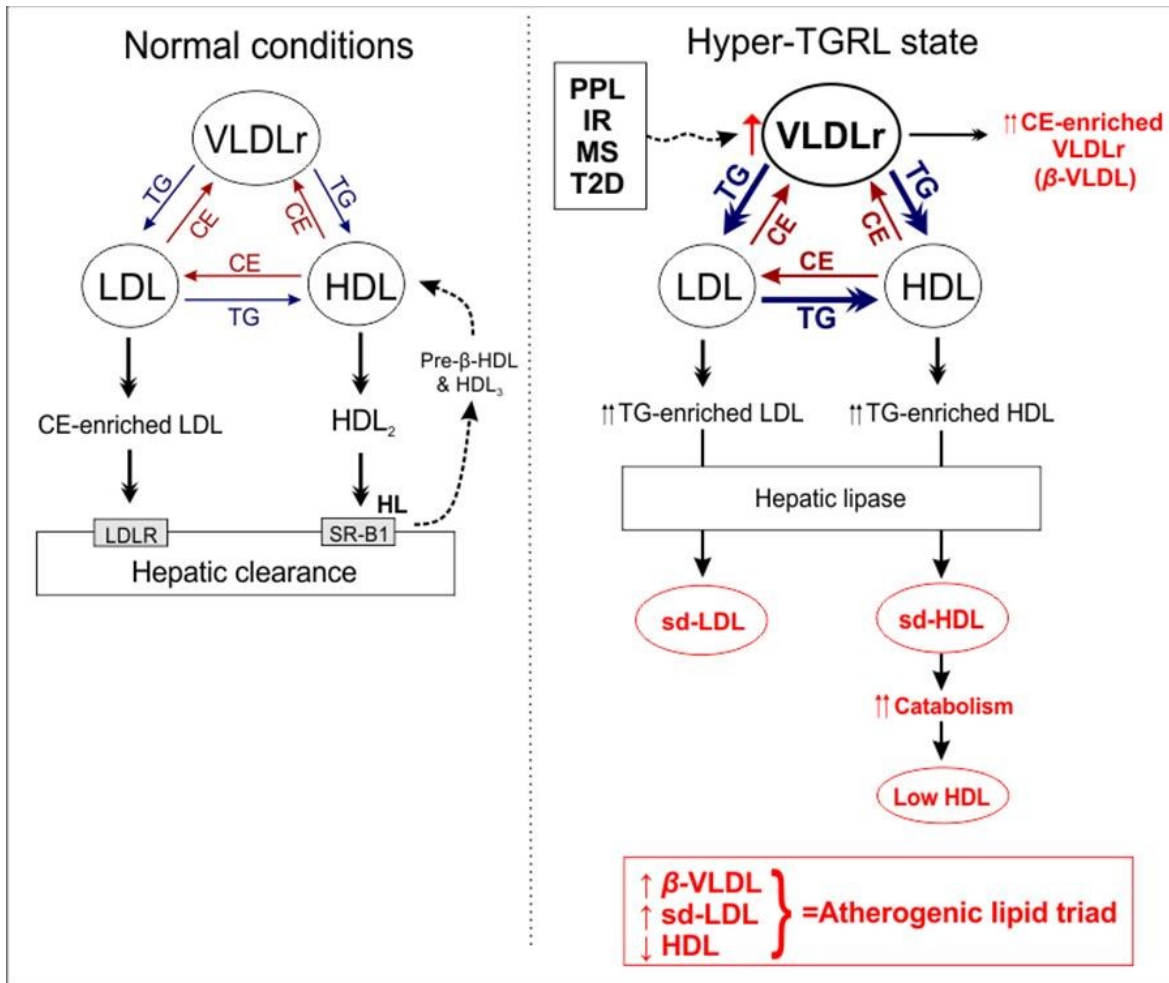


Figure 1.5. CETP-mediated lipoprotein modification

Diagrammatic representation of CETP-mediated modification of lipoproteins in hyper-TGRL states compared to normal steady state conditions. Under steady state conditions, CETP mediates the transfer of CE from HDL to VLDL remnants and LDL in exchange for TGs, generating CE-enriched LDL and a slightly TG-enriched HDL₂. CE-enriched LDL is cleared by the liver via LDLR pathway, whereas the TG content of HDL₂ along with its CE are selectively taken up by SR-B1 releasing lipid-poor apo A-I and HDL₃ back into circulation. In the presence of high levels of TGRL (predominantly VLDLs), as occurs in pp lipemia (PPL), type 2 diabetes (T2D), MS, and insulin resistance (IR), there is excessive transfer of TGs from VLDL and its remnant particles to LDL and HDL with CE flowing in the opposite direction generating a CE-depleted TG-enriched LDL and HDL along with a CE-enriched VLDLr (β-VLDL). Removal of the TG content of TG-enriched LDL and HDL generates small dense particles. sd-HDL undergoes rapid catabolism leading to a drop in circulating HDL levels. The triad of elevated β-VLDL and sd-LDL with low HDL is known as the “atherogenic lipid triad”.

1.2.4. Hypertriglyceridemia; definition, causes and atherogenicity

Hypertriglyceridemia is a general term referring to an increase in total TG levels in plasma. Since TGs are strictly carried within TGRLs, accumulation of these particles in the blood whether due to over-production or defective clearance will lead to hypertriglyceridemia (Boren et al., 2014). Despite the recognition of the superiority of non-fasting TG levels as predictors for CAD risk, lack of standardisation and population-based reference values hamper their use in clinical guidelines (Boren et al., 2014). The diagnosis of hypertriglyceridemia is thus based on fasting levels and has been defined as: i) normal if <150 mg/dl; ii) mild for levels between 150–200 mg/dl; iii) moderate for levels between 200 and ~990mg/dl; and iv) severe for levels > 990 mg/dl (Hegele et al., 2014). Levels above 2000 mg/dl are classified as very severe hypertriglyceridemia and warrants immediate attention due to the increased risk of developing pancreatitis, whereas mild-to-moderate elevations are associated with increased CAD risk (Berglund et al., 2012).

Abnormalities in TG metabolism may arise from a genetic defect in one or more genes encoding key regulators of TGRL metabolism or may be secondary to environmental triggers and other disease processes (Berglund et al., 2012). Elevations in TG levels occurring as a single monogenic disorder are rare and are usually due to homozygous or compound heterozygous large-effect loss-of-function mutations in genes that encode key elements of TGRL catabolism such as LPL and APOC2 (Hegele et al., 2014). Most of these patients present early during their childhood with severe hypertriglyceridemia and CM accumulation in circulation. On the other hand, the majority of patients with hypertriglyceridemia have a complex genetic etiology characterised by the occurrence of multiple small-effect mutations resulting in a cumulative disturbance in TG

metabolism (Hegele et al., 2014). Common variants linked to hypertriglyceridemia were identified using a genome-wide association study (GWAS) and include; APOA5, GCKR, LPL, and APOB (Johansen and Hegele, 2011). A combination of both common small-effect and rare large-effect mutations may also occur. In the pre-genomic era the classification of hypertriglyceridemic phenotypes, the Fredrickson classification, was based on the pattern of lipoprotein fractions seen in the plasma of these patients. Looking now at their genotype it appears that these phenotypes are quite similar at the molecular level (Table-1.2) (Hegele et al., 2014; Johansen and Hegele, 2011). It can thus be extrapolated that the body's metabolic handling of TGs is dictated by the interactions between such genetic variants and that the final outcome represents the sum of the protective and harmful effects of these variants (Berglund et al., 2012; Hegele et al., 2014). These variations may also explain the great variability in plasma TG levels observed in the population (Berglund et al., 2012; Hegele et al., 2014).

Hypertriglyceridemia is also a common occurrence in the context of other disease processes. Secondary causes of hypertriglyceridemia include; obesity, excessive alcohol consumption, T2D, the MS, renal disease, pregnancy, SLE and medications (Hegele et al., 2014). The commonest setting of hypertriglyceridemia is in association with the MS and T2D where it is attributed to IR. Insulin inhibits adipose tissue lipolysis, apo B synthesis and VLDL secretion by the liver (Adiels et al., 2008). Consequently, IR enhances hepatic uptake of FFAs by increasing their mobilisation from adipose tissue. The enhanced hepatic uptake of FFA along with increased apo B synthesis results in an augmented production of VLDL by the liver (Adiels et al., 2008). Renal disease, such as the nephrotic syndrome, is also associated with raised TG levels thought to be due to

enhanced production of VLDL by the liver (Berglund et al., 2012). On the other hand, the hypertriglyceridemia seen in SLE is a result of defective LpL-mediated catabolism of TGRL due to the presence of autoantibodies against LpL and apo C-II (Borba et al., 2006). Taken together, hypertriglyceridemia can be viewed as a multifactorial disease where the body's ability to handle TG is determined by the genetic make-up of an individual together with environmental and metabolic stressors (Hegele et al., 2014; Johansen and Hegele, 2011).

Table 1.2. Summary of classical hyperlipoproteinemia phenotypes.

Fredrickson hyperlipoproteinemia phenotype		WHO ICD number	Main lipid change	Primary lipoprotein change	Genetics
Familial hyperchylomicronemia	Type 1	E78.3	↑ TGs	↑ CM	Monogenic autosomal recessive due to mutant alleles of LPL, APOC2, APOA5, LMF1, or GPIHBP1; presentation mainly pediatric or early adulthood.
Familial hypercholesterolemia	Type 2A	E78.0	↑ CHOL	↑ LDL	Monogenic autosomal codominant; heterozygous form results from one mutant allele of LDLR, APOB, or PCSK9; homozygous form results from two mutant alleles of these genes or LDLRAP1.
Combined hyperlipoproteinemia	Type 2B	E78.2 E78.4	↑ CHOL ↑ TGs	↑ VLDL ↑ LDL	Polygenic; combined SNPs and excess of rare variants in hypertriglyceridemia-associated genes from GWAS together with LDL-associated SNPs.
Dysbetalipoproteinemia	Type 3	E78.2	↑ CHOL ↑ TGs	↑ IDL	Polygenic; combined SNPs and excess of rare variants in hypertriglyceridemia-associated genes from GWAS together with APOE E2/E2 homozygosity or mutant APOE.
Primary or simple hypertriglyceridemia	Type 4	E78.1	↑ TGs	↑ VLDL	Polygenic; combined SNPs and excess of rare variants in hypertriglyceridemia-associated genes from GWAS.
Mixed hypertriglyceridemia	Type 5	E78.3	↑ CHOL ↑ TGs	↑ VLDL ↑ CM	Polygenic; combined SNPs and excess of rare variants in hypertriglyceridemia-associated genes from GWAS with higher burden of risk alleles than for hyperlipoproteinemia type 4.

APOA5, gene encoding apo A5; LMF1, gene encoding lipase maturation factor 1; APOB, gene encoding apo B; APOC2, gene encoding apo C-II; APOE, gene encoding apo E; GPIHBP1, gene encoding glycosylphosphatidylinositol-anchored HDL-binding protein 1; PCSK9, gene encoding proprotein convertase subtilisin/kexin type 9; SNPs, single nucleotide polymorphisms; WHO, World Health Organization; ICD, International Classification of Disease. Adopted from (Hegele et al., 2014; Johansen and Hegele, 2011).

The feature shared by all of the above conditions is accumulation of TGRLs in circulation. Accumulation of TGRLs in the circulation does not only occur in association with disease conditions but can also occur in day-to-day activities in the form of pp lipemia. Following meal ingestion, an increase in TG levels occurs in two phases; an initial increase attributed to an influx of CMs coming from the intestine followed by a more delayed peak representing a mixture of hepatic derived VLDLs and intestinal derived CMs (Zilversmit, 1995). Both nascent particles compete for the same lipolytic pathway for the degradation of their TG content with CMs being the favourable substrate (Boren et al., 2014). This implies that in the presence of excessive amounts of CMs in the blood, as it occurs postprandially, there is a delay in the catabolism of VLDLs resulting in their accumulation in the circulation and an increase in their residence time (Karpe, 1999). The growing pool of VLDL and VLDLr particles in the plasma drives a series of unfavourable modifications in the size and composition of several lipoproteins rendering them more atherogenic (Karpe, 1999; Steiner, 1993). Nascent TGRLs (CMs and VLDL) are thought to be too large to seed themselves into arterial walls, however, their smaller degradation remnants are capable of depositing themselves into the arterial wall (Stender and Zilversmit, 1981). Apart from size reduction, the core of VLDLr particles undergoes extreme modifications under the influence of CETP-mediated lipid exchange resulting in their enrichment with CE. Under normal conditions VLDLr particles contain more TGs than CE, however, in the presence of hypertriglyceridemia their CE content becomes greatly enhanced. It is thought that these small CE-enriched VLDLr particles, known as β -VLDL, are capable of delivering substantial amounts of CHOL into the arterial walls. The role of pp lipemia in CAD was

emphasised by Patsch et al who showed that the TG handling ability of the body in response to a fat tolerance test distinguished between CHD subjects and healthy controls (Patsch et al., 1992; Veniant et al., 2000). It has also been reported by Tatami et al that the extent of CAD correlated positively with the levels of CHOL-rich VLDL and IDL (Tatami et al., 1981). TGRLs were also found to have a direct effect on vascular walls by enhancing the TNF- α -induced inflammatory response and VCAM-1 surface expression by endothelial cells (Ting et al., 2007; Wang et al., 2013; Wang et al., 2011). In addition, ppTGRLs have also been shown to induce the secretion of chemokines by MØs and promote MO migration in vitro (Napolitano et al., 2013). All of these reports favour a pathogenic role for TGRLs not only in atherogenesis but also in the context of other disease processes mandating a better understanding of the mechanisms underlying their pathogenicity.

1.2.5. Hyperlipidemic animal models

Hypertriglyceridemia is a feature of a number of currently available murine models developed primarily for the study of metabolically complex disease processes such as obesity, atherosclerosis, and the MS. In this context, hypertriglyceridemia is part of a complex disorder rather than the sole driving force. In general terms, hyperlipidemic mouse models are classified according to the disease process dominating the phenotype and include; models of obesity, models of atherosclerosis, and models of lipodystrophy (Kennedy et al., 2010). Almost all of these models have been utilised in studying the MS (Kennedy et al., 2010).

1.2.5.1. Murine models of obesity

Obese mouse models can be generally divided into those with disruption of the leptin axis, or those with a disruption in the central melanocortin system (Kennedy et al., 2010). Disturbances in the leptin axis are secondary to either a deficiency in leptin itself, as seen in the leptin-deficient ($\text{Lep}^{\text{ob/ob}}$) mice, or a deficiency in its receptor, as occurs in the leptin receptor-deficient ($\text{LepR}^{\text{db/db}}$) mouse models (Kennedy et al., 2010). Both models are characterised by obesity with hyperphagia and decreased energy expenditure. Depending on the mouse strain, the obesity may be accompanied by either diabetes or IR (Kennedy et al., 2010). With regards to their lipid profile, these mice exhibit elevated levels of plasma CHOL predominantly accounted for by an elevation in HDL rather than VLDL or LDL (Kennedy et al., 2010). They also have global hormonal abnormalities affecting the hypothalamic-pituitary-adrenal (HPA), thyroid, and reproductive axes (Kennedy et al., 2010). Another murine model of obesity includes mice with defective signalling in the melanocortin system implicated in the central regulation of energy homeostasis. Mice deficient in melanocortin 4 or melanocortin 3 receptors ($\text{MC4-R}^{-/-}$ and $\text{MC3-R}^{-/-}$, respectively) develop behavioural obesity with hyperphagia, hyperglycemia, hyperinsulinemia, and hypometabolism. However, little is known about the lipid and lipoprotein profile in these animals (Kennedy et al., 2010). The agouti yellow obese (A^y/a) mouse model is another model of defective melanocortin signalling attributed to the presence of the agouti protein shown to block signalling through the MC4 receptor (Lu et al., 1994). In addition to obesity these mice develop hyperphagia, IR, as well as hypertension (Carroll et al., 2004; Kennedy et al., 2010).

1.2.5.2. Murine models of lipodystrophy

Dyslipidemia in the form of hypertriglyceridemia with low HDL levels is commonly seen in lipodystrophies (Simha and Garg, 2009). Human lipodystrophies constitute a group of inherited or acquired disorders characterised by total or partial loss of adipose tissue (Savage, 2009). Several mouse models mimicking the phenotype of human generalised lipodystrophy have been generated, including knock-out mice lacking transcription factor C/EBP α or PPAR γ , both known to be crucial for adipocyte differentiation, and transgenic mice such as A-ZIP/F-1 and aP2-SREBP-1c mice (Kennedy et al., 2010; Savage, 2009). A detailed discussion of these models is beyond the scope of this introduction, but what is of relevance is that all of these models are characterized by a mixture of metabolic disturbances including; reduced body fat, dyslipidemia, impaired insulin sensitivity and hyperglycemia, not just hypertriglyceridemia (Kennedy et al., 2010; Savage, 2009).

1.2.5.3. Murine models of atherosclerosis

Mice are naturally resistant to atherosclerosis, an advantage that may be attributed to their favourable high HDL and low VLDL and LDL lipoprotein profile (Jawien et al., 2004). Disturbing this natural balance by genetic ablation of key receptors/proteins involved in lipoprotein metabolism resulted in the development of strains susceptible to atherosclerosis (Getz and Reardon, 2012). Mice lacking the LDLR and apo E have been extensively used in atherosclerosis research. The apo E-deficient (apo E^{-/-}) mouse lacks the crucial apo E ligand mediating the hepatic uptake of apo B-containing lipoproteins by the LDLR and LRP receptors (Getz and Reardon, 2006). This uptake is especially important for the clearance of CMr from circulation. The apo E^{-/-} knockout model shows a 5-fold elevation in CHOL levels and develop complex atherosclerotic lesions despite

feeding a low-fat (LF) chow diet (Jawien et al., 2004). Feeding high-fat (HF) diet greatly accelerates the process with CHOL levels exceeding (1000 mg/dl) (Getz and Reardon, 2012). Their lipoprotein profile is characterised by the accumulation of lipoprotein remnants including VLDL, IDL and CMr (Getz and Reardon, 2006; Jawien et al., 2004). The realisation that the effects of apo E extend beyond lipid metabolism to include MØ biology and immune function constitute the major drawback of the use of apo E^{-/-} model in atherosclerosis research (Getz and Reardon, 2012).

The function of the LDLR, on the other hand, seems to be confined to lipid and lipoprotein homeostasis making it a plausible model for studying the effects of lipoprotein disturbances in atherosclerosis (Getz and Reardon, 2012). The LDLR belongs to an endocytic family of receptors mediating cargo transport from the extracellular environment to intracellular sites of processing and degradation (Strickland et al., 2002). The LDLR itself is responsible for the uptake of apo E and apo B-containing lipoprotein particles (Strickland et al., 2002). Chow-fed Ldlr^{-/-} mice exhibit modest elevations in CHOL levels (approximately 250 mg/dl) when compared to apo E^{-/-} mice. The elevation is mainly in the LDL fraction of lipoproteins with atherosclerotic lesions developing very slowly. However, these mice are extremely diet-responsive and the addition of HF diet results in a marked increase in CHOL levels and the development of advanced atherosclerosis (Getz and Reardon, 2006; Jawien et al., 2004). Following HF diet modification, the lipoprotein profile differs slightly with an accumulation in VLDL and VLDLr in addition to LDL (Getz and Reardon, 2006). What is worth mentioning is that the type of diet determines the extent of lipoprotein derangement in Ldlr^{-/-} and, eventually, susceptibility to atherosclerosis. In a study done

by Merkel et al, $Ldlr^{-/-}$ mice were fed four isocaloric diets enriched with saturated fatty acid (SFA), monounsaturated fatty acids (MUFA), polyunsaturated fatty acids (PUFA) or carbohydrates (CARB). $Ldlr^{-/-}$ receiving the MUFA and CARB-enriched diets had significantly increased atherosclerosis with higher VLDL and LDL cholesterol levels when compared to their SFA and PUFA-fed counterparts (Merkel et al., 2001). Interestingly, the area of atherosclerotic lesion correlated positively with the levels of VLDL cholesterol (Merkel et al., 2001), emphasising the role of this lipoprotein subset in the pathogenesis of atherosclerosis. This was further emphasised in a mixed murine model characterised by over-expression of the human apoB-100 on the $Ldlr^{-/-}$ background, $Ldlr^{-/-}$ apo B-100 transgenic model, resulting in a marked increase in plasma TG and LDL levels with increased atherosclerosis (Getz and Reardon, 2006; Veniant et al., 2001). The development of atherosclerosis in the combined transgenic strain was attenuated by the lack of hepatic VLDL secretion (Getz and Reardon, 2006). These features make the $Ldlr^{-/-}$ a favourable model to study the pathogenic effects of TGRL remnants, however these mice develop hypercholesterolemia rather hypertriglyceridemia. Another model that have been extensively studied by Johnston's group is the poloxamer 407 (P-407)-induced model of hyperlipidemia. This is a chemically induced model that results in profound hyperlipidemia largely made of hypertriglyceridemia (Johnston, 2004).

1.2.6. Poloxamer 407 (P-407) model

Poloxamers are a family of non-ionic surfactants consisting of alternating units of hydrophobic propylene oxide and hydrophilic ethylene oxide (Cogger et al., 2006; Schmolka, 1994). P-407 is a member of the family with a central hydrophobic propylene

oxide chain flanked by two hydrophilic ethylene oxide chains (Schmolka, 1994; Singh-Joy and McLain, 2008). Due to its structure and amphiphilic properties, P-407 gained widespread use in pharmaceutical preparations as a solubilizing agent, and in cosmetics as an emulsifying and cleansing agent (Cogger et al., 2006; Singh-Joy and McLain, 2008). The administration of P-407 results in a dose-dependent increase in plasma lipid levels in rodents (Blonder et al., 1999; Palmer et al., 1998; Wout et al., 1992). A single intraperitoneal (i.p.) injection of 0.5 g/kg P-407 into C57BL/6 (B6) mice results in profound elevations in the plasma levels of both CHOL (>500 mg/dl) and TGs (>5000 mg/dl) that are maintained for a minimum of 96 hrs (Palmer et al., 1998). TGs appear to be more sensitive to the P-407-mediated effects than their CHOL counterparts, showing up to 60-fold increase in their level compared to an 8-fold increase in the latter upon P-407 administration (Palmer et al., 1997). Chronic P-407 treatment (4-5 months) causes sustained hyperlipidemia with the eventual development of atherosclerosis in B6 mice in the absence of dietary modification (Johnston, 2004; Palmer et al., 1998).

The hyperlipidemic effect of P-407 is largely mediated through its ability to inhibit LpL (Palmer et al., 1997). The inhibition of LpL results in accumulation of TGRLs with subsequent increase in both TGs and CHOL. The higher content of TGs in TGRLs compared to CHOL would explain the profound effect of P-407 on plasma TG levels compared to the more modest effect on CHOL levels. The inhibitory effect of P-407 extends to other lipases including HL (Johnston, 2010). The hypercholesterolemic effect of P-407 has been attributed to the possible enhancement of hepatic 3-hydroxy-3-methylglutaryl coenzyme A (HMG-CoA) reductase, the rate-limiting enzyme in CHOL

synthesis, but data are controversial. The *in vitro* biologic activity of hepatic microsomal HMG-CoA reductase was unaffected by the presence of P-407 (Johnston and Palmer, 1997), whereas its *in vivo* activity was different in mice and rats. A single i.p. injection of P-407 in rats led to an increase in hepatic microsomal HMG-CoA reductase activity that peaked 15 hrs post injection followed by a decline to normal levels (Johnston and Palmer, 1997). On the other hand, no effect of P-407 on microsomal hepatic HMG-CoA reductase activity was detected following its chronic administration in B6 mice (Johnston et al., 1999). The same mice actually showed a reduction in HMG-CoA reductase mRNA levels in the liver (Johnston et al., 1999), making it difficult to draw any conclusions on the effect of P-407 on HMG-Co A reductase. The effect of P-407 on LDLR and SR-B1 has also been investigated by measuring their protein expression in the liver following P-407 administration. Acute administration P-407 in mice showed no changes in the hepatic protein expression of SR-B1, whereas the expression of the LDLR protein was greatly reduced (Leon et al., 2006). Overall, the hyperlipidemic effect of P-407 seems to be largely mediated by its inhibition of LpL, however, an effect on HMG-CoA reductase cannot be ruled out. Down-regulation of the LDLR may enhance the phenotype generated by P-407 by delaying the clearance of the accumulated lipoproteins. Such effects induce drastic changes in the lipoprotein profile of P-407 treated animals. In fact, P-407 administration results in massive expansion of the VLDL lipoprotein fraction along with an increase in IDL and LDL particles in the blood (Johnston et al., 1999; Loginova et al., 2013). While B6 mice carry their CHOL mainly in the HDL fraction, analysis of CHOL distribution among the different lipoproteins in P-407 treated animals showed a shift from HDL to VLDL, IDL and LDL fractions (non-HDL

CHOL) (Johnston et al., 1999; Loginova et al., 2013). TGs, on the other hand, were almost entirely associated with the VLDL lipoprotein fraction (Johnston et al., 1999; Loginova et al., 2013). These changes in lipid and lipoprotein profile resemble those seen in type 2b, type 3, and type 4 hyperlipoproteinemia in humans making P-407 a suitable model for the study of such conditions (Johnston, 2004; Loginova et al., 2013). The P-407 hyperlipidemic model has been extensively explored by Johnston's group as an alternative model for atherosclerosis with a favourable safety profile. Chronic administration of 0.5g/kg P-407 for a period of 200 days was well tolerated by B6 mice with no evidence of hepatic toxicity throughout the experimental period based on normal plasma AST and ALT levels (Johnston et al., 1999; Johnston et al., 2000). In addition, no gross liver abnormalities were visible neither was there any difference in its CHOL content when compared to controls (Johnston et al., 2000; Palmer et al., 1998). However, the livers of P-407 treated mice did show accumulation of foamy MØs (Korolenko et al., 2012). Moreover, P-407 treatment did not induce endothelial proliferation or affect cell viability when used with human umbilical vein endothelial cells (HUVEC) neither did it affect their production of IL-6 and IL-8 (Johnston et al., 2003). The production of nitric oxide (NO) by peritoneal MØs was also unaltered by the addition of P-407 (Johnston et al., 2003). Despite this favourable profile, there were reports of some minor side effects occurring in mice injected with P-407. These included the development of splenomegaly due to red pulp expansion secondary to sequestration of lipid-containing macrophages (Johnston et al., 1993). They also reported a 50% reduction in red blood cell (RBC) parameters like: RBC count, hemoglobin, hematocrit (Hct) in mice injected with the compound (Johnston et al.,

1993). In addition, few studies raised the possibility of altered renal filtration capacity associated with the use of P-407, however, in mice these toxic effects were seen with high doses of P-407 ranging between 1.7-5.0 g/kg body weight (Abe et al., 1990; Dumortier et al., 2006). Overall, the P-407-induced model of hyperlipidemia appears to be a safe, simple, reproducible, and inexpensive model for the generation of hyperlipidemia that avoids the use of genetically modified mice as well as dietary modifications which, in themselves, may be inflammatory (Breslow, 1996; Johnston, 2004). Furthermore, the hyperlipidemic state generated by P-407 is largely driven by TGs with a lipoprotein profile similar to that seen in genetic as well as secondary causes of hypertriglyceridemia without invoking changes in other metabolic pathways as occurs in models of the MS.

1.2.7. Conclusion

Hypertriglyceridemia is a pressing problem in many societies around the world. The growing epidemic of obesity and T2D promoted by sedentary lifestyle and fatty diet has contributed to the increased burden of hypertriglyceridemia and its associated hyper-TGRL state across the globe. The realisation that the pathogenic potential of hypertriglyceridemia may be operating on daily basis is quite alarming. Repetitive transient elevations in plasma TGs and TGRLs following each meal can have great implications on the well-being of an individual. Although such elevations are amenable to lifestyle changes, hypertriglyceridemia occurring in the context of a more global metabolic disturbance may not be as responsive. A better understanding of the pathophysiologic mechanisms operating in hypertriglyceridemia and its effects on the homeostatic balance of the body is deemed necessary. The lipid profile induced by P-

407 hyperlipidemic model is similar to that observed in many hypertriglyceridemic conditions. This along with its simplicity and safety makes it a suitable model to begin delineating the effects of hypertriglyceridemia on the body.

1.3. The Mononuclear Phagocytic System (MPS)

Mobile circulating MOs and tissue-fixed MØs constitute a subset of leukocytes collectively known as “mononuclear phagocytes” (Geissmann et al., 2010). The widespread tissue distribution of these mononuclear phagocytes, along with their powerful phagocytic capacity has endowed them with the ability to perform diverse functions and led to their identification as key regulators of many organ systems (Tugal et al., 2013). MØs are present in almost every organ in the body and play crucial roles in host defence and tissue homeostasis (Tauber, 2003). The realisation that tissue MØs are replenished from bone marrow (BM)-derived circulating MOs led to their classification into a linear developmental system known as “The mononuclear phagocytic system (MPS)” (van Furth et al., 1972). The MPS was later expanded to include dendritic cells (DCs), which are specialised cells that share many similarities with MØs such as their hematopoietic origin but are far superior in antigen presentation and possess the ability to migrate from their tissue sites to lymph nodes to prime naïve T-cell (Hashimoto et al., 2011). Since its description, the MPS has been challenged by several discoveries. The realisation that not all tissue MØs arise from MO precursors and that their maintenance under steady-state conditions was largely MO independent led to a great shift in the understanding of the MPS (Hashimoto et al., 2013; Schulz et al., 2012). Moreover, the intermediary role depicted for MOs as mere precursors for tissue MØs was challenged by the demonstration of their phenotypic and functional heterogeneity calling for a re-evaluation of their functions in a variety of infectious and inflammatory conditions (Cros et al., 2010; Geissmann et al., 2003; Nahrendorf et al., 2007; Serbina et al., 2008). The detrimental role of MOs and MØs in atherosclerosis is undisputed. Hyperlipidemia drives lipid deposition within the vascular wall activating the

overlying endothelium and triggering MO recruitment (Moore and Tabas, 2011). Additionally, MO-derived MØs within the atherosclerotic plaque contribute to disease progression through secretion of inflammatory mediators that amplify local inflammation (Moore and Tabas, 2011). In a murine model of hypercholesterolemia, only the Ly6C^{high} MO subset migrated into the atherosclerotic lesion giving rise to MØs (Swirski et al., 2007). Whereas following myocardial infarction (MI), MO recruitment into the injured myocardium included both the Ly6C^{high} and Ly6C^{low} subsets with each performing a distinct function (Nahrendorf et al., 2007). These findings highlights the biological significance of the functional and phenotypic diversity in MOs calling for a better understanding of their unique and distinct roles in homeostasis as well as in pathological processes. Such understanding will enable the development of specific therapeutic interventions that can affect each subset independently. This section serves to present an overview on MO heterogeneity at the phenotypic, functional and developmental level. I will also discuss MØ heterogeneity briefly with emphasis on their origin and diverse activation states. This will be followed by a short account on their role in lipid disturbances.

1.3.1. MO heterogeneity

MOs are a subset of leukocytes that arise from BM precursors and get released into the circulation as non-dividing cells (Yona and Jung, 2010). They represent 10% and 4% of circulating peripheral blood Leukocytes in humans and mice, respectively (Auffray et al., 2009). Morphologically, MOs are irregular cells having an oval- or kidney-shaped nucleus with a high cytoplasm-to-nucleus ratio and the presence of cytoplasmic vesicles (Auffray et al., 2009). The realisation that MOs can migrate into tissues giving rise to

tissue MØs along with their short half-life have placed them as intermediary cells in the MPS serving mainly to replenish tissue resident MØs and DCs (van Furth et al., 1972; Yona and Jung, 2010). This conventional view has been challenged by the realisation that not all tissue MØs and DCs arise from circulating MOs, and that MOs represent a heterogeneous group of cells both phenotypically and functionally (Ziegler-Heitbrock, 2014). The existence of distinct MO subsets has been acknowledged in humans since the 1980s (Passlick et al., 1989). Initially, MOs were separated into two subsets based on their size and density using elutriation (Grage-Griebenow et al., 2001). The majority of MOs were of a large size and high density exhibiting higher peroxidase activity and interleukin-1 (IL-1) secretion (Grage-Griebenow et al., 2001). On the other hand, the smaller lower density MOs were less phagocytic, expressed higher HLA-DR on their surface and secreted more interferon- α (IFN- α) (Grage-Griebenow et al., 2001). Following these early reports, surface marker expression replaced size and density separation as means for MO subset identification (Grage-Griebenow et al., 2001). The first marker used was Fc γ receptor-I (Fc γ R-I), also known as CD64, dividing MOs into; CD64⁺ and CD64⁻ subsets (Grage-Griebenow et al., 2001). CD64⁺ MOs were larger powerful phagocytes capable of secreting higher amount of pro-inflammatory cytokines including; IL-1, interleukin-6 (IL-6), and tumor necrosis factor- α (TNF- α), whereas the CD64⁻ MOs were smaller with higher major histocompatibility complex (MHC) class I and II expression and a higher capacity to produce IFN- α (Grage-Griebenow et al., 2001). Other surface markers were also probed as means for MO subset identification. The detection of human peripheral blood MOs have long been based on their high expression of CD14, a glycosylphosphatidylinositol (GPI)-linked glycoprotein that

functions as the surface receptor for lipopolysaccharide (LPS) (Gordon et al., 1995). Ziegler-Heitbrock's group noticed the existence of a minor MO population with lower expression of CD14 (Passlick et al., 1989). Better delineation of this subpopulation was achieved through co-staining with anti-CD16 antibody which defined this population as CD16⁺, whereas the "classical" CD14^{high} MOs were CD16⁻ (Passlick et al., 1989; Ziegler-Heitbrock et al., 1993). Further analysis revealed more phenotypic as well as functional differences between these subsets (Ziegler-Heitbrock et al., 1993). Classical CD14^{high} CD16⁻ MOs constituted approximately 90% of total circulating pool and were shown to express CD62L (L-selectin), and CCR2 (the chemokine receptor for monocyte chemotactic protein-1 (MCP-1)), higher levels of CD11b, and lower levels of the fractalkine receptor CX₃CR1 when compared to the CD16⁺ MOs (Cros et al., 2010; Geissmann et al., 2003; Weber et al., 2000; Ziegler-Heitbrock et al., 1993). These MOs displayed strong phagocytic ability with higher capacity for reactive oxygen species (ROS) production and pro-inflammatory cytokine secretion (Grage-Griebenow et al., 2001; Passlick et al., 1989; Ziegler-Heitbrock et al., 1993). On the other hand, the smaller less granular CD14^{dim} CD16⁺ MOs formed the remaining 10% of the circulating pool and showed higher MHC class II and adhesion molecule very late antigen-4 (VLA-4) (VCAM-1 receptor) expression on their surface (Grage-Griebenow et al., 2001; Passlick et al., 1989; Ziegler-Heitbrock et al., 1993). These "non-classical" CD14^{dim} CD16⁺ MOs expressed higher levels of CX₃CR1, CD11c, and CCR5 (the receptor for MIP-1 α) on their surface when compared to the classical subset but lacked surface CCR2 and CD62L expression (Cros et al., 2010; Geissmann et al., 2003; Weber et al., 2000). In addition to morphological and phenotypic differences, these subsets differed in

the repertoire of cytokines they produce, however, results are controversial. An extensive body of evidence supports the ability of non-classical MOs to produce pro-inflammatory cytokines such as: TNF- α , IL-1, and IL-6 in response to LPS stimulation (Akiyama et al., 1985; Belge et al., 2002; Frankenberger et al., 1996; Skrzeczynska-Moncznik et al., 2008), however, similar results were not obtained by others (Cros et al., 2010). The enhanced secretion of pro-inflammatory cytokines by CD14^{dim} CD16⁺ MOs was accompanied by lack of IL-10 production leading to their designation as “pro-inflammatory” MOs which was further enforced by the demonstration of their expansion in a variety of human inflammatory and infectious diseases (Belge et al., 2002; Frankenberger et al., 1996; Ziegler-Heitbrock, 2007). Intriguingly, CD14^{dim} CD16⁺ MOs were found to crawl along the luminal side of the endothelium following their adoptive transfer into mice, a behaviour consistent with their reported high expression of VLA-4 (Cros et al., 2010). Additionally, these cells were shown to respond strongly to viral and nucleic acid signals via Toll-like receptor 7 and 8 (TLR-7/8) activation suggesting a role in sensing virally infected and damaged cells as they patrol the endothelium (Cros et al., 2010). Another level of complexity was added by the realisation that heterogeneity existed within the CD16⁺ subsets itself with the identification of yet another population that expressed CD14 at levels comparable to those observed on classical MOs (Skrzeczynska-Moncznik et al., 2008; Wong et al., 2012). On flow cytometry plots, this third CD14^{high} CD16⁺ subset is characteristically seen in the transitional zone between the classical CD14^{high} CD16⁻ and the non-classical CD14^{dim} CD16⁺ MOs leading to its designation as the “intermediate” subset, whether they represent a distinct subset by themselves or merely a maturation intermediate between the previous two remains to

be identified (Fig-1.6A) (Wong et al., 2012). Intermediate CD14^{high} CD16⁺ MOs were shown to express higher levels of CD11b with a phagocytic ability comparable to the CD14^{high} CD16⁻ monocytes, while concomitantly sharing features with CD14^{dim} CD16⁺ MOs such as high expression levels of HLA-DR and CD86 on their surface (Skrzeczynska-Moncznik et al., 2008). Whether CD14^{high} CD16⁺ MOs are skewed toward one subset than the other was explored using gene expression profiles, with some investigators showing CD14^{high} CD16⁺ MO clustering with the classical CD16⁻ subset, whereas others reported a resemblance to non-classical CD14^{dim} CD16⁺ (Wong et al., 2012). What is unique to intermediate MOs is their ability to secrete higher levels of IL-10 in response to LPS stimulation in comparison to the other two subsets (Skrzeczynska-Moncznik et al., 2008). Our understanding of this cellular subset is very primitive and more studies are required to fully understand their biologic role. Taken together, human MOs can be classified into 3 populations based on their CD16 and CD14 expression; the classical “CD14^{high} CD16⁻” MOs, the non-classical “CD14^{dim} CD16⁺” MOs, and the intermediate “CD14^{high} CD16⁺” MOs with each subset having distinct phenotypic and functional characteristics (Wong et al., 2012). The finding that many other species exhibited heterogeneity in their MOs fuelled research into this rapidly expanding field. MO subsets with features resembling those observed in humans were reported in mice, rats, pigs, cows, and horses (Ziegler-Heitbrock, 2014), of which only murine MO subsets will be discussed in further detail below.

1.3.1.1. Murine MOs:

Murine MOs are identified by their mononuclearity displayed as low side-scatter (lo-SSC) on the flow cytometer and their myeloid origin identified by their co-expression of

CD115 (the M-CSF receptor) and CD11b while lacking B, T, NK, and DC cell markers (Geissmann et al., 2003; Sunderkotter et al., 2004). Murine MO subsets are distinguished based on their differential expression of CX₃CR1 and/or Ly6C. CX₃CR1 is the sole member of the CX₃C family of cytokines thought to mediate leukocyte adhesion, while Ly6C is a GPI-anchored molecule that is expressed by MOs, granulocytes, a subset of NK cells and plasmacytoid DCs (pDCs) (Auffray et al., 2009; Jung et al., 2000). The development of the CX₃CR1^{GFP} mutant mice facilitated tracking of MOs in *in vivo* biological systems advancing our knowledge in their biology. These mice were generated through targeted replacement of CX₃CR1 gene with cDNA of EGFP which resulted in GFP labelling of all peripheral blood MOs, subsets of NK cells and DCs as well as Langerhans cells and microglia (Jung et al., 2000). The intensity of GFP labelling within CD11b⁺ F4/80⁺ peripheral blood MOs distinguished two discrete subsets; the GFP^{low} (CX₃CR1^{low}), and the GFP^{high} (CX₃CR1^{high}) MOs (Geissmann et al., 2003; Palframan et al., 2001). As with the human counterparts, the two subsets differed greatly with respect to both phenotype and function. The GFP^{low} MOs were larger and much granular with higher expression of CD62L, CCR2, and Ly6C (Geissmann et al., 2003; Palframan et al., 2001). While the smaller less granular GFP^{high} MOs lacked both CD62L and CCR2, with lower expression of Ly6C and higher expression of the lymphocyte-function associated antigen 1 (LFA-1) (Geissmann et al., 2003; Palframan et al., 2001). In wild type (WT) mice, MO subsets can be identified based on their differential surface expression of Ly6C into; Ly6C^{high} and Ly6C^{low} MOs which corresponded to the GFP^{low} and GFP^{high} subsets, respectively (Geissmann et al., 2003; Sunderkotter et al., 2004). Because Ly6C antigen can be recognised by a variety of

antibodies including the commonly used Gr1 antibody, Ly6C^{high} and Ly6C^{low} MOs has been referred to as Gr1^{high} and Gr1^{low}, respectively in the literature. The Gr1 antibody (clone: RB6-8C5) does not only recognise Ly6C but also the granulocyte marker Ly6G. Based on their high Ly6C/Ly6G and lower CD115 expression granulocytes can easily be separated from the monocytic pool (Auffray et al., 2009). Given their phenotypic similarity, murine Gr1^{high} (CX₃CR1^{low}) MOs have been compared to the human CD14^{high} CD16⁻ subset, while Gr1^{low} (CX₃CR1^{high}) MOs were considered analogous to the human CD14^{dim} CD16⁺ MOs (Fig-1.6B) (Geissmann et al., 2003; Ingersoll et al., 2010). The similarities between human and mouse MO subsets extend beyond surface marker expression to include an array of gene expression profiles found to be conserved between the two species (Ingersoll et al., 2010). Whether the phenotypic heterogeneity in murine MOs entails diversity in function as observed with their human counterparts was a subject of extensive research. GFP^{low} (CX₃CR1^{low}) MOs are preferentially recruited into inflamed tissue in a CCR2-dependent manner, whereas GFP^{high} (CX₃CR1^{high}) MOs were reported to home to uninfamed tissue in a manner dependent on CX₃CR1 (Geissmann et al., 2003; Palframan et al., 2001; Sunderkotter et al., 2004). In line with these findings, circulating levels of Ly6C^{high} MOs were reported to increase in a variety of infectious and inflammatory conditions including atherosclerosis where they have been shown to be preferentially recruited into the atherosclerotic plaque leading to their designation as “inflammatory” MOs (Arnold et al., 2007; Geissmann et al., 2003; Serbina et al., 2008; Sunderkotter et al., 2004; Swirski et al., 2007). On the other hand, Gr1^{low} MOs were able to populate tissues under steady state conditions leading to their designation as “resident” MOs (Geissmann et al., 2003). Ly6C^{low} MOs

have been shown to migrate into tissues under certain conditions, such as the injured myocardium following MI where their recruitment was associated with healing and tissue remodelling (Nahrendorf et al., 2007). Expansion of the circulatory numbers of these cells was reported in Yaa (Y-linked autoimmune acceleration) model of lupus-like autoimmune disease where they displayed enhanced expression of surface CD11c (Amano et al., 2005). An intriguing function of the Ly6C^{low} MOs was unveiled using intravital microscopy, where they were shown to crawl along the luminal side of the endothelium in an LFA-1-dependent manner (Auffray et al., 2007). The above findings suggest a great diversity in the function of MO subsets with the Ly6C^{high} subset exhibiting a pro-inflammatory phenotype whereas the Ly6C^{low} subset is mainly concerned with house-keeping functions and endothelial monitoring. These differential roles were highlighted in a murine model of MI where both MOs were recruited into the injured myocardium in a sequential manner and had divergent effects on cardiac tissue (Nahrendorf et al., 2007). Ly6C^{high} MOs were recruited early and contributed to clearance of debris and necrotic tissue, whereas Ly6C^{low} MOs entered the heart at a later stage promoting healing and tissue remodelling (Nahrendorf et al., 2007). In vitro functional characterisation of these subsets showed that both were capable of differentiating into F4/80^{high} MØs and CD11c^{high} DCs in response to *in vitro* stimulation with M-CSF and GM-CSF + IL-4, respectively (Geissmann et al., 2003; Sunderkotter et al., 2004; Swirski et al., 2009). There was a propensity of Ly6C^{high} MOs to give rise to MØs, while Ly6C^{low} MOs were better at generating DCs (Swirski et al., 2009). Whether this differentiation bias is applicable *in vivo* needs more confirmation.

Collectively, these findings challenge the long held belief that MOs serve mainly as circulating precursors to tissue MØs promoting them as effector cells with specialised functions in homeostasis as well as inflammation. Whether these cells arise from the same BM precursor is currently debatable. The following section discusses briefly MO origin presenting the argument supporting each view.

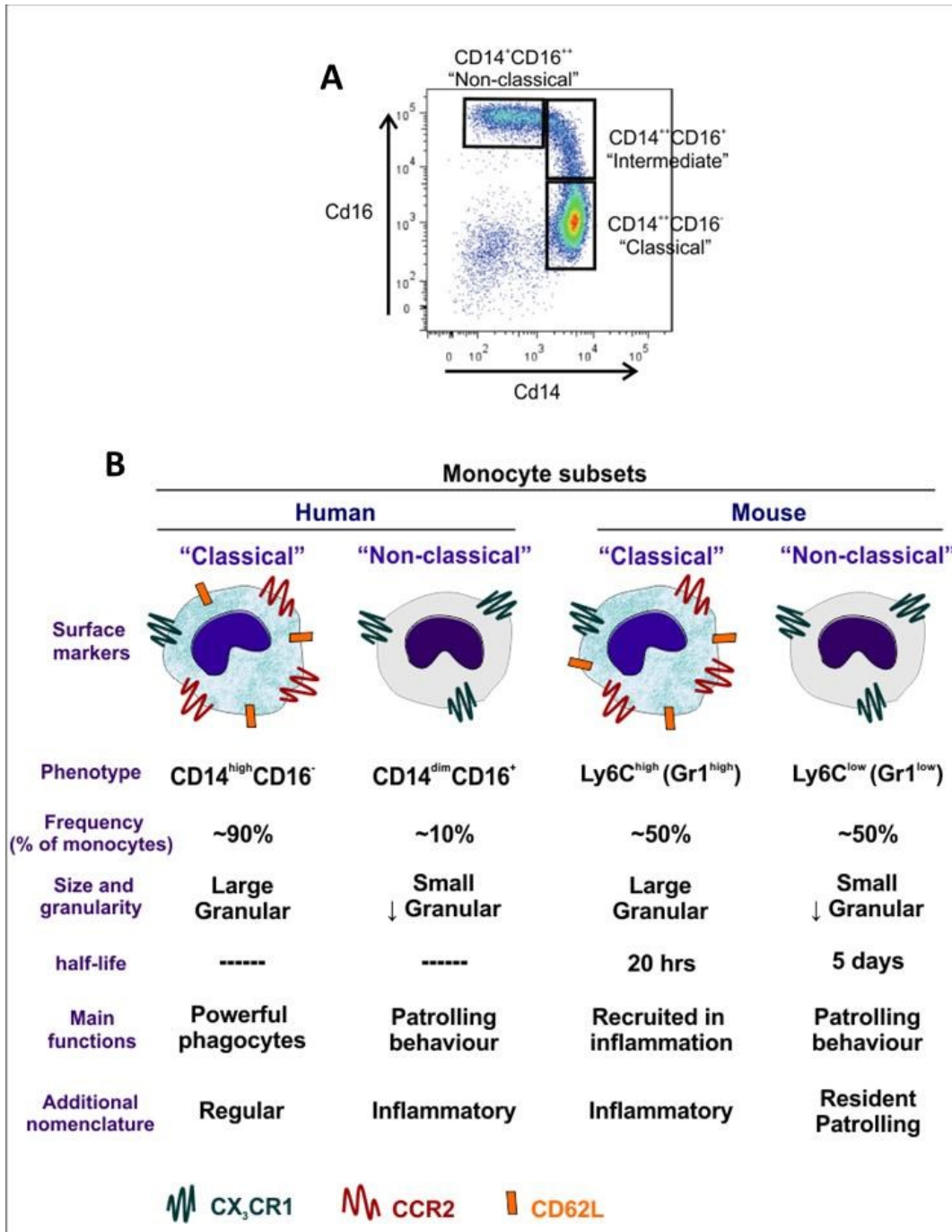


Figure 1.6. MO subsets in humans and mice.

(A) Flow cytometry plot of human MO subsets showing characteristic "banana-shaped" appearance (Wong et al., 2012). (B) A comparison between the two major subsets in human and mice. Adopted with modifications from (Geissmann et al., 2003; Strauss-Ayali et al., 2007; Wong et al., 2012).

1.3.1.2. MO origins

As with all other blood and immune cell types, MOs develop from hematopoietic stem (HSCs) cells located in the BM (Rieger and Schroeder, 2012). The generation of MOs from hematopoietic progenitors follows successive commitment steps characterised by declining self-renewal and multilineage capacity until one-lineage commitment ensues giving rise to mature terminally-differentiated cells (Rieger and Schroeder, 2012). In murine BM, HSCs reside in a small population of cells characterised by lack of lineage-specific marker expression (Lin^-) while expressing CD117 (c-Kit) and stem cell antigen (Sca-1) (Iwasaki and Akashi, 2007a; Rieger and Schroeder, 2012). Within this (Lin^- Sca-1 $^+$ c-Kit $^+$) population of cells, also known as the “LSK”, the most primitive HSCs with long-term self-renewal capacity (LT-HSCs) are found in the CD34 $^-$ fraction and constitute around 0.01% of total BM cells (Iwasaki and Akashi, 2007a). The CD34 $^+$ fraction of LSKs represent HSCs with more restricted self-renewal capacity known as short-term HSCs (ST-HSCs) or multi-potent progenitors (MPPs) (Iwasaki and Akashi, 2007a). Given that the LSK population contains progenitors with multipotent potential, lineage-restricted progenitors were sought outside the LSK population and the first population to be identified was the common lymphoid progenitor (CLP) (Iwasaki and Akashi, 2007a). The CLP population is the first to upregulate the receptor for interleukin-7 receptor- α (IL-7R α) and is identified as IL-7R α^+ Lin^- Sca-1 $^{\text{low}}$ c-Kit $^{\text{low}}$. This population has lost myelo-erythroid differentiation potential but possesses full lymphoid potential giving rise to T-, B-, and NK-cell lineages (Kondo et al., 1997). Since IL-7R α expression marks lymphoid commitment, myeloid progenitors were sought in the IL-7R α^- population (Akashi et al., 2000). In fact, a clonogenic myeloid progenitor that gave rise to all myeloid cell lineages including; granulocytes (neutrophils, eosinophils, and basophils),

monocytes-macrophages, erythrocytes, and megakaryocytes was identified as IL-7R α ⁻ Lin⁻ Sca-1⁻ c-Kit⁺ (Akashi et al., 2000). This population was further divided according to its Fc γ RII/III and CD34 expression into 3 different populations with distinct differentiation potential; the Fc γ R^{low} CD34⁺, Fc γ R^{low} CD34⁻, and Fc γ R^{high} CD34⁺ (Akashi et al., 2000). The double positive Fc γ R^{high} CD34⁺ population gave rise to colonies with granulocyte macrophage cell potential and was called the granulocyte macrophage progenitor (GMP), whereas the double negative Fc γ R^{low} CD34⁻ generated colonies with megakaryocyte erythrocyte cell commitment and was thus termed megakaryocyte erythrocyte progenitor (MEP) (Iwasaki and Akashi, 2007b). The Fc γ R^{low} CD34⁺ population had the capacity to differentiate into both GMPs and MEPs giving rise to all types of myeloid cells, which indicated that this population lies upstream of the former two and was thus termed the common myeloid progenitor (CMPs) (Akashi et al., 2000; Iwasaki and Akashi, 2007b). Although this simple model of sequential lineage restriction with definitive myeloid and lymphoid commitment occurring at the CMP and CLP stage, respectively has been very useful in stem cell research, it is being challenged by recent evidence showing that lineage restriction starts at a much earlier stage and within the multilineage MPP compartment (Iwasaki and Akashi, 2007a; Swirski et al., 2014).

Cells of the MPS system including MOs, many M ϕ s and most DCs share similar origin arising from the GMP population in the BM (Auffray et al., 2009). In addition to mononuclear cells, GMPs are capable of differentiating into polymorphonuclear (PMNs) phagocytes and their selective differentiation into either one of the two populations is controlled by transcription factors (TFs) that regulate the activation and/or silencing of a set of genes that determine the fate of GMP differentiation (Iwasaki and Akashi, 2007a).

PU.1 is an important regulator of myeloid cell differentiation and commitment toward MO/MØ fate (Auffray et al., 2009; Iwasaki and Akashi, 2007a, b). PU.1 is required for the generation of CMPs from multipotent progenitors promoting their differentiation towards GMP lineage through antagonistic inhibition of the pro-MEP TF, GATA-1 (Rieger and Schroeder, 2012). PU.1 is also responsible for driving lineage choice at the GMP stage towards MO/MØ production at the expense of granulocytes by antagonising C/EBP α , a TF necessary for granulocyte development (Auffray et al., 2009). In line with these changes in TF, a specific BM progenitor capable of generating MOs, many MØ and most DCs but not granulocytes have been identified. These cells share the phenotype of GMPs, i.e. Lin⁻ Sca-1⁻ IL-7R α ⁻ c-Kit⁺ CD34⁺ Fc γ R⁺, in addition to CD115 and CX₃CR1 expression and were called MØ/DC progenitor (MDP) (Auffray et al., 2009; Fogg et al., 2006). These MDPs are the first cells to express CX₃CR1 and thus it is thought that this chemokine receptor marks commitment to MO/MØ/DC lineages (Auffray et al., 2009). MDP differentiation gives rise to MOs, several MØ populations, and the common DC precursor (CDPs), which in turn generates pDCs and the precursors of cDCs (pre-DCs) (Auffray et al., 2009; Fogg et al., 2006; Geissmann et al., 2010). Although the exact relation of MDPs to GMPs has not been well identified, the differentiation potential suggests that these cells lie downstream of GMPs and represent a more committed progenitor to mononuclear cell lineage (Fogg et al., 2006; Geissmann et al., 2010). Furthermore, plausible evidence supports the presence of yet another more committed BM progenitor for MOs and MØs that have lost DC differentiation potential giving rise to both MO subsets and some tissue MØ and was thus called common MO progenitor (cMoP) (Hettinger et al., 2013). Despite the recognition of

progenitors that are more committed toward mononuclear phagocyte and MO differentiation, such as the MDP and cMoP respectively, the intermediary steps taking place between MDP and mature MO development remain unclear (Hanna et al., 2011). The identification of two distinct MO subsets raised the question as to whether they arise from the same BM progenitor or whether their heterogeneity extends to their BM precursors as well. The presence of more committed progenitors downstream of the MDP/cMoP stage that favour the differentiation towards one subset over the other remains debatable and at the moment two views seem to dominate the picture. The first argues in favour of a shared progenitor for both subsets and is based on the observation that BM MOs are almost exclusively of the Ly6C^{high} phenotype, and, when in culture, sorted Ly6C^{high} MOs lose their Ly6C expression (Sunderkotter et al., 2004). These observations led investigators to hypothesise that Ly6C^{low} MOs arise from Ly6C^{high} subset as the latter loses its surface expression of Ly6C following their release from the BM (Sunderkotter et al., 2004). In line with this hypothesis, the first MOs to appear following clodronate depletion of peripheral blood MOs were exclusively of the Ly6C^{high} phenotype, while the appearance of Ly6C^{low} subset lagged behind and were only evident by day 7 following clodronate depletion (Sunderkotter et al., 2004). This was further supported by tracking MO maturation through either BrdU incorporation or Dil-labelling. Injection of Dil-loaded liposomes 48 hrs following clodronate depletion labels the vast majority of MOs which are of the Ly6C^{high} phenotype while no labelling occurs in the Ly6C^{low} subset (Sunderkotter et al., 2004). Three days following Dil-labelling, Dil⁺ Ly6C^{low} MOs started to appear indicating that these cells were derived from their Ly6C^{high} predecessors (Sunderkotter et al., 2004). Similar results were

obtained using pulse 5-bromo-2-deoxyuridine (BrdU) labelling of MOs (Yona et al., 2013). The second view argues in favour of lineage dichotomy with each subset arising from a BM precursor independent of the other. Evidence supporting this view came from the observation that certain knockout murine models affect one subset irrespective of the other. CCR2^{-/-} mice demonstrate a severe drop in circulating levels of Ly6C^{high} MOs with only a minimal effect on the Ly6C^{low} counterparts, which argues against the derivation of the latter subset from the former (Tsou et al., 2007). Ly6C^{high} MOs were shown to accumulate in the BM of these mice supporting a role for CCR2 in the mobilisation of this subset from BM (Tsou et al., 2007). The opposite was seen in mice deficient in the transcription factor NR4a1 (Nr4a1^{-/-} mice) that displayed greatly reduced circulating levels of Ly6C^{low} monocytes with minimal affection of the Ly6C^{high} compartment implicating a role for this TF in the differentiation and survival of Ly6C^{low} subset (Hanna et al., 2011). The two mechanisms may actually be operating in parallel in a single biologic system. Which of the two arguments will stand the test of time is yet to be realised. A summary of MO development and main phenotypes is shown in Fig-1.7.

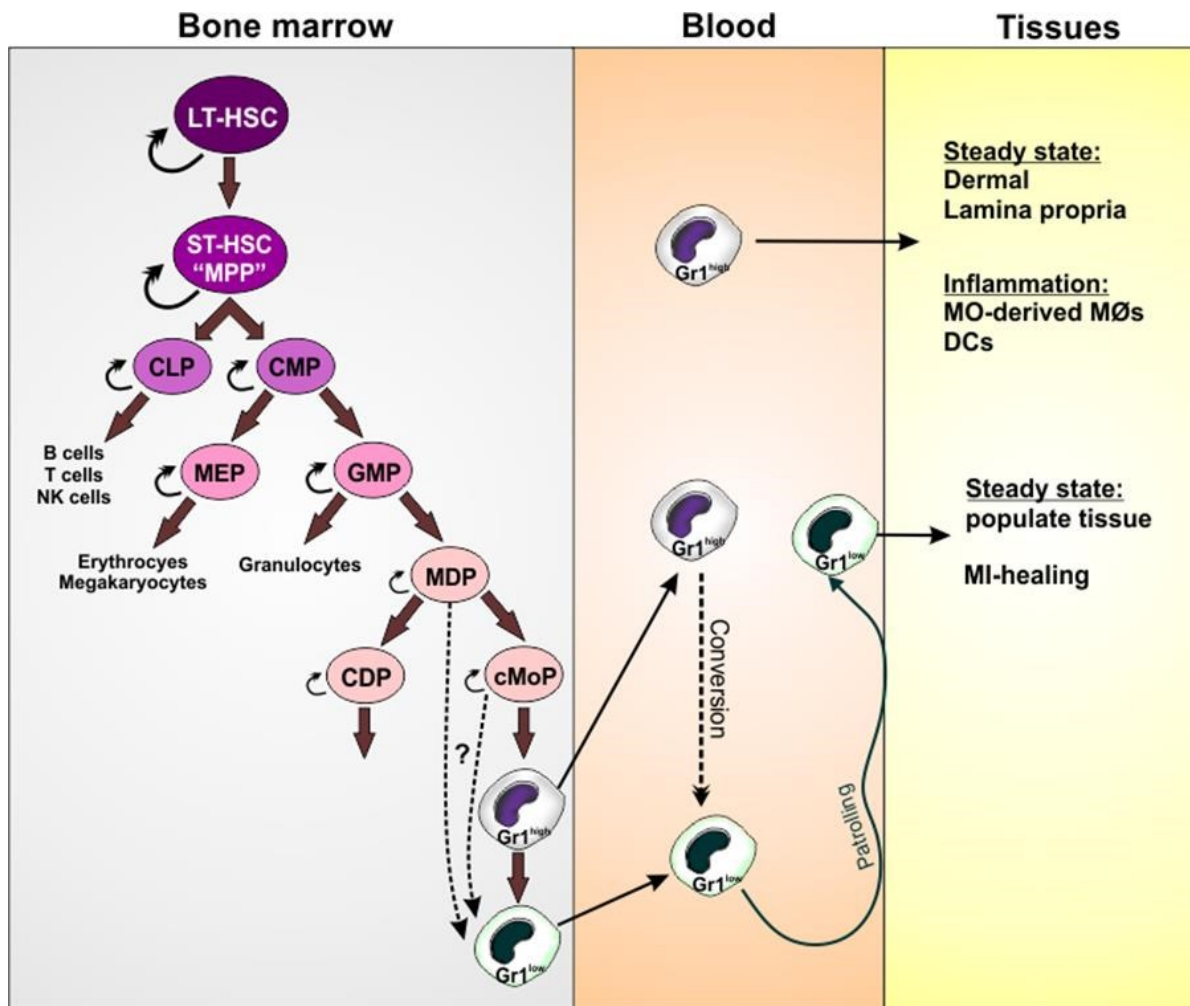


Figure 1.7. MO development

Successive commitment steps in the BM give rise to MØ/DC progenitor (MDP) followed by a more restricted progenitor for MOs (cMoP). The cMoP gives rise to Gr1^{high} MOs that get released into the circulation. Gr1^{high} MOs in the BM and blood stream may give rise to the Gr1^{low} subset by losing Gr1 expression. Whether Gr1^{low} MOs can arise directly from MDP and/or cMoP is yet to be clarified. In the circulation, Gr1^{low} MOs patrol the endothelium and may home to uninfamed tissue under steady state conditions or certain inflammatory conditions as in MI where they give rise to healing type MØs. Gr1^{high} may replenish MØs under steady state conditions in certain locations such as dermis, and intestinal lamina propria and are rapidly recruited to inflamed tissue giving rise to MØs.

1.3.2. MØ heterogeneity

MØs, or “large eaters” as the name implies, are professional phagocytes that reside in tissues all over the body and perform various key roles in several aspects of the organism’s biology, including development, homeostasis, and defence against invading pathogens (Wynn et al., 2013). The diversity in MØ functions is matched by marked heterogeneity in their phenotype, activation states, as well as origin. Their nomenclature was not spared either, with certain MØs acquiring special names at their tissue resident sites, such as Kupffer cells of the liver, Langerhan’s cell in the skin, and microglia of the nervous system. This marked heterogeneity in resident tissue MØs is not only organ dependent but is also evident within the same organ, as occurs in the spleen (Gordon and Pluddemann, 2013). These cells have long been thought to arise from circulating MOs as the latter migrates into tissues (van Furth et al., 1972). This view has been challenged by the recognition that certain tissue resident MØs maintain themselves throughout adult life with minimal contribution from circulating MOs (Hashimoto et al., 2013; Yona et al., 2013). This was initially reported for resident MØ populations in the brain (the microglia) and epidermis (Langerhan’s cells (LC)), and later extended to include almost all tissue resident MØs at different locations in the body (Ginhoux et al., 2010; Ginhoux and Jung, 2014; Ginhoux and Merad, 2010; Hashimoto et al., 2013; Yona et al., 2013). A marked exception was seen with intestinal tissue resident MØs which derive primarily from circulating $\text{Ly6C}^{\text{high}}$ MOs (Bogunovic et al., 2009). It was then realised that tissue resident MØs arise from embryonic stem cells that seed the tissues of the growing embryo during development and maintain themselves throughout adult life independently of circulating MOs (Hashimoto et al., 2013; Schulz et al., 2012). During embryonic development, MØs arise from two distinct hematopoietic waves; an

initial “primitive” wave followed by the establishment of more “definitive” hematopoiesis that persist throughout adulthood (Jagannathan-Bogdan and Zon, 2013; Orkin and Zon, 2008). The aim of primitive hematopoiesis is to provide erythrocytes to meet the oxygen demands of the rapidly growing embryo and, additionally, MØs to clear debris and apoptotic cells that arise during the process (Jagannathan-Bogdan and Zon, 2013). In mice, this phase is transient and occurs in the yolk sac (YS) between embryonic days 7-11 (E7-11) (Orkin and Zon, 2002). The first YS-derived MØs arise without MO intermediates and are evident by embryonic day 8 (E8) (Wynn et al., 2013). Around E10.5, HSCs start appearing within the hematogenic endothelium of the aorto-gonadomesonephros (AGM) region marking the beginning of the definitive phase of hematopoiesis (Bertrand et al., 2010; Boisset et al., 2010; Kissa and Herbomel, 2010). Whether the HSCs within the AGM region represent cells that have migrated from the initial YS HSCs or whether they are generated de novo independent of their YS counterparts remains a matter of debate (Orkin and Zon, 2002, 2008). Soon after the appearance of HSCs in the AGM region, these cells along with HSCs from the YS seed the fetal liver where they undergo expansion and differentiation establishing definitive hematopoiesis and giving rise to circulating MOs and MØs (Wynn et al., 2013). Soon thereafter, hematopoiesis appears in the spleen and, nearer to birth, in the BM as fetal HSCs migrate to these sites establishing definitive hematopoiesis with the latter continuing to be the major site for hematopoiesis throughout adult life (Rieger and Schroeder, 2012). YS-derived MØs circulate the blood and colonise the tissues of the developing embryo as early as E9.5 giving rise to F4/80^{high} CD11b⁺ MØs that included several key MØ populations such as brain microglia, liver Kupffer cells, epidermal LCs,

splenic red pulp MØs, pancreatic islet MØs, as well as to MØs in the lung and kidney (Schulz et al., 2012). As fetal hematopoiesis kicks in, these F4/80^{high} MØs were joined by another population of HSC-derived F4/80^{low} CD11b^{high} MØs (Schulz et al., 2012). Thus, tissue resident MØs arise from two different progenitors, YS embryonic stem cells and fetal HSCs which give rise to two distinct MØ populations namely F4/80^{high} MØs and F4/80^{low} MØs, respectively with each developing independently of the other (Fig-1.8) (Schulz et al., 2012). The contribution of each progenitor to resident MØ populations seem to be organ dependent with microglia showing exclusive derivation from YS-progenitors followed by LCs, whereas MØ populations in the kidney, lung, spleen, and pancreas display mixed origins (Fig-1.8) (Schulz et al., 2012; Sieweke and Allen, 2013). The embryonic establishment of these MØ populations along with their self-renewal ability enabling them to persist throughout adult life with minimal replenishment from circulating MOs questioned the contribution of MO-derived MØs to the tissue resident pool (Hashimoto et al., 2013; Yona et al., 2013). The contribution of MO-derived MØs to tissue resident MØ populations seems to be tissue and context dependent. Under steady state conditions, the majority of tissue resident MØs are maintained through self-renewal with minimal contribution from circulating MOs, this is especially true for microglia, Kupffer cells, splenic red pulp MØs, alveolar and peritoneal MØs (Hashimoto et al., 2013; Yona et al., 2013). Yet certain MØ populations such as intestinal, dermal, and splenic marginal zone MØs appear to be extremely dependent on continuous replenishment from circulating MOs under steady state conditions (Bogunovic et al., 2009; Ginhoux and Jung, 2014; Tamoutounour et al., 2013; Varol et al., 2009). Maintenance of intestinal lamina propria MØs and DCs depends on a

continuous flow of Ly6C^{high} MOs under steady state conditions (Bogunovic et al., 2009; Varol et al., 2007). It is reasonable to argue that MØs at these sites are in constant contact with the environment subjecting them to the injurious effects of various microorganisms and toxic material justifying the need for regular renewal from circulating MOs (Ginhoux and Jung, 2014). However, the lung who is also subjected to constant exposure to environmental stresses does not exhibit a similar phenomenon (Ginhoux and Jung, 2014; Hashimoto et al., 2013). Despite the selective dependence on MO-derived MØs under steady-state conditions, it is widely accepted that organ inflammation is associated with massive recruitment of Ly6C^{high} MOs giving rise to tissue resident MØs capable of responding to local environmental cues (Ginhoux and Jung, 2014). A lot of complexity surrounds the origin and maintenance of tissue resident MØs which appear to be tissue and context dependent contributing to the extreme plasticity of these cells. A summary of MØ origin is shown in Fig-1.8.

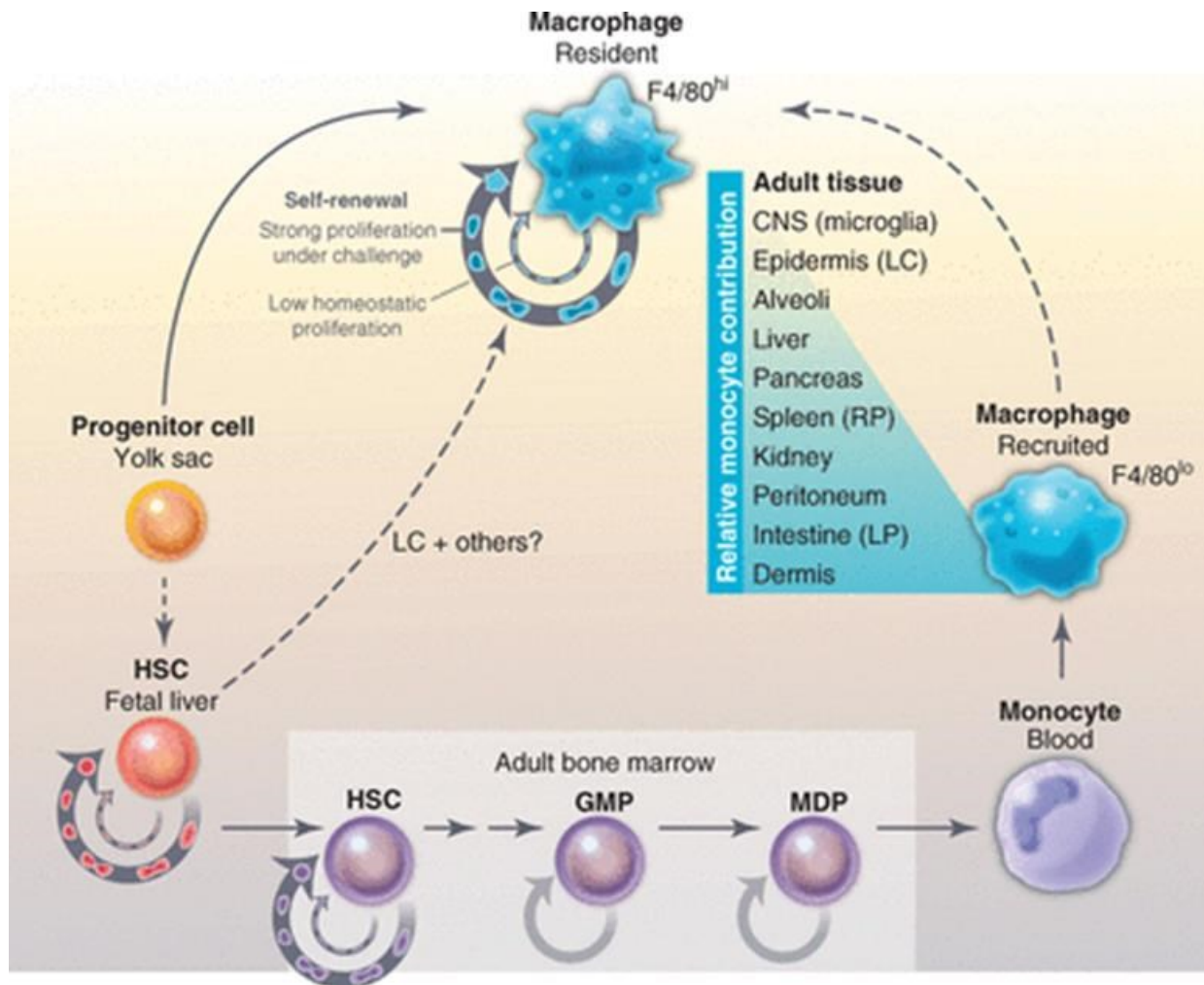


Figure 1.8. The origin of tissue resident MØs.

The majority of tissue resident MØs arise from YS progenitor during early embryonic life and seed the embryonic tissues giving rise to a population of F4/80^{high} tissue resident MØs that persist throughout adult life and maintain through self-renewal. Once fetal liver hematopoiesis gets established, HSCs in the fetal liver give rise to another population of F4/80^{low} tissue MØs that join the YS-derived resident MØs. These MO-derived MØs are continuously replenished by the BM and their contribution to resident tissue MØs is tissue and context dependent. Although MO-derived MØs do not contribute to microglia, intestinal lamina propria cells are greatly dependent on the continuous influx of MO from circulation. During inflammation, MO-derived MØs can be rapidly recruited to many organs giving rise to tissue MØs that can contribute to the local inflammatory response (Sieweke and Allen, 2013). Figure reprinted from (Sieweke and Allen, 2013).

MØ heterogeneity extend beyond their developmental diversity to include their functional state which enables them to respond specifically and appropriately to an array of environmental stimuli, a property endowed by their extensive repertoire of surface molecules and receptors. MØs have long been viewed as the executing arm of the adaptive immune system whose main role in host defence revolves around clearance of the offending agent (Mosser and Edwards, 2008). Apart from host defence, these powerful phagocytes have also been shown to contribute to normal homeostatic processes such as development and tissue remodelling where a full-blown inflammatory response would be unfavourable. MØs were shown to alter their response according to the environmental signals they receive (Gordon et al., 1995; Mosser and Edwards, 2008). IFN- γ , the prototypic Th1 cytokine, induces a strong cytotoxic MØ response, whereas IL-10 favours a more anti-inflammatory state (Gordon et al., 1995). These divergent activation states led investigators to classify MØs into two opposing phenotypes; the M1, or “classically-activated” MØs and the M2, or “alternatively-activated” phenotype (Wynn et al., 2013). Classically-activated MØs comprise those with enhanced cytotoxic ability brought about through IFN- γ activation (Wynn et al., 2013). Whereas the M2 phenotype includes an array of activation states that share a homeostatic and reparatory function (Davies et al., 2013). It is becoming greatly accepted that the spectrum of MØ activation states represent a continuum rather than a clear dichotomy in function/activation as initially proposed and thus its exact definition becomes quite challenging (Mosser and Edwards, 2008). A useful and informative classification of MØs was proposed by Mosser and Edwards who suggested their functional classification into three categories based on their predominant activation

phenotype, namely host defence, wound healing and immune regulation (Mosser and Edwards, 2008). Host defence or classically activated MØs are characterised by their enhanced microbicidal and tumoricidal ability and the secretion of pro-inflammatory cytokines (Mosser and Edwards, 2008). Activation of MØs towards a pro-inflammatory phenotype requires stimulation by both IFN- γ and TNF- α and results in the secretion of an array of inflammatory cytokines such as IL-1, IL-6 and IL-23 with the eventual eradication of the offending agent (Mosser and Edwards, 2008). This phenotype is vital for host defence, however, its excessive or uncontrolled activation may lead to persistent inflammation with on-going damage to host tissue as occurs in various autoimmune diseases (Mosser and Edwards, 2008). On the other hand, MØs may acquire a “wound healing” phenotype characterised by enhanced ability for collagen synthesis and extracellular matrix production when exposed to IL-4 stimulation (Mosser and Edwards, 2008). IL-4 is secreted primarily by basophils and mast cells and constitutes one of the signature cytokines for Th2-type immune response. When dysregulated, wound healing MØs can contribute to excessive extracellular matrix deposition and tissue fibrosis seen in many disease conditions (Mosser and Edwards, 2008). Another regulatory MØ phenotype can be brought about through a variety of stimuli including; glucocorticoids, IgG immune complexes, prostaglandins and apoptotic cells resulting in enhanced production of anti-inflammatory IL-10 (Mosser and Edwards, 2008). However, full activation of this anti-inflammatory state requires the co-presence of a second powerful stimulus such as TLR ligand (Mosser and Edwards, 2008). These regulatory MØs appear to be less effective in pathogen killing and matrix production but express high levels of co-stimulatory molecules (CD80 and CD86), suggesting a role in

shaping the T-cell response (Mosser and Edwards, 2008). It is worth noting that most of these phenotypes have been largely described under *in vitro* conditions and their application in the complex biologic system is under investigation. Nonetheless, they provide an excellent platform from which *in vivo* research can build on.

From the above it becomes clear that MØs are endowed with extreme plasticity which enables them to respond selectively and appropriately to a wide range of environmental stimuli. Whether this functional diversity in MØs is solely the product of their interaction with their environment or represents more hard-wired differences dictated by their developmental origin is currently a matter for open discussion.

1.3.3. The role of MOs and MQs in hyperlipidemia

MOs and MØs have been identified as crucial players in the pathogenesis of atherosclerosis, the hallmark of lipid-mediated diseases (Swirski et al., 2009). Hyperlipidemia drives lipid and lipoprotein accumulation into the vascular wall causing inflammation of the overlying endothelium which triggers MO recruitment into the subendothelial space (Moore and Tabas, 2011). Recruited MOs rapidly differentiate into MØs capable of engulfing large amounts of the accumulated lipids (Moore and Tabas, 2011; Swirski et al., 2009). Lipid accumulation within MØs transforms these cells into the characteristic foam cells which get integrated into the atherosclerotic plaque contributing to the physical bulk of the disease (Swirski et al., 2009). Additionally, activated MOs and MØs can contribute to the progression of the disease by secreting large amounts of pro-inflammatory mediators triggering further recruitment and amplifying the pathological process (Moore and Tabas, 2011). In fact, under conditions of hypercholesterolemia, lesion size was found to correlate positively with the degree of

monocytosis (Combadiere et al., 2008). Targeting MO recruitment by inhibition or ablation is an attractive therapeutic approach, however, given the crucial role played by MOs in host defence and homeostasis their indiscriminate ablation or the manipulation of their function can carry serious consequences (Swirski et al., 2009). With the recognition of MO diversity and their divergent functions, selective manipulation of distinct subsets seems like a more viable option. Generation of selective therapeutic approaches requires deep understanding of the differential role played by each subset under inflammatory and homeostatic conditions. A differential role for these subsets in hyperlipidemia was demonstrated in a murine model of diet-induced hypercholesterolemia that showed a progressive increase in circulating Ly6C^{high} MOs with their preferential recruitment into the atherosclerotic plaque (Combadiere et al., 2008; Swirski et al., 2007). Blocking the recruitment of this MO subset using the CCR2^{-/-} mouse decreased lesion formation in these mice (Boring et al., 1998; Combadiere et al., 2008). These findings suggest Ly6C^{high} MOs as the primary offenders in the atherosclerotic process, however, a role for the Ly6C^{low} MO subset cannot be excluded. In fact, some investigators reported a parallel, yet moderate, increase in circulating levels of Ly6C^{low} MOs in apoE^{-/-} hypercholesterolemic mice which correlated positively with lesion size implicating a role for this subset in the pathogenesis of atherosclerosis (Combadiere et al., 2008). Maximal inhibition of lesion development in atherosclerotic animal models was achieved through blockage of various chemokines some of which are known to be powerful recruiters for the Ly6C^{low} subset (Combadiere et al., 2008). Whether the role of Ly6C^{low} MOs under these conditions is additive to that of the Ly6C^{high} subset or whether they serve to control the inflammation has not been

determined. An anti-inflammatory and reparative role for the Ly6C^{low} subset has been suggested based on findings in MI murine model (Nahrendorf et al., 2007). Delineation of the role of this particular subset under such circumstances can provide alternative therapeutic potentials. Hypertriglyceridemia poses a threat to the general well-being analogous to that observed for hypercholesterolemia. The current sedentary life style and western-type diet puts the body under constant threat of the harmful effect of hypertriglyceridemia and its associated hyper-TGRL state (Zilversmit, 1995). A hyper-TGRL state is also seen in a variety of disease processes ranging from metabolic disorders such as the MS and T2D to generalised inflammatory conditions such as SLE contributing to enhanced morbidity and mortality under these situations (Borba et al., 2006; Carvalho et al., 2008; Grundy, 1998). Given the intravascular location of MOs, it would be reasonable to speculate a role for these cells in mediating the effects of such an environment. MOs were shown to internalise lipid particles and exhibit enhanced adhesion to the endothelial surface under conditions of hypertriglyceridemia (Gower et al., 2011). The specific role of each MO subset under conditions of hypertriglyceridemia is yet to be determined, however, a differential role is suggested by the pattern of gene profile expression. Gene clusters concerned with lipid and TG metabolism were found to be highly upregulated in Ly6C^{low} MOs when compared to the Ly6C^{high} subset (Ingersoll et al., 2010). In addition, these cells were shown to express higher levels of scavenger receptor CD36, a receptor involved in lipid uptake (Ingersoll et al., 2010). These findings along with their well-documented patrolling behaviour put this subset as a plausible mediator of the effects of a hyper-TGRL environment warranting further investigation into the subject.

1.3.4. Conclusion

MOs and MØs are key effector cells of the immune system performing critical roles in normal homeostasis and host defence. Their dysregulated or excessive activation can lead to unrelenting inflammation resulting in extensive tissue damage and organ dysfunction. Our knowledge about these elegant cells is rapidly changing and there is immense evidence showing that they are far from being homogenous. Extreme heterogeneity exists within MOs as well as MØs and involves all aspects of their biology including phenotype, origin and function. Studies into the functional heterogeneity of these cells uncovered distinct and at times opposing roles under similar disease conditions (Nahrendorf et al., 2007). These findings carry great potential for selective therapeutic targeting of these cells promoting favourable effects while inhibiting unfavourable consequences. The location of these cells within the vascular tree brings them in close proximity to changes in circulating levels of various metabolic products including lipids and lipoproteins. The levels of lipids, specifically TGs and TGRLs, are subject to dietary and hormonal influences and undergo great fluctuations over the day. The effect of such fluctuations on MO homeostasis needs more clarification. Given the role these cells play in hypercholesterolemia and atherosclerosis, it is reasonable to hypothesise that a hyper-TGRL environment may incite similar changes in MO behaviour. One of the aims of my study is to investigate the effect of a hyper-TGRL environment on the behaviour of MOs and MØs, with emphasis on the behaviour of each subset under those conditions.

1.4. The atherogenic lipid profile and kidney disease

The toxic effects of abnormal lipid metabolism extend beyond atherosclerosis to include various other organs. The immense ability of the kidneys to clear metabolic waste products and excess dietary requirement through the continuous filtration of large amounts of blood on daily basis makes them quite susceptible to the injurious effects of hyperlipidemia. In fact, renal disease complicates the course of various metabolic disorders such as T2D and the MS characterised by gross abnormalities in lipid and lipoprotein metabolism (Hung et al., 2013). Conversely, kidney disease such as the nephrotic syndrome may cause hyperlipidemia and its occurrence is thought to invoke further damage resulting in a progressive loss in renal function (Ruan et al., 2009). Whether hyperlipidemia alone is capable of inducing renal damage or whether it enhances damage in pre-existing renal disease is yet to be determined (Bobulescu, 2010). However, there is general agreement that the concomitant presence of hyperlipidemia in the course of renal disease accelerates its progression (Bobulescu, 2010; Keane, 2000). Evidence supporting a role for hyperlipidemia in enhancing end organ damage comes from patient with SLE. SLE is a chronic autoimmune inflammatory disease characterized by the development of auto-antibodies against a wide range of self-antigens inciting a generalised inflammatory state (Wade and Major, 2011). The autoimmunity and inflammation that occur in SLE are linked to marked changes in lipid and lipoprotein metabolism (Borba et al., 2006; Carvalho et al., 2008). These patients were shown to exhibit low LpL activity resulting in decreased degradation of circulating TGRLs leading to the development of the “lupus pattern” of dyslipoproteinemia characterized by hypertriglyceridemia, elevated VLDL levels and depressed levels of HDL (Borba et al., 2006; Carvalho et al., 2008). This complex

environment was shown to accelerate the development of atherosclerosis in these patients (Rubin et al., 1985). Even after conventional cardiovascular risks are taken into account, SLE patients show a 7.5-fold increased risk for coronary heart disease (Manzi et al., 1997). The increasing recognition of atherosclerosis as an inflammatory disease led to the proposition that the interplay between the SLE-driven inflammatory environment and its resultant dyslipidemia have an additive effect on end organ damage accelerating the atherosclerotic process. The systemic nature of the disease places other organs under the risk of enhanced inflammatory injury. Renal involvement complicates the course of disease in approximately 40-75% of SLE patients carrying significant morbidity and mortality (Golbus and McCune, 1994; Tisseverasinghe et al., 2006). With the increasing appreciation of the role of hyperlipidemia in renal disease, the question arises as to whether its occurrence in the course of inflammatory renal disease exacerbates the underlying inflammatory process enhancing progression of renal injury. Evidence supporting this hypothesis comes from a murine model developed in the lab of my supervisors, where the combination of SLE and hyperlipidemia enhanced not only atherosclerosis but also renal inflammation (Lewis et al., 2012). A link between hyperlipidemia and a worse renal outcome have also been demonstrated in patient with SLE (Tisseverasinghe et al., 2006). Despite these observations, the mechanisms underlying lipid-mediated renal injury, specifically the role of a hyper-TGRL state remains unclear. An additional aim of this study was to investigate the effects of a hyper-TGRL environment on the progression of inflammatory renal disease. To do that I resorted to a murine model of immune-mediated inflammatory renal injury, namely accelerated nephrotoxic nephritis (aNTN). Given the crucial role played by MOs and

MØs in atherosclerosis it seems reasonable to speculate a role for these cells in lipid-mediated renal injury as well which I will also attempt to delineate using this model. This section is concerned with presenting the evidence supporting the role of lipids in renal injury followed by a brief description of aNTN model intended for use in the current study highlighting the role of MOs and MØs in this model.

1.4.1. The role of lipid in renal disease

Progressive loss of renal function complicates the course of many immunological and non-immunological renal diseases. In cases of the MS and diabetes, hyperlipidemia precedes the development of renal disease and is thought to contribute to its progression (Hung et al., 2013). Alternatively, hyperlipidemia may be a consequence to renal disease such as the nephrotic syndrome where the primary damage triggers a series of events leading to elevations in plasma lipids and lipoproteins (Ruan et al., 2009). This induced hyperlipidemic state is thought to perpetuate existing inflammation causing further deterioration in renal function and the development of end stage renal disease (ESRD) (Keane, 2000). Following the development of renal failure and ESRD, a vicious circle is incited where declining renal function leads to further elevations in plasma lipids causing more damage to the kidney (Bobulescu, 2010). In fact, elevated levels of serum CHOL were associated with worse renal outcome in patients with SLE (Tisseverasinghe et al., 2006). Hyperlipidemia has been recognised as an independent risk factor for progressive loss of renal function (Keane, 2000). Evidence supporting the detrimental effects of hyperlipidemia in the context of inflammatory renal disease comes from animal models as well. New Zealand black and white mice (NZBxW), known to develop spontaneous lupus, get worse renal disease with increased mortality when fed

HF diet (Kelley and Izui, 1983). Whether lipids *per se* can induce renal injury or whether they only contribute to the enhancement of pre-existing renal disease is yet to be confirmed. It has been reported that patients with LCAT deficiency, a primary lipid disorder, develop glomerular lipid deposition and glomerulosclerosis with eventual reduction in renal function (Keane, 2000). Animal models have also supported a role for lipids in the induction of renal disease. Guinea pigs fed a HF diet exhibited glomerular lipid deposition with enhanced cellularity and mesangial matrix expansion (Al-Shebeeb et al., 1988). Rats were shown to develop higher proteinuria when fed a high CHOL diet (Joles et al., 2000). All of the above support a role for hyperlipidemia, specifically hypercholesterolemia in renal disease; whether hypertriglyceridemia carries a similar risk awaits further clarification. Obese Zucker rats, known to have elevated TG and VLDL levels were shown to develop proteinuria and progressive renal injury (Kamanna and Kirschenbaum, 1993). In addition, a hyper-TGRL state accompanies many metabolic disorders such as T2D and the MS known to be complicated by the development of renal disease (Hung et al., 2013). These observations carry serious implications given the current epidemic of hypertriglyceridemia and its associated hyper-TGRL state calling for more studies to address this issue.

1.4.2. Accelerated nephrotoxic nephritis (aNTN)

To study the effects of a hyper-TGRL state on the progression of inflammatory renal disease I resorted to the immune-mediated glomerular inflammatory model of nephrotoxic nephritis (NTN) (Masugi and Sato, 1934). The NTN model is a model of antibody-mediated inflammatory injury against an implanted foreign antibody in the renal glomerulus (Masugi and Sato, 1934; Robson et al., 2003). The injury is brought

about by the administration of heterologous antibodies directed against the glomerular basement membrane (GBM) where they become fixed triggering an inflammatory response which leads to the initial glomerular injury, i.e. “the heterologous phase of the disease” (Dixon et al., 1961; Masugi and Sato, 1934). This is followed by the development of a host immune response against the implanted heterologous anti-GBM antibodies causing further damage in the glomerulus (Dixon et al., 1961). The host’s immune response against the heterologous antibodies, known as the “autologous” phase of the disease, can be accelerated by immunizing the host with IgG from the species supplying the nephrotoxic serum (NTS) prior to its administration (Nagai et al., 1982). This is known as accelerated NTN (aNTN), and is widely used to induce NTN in mice due to the inherent resistance of this species to the development of glomerular lesions comparable to those seen in nephritic rats and rabbits using a similar dose of NTS (Otten et al., 2009; Robson et al., 2001). This aNTN model represent the model used in the current report and involves the i.v. injection of sheep NTS into mice that have been pre-immunised with purified sheep IgG in complete Freund’s adjuvant (CFA) (Pickering et al., 2002). Sheep NTS consist of sheep IgG directed specifically against constituents of murine GBM, generated through repetitive immunization with lyophilised murine glomeruli in CFA (Pickering et al., 2002; Robson et al., 2001). Following the administration of sheep NTS, the anti-GBM antibodies deposit into the glomerulus inciting an inflammatory reaction. Prior immunisation of mice with purified sheep IgG serves to speed up the process by inducing the generation of mouse anti-sheep IgG antibodies. The interaction of mouse anti-sheep IgG with the implanted sheep anti-GBM antibodies exacerbates the initial glomerular damage.

The pathogenic mechanisms implicated in the glomerular injury induced by the NTN model are complex and vary in response to several factors including: the animal species and strain used, the amount and source of NTS, the intensity of the host's immune response against the implanted antigen, as well as the phase of the disease (Assmann et al., 1985; Cochrane et al., 1965; Schrijver et al., 1990; Simpson et al., 1975; Unanue and Dixon, 1965; Unanue et al., 1967). In general terms, it is thought that complement and PMNs are key players in mediating glomerular damage during the heterologous phase of the disease (Cochrane et al., 1965; Unanue and Dixon, 1964). Evidence pointing towards a role for complement in NTN came from the observations of low serum complement levels in patients with glomerulonephritis (GN) as well as in experimental GN which was further emphasised by the late occurrence of experimental NTN in animals injected with avian NTS, known to be a poor complement fixer (Lange et al., 1951; Masugi and Sato, 1934; Vogt and Kochem, 1961). Later it was found that decompemented rats and complement-deficient mice develop a milder disease than their complement-intact counterparts (Lindberg and Rosenberg, 1968; Unanue and Dixon, 1964). Despite the clear role for complement during the heterologous phase of NTN in rats, its role appears to be less crucial in mediating nephrotoxic renal damage in other species such as guinea pigs and in certain mouse strains indicating the existence of complement-independent mechanisms that can operate to induce glomerular damage under such circumstances (Couser et al., 1977; Schrijver et al., 1990; Simpson et al., 1975; Taranta et al., 1963; Unanue and Dixon, 1964; Unanue et al., 1967). Along with complement, PMNs have also been shown to play a crucial role in glomerular injury during the heterologous stage of the disease (Cochrane et al., 1965). PMNs were

detected in the glomeruli of rats and mice injected with NTS as early as 2-2.5 hrs following injection of the NTS and their numbers correlated with the degree of proteinuria (Assmann et al., 1985; Cochrane et al., 1965). Moreover, their depletion ameliorated the proteinuria and glomerular damage seen following NTS injection (Cochrane et al., 1965). In most cases, this early PMN accumulation is complement-dependent since complement depletion or deficiency resulted in fewer PMNs in the glomerulus and a milder disease, however, in certain animal species/strains, PMN accumulation in the glomerulus following NTS administration was observed even in the absence of complement arguing against complete dependence of PMN recruitment on complement system activation (Cochrane et al., 1965; Hebert et al., 1998; Schrijver et al., 1990). It thus appears that during the heterologous phase, the implanted foreign antibodies trigger complement activation which in turn releases chemotactic factors that cause PMN recruitment into the glomerulus (Cochrane et al., 1965). Under certain conditions, PMN recruitment can occur independently of complement participation and may be mediated by their direct interaction with the implanted antibody through their Fc receptors (Schrijver et al., 1990). The second or “autologous” phase of the NTN model, is mainly driven by the interaction of the host’s autologous antibodies with the foreign implanted nephrotoxic antibodies in the glomerulus (Unanue and Dixon, 1965). The extent of renal damage induced during the autologous phase is dependent on the strength of the host’s immune response and hence, the amount of autologous antibodies formed against the implanted antigen (Unanue and Dixon, 1965). This is evident by the development of a more severe nephritis in rats immunised against the heterologous antibody when compared to non-immunised animals (Unanue and Dixon,

1965). Moreover, nephritic renal injury during the autologous phase of NTN was abolished in rats made tolerant at birth to IgG of the species supplying the NTS (Hammer and Dixon, 1963). PMN infiltration was shown to be a key event in inducing glomerular damage during this phase as well since their depletion resulted in lower serum creatinine levels and less proteinuria in nephritic rabbits (Naish et al., 1975; Thomson et al., 1976). However, and in contrast to the heterologous phase, their recruitment during the autologous phase of the disease is complement-independent as complement depletion had no effect on glomerular PMN counts nor the progression of the disease in nephritic rabbits (Thomson et al., 1976). Although some studies reported the participation of the complement system during this stage of the disease, its role in bringing about damage is less clear (Thomson et al., 1976; Unanue and Dixon, 1964). Apart from complement activation, Abs can induce injury through direct interaction with Fc γ receptors (Fc γ R) present on the surface of many immune effector cells leading to their activation and the release of inflammatory mediators causing more damage (Otten et al., 2009; Sylvestre and Ravetch, 1994). Fc γ Rs are mainly expressed on cells of hematopoietic lineage including M ϕ (Tarzi and Cook, 2003; Tarzi et al., 2003). In fact, glomerular M ϕ accumulation have been observed in the glomeruli of rats and mice following the induction of NTN especially in the accelerated model where M ϕ involvement is thought to play a major role in its pathogenesis (Huang et al., 1997; Schreiner et al., 1978; Tarzi and Cook, 2003; Tarzi et al., 2003; Tarzi et al., 2002). T-cells are central to this M ϕ -dependent response since their depletion reduced the numbers of infiltrating glomerular M ϕ s and attenuated the glomerular damage (Huang et al., 1997). It thus appears that the pathogenic mechanisms operating in the more

active disease, i.e. aNTN, where the autologous and heterologous phases tend to blend together, differ from those observed with the direct heterologous NTN with injury in the former being largely T-cell- and MØ-dependent (Huang et al., 1997; Tarzi and Cook, 2003). The central role of MØs in mediating glomerular damage in aNTN as well as the toxic effects of accumulated lipids, makes it a suitable model to study the effects of a hyperlipidemic environment on enhancing renal injury under inflammatory conditions which is one of the aims of my study.

1.5. Summary

Disturbances in lipids and lipoprotein metabolism are endemic in our society. The devastating effects of hypercholesterolemia on the cardiovascular system are well documented and have been the subject of extensive research. Hypertriglyceridemia, on the other hand, did not receive similar attention. This is quite surprising given that TGs constitute the majority of ingested fat in our diet. Moreover, disturbances in TG metabolism complicate a range of metabolic and inflammatory conditions enhancing end organ damage. How TGRLs mediate their damaging effects is not well understood. The role of MOs in atherosclerosis is well documented. These cells have been viewed as circulating immune effector cells concerned mainly with the replenishment of tissue MØs under inflammatory and steady state conditions. The recent recognition of their heterogeneity is promoting a more specialised role for MOs and their subsets in disease pathogenesis. Gr1^{low} MOs have been reported to constantly patrol the luminal side of the endothelium putting them at the front line against fluctuating levels of TGRLs. Understanding the potential effects of such repetitive strain on the behaviour of these cells can help understand the homeostatic role of these cells in such an environment and may lend insight into their pathological role.

1.6. Aims of my project

The general aim of my project was to delineate the effects of hypertriglyceridemia and a hyper-TGRL state on the behaviour of MOs and the impact of such an environment on kidney injury.

1.6.1. My specific aims

- Establish a favourable non-inflammatory hyper-TGRL state in murine B6 mice using P-407 compound. The experiments conducted to achieve this aim are shown in chapter 3 of the results section.
- Study the effects of a hyper-TGRL state on MOs and MO subset behaviour in vivo. The results obtained from this set of experiments will be discussed in chapter 4 of the results section.
- Finally, to investigate the impact of a hyper-TGRL environment on inflammatory end organ damage using the kidney as the target organ. Results concerning this aim are discussed in chapter 5 of the results section.

CHAPTER 2- Material and Methods

2.1. Mice

C57BL/6 (B6) and C57BL/6.CD45.1 mice were commercially purchased from Charles River UK or Harlan UK. B6.129P-Cx3cr1tm1Litt/J (Cx3cr1^{gfp/gfp}) and Ldlr^{-/-} mice were purchased from Jackson Laboratories (Bar Harbor, USA). Cx3cr1^{gfp/+} mice were obtained by breeding Cx3cr1^{gfp/gfp} mice with B6 mice. Mice of 8-12 weeks of age (weighing between 18-20g) were used for all experiments. All animals were housed in individually ventilated cages and maintained on normal chow diet and water ad libitum. Animals were handled in accordance with institutional guidelines and procedures approved by the UK Home Office. Ldlr^{-/-} were fed normal laboratory chow diet until 10 weeks of age and then received either a high fat (HF) Western-type diet (15% cocoa butter, 1% corn oil, 0.25% cholesterol, 40.5% sucrose, 10% cornstarch, 20% casein, free of cholate, total fat content 16%; Arieblok Diet W, cat. 4021.06), or a low fat (LF) semisynthetic reference diet (54.3% glucose, 10% cornstarch, 5% soya oil, 20% casein, no added cholesterol, total fat content 5.2%; Arieblok Reference Diet, cat. 4068.02). Both diets were purchased from Hope Farms, Woerden, Netherlands. Animals were sacrificed either by terminal anaesthesia using hypnorm (fentanyl citrate and fluanisone) mixed with midazolam and distilled H₂O in a ratio of 1:1:2, or in a CO₂ chamber.

2.2. Preparation of P407

Poloxamer 407 solution of 50mg/ml was prepared by dissolving the agent (Pluronic F-127, cat. P2443, Sigma-Aldrich, Dorset, UK) in previously cooled sterile PBS. The solution was kept stirring at 4°C to facilitate dissolution. To ensure that mice receive the

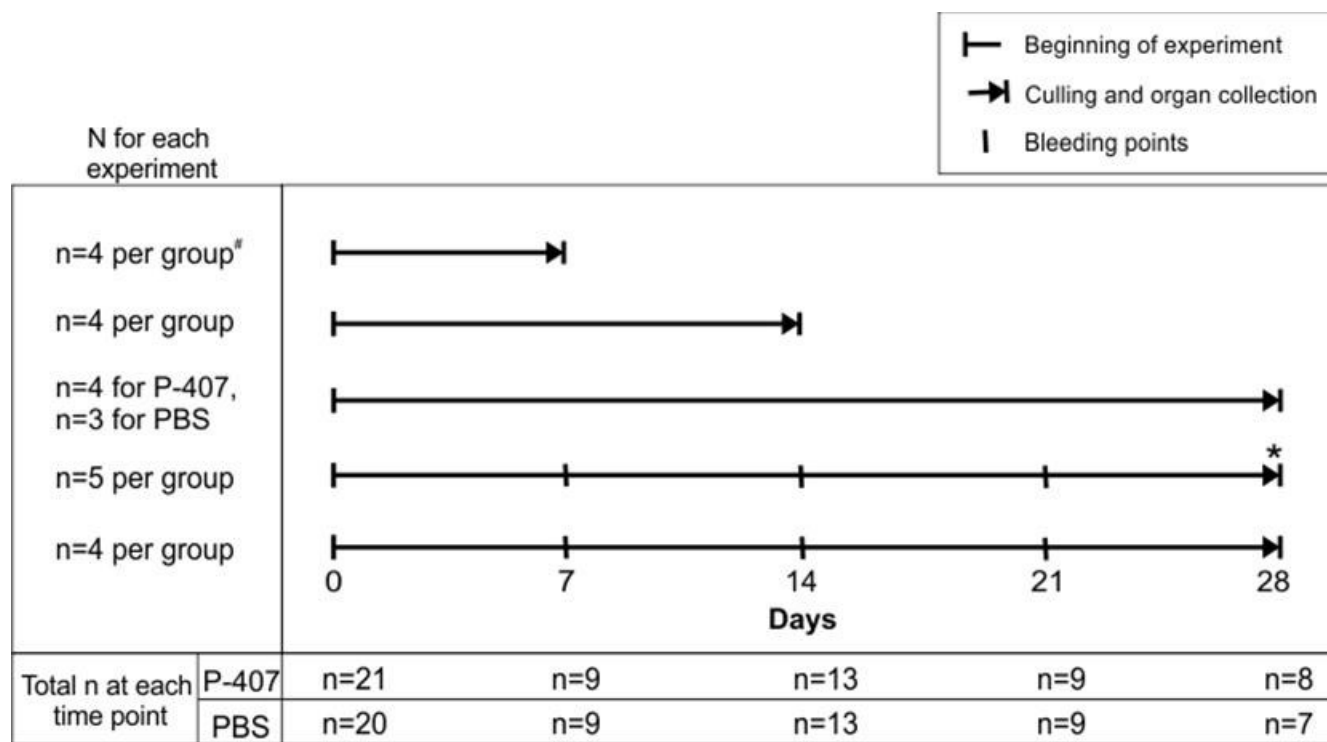
same volume of injection despite the different dosages, two further serial dilutions of the stock solution were prepared; 25mg/ml and 12.5mg/ml. The mice were injected i.p. with a volume of 200µl of one of the concentrations (50, 25, or 12.5mg/ml) giving a total dose of 10, 5, and 2.5mg of P-407, respectively. Throughout the dissertation the total dose will be used to refer to the amount of P-407 injected.

2.3. Experimental design

The induction of a hyper-TGRL state was initially achieved by injecting P-407 i.p. every 72hrs which was changed to a 48-hourly regimen following the P-407 trough level results. The dosing regimen was further modified during the course of my PhD to three times a week, namely every Monday, Wednesday, and Friday. The dosing schedule used for each experiment is indicated in the results section.

To study the effect of a hyper-TGRL environment on MOs, a time course experiment was performed. In this experiment, chow-fed B6 mice were injected with either 5 or 10mg P-407 i.p. three times a week over a period of 28 days. To record the changes in PB cells, the mice were bled at the beginning of the experiment before the commencement of PBS/P-407 injections (Baseline, day 0) and on weekly basis thereafter, namely, at days 7, 14, 21, and 28. At the end of the experiment, mice were culled and organs including: liver, heart, and kidney were collected. Two 28-day time course experiments were performed for the 10mg P-407 dose (n=5 per group in one experiment and n=4 per group in the other) while only one time course experiment was done for the 5mg P-407 dose. For the 10mg P-407 dose more experiments were conducted to enable the examination of organs at the different time points including; (i) a third 28-day experiment (n=4 for P-407 group and n=3 for PBS), (ii) a 14-day

experiment (n=4 per group), and (iii) a 7-day experiment (n=4 per group). In all of these experiments, chow-fed B6 mice were injected i.p. thrice weekly with either 10mg P-407 or PBS and organs including: heart, liver, and kidney were collected at the time of culling. In these experiments, blood samples were obtained only at baseline (day 0) and on the final day (day 28, 14, or 7, respectively). A graphic representation of the above experimental design is shown in Fig-2.1. The peripheral blood data for the time course experiment shown in chapter 4 of the results section represent pooled data of the above 5 experiments (Fig-2.1).



* PB data missing at this time point in this experiment.

Groups denotes P-407 and PBS-injected groups.

Figure 2.1. Experimental design for time course PB and lipid data.

This is a detailed depiction of the experimental design used to generate the pooled PB data for the 10mg P-407 dose shown in chapter 4 of the results section. Two independent 28-day time course experiments were conducted (n=5 per group in one experiment and n=4 per group in the other) where chow-fed B6 mice were injected i.p. three time a week with either 10mg P-407 or PBS over a period of 28 days. The mice were bled at the beginning of the experiment before commencing the injections (day 0) and on weekly basis thereafter, namely on days 7, 14, 21, and 28. At the end point (day 28), organs including: liver, heart, and kidney were collected for CD68 staining. A third 28-day experiment was done where blood was analysed only at days 0 and 28 (n=3 for PBS group and n=4 for P-407). To enable analysis of organs for CD68 staining at earlier time points, two more experiments were performed where chow-fed B6 mice were injected i.p. thrice weekly with either 10mg P-407 or PBS for 7 and 14 days (n=4 per group for each experiment). In the 7 and 14-day experiments, the mice were bled at day 0 and at the end of the experiments, i.e. days 7 and 14, respectively.

2.4. Lipid levels and lipoprotein profiles

Plasma CHOL and TG levels were measured by a colorimetric assay using the Cholesterol and Triglyceride Infinity Reagent (TR13421 & TR22421, respectively, Thermo-Scientific, Middletown, USA). In a 96-well MaxiSorp plate, 5µl/well of sample/standard was applied. The optimal sample dilution was 1:8 if lipid levels were within the normal range, whereas 2 dilutions (1:32 and 1:64) were used if lipid levels were high. This was followed by the addition of 200µl/well of the reagent. The plate then was incubated for 10min at room temperature (RT) and read at 492nm and 620nm. The standard used was a calibration serum, provided by the manufacturer, containing known amounts of lipid (CAL 2350, RANDOX laboratories Ltd., Antrim, UK).

Lipoprotein profiles were generated by fast protein liquid chromatography (FPLC) using a size-exclusion column (Superose 6, PC 3.2/30, GE Healthcare, UK). Fresh serum samples (50µL serum) from individual mice were diluted 50:50 in sterile filtered PBS, centrifuged at 14000 rpm for 30 minutes and the pellet discarded. 100µL of diluted serum was loaded onto a SMART FPLC machine (Pharmacia Biotech AB, Uppsala, Sweden) and eluted with PBS at a flow rate of 30µL/min for 133 minutes. The machine was programmed to discard the first 650µL and to receive 40 fractions of 35µL each (a further 2mL of eluate was discarded). Fractions were promptly assayed for CHOL and TG levels as described above and the lipoprotein profiles were averaged (five serum samples per curve). Serum samples for this analysis were obtained at the time of sacrifice and were fasting specimens.

2.5. Renal functional analysis

2.5.1. Proteinuria and hematuria

Proteinuria and hematuria were assessed by adding urine to Hema-Combistix urine reagent strips (Siemens, Frimley, UK). For hematuria the strips detected: negative, trace, 1+, 2+ and 3+. For proteinuria the strips detected: negative, trace, 1+ (0.3 g/l), 2+ (1 g/l), 3+ (3 g/l) and 4+ (≥ 20 g/l).

2.5.2. Albuminuria

Mice were placed in metabolic cages for 24 hours to facilitate urine collection for quantification of albuminuria. Albuminuria was quantified by radial immunodiffusion using a rabbit anti-mouse albumin antibody (AbD Serotec, Oxford, UK), with purified mouse albumin (Sigma-Aldrich, Dorset, UK) as a standard. Ten millilitres aliquots of 1.2% agarose were prepared by dissolving 1.2g agarose in 100ml 1x PBS, and were equilibrated at 55°C prior to the addition of 150 μ l of rabbit anti-mouse albumin antibody. Following mixing, the gel was poured onto a 3-inch glass plate and allowed to set at 4°C for 30 minutes. Wells of a known volume were then formed in the gel and arranged in a 7x4 matrix. A standard curve was generated using double dilutions of purified mouse albumin in 1x PBS, starting from a concentration of 10mg/ml down to 0.078mg/ml. Analysis of proteinuria using urine reagent sticks determined whether urine samples were added neat to the wells or at a dilution of 1:10. Urine samples with 3+ or 4+ proteinuria by urine dipstick were diluted 1:10 in 1x PBS, whilst those with $\leq 2+$ proteinuria were added neat. 5 μ l of urine or standard was added to each well, and the gel was then left in a wet box overnight at 4°C. 1xPBS was then used to wash the gel three times after which the gel was dried on gel bond. Pre-wetted 3MM paper was then

placed on top of the gel followed by a stack of towels and a weight for an hour at room temperature. The gel bond (with the transferred gel) was dried and placed in Coomassie blue for approximately 30 minutes until stained. Gels were destained using destain solution: 1500mls methanol, 500mls glacial acetic acid and 3000mls distilled water. The diameter of each ring was measured using a graduated magnifying lens and the concentration of albumin in each sample calculated by reference to the standard curve.

2.5.3. Plasma urea

Plasma urea was measured using a urea/ammonia UV method kit (Boehringer Mannheim/ R-Biopharm, Darmstadt, Germany). 100 μ L of reaction mixture containing buffer with 2-oxoglutarate and NADH (nicotinamide-adenine dinucleotide) was added to wells of a NUNC Maxisorp ELISA plate, followed by the addition of 200 μ L of freshly ddH₂O into each well. Plasma samples (10 μ L, diluted 1:10) or a standard amount of urea solution (5mmol/L) were then added in duplicate to the plate. This was followed by the addition of 2 μ L of urease to one set of wells. Five minutes following the addition of the urease enzyme, the plate was read in an ELISA reader at 340nm. Then, 2 μ L of GIDH (glutamate dehydrogenase) was added to all wells and the plate re-read at 340nm after 20mins.

The principle of this test is as follows; in the presence of urease, urea is hydrolysed to ammonia and carbon dioxide (CO₂). The addition of GIDH in the presence of NADH and 2-oxoglutarate causes the ammonia to react with the 2-oxoglutarate giving rise to L-glutamate while NADH gets oxidized to NAD⁺ in the reaction. The amount of oxidised NADH generated is proportionate to the amount of ammonia in the sample. Since plasma contains both urea and ammonia it becomes necessary to differentiate the

amount of oxidised NADH coming from each. In the first set of wells, the amount of NADH oxidised in that reaction reflects that coming from both urea and ammonia (A1) since these wells received both urease and GIDH. Whereas the amount of oxidised NADH in the second set of wells reflects the amount of ammonia alone since those wells received only GIDH (A2). By subtracting A2 from A1 the amount of oxidised NADH coming solely from urea is calculated. In other words, the second duplicate is used to subtract the background concentration of ammonia in each sample (which is generally very low). The fall in OD gives a linear value for the conversion of NADH.

2.6. Hematocrit measurement

Blood was collected via tail bleed directly into ammonium heparin capillary tubes (VWR International Ltd, Lutterworth, UK). The tubes were then centrifuged at 13,000rpm for 5 minutes after which hematocrit was calculated by measuring the packed cell height to total height ratio.

2.7. Flow cytometry studies

Flow cytometry analysis was done for the determination of leukocytes in peripheral blood, MOs and MO precursors in the BM, and MØs in several organs. All samples were run on BD FACSVerse (BD Biosciences, CA, USA), and data analysed using FlowJo software, version 7.6.5 (TreeStar Inc, Ashland, OR, USA). The tissue processing and staining protocol for each study will be discussed separately below.

2.7.1. Peripheral blood flow cytometry

Peripheral blood flow cytometry analysis was done for the determination of leukocyte numbers and frequencies. A “lyse no wash” protocol and beads were used to enable the determination of absolute cell counts. Mice were bled via tail bleed and blood was

collected onto a clean piece of parafilm. Thirty microlitres of blood were immediately pipetted into FACS tubes containing 30µl of PBS 5% EDTA taking care to avoid blood clot formation and samples were kept on ice. Fc receptors were blocked by incubating the samples with 30µl of 2.4G2 (anti-CD16/32 antibody) for 15 min at 4°C. This was followed by the addition of 30µl of monoclonal antibody (mAb) mix containing; anti-mouse antibodies directed against Thy1.2, CD115, CD11b, CD19, and Gr1 diluted in FACS buffer (PBS 1% BSA 0.01% sodium azide), details of the antibodies used are provided in table-2.1. Cells were allowed to incubate for 30 minutes at 4°C with the mAb mix in the dark. Red blood cells were then lysed by incubating the samples with 120µl of FACS lysing solution (BD) diluted 1/10 in dH₂O for 10 minutes at RT. Thirty microlitres of AccuCheck counting beads (Invitrogen, cat # PCB100) were added just before running the samples on BD FACSVerse.

2.7.2. Bone marrow flow cytometry

Femur and tibia were harvested carefully, without breaking the bone, to avoid blood contamination. Collected bones were placed into RPMI medium enriched with glutamine and antibiotics. Bones were then cleaned and flushed using RPMI 10% fetal calf serum (FCS). Cell suspension was collected into 15ml Falcon tubes and spun down at 1200 rpm for 5 min. RBCs were lysed by re-suspending the pellet in 1ml RBC lysis buffer for 2min. The cells were then washed and re-suspended in 3ml RPMI 10% FCS for counting.

Staining was done on four million cells per sample. Initially, cells were stained with 100µl of Dead/Live (D/L) marker (near-IR fluorescent reactive dye, Life Technologies, cat # L10119) diluted 1/2000 in PBS for 15 minutes at RT. The cells were then washed

and re-suspended in 30µl 2.4G2 for 20 minutes at 4°C followed by the addition of 100µl of a mAb mix containing anti-mouse antibodies directed against CD3, B220, CD49b (FITC) (constituting lineage markers-Lin), CD115 (PE), CD117 (PE-Cy7), CD11b (APC), CD34 (PerCP-Cy5.5), Gr1 (V450), and Sca1 (V500). Following 30 minute incubation, the cells were washed and re-suspended in 300µl of FACS buffer ready for analysis. HSCs were identified as (live Lin⁻ CD117⁺ Sca1⁺ CD34⁻), MEPs as (live Lin⁻ CD117⁺ Sca1⁻ CD34⁻), while a population constituting of both CMPs and GMPs were identified as (live Lin⁻ CD117⁺ Sca1⁻ CD34⁺).

BM staining for MDPs and MO subsets was done on a separate experiment. BM was collected and processed as previously described. One million cells per sample were placed in FACS tubes, washed and re-suspended in 100µl 2.4G2 for 30 min at 4°C. Cells were washed and stained with 100µl of primary mAb mix containing; anti-mouse antibodies against Gr1 (Alexa 488), CD62L (PE), CD115 (Biotin), CD11b (V450), CD117 (PE-Cy7). One hour later, the cells were washed and re-suspended in 100µl of streptavidin-APC (BD, cat # 554067) diluted 1/100 for 1 hr at 4°C. The cells were then washed and re-suspended in 300µl of FACS buffer ready to be analysed. MDPs were identified as CD117⁺ CD115⁺, while MOs were identified as CD117⁻ CD115⁺ CD11b⁺. MO subsets were identified from the MO gate as Gr1^{high} CD62L⁺ and Gr1^{low} CD62L⁻ MOs. Details of the antibodies used in this section are found in table 2.1.

2.7.3. Organ flow cytometry

Organ flow cytometry analysis was done in BM transplant and adoptive transfer experiments to detect recruited MOs/MØs under the influence of P-407-induced hyper-TGRL state. To avoid blood contamination, mice were perfused transcardially with PBS

followed by organ collection (liver, heart, kidney and spleen) into RPMI 10% FCS medium enriched with glutamine and antibiotics. Isolated organs were finely diced, for the kidney the capsule was removed, and digested in 2ml of digestion medium containing; 3% FCS, 1mg/ml collagenase D (Roche), 100U/ml DNase I (Roche) and 2.4mg/ml Dispase in PBS at 37°C for 30 minutes on a rotator. The digested cell suspension was then passed through 70µm cell strainers and 20µl/ml of 0.5M EDTA was added to stop the digestion reaction. Cells were then topped up with medium, washed and counted.

Staining was done on 5 million cells per sample. Cells were first washed in FACS buffer and then re-suspended in 30µl of 2.4G2 (anti-CD16/CD32) and 15µl of normal mouse serum (NMS) for 20 minutes at 4°C. Staining for surface markers was performed by the addition of 100µl of mAb mix. For BMT experiment the mAb mix consisted of anti-mouse antibodies directed against F4/80 (PE), CD11b (PE-Cy7), MHC class II (PerCP-eFluor 710), CD45.2 (APC-Cy7), CD115 (APC), and Gr1 (V450). While for the adoptive transfer experiment, the mAb mix contained anti-mouse antibodies directed against F4/80 (PE), CD45.2 (APC-Cy7), CD115 (APC), MHC class II (PerCP-Cy5.5), and Gr1 (V450). Cells were allowed to incubate with mAb mix for 1 hr at 4°C before they were washed and re-suspended in 300µl of FACS buffer for analysis. Details of the antibodies used in this section are found in table 2.1.

Table 2.1. List of antibodies used in flow cytometry studies.

Antigen	Format	Clone	Used form (conjugate)	Dilution	Source	Cat. no
B220	Rat anti-mouse	RA3-6B2	FITC	1/100	Biolegend	103206
CD115	Rat anti-mouse	AFS98	APC	1/200	eBioscience	17-1152-82
			PE	1/200	eBioscience	12-1152-83
			Biotin	1/50	eBioscience	13-1152-82
CD117 (c-kit)	Rat anti-mouse	2B8	PE-Cy7	1/100	eBiosciences	25-1171-82
CD11b	Rat anti-mouse	M1/70	APC	1/100	eBioscience	17-0112-82
			PE-Cy7	1/100		
			eFluor 450	1/100		48-0112-82
CD19	Rat anti-mouse	1D3	APC-Cy7	1/100	BD	557655
CD3ε	Rat anti-mouse	145-2C11	FITC	1/100	Biolegend	100306
CD34	Rat anti-mouse	HM34	PerCP-Cy5.5	1/100	Biolegend	128608
CD45.2	Rat anti-mouse	104	APC-Cy7	1/100	BD	560694
CD49b	Rat anti-mouse	DX5	FITC	1/100	BD	553857
CD62L	Rat anti-mouse	MEL-14	PE	1/100	BD	553151
F4/80	Rat anti-mouse	BM8	PE	1/100	eBioscience	12-4801-82
Gr1	Rat anti-mouse	RB6-8C5	V450	1/100	BD	560453
			Alexa-488		eBioscience	53-5931-82
MHC class II (I-Ab)	Rat anti-mouse	AF6-120.1	PerCP-eFluor 710	1/600	eBiosciences	46-5320-82
Sca1 (Ly6A/E)	Rat anti-mouse	D7	V500	1/100	BD	561228
Thy1.2 (CD90.2)	Rat anti-mouse	53-2.1	PE	1/100	Biolegend	140308

2.8. Histologic studies

2.8.1. Light microscopy

2.8.1.1. Glomerular histology

Harvested kidneys were fixed in Bouin's solution (Sigma-Aldrich, Dorset, UK) for 2-4 hours and then transferred to 70% ethanol until time of processing. The kidneys were later embedded in paraffin, sectioned and stained with periodic acid-Schiff (PAS). Paraffin embedding, sectioning, and staining of tissue were performed by Ms Lorraine Lawrence. Sections were examined by light microscopy and scored for glomerular cellularity in a blinded fashion (Prof. H. T. Cook). Glomerular histology was graded as follows: grade 0, normal; grade 1, segmental hypercellularity in 10–25% of the glomeruli; grade 2, hypercellularity involving >50% of the glomerular tuft in 25–50% of glomeruli; grade 3, hypercellularity involving >50% of the glomerular tuft in 50–75% of glomeruli; and grade 4, glomerular hypercellularity in >75%.

2.8.1.2. Hematoxylin & eosin (H & E) staining

For H & E staining, liver, heart, kidney and spleen were fixed in formalin followed by their transfer into 70% ethanol. Fixed tissues were then embedded in paraffin, sectioned and stained with H & E stain. Paraffin embedding, sectioning, and staining of tissue were performed by Ms Lorraine Lawrence. H & E stained tissue was examined for the presence of foam cells.

2.8.1.3. PAS-diastase (PAS-D) staining of the liver

Formalin fixed liver tissue have also been sent for PAS-diastase staining to enable the differentiation between foam cells and hepatocytes. Diastase is an enzyme capable of breaking down glycogen. PAS stains glycogen with a magenta colour. Pre-treatment of

the section with diastase, breaks down glycogen resulting in a lighter staining with PAS. The difference in PAS intensity before and after diastase treatment indicates the presence of glycogen. Given that hepatocytes are rich in glycogen, this difference in PAS intensity should differentiate them from foam cells that lack glycogen. PAS and PAS-D staining were performed by Ms Lorraine Lawrence.

2.8.2. Immunohistochemistry (IHC) staining

2.8.2.1. IHC staining for CD68

Following organ collection, portions of liver, heart, kidney, and spleen were fixed in periodate-lysine-paraformaldehyde (PLP) solution for 4 hrs at 4°C and followed by their transfer into 7% sucrose in PBS where they were kept overnight at 4°C. The next day, tissues were embedded in OCT embedding matrix (CellPath Ltd., Powys, UK), snap frozen in pre-cooled isopentane over dry ice and stored at -80°C. PLP was prepared fresh on the day of organ collection by mixing 200ml of lysine stock solution with 100ml of 4% paraformaldehyde solution followed by the addition of 0.214 g of sodium meta-periodate (S-1147, Sigma) per 100ml of the mixture. Lysine stock solution was prepared the day before by mixing 100ml of 0.2M lysine monohydrochloride (cat. L5626, Sigma-Aldrich) to an equal volume of 0.1M disodium hydrogen orthophosphate (cat. 301586N, GPR) adjusting the pH of the solution to 7.4.

PLP-fixed frozen sections were cut at a thickness of 5µm, dried in acetone for 15 minutes (immersed for 15 minutes and allowed to air dry) and stored at -80°C until use. Slides were defrosted for 10 minutes and the sections then encircled using a PAP pen (Invitrogen, Paisley, UK). Endogenous peroxidase was blocked by incubating the sections with 0.3% of hydrogen peroxide (H₂O₂) for 10 minutes at RT. Sections were

then rinsed in dH₂O and unspecific binding blocked by applying 10% Marvel milk diluted in PBS for 30 minutes. The sections were then rinsed in PBS and incubated in a moist chamber for 1 hr with rat anti-mouse CD68 antibody (clone: FA-11, cat. MCA 1957, AbD serotec) diluted 1/200 in PBS. Following incubation, the sections were rinsed 3 times in 1xPBS and CD68 staining was detected using Polink-2 plus HRP detection kit (cat. D46-18, GBI labs) following the manufacturer's instructions. Briefly, detection involved the application of a rat antibody enhancer for 10 minutes followed by polymer-HRP for another 10 minutes with several washes in PBS in between. Staining was developed using 3,3'-Diaminobenzidine (DAB) supplied by the kit, followed by counterstaining with hematoxylin for 1 minute (Harris hematoxylin, cat. HHS 32, Sigma). Stained sections were allowed to dry and mounted using histomount. Sections were imaged using an Olympus microscope with digital camera and analysed using Image Pro Plus software (Media Cybernetics, Silver Spring, USA). For the liver and heart, images were taken for 5 different fields at x20 magnification. While for the kidney, images were taken for 10-20 glomeruli per section at x40 magnification. Images for the same organ from one set of experiment were captured under identical lighting, microscope, camera, and PC conditions. Using Image Pro Plus software, CD68 staining of liver and heart were quantified by selecting a field and measuring its area along with the area of brown staining within that field for every image. With the help of a grid, the selected field area was kept constant between the different images to enable comparison of brown (CD68)-stained area between the different images. Percent brown area per field is then calculated by dividing the measured brown area over the total area of selected field. For each mouse, percent brown area per field was calculated for 5 independent fields which

were averaged to obtain the mean % brown area per field for each mouse. In the kidney, glomerular CD68 staining was quantified by drawing around the glomerulus measuring its area followed by calculating the area of brown staining within the selected glomerulus using Image Pro Plus software. Percent brown glomerular area is then calculated by dividing the measured brown glomerular area over total glomerular area for the selected glomerulus. For each section, percent brown glomerular area was calculated for 10-20 glomeruli which were then averaged to obtain the mean % brown glomerular area for each mouse.

2.8.2.2. Immunofluorescent staining for mouse CD68, Ki-67, C3 and IgG

Portions of liver, heart, and kidneys were placed in 1x PBS on collection and then transferred into 15 x 15 x 5mm plastic moulds (Dispomould, CellPath Ltd., Newtown, UK) containing OCT embedding matrix (CellPath Ltd., Powys, UK). They were then snap frozen in isopentane pre-cooled over dry ice and stored at -80°C until cut on a cryostat (Bright Instruments, Huntingdon, UK). Frozen sections were cut at a thickness of 5µm, dried in acetone (immersed for 15 minutes and allowed to air dry) and stored at -80°C until use. Liver, heart and kidney frozen sections were double stained for murine CD68 and Ki-67, whereas murine C3 and IgG staining was done only on kidney sections. On the day of staining, slides are defrosted for 10 minutes and the sections were encircled using a PAP pen (Invitrogen, Paisley, UK).

For mouse C3 and mouse IgG staining, sections were blocked using 60µl of 20% normal goat serum (diluted in 1x PBS) for 30 minutes at room temperature. For C3 staining: 60µl of fluorescein-isothiocyanate (FITC)-labelled polyclonal goat antimouse C3 (MP Biomedical, Cambridge, UK) diluted 1:100 in 1x PBS was applied for 1 hour at

room temperature. For mouse IgG staining: a FITC-conjugated polyclonal goat anti-mouse IgG Fc γ -chain specific antibody (Sigma-Aldrich, Dorset, UK) diluted 1:200 in 1x PBS was used. Sections were then washed three times in 1x PBS and mounted using Vectashield Hard Set mounting medium (Vector Laboratories, Peterborough, UK). Sections were kept covered in the dark at 4°C and left overnight for the mounting medium to set. Murine C3 and IgG stained sections were visualised using an Olympus fluorescent microscope with digital camera (Olympus, Southend, UK) and images analysed using Image-Pro Plus software (Media Cybernetics, Silver Spring, USA). Ten glomeruli were examined per section with the mean fluorescence intensity expressed in arbitrary fluorescence units (AFU).

For murine CD68 and Ki-67 double staining, sections were blocked for 1 hrs with 100 μ l of 20% normal rabbit serum diluted in PBS at RT. Following blocking, sections were stained sequentially with 100 μ l of rat anti-mouse CD68-Alexa Fluor 488 (clone: FA-11, cat # 137012, Biolegend) diluted 1/200 in PBS for 1 hr followed by rat anti-mouse Ki-67 eFluor 570 (clone: SolA15, cat # 41-5698-82, eBioscience) diluted 1/400 in PBS for 3 hrs. Sections were washed 3x in PBS in between and staining was done in a dark moist chamber at RT. Finally, sections were washed thrice in PBS, 2 minutes each and the slides were mounted using Vectashield Hard Set mounting medium (Vector Laboratories, Peterborough, UK). Spleen tissue was used as positive control and appropriate isotype control antibodies were included into the staining. Staining was visualized using Leica SP5 confocal microscope with the help of Dr. Kevin Woollard and images were acquired with a 40 or 63 x oil immersion objective.

2.9. Cytokine/chemokine levels

Cytokine and chemokine measurement was done on murine plasma collected on day 28 following P-407 or PBS treatment. The measured cytokines and chemokines included TNF- α , IL-6, IL-8, IL-10, IFN- γ , macrophage inflammatory protein 1- α (MIP-1 α , CCL3), and monocyte chemoattractant protein-1 (MCP-1, CCL2) and the measurement was done using a bead multiplex assay (eBioscience) according to the manufacturer's instructions. This allows detection of several cytokines in a single well using small sample volume. Briefly, in a 96-well filter plate, samples/standard were allowed to react with specific antibodies coupled to colour and size-coded beads and directed against cytokines/chemokines. After a series of washes to remove unbound protein, biotinylated detection antibodies directed against a specific epitope on the cytokine are added forming a sandwich of antibodies around the cytokine. The reaction mixture is then detected using streptavidin-PE that binds the biotinylated antibody. After a series of washes, the reaction mixture was re-suspended and the constituents of plate were read on the flow cytometer which identifies and quantifies each specific reaction based on bead colour and fluorescence. Bead fluorescence emission was detected using FACSVerse (BD Biosciences) and data analysed using Flow Cytomix (eBiosciences).

2.10. Enzyme linked immunoassays (ELISA)

2.10.1. Plasma C3 levels

Plasma C3 levels were measured using sandwich ELISA. The capture antibody was: polyclonal goat anti-mouse C3 antibody (MP Biomedical, Cambridge, UK) and the detection antibody was the same antibody but conjugated to horseradish peroxidase (HRP) (MP Biomedical, Cambridge, UK). The standard curve was generated using

acute phase serum containing a known quantity of C3 (Calbiochem, Hertfordshire, UK) and used as a reference to quantify samples. NUNC Maxisorp 96-well polystyrene plates were coated with polyclonal goat anti-mouse C3 capture antibody (Calbiochem, San Diego, CA) diluted 1:8000 in 0.1M NaHCO₃ (pH9.5) and incubated overnight at 4°C. Plates were washed once with wash buffer (50mM Tris base pH7.4, 150mM NaCl, 0.2% Tween20). Plates were blocked with assay diluent, consisting of 2% BSA in wash buffer, for 1h at RT and washed twice. Plasma samples were diluted 1:12000 in assay diluent. Standards of mouse C3 were obtained using an acute phase serum (Calbiochem) containing a known amount of mouse C3 (263µg/mL), starting at a dilution of 1:500 (i.e. 658 526ng/mL). 50µL/well of diluted sample or standard was added to plates for 1h at RT. After washing 5 times, detection antibody (HRP-conjugated form of capture antibody) (MP Biomedical, USA) was added at a dilution of 1:25000 for 1h at RT. After 5 washes, plates were developed by adding 50µl of HRP substrate tetramethylbenzidine (TMB) substrate (prepared by mixing equal volumes of solutions A and B) the reaction was stopped with 20µl stop solution, and the plates read at 450 and 540nm.

2.10.2. Immune response measurement

The immune response of mice against sheep IgG was measured using sandwich ELISA method: the capture antibody was sheep IgG (IgG from sheep, I5131-100mg, cat. 1000975031, Sigma) while the detecting antibody was a peroxidase-conjugated Affini-pure sheep anti-mouse IgG (#515-035-062, Jackson ImmunoResearch Laboratories). NUNC Maxisorp 96-well polystyrene plates were coated with 100µl/well of Sheep IgG at a concentration of 3.5µg/ml diluted in coating buffer (0.1M NaHCO₃, pH9.5) and

incubated overnight at 4°C. Plates were washed three times with PBS/0.05 Tween and blocked with 200µl/well of 1% BSA in PBS for 1hr at 37°C and washed 3 times in PBS/0.05 Tween. Then samples were added 100µl/well and incubated for 1 hour at 37°C. Each sample was diluted 12 times in blocking buffer (1% BSA in PBS) starting at 1/400 and double diluting up to 1/819200. All sample dilutions were applied to the plate in one row with one well on each plate receiving blocking buffer only. After washing 3 times in PBS/0.05 Tween, the reaction was detected by adding 100µl/well of the peroxidase-conjugated sheep anti-mouse IgG diluted 1/1000 in washing buffer and incubated for 1 hour at room RT. This was followed by 3 washing steps and the plate was developed using 100µl/well HRP substrate (TMB substrate reagent set, #555214, BD Biosciences) (A+B equal volume) and stopped using 40µl stop solution (#DY994, R&D systems). The immune response was analysed by selecting the titre (dilution) that corresponds to the OD that is double the OD the blocking buffer alone for each sample. This method allows for relative determination of the immune response rather than measuring the actual levels of the mouse IgG.

2.11. BrdU pulsing and staining

BrdU pulsing was done as described by Yona et al (Yona et al., 2013). Three doses of 2mg BrdU (5-bromo-2-deoxyuridine, BD Pharmingen) were administered i.p. 3 hrs apart. BrdU incorporation in blood monocytes was assessed by bleeding the mice 1, 3, and 5 days following BrdU injection. Monocytes were then stained for BrdU according to manufacturer's instructions (APC BrdU Flow Kit, BD Pharmingen). In brief, 30µl of blood were collected into FACS tubes containing 30µl of PBS 5% EDTA, followed by 1 minute incubation with 30µl of RBC lysis buffer at RT. The cells were then washed once with

medium (RPMI 10% FCS enriched with glutamine and antibiotics) and re-suspended in 50µl 2.4G2 for 30 minutes at 4°C to block unspecific binding. This was followed by surface staining with 50µl of mAb mix containing; anti-mouse antibodies directed against Thy1.2 (FITC), CD115 (PE), MHC class II (PerCP-Cy5.5), CD11b (PE-Cy7), CD19 (APC-Cy7), and Gr1 (V450) for the 30 minutes at 4°C. After a washing step, cells were fixed in 100µl of Cytofix/cytoperm solution (supplied by kit) for 15 minutes at RT followed by washing with Perm/wash buffer (supplied by kit). The cells were then permeabilised for 10 minutes using Cytoperm permeabilisation buffer and washed once with Perm/wash buffer. The cells were then re-fixed in 100µl Cytofix/cytoperm solution for 5 minutes followed by washing and DNA digestion using 100µl of 300µg/ml DNase for 1 hr at 37°C. Following DNA digestion, cells were washed and stained for BrdU by incubating with 50µl anti-BrdU-APC diluted 1/50 in Perm/wash buffer for 20 minutes at RT. The cells were then washed and re-suspended in 300µl FACS buffer for analysis.

2.12. Intravital microscopy and image analysis of the ear

Mice were treated with PBS or P-407 (10mg) for 7 days and under anesthesia ear placed on custom microscopy plate for imaging. Animals were kept warmed and tissue superfused with warmed fresh saline. For dermal ear imaging, mice were injected with 70kDa Tetramethylrhodamine-dextran (Molecular Probes) to label vasculature. Over 1hr, tissue vasculature was imaged using Leica SP5 confocal microscope using 20x objective. Imaging exposure was kept minimal to prevent phototoxicity. Areas of interest were analysed using Imaris (Bitplane, version 7.7) and numbers of cells analysed within defined region of interest (ROI). Intravital microscopy was performed by Dr Kevin Woollard.

2.13. Bone Marrow Transplantation (BMT):

Eight week-old female B6 mice were irradiated at 8 Gy using a ¹³⁷Cs c-ray source and reconstituted with 10⁷ bone marrow cells from Cx3cr1^{gfp/+} mice. Two months later 3 mice were culled and organs (liver, heart, kidney and spleen) were examined for GFP⁺ cells to determine baseline before undertaking a P-407 experiment. Organ collection and staining was described in the flow cytometry studies section.

2.14. Adoptive transfer experiment

Gr1^{low}GFP^{high} or Gr1^{high}GFP^{low} blood monocytes were sorted from CD45.2 Cx3cr1^{gfp/gfp} mice using Aria II FACS (Becton-Dickson). 0.1x10⁶ Gr1^{low}GFP^{high} or Gr1^{high}GFP^{low} sorted monocytes (>95% purity) were injected i.v. into congenic CD45.1 B6 mice. At 16 hrs mice were injected with 3µg of antibody against CD11b to exclude blood contamination. Mice were perfused with PBS, and organs (liver, heart, kidney and spleen) collected, processed and stained as described in flow cytometry studies section. Adoptive transfer was performed by Dr. Lucie Baudino.

2.15. Serum nephrotoxic nephritis

Nephrotoxic nephritis (NTN) was induced by the intravenous injection of 200µl of sheep nephrotoxic serum (NTS), a sheep IgG serum fraction containing anti-mouse GBM antibodies. Five days prior to administration of the NTS, mice were pre-immunised with an intra-peritoneal injection of 200µg of sheep IgG (Sigma-Aldrich, Dorset, UK) in CFA (Sigma-Aldrich, Dorset, UK). The sheep IgG in CFA was prepared as an emulsion containing 4mls of 1x PBS, 5mls of CFA and 10mg of sheep IgG. The final concentration of sheep IgG in the emulsion was 200 micrograms per 200µl (the injection volume). Urinalysis was recorded prior to immunisation and every other day following

NTS injection. At the end of the experiment, mice were placed in metabolic cages overnight in order that urine could be collected for formal quantification of albuminuria. Mice were culled 2 weeks following the injection of the NTS.

2.16. Statistical analysis

Parametric data are presented as the mean \pm SD. For parametric data, comparisons between two groups was done using unpaired or paired t-test as indicated in the figure legend, whereas comparisons between 3 or more groups were conducted using one way analysis of variance with Bonferroni's multiple comparison test. For non-parametric data, comparisons between two groups were conducted using Mann-Whitney test, whereas comparisons between 3 or more groups were done using Kruskal-Wallis test. Data were analysed using GraphPad Prism version 3.0 for Windows (GraphPad Software, San Diego, USA). P value of <0.05 was considered significant.

CHAPTER 3- P-407-INDUCED MODEL OF HYPERLIPIDEMIA

3.1. Introduction

The first aim of my study was to establish a model of hyperlipidemia driven mainly by an increase in TGRLs without other confounding metabolic abnormalities as occurs in animal models of the metabolic syndrome, and different from CHOL-driven hyperlipidemia models used in atherosclerosis research. In order to achieve this, I used a drug-induced model of hyperlipidemia that have been extensively described by Johnston et al (Johnston, 2004).

The model involves the use of a compound known as P-407 shown to induce a dose-dependent elevation in plasma lipids when injected into chow-fed B6 mice. The effect has been shown to be mediated through the inhibition of LpL, the enzyme responsible for the hydrolysis of the TG content of TGRLs (Johnston, 2004; Johnston and Palmer, 1993). Given its mechanism of action, the P-407 model was considered a suitable candidate. However, and before embarking on large scale experiments, I conducted a set of preliminary experiments that aimed at: i) establishing the dose and frequency of P-407 injections; ii) determining the P-407-induced lipoprotein profile; iii) testing for any potential side effects. The results of these preliminary experiments are outlined in this chapter.

3.2. Establishing the dosage of P-407

The aim of the first experiment was to delineate the degree of lipid elevation achieved with P-407 and to determine the dose to use in subsequent experiments. Guided by previous work of Johnston et al (Johnston et al., 2000), a maximum dose of 10mg P-407 in B6 mice weighing approximately 20g (equivalent to a dose of 0.5g/kg body

weight) was used. In addition, two lower doses were tested, 5 and 2.5mg P-407, to assess the dose-response effect of P-407 on plasma lipids. Chow fed B6 mice were injected i.p. every 72hrs with one dose (n=3, per group) over a period of 28 days, with a PBS-injected mouse serving as a control. Blood for plasma lipid measurements was collected at 1, 7, 14, 21, and 28 days following P-407 injection.

A dose-dependent increase in the plasma levels of both TG and CHOL levels was observed upon P-407 injection (Fig-3.1). In agreement with previous reports (Johnston and Palmer, 1993), the elevation was more pronounced in plasma TGs than in plasma CHOL, with approximately 70, 15, and 6-fold increase in plasma TG levels compared to an 18, 6, and 4-fold increase in CHOL in the 10, 5, and 2.5mg P-407-injected groups, respectively in comparison to control levels (Table-3.1).

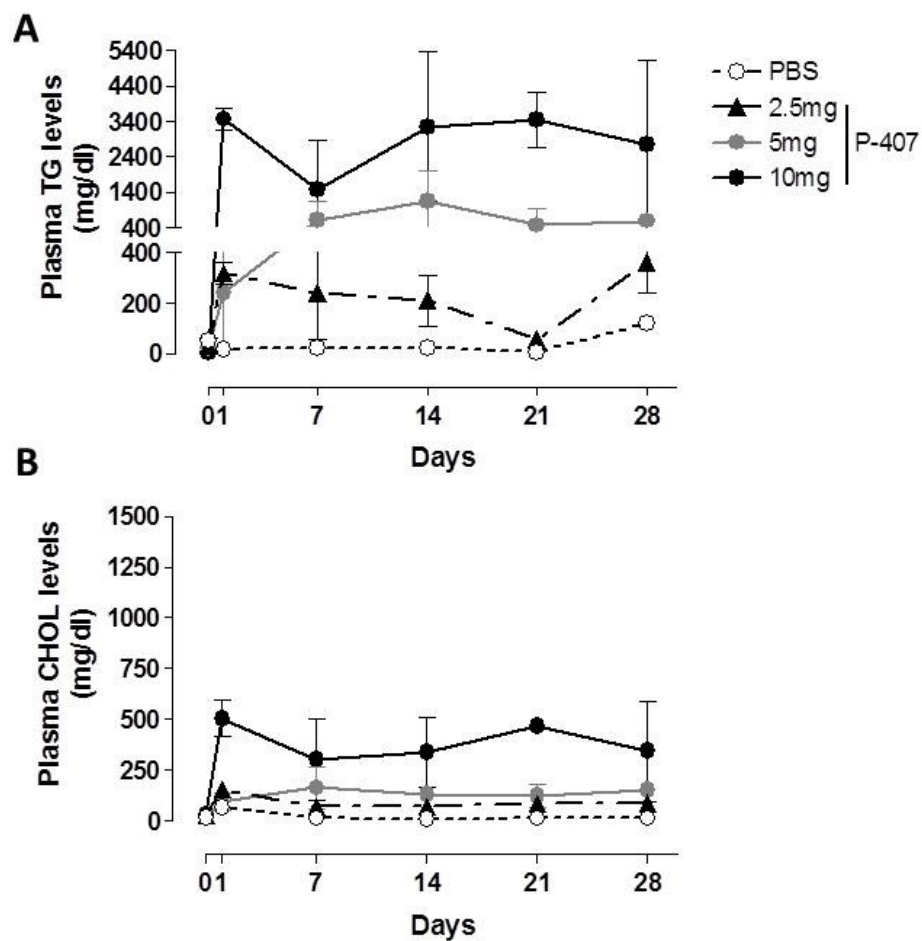


Figure 3.1. Dose-dependent effect of P-407 on plasma lipid levels.

The effect of injecting 10, 5, and 2.5mg of P-407 i.p. every 72hrs on the non-fasting plasma levels of (A) TG and (B) CHOL in chow-fed B6 mice over a period of 28 days. n=3 for each P-407 group, n=1 for PBS group. Data are expressed as mean \pm SD.

Table 3.1. Comparison of mean lipid level elevation over the experimental period between the different groups.

		TG		CHOL	
		Mean \pm SD (mg/dl)	Fold increase	Mean \pm SD (mg/dl)	Fold increase
P-407 (n=3/group)	10mg	2884.6 \pm 868.6*	\approx 70x	392.2 \pm 89.6*	\approx 18x
	5mg	615 \pm 262.7*	\approx 15x	133.7 \pm 27.1*	\approx 6x
	2.5mg	237.4 \pm 65.6*	\approx 6x	93.2 \pm 35.9*	\approx 4x
PBS (n=1)		40.1	NA	22.2	NA

* The mean level in the P-407 injected groups reflects the mean elevation following P-407 administration over the experimental period excluding baseline levels (before P-407 administration) from the calculation for these groups. For the PBS group, the mean level reflects the mean of all lipid levels obtained over the experimental period. Fold increase is in comparison to control level. NA=not applicable.

The increase in both TG and CHOL levels induced by P-407 was not steady and notable fluctuations were observed especially in TG levels (Fig-3.1). These fluctuations caused lipid levels to drop to values comparable to those obtained in the control group particularly with the use of the lowest dose, i.e. 2.5mg. This along with the fact that the lipid elevation achieved by the 2.5mg group was not high enough for the aim of the study, led to its exclusion as a possible dose to be used in subsequent experiments. As for the 10 and 5mg P-407 dosages, the observation mandated the establishment of a better dosing regimen.

To this end, the P-407 trough level was assessed to establish the best dosing regimen that will achieve relatively stable elevation in plasma lipid levels. The P-407 trough level was measured by recording the changes in total plasma TG and CHOL levels over a period of 96 hrs following a single i.p. injection of either 10 or 5mg P-407 into B6 mice kept on chow diet. Mice were bled before the injection and 6, 24, 48, 72, and 96 hours following the P-407 injection (Fig-3.2).

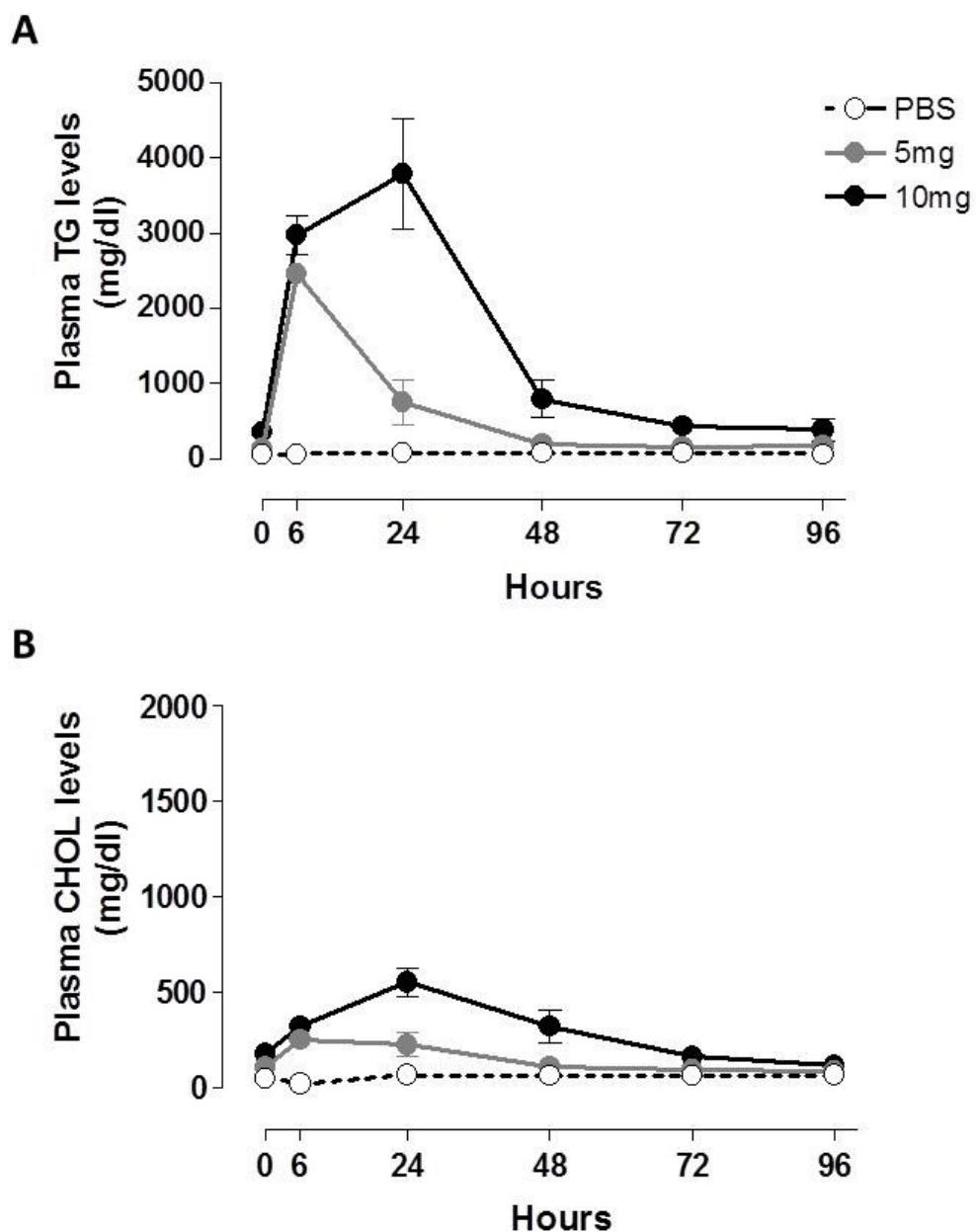


Figure 3.2. P-407 trough levels.

Changes in non-fasting plasma TG (A) and CHOL (B) levels following a single i.p. injection of 5mg (n=3) or 10mg (n=3) P-407 compared to the PBS injected control (n=1). Data presented as mean \pm SD.

A single administration of P-407 resulted in a sharp elevation of plasma TGs as early as 6 hours post injection. Peak TG levels were observed at 6 and 24-hours following 5 and 10mg P-407 injection (2464 ± 76.89 and 3784 ± 730.1 mg/dl, mean \pm SD), respectively compared to a mean level of (66.3 ± 9.3 , mean \pm SD) in the control group. After reaching peak levels, the plasma TG concentrations declined sharply by 24 and 48 hours following 5 and 10mg P-407 injection, respectively. At these time points, the levels of TGs dropped to a mean level of (754.2 ± 299.9 and 795.1 ± 254.6 mg/dl, mean \pm SD) in the 5 and 10mg P-407 injected groups, respectively, corresponding to approximately forth their peak concentrations (Fig-3.2).

Following this abrupt decline, TG levels continued to decrease, gradually approaching baseline levels by approximately 96 hours (Fig-3.2). Similar kinetics were observed with regards to CHOL levels. However, the changes in CHOL levels were much more modest than those observed for TGs. Peak CHOL levels of 251.1 ± 17.3 and 553.1 ± 75.6 mg/dl (mean \pm SD) were reached after 6 hours for 5mg P-407 injection and after 24-hours for the 10mg P-407 dose, compared to a mean level of 54.7 ± 18.3 mg/dl in the control group (Fig-3.2).

The observed sharp drop in plasma TG and CHOL levels by 48 hours of P-407 injection prompted a revision of the dosing schedule from a 72-hourly to a 48-hourly regimen in order to maintain a more steady elevation of plasma lipids. In addition, based on the above results it was decided to continue with the 5mg and 10mg P-407 doses, whereas the increase seen in lipid levels with the 2.5mg P-407 dose was considered inadequate and thus it was abandoned.

3.3. P-407-induced lipoprotein profile

The differential impact of distinct lipoprotein classes on the risk of CVD is well established (Veniant et al., 2001) and thus I analysed the lipoprotein profile induced by P-407. To this end chow diet-fed B6 mice were injected every other day with 5mg (n=5) or 10mg P-407 (n=3) for 4 weeks. PBS-injected mice served as the control group (n=3). At the end of the 4 weeks, mice were culled and serum was collected for the determination of lipoprotein distribution using FPLC. Contrary to humans who carry most of their circulating CHOL packaged in LDL, B6 mice have been shown to carry their CHOL mainly in the form of HDL (Ishibashi et al., 1993; Jawien et al., 2004; Kennedy et al., 2010). In accordance with what have been reported for B6 mice, the PBS-injected group showed a predominance of the HDL class of lipoproteins in their plasma (Fig-3.3). The injection of P-407, regardless of the dose, caused a dramatic shift in the lipoprotein distribution from HDL to VLDL predominance (Fig-3.3). This is not surprising given the mechanism of action of P-407 which is largely dependent on the inhibition of LpL with the consequent accumulation of VLDL in circulation. Looking at Fig-3.3, it can also be appreciated that the increase in circulating levels of both TG and CHOL induced by P-407 is largely attributed to an expansion of the VLDL fraction of lipoproteins. It is also worth noting that the P-407-induced increase in VLDL was accompanied by a decrease in HDL. An inverse relationship between TG levels and HDL is well documented in the literature (Berglund et al., 2012; Grundy, 1998).

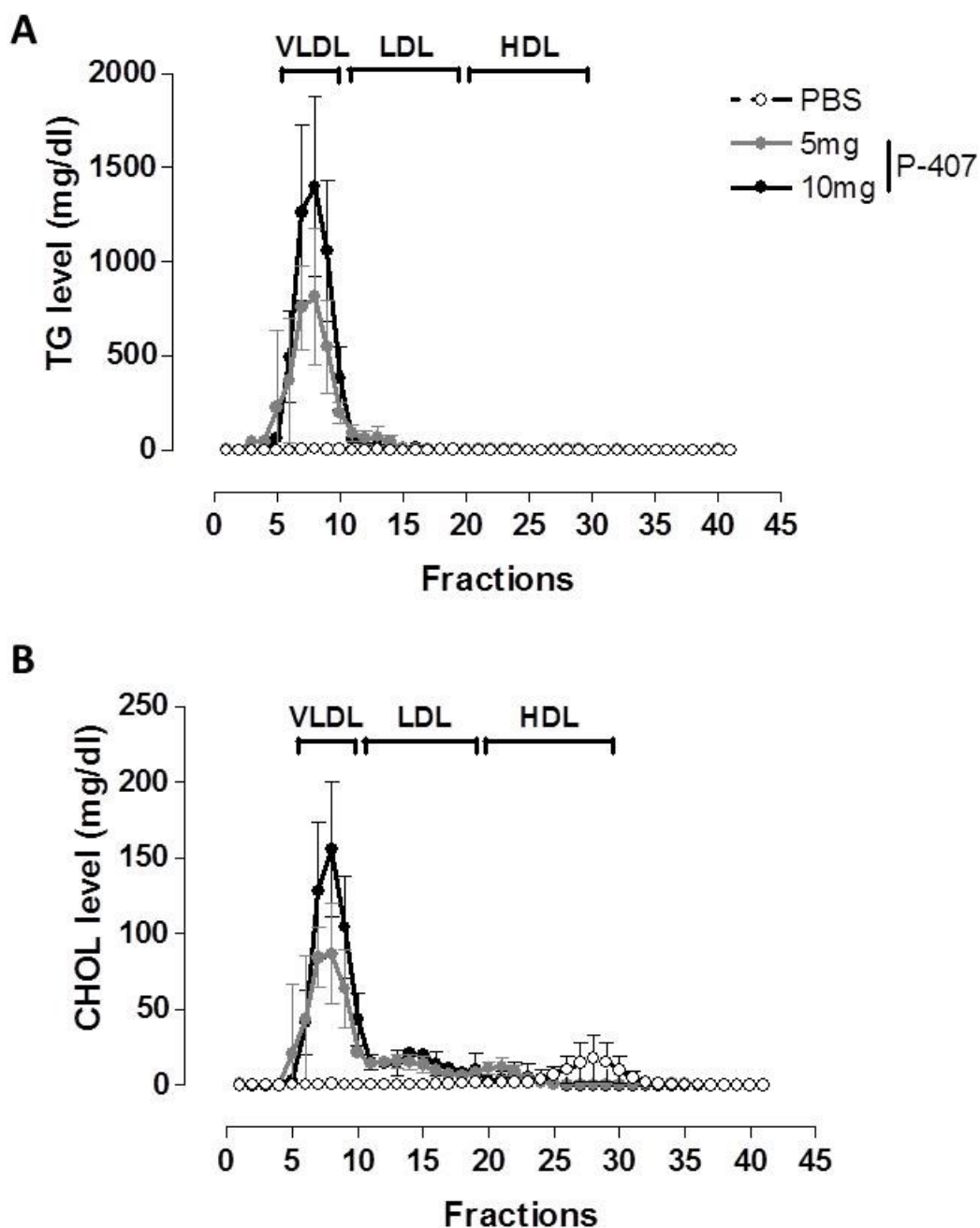


Figure 3.3. P-407-induced lipoprotein profile.

The distribution of TGs (A) and CHOL (B) among the different lipoproteins in P-407 induced hyperlipidemia assessed by Superose 6 chromatography. Chow-fed B6 mice were injected with either PBS, 5 or 10mg P-407 i.p. every 48hrs for 4 weeks. Serum for FPLC was collected at the end of the 4 weeks following an overnight fast. VLDL corresponds to fractions 5 to 10, LDL corresponds to fractions 11 to 19, and HDL corresponds to fractions 20 to 30. Data presented as mean \pm SD.

3.4. Side-effects of P-407

Having determined the lipid profile induced by P-407 and established the dose to be used for the purpose of my study, I then assessed whether the compound had potential adverse effects. P-407 has been described as an inert compound with no toxic effects (Johnston et al., 1993). However, splenomegaly, hematologic abnormalities particularly decreased RBC parameters, as well as alterations in renal function have been observed (Abe et al., 1990; Johnston et al., 1993; Li et al., 1996). Most of these side effects were reported with doses exceeding 1g/kg body weight, which is much higher than the maximum dose I intended to use. Despite that, I conducted some experiments to delineate the occurrence of such side effects with the proposed doses. Toxicity experiments were conducted using the 10mg dose, as it was the maximum dose planned for use in the current study. Chow-fed B6 mice were injected every other day for a period of 28 days with either PBS (n=6) or 10mg P-407 (n=7). Baseline body weight was recorded and blood was collected via tail bleed for hematocrit measurement before starting the injections. At the end of the experiment, spot urine examination for the presence of blood and protein was performed using dipstick urinalysis and blood was collected for plasma lipid and hematocrit measurements. Tissues were harvested for histological analysis and the spleen was weighed prior to fixation.

As expected, the 10mg P-407 injection resulted in an increase in plasma TG and CHOL levels (Fig-3.4A & B). The P-407-injected mice continued to look healthy, showed no reduction in their body weight (Fig-3.4C), and no increase in morbidity or mortality. However, as described by other investigators (Johnston et al., 1993), there was a significant drop in the percent hematocrit value in the P-407-injected group after 28 days of 10mg P-407 administration when compared to its corresponding baseline level

(day 0) ($43.2 \pm 0.75\%$ vs 35.57 ± 1.71 , mean \pm SD, $P < 0.0001$, paired t-test) (Fig-3.4D).

The size of the spleen was found to be significantly increased in the P-407-injected mice when compared to controls ($P = 0.0067$, unpaired t-test) (Fig-3.4E).

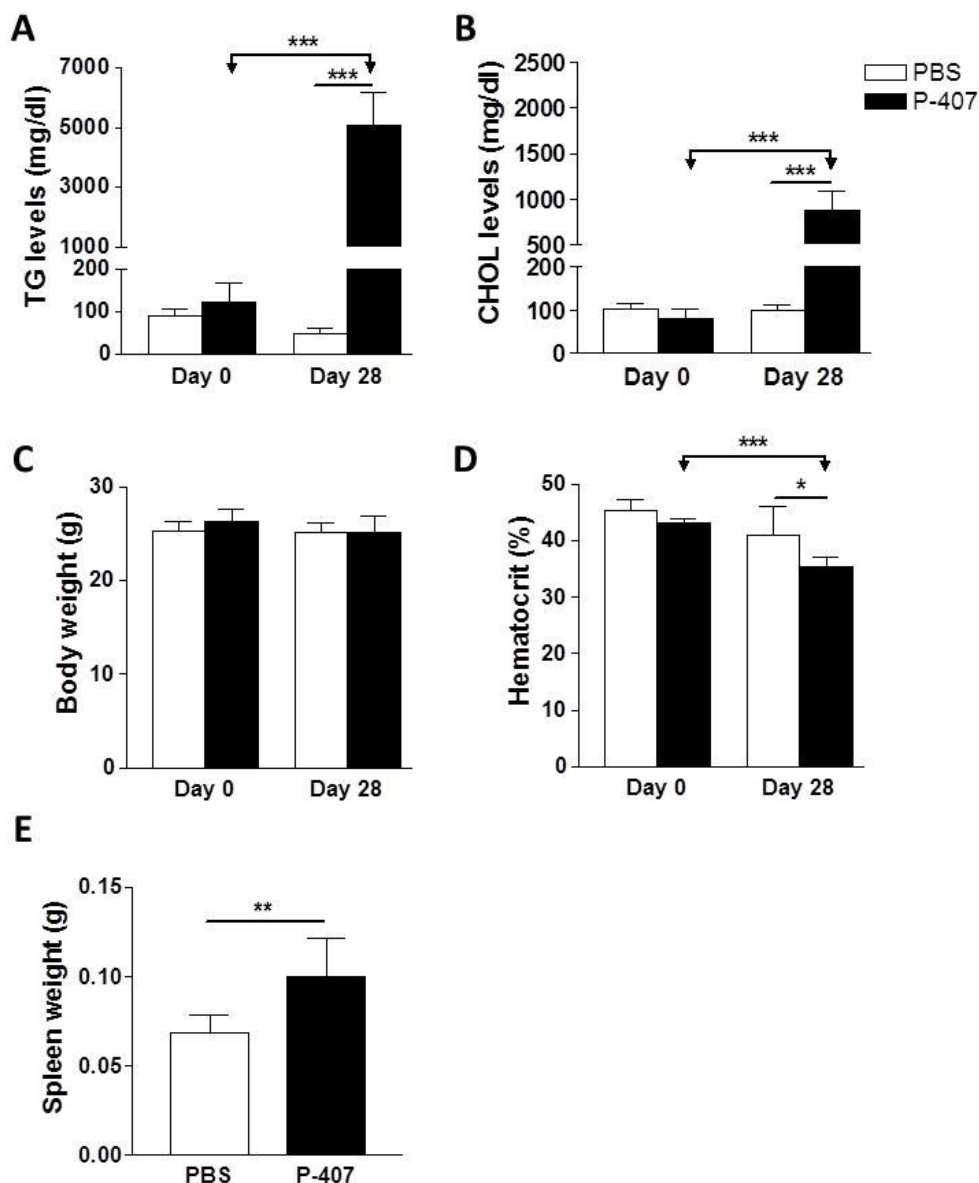


Figure 3.4. Effect of P-407 on body weight, spleen and hematocrit

The effects of P-407 administration on non-fasting plasma levels of TG (A) and CHOL (B), total body weight (g) (C), % haematocrit (D), and spleen weight (g) (E) in chow-fed B6 mice receiving 10mg P-407 i.p. every 48hrs for a period of 28 days. For figures (A to D) values for P-407 group (n=7) were compared to those of the PBS group (n=6) at baseline (day 0), prior to any intervention, and following 28 days of P-407/PBS injections (day 28). Data are presented as mean \pm SD. P value calculated using unpaired t-test when comparing between two different groups and paired t-test when comparing between days 0 and 28 within the same group. *P<0.05, **P<0.01, ***P<0.001.

Upon histological examination, H&E-stained spleen sections revealed no abnormalities apart from the presence of foam cells in the red pulp of the spleen that were absent in the control sections (Fig-3.5). An observation extended to the heart and liver as well (Fig-3.5). In the heart, foam cells were mainly seen in the vicinity of blood vessels. Histological examination of H&E-stained kidney sections showed no abnormalities or foam cells (Fig-3.5). In addition, urine dipstick analysis after 28 days of P-407 injection showed no hematuria and no proteinuria in the P-407 injected group when compared to controls (Fig-3.6A & B).

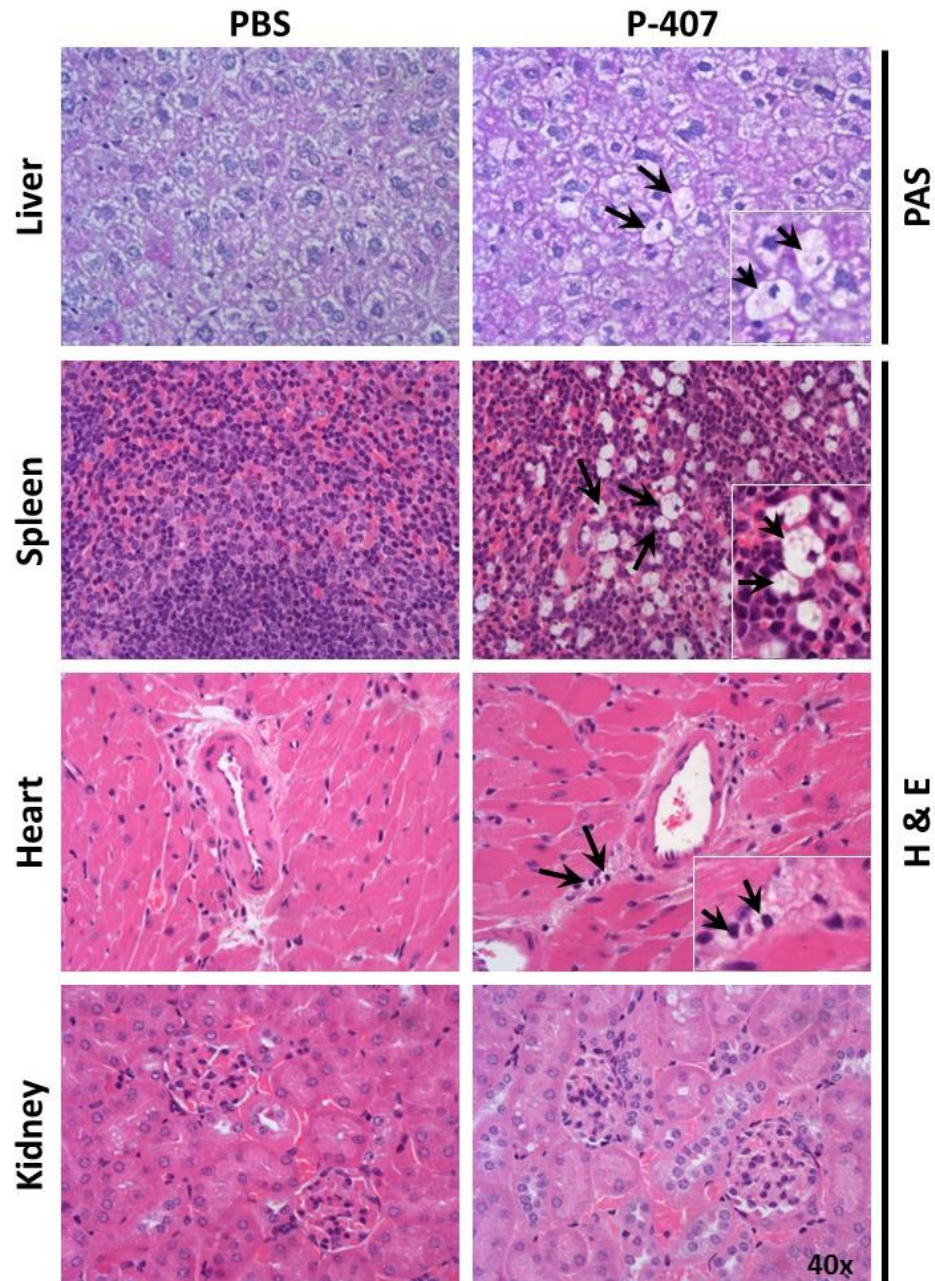


Figure 3.5. Histological examination of tissues following 28 days of P-407 induced hyper-TGRL state.

Representative pictures of H&E-stained sections from the spleen, heart and kidney as well as PAS-stained liver sections collected from chow-fed B6 mice after 28 days of receiving either PBS or 10mg P-407 i.p. every 48hrs. Black arrows indicate foam cells. 40x magnification. Zoomed in images of liver, spleen, and heart were taken at 100x power field using oil-immersion.

Lastly, to ensure that the P-407-induced hyperlipidemia does not incite a systemic inflammatory reaction that may influence the behaviour of MOs and MØs, the plasma levels of several key inflammatory cytokines were measured. These included: TNF- α , IL-6, MCP-1 (CCL2), CXCL1 (the murine homologue for interleukin-8, IL-8), MIP-1 α (CCL3), IL-10, and IFN- γ . Using a cytokine multiplex assay the plasma level of these cytokines was determined after 28 days of 10mg P-407 injection in chow-fed B6 mice (n=4) with a PBS injected group (n=4) serving as controls. Of the cytokines measured, IL-6, IL-10, and IFN- γ were undetectable. TNF- α level was also undetectable with the exception of one mouse in the P-407 group that showed a negligible level of 31.27 pg/ml. MCP-1, CXCL1, and MIP-1 α showed a tendency to be slightly higher in the P-407 injected mice when compared to controls, however, the differences was not significant, Fig-3.7A to G. Moreover, examination of the abdominal cavity of repeatedly injected mice did not show gross signs of inflammation.

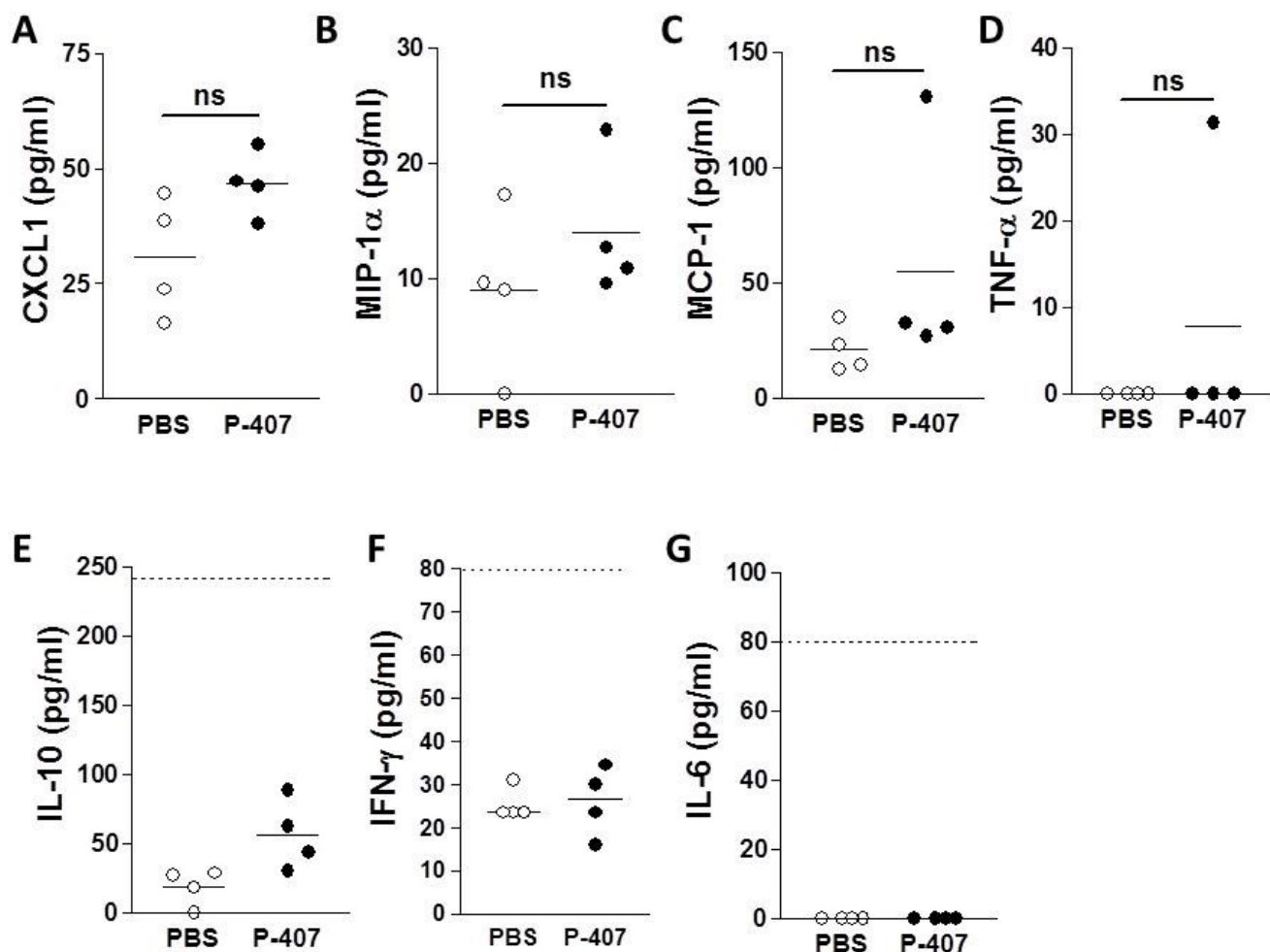


Figure 3.7. Plasma levels of different inflammatory cytokine/chemokines following 28 days of P-407-induced hyper-TGRL state.

Plasma levels of (A) IL-8, (B) MIP-1 α , (C) MCP-1, (D) TNF- α , (E) IL-10, (F) IFN- γ , and (G) IL-6 measured after 28 days of i.p. administration of either PBS or 10mg P-407 injection every 48hrs in chow-fed B6 mice (n=4 per group). Horizontal bars denote the mean. P value calculated using unpaired t-test, ns = not significant. Horizontal dotted line in (E to G) denotes the limit of detection of the assay.

3.5. Conclusion

The P-407 model induces a hyperlipidemic state driven by the accumulation of TGRLs resulting in massive hypertriglyceridemia and a lipid profile that carries great resemblance to the atherogenic lipid triad seen in hypertriglyceridemic conditions. This hyper-TGRL state occurs in the absence of other metabolic derangements and without invoking a generalised inflammatory response. Taken together, the ease of use of the P-407 model along with its favourable hyper-TGRL state makes it a plausible model to study the effects of such an environment on the behaviour of MOs.

3.6. Summary

- The P-407 model induces a dose-dependent hyperlipidemia largely driven by an increase in TGs and TGRLs with a lipoprotein profile closely related to the atherogenic lipid profile seen in hypertriglyceridemic subjects.
- The P-407-induced hyper-TGRL state is not associated with profound side effects that can adversely affect the results of this study.
- The P-407 model did not invoke a generalised inflammatory response that can influence the behaviour of MOs.

3.7. Discussion

Many factors contribute to the development of hypertriglyceridemia including; overweight, physical inactivity, excess alcohol intake as well as the presence of other metabolic disturbances such as T2D and the MS (Berglund et al., 2012). Severe hypertriglyceridemia occurs in combined familial hyperlipidemia (CFH) and familial hypertriglyceridemia with the former being considered the commonest genetic lipid disorder associated with atherosclerosis (Hassing et al., 2012). Studying the effects of

hypertriglyceridemia and a hyper-TGRL state has been hampered in part by the extreme variability in TG metabolism between human subjects and by its existence in conjunction with other metabolic abnormalities. Similarly in animal models, the occurrence of hypertriglyceridemia is invariably associated with hyperglycemia and IR as is the case in murine models of obesity and the MS making it difficult to discern its specific role in the pathogenic process (Kennedy et al., 2010). While in the hyperlipidemic model of atherosclerosis, its presence is superimposed by a much higher elevation in CHOL levels (Jawien et al., 2004). The pressing problem of hypertriglyceridemia in today's society fuelled by current dietary habits and a sedentary life style demands better understanding of its pathogenic effects. In an attempt to gain better insight into the pathogenic effects of hypertriglyceridemia and a hyper-TGRL state, I investigated the use of the chemically-induced model described by Johnston et al using the compound P-407 (Johnston, 2004). P-407 is a surfactant shown to induce a dose-dependent hyperlipidemia in rodents (Palmer et al., 1997). In line with what has been reported by Johnston et al, I observed a dose-dependent hyperlipidemia characterised mainly by an increase in TGs (Fig-3.1). The ability to tailor the hypertriglyceridemic response by varying the dose of P-407 is a great advantage. In the clinical setting, moderate hypertriglyceridemia is commonly seen in association with the MS and T2D, whereas the more severe phenotype is reserved for those with the genetic susceptibility to develop CFH and other related diseases. The choice to pursue the study using 10 and 5mg dosage of P-407 was based on the resemblance of their hypertriglyceridemic state to that seen in severe and moderate hypertriglyceridemia, respectively where most of the link to end organ damage has been described.

The hypertriglyceridemic effect of P-407 is mediated largely through its inhibition of LpL, the major enzyme responsible for hydrolysing TGRLs including VLDLs and CMs (Johnston and Palmer, 1993; Palmer et al., 1997). In agreement with its mechanism of action, the P-407-induced lipoprotein profile was characterised by massive expansion of the VLDL lipoprotein fraction in P-407-injected mice when compared to controls (Fig-3.3). VLDL is responsible for transporting endogenously synthesised TGs to peripheral tissues, making it one of the major carriers of TGs in circulation. However, in addition to their TG rich core, VLDLs carry a small amount of CHOL as well. Thus, it is not surprising that an increase in plasma VLDL concentration would be accompanied by a parallel increase in CHOL levels. In fact, analysis of plasma lipid levels showed that the massive hypertriglyceridemia was accompanied by a much more moderate increase in CHOL levels (Fig-3.1). It has been suggested by Johnston et al that the hypercholesterolemic effect observed with P-407 is due to its effect on HMG-CoA reductase, the rate limiting enzyme in CHOL synthesis (Johnston et al., 1999). Although this mechanism cannot be ruled out in the current study, it appears that the hypercholesterolemia may be mediated by the same mechanism causing the hypertriglyceridemia i.e. inhibition of LpL and accumulation of VLDL. This argument is based on the lipid profile showing CHOL to be mainly derived from the VLDL fraction (Fig-3.3), along with the great discrepancy between the elevations seen in TG levels and CHOL (Fig-3.1) which may be a mere reflection of their disproportionate distribution within the VLDL particle itself. In addition to VLDL accumulation, the P-407-induced lipid profile revealed a tremendous drop in HDL levels (Fig-3.3). Elevated VLDL levels along with decreased HDL are components of the atherogenic lipid triad known to be induced

by hypertriglyceridemia (Grundy, 1998). Hypertriglyceridemia and the accumulation of TG-rich VLDLs has a domino effect on the composition of other lipoprotein fractions including LDL and HDL with the resultant accumulation of the atherogenic sd-LDLs and a profound drop in cardio-protective HDLs (Grundy, 1998; Krauss, 1998). Thus the P-407-induced model of hypertriglyceridemia induces a lipoprotein phenotype similar to that observed in human subjects with hypertriglyceridemia. More importantly, the P-407-induced changes in TGs and lipoproteins has been reported to occur in the absence of metabolic derangements in glucose metabolism and insulin, the commonest metabolic abnormalities associated with hypertriglyceridemia in murine models, making it a plausible model to study the effects of hypertriglyceridemia and a hyper-TGRL state in the absence of other confounding factors (Johnston and Waxman, 2008).

Despite its safety profile, a few side effects have been reported with the use of P-407 warranting further investigation. Abe et al reported the occurrence of renal toxicity in mice receiving a dose ranging from 1.7-5 g/kg body weight which is much higher than the dose used in this report (Abe et al., 1990; Dumortier et al., 2006). Since one of the aims of my study is to investigate the effect of a hyper-TGRL state on enhancing kidney damage in a model of renal disease it was necessary to investigate the risk of renal toxicity with the dose I intended to use. Administration of 10mg (0.5g/kg body weight) P-407 was not associated with signs of renal damage as judged by the absence of hematuria and gross proteinuria on urine dipstick analysis as well as normal histological appearance making it a safe dose to use in the current investigation (Fig-3.5-6). Thus, the occurrence of renal toxic effects seems to be related to the use of higher doses of P-407. On the other hand, we observed a drop in hematocrit levels along with

splenomegaly in mice injected with P-407 when compared to controls (Fig-3.4). Whether splenomegaly is the cause or the consequence of the drop in hematocrit has not been determined. However, a similar observation has been reported by Johnston et al who also showed red pulp expansion of the spleen, the splenic site for RBC clearance (Johnston et al., 1993). I observed accumulation of foam cells in the red pulp area of the spleen following 28 day treatment of P-407, an observation that has been extended to other tissues including the heart and liver (Fig-3.5). Foam cells are MØs that have accumulated excessive amounts of lipids into their cytoplasm resulting in its clear foamy appearance. Hence their presence may signify lipid deposition into these tissues secondary to the high circulating levels of TGRLs. Apart from foam cells, I did not observe any gross histologic abnormalities in the examined tissues (Fig-3.5). Another important aspect to consider was whether this P-407-induced hyper-TGRL state provokes a generalised inflammatory response, which has been reported with some hyperlipidemic models such as apoE^{-/-} model of atherosclerosis (Lohmann et al., 2009). Investigating the occurrence of inflammation with the P-407-induced hypertriglyceridemia is deemed necessary given that the major aim of my study is to delineate the effects of such an environment on MO behaviour, which are known to be avid responders to inflammatory cues. To this end, in the plasma of P-407-injected mice I was unable to detect TNF- α , IL-6, and IFN- γ , the major cytokines implicated in inflammation (Fig-3.7D, F & G). Furthermore, there was no significant difference in the levels of the major chemokines; MCP-1 and MIP-1 α known to have a direct effect on MO and MØs (Fig-3.7C & B). However, it is important to note that the number of mice in each group (n=4) is too small to draw any firm conclusions and despite the absence of

significant detectable changes in the levels of the aforementioned cytokines/chemokines under the influence of P-407, further investigations are required to definitively exclude an effect for P-407 on the production of such inflammatory mediators.

CHAPTER 4- THE EFFECTS OF P-407-INDUCED HYPER-TGRL ENVIRONMENT ON PERIPHERAL BLOOD MONOCYTES AND TISSUE MACROPHAGES

4.1. Introduction:

The effects of lipids on MOs and MØs have been extensively studied in the context of murine atherosclerosis models using genetically modified mice, such as apoE^{-/-} and Ldlr^{-/-} animals. In these models, hyperlipidemia is characterized mainly by an increase in plasma CHOL levels rather than TGs. One of the shortcomings of such models is that it involves the use of high-fat diet, which by itself has been shown to be pro-inflammatory (Liao et al., 1993), making it difficult to distinguish the effect of lipids from that of the pro-inflammatory condition. The atherogenic potential of pp lipemia and the hyper-TGRL state is rapidly gaining recognition (Karpe, 1999; Sarwar et al., 2007; Steiner, 1993; Zilversmit, 1995). This carries great implications given that our bodies are burdened by an intense influx of TGRLs after each meal, especially with the HF content of the western diet. It has thus become increasingly interesting to delineate the effect of such TGRL-rich environment on the behaviour of PB MOs and MØs, being the major players in the pathogenesis of atherosclerosis. The non-inflammatory TGRL-driven state of hyperlipidemia induced by P-407 makes it a plausible model to study the effects of such an environment on the behaviour of PB MOs and tissue MØs.

This chapter deals with the experiments aimed at delineating the effects of a high-TGRL environment on the behaviour of MOs and tissue MØs. Given the heterogeneity of MOs, I first sought to check whether the hyper-TGRL environment had a differential effect on the numbers/phenotype of peripheral blood MO subsets. The consistent phenotype

observed in MOs induced by the P-407-induced hyper-TGRL environment was intriguing and triggered a series of subsequent experiments that aimed at understanding the mechanism behind such observations.

4.2. The effect of P-407-induced hyper-TGRL environment on PB MOs

To study the effect(s) of a hyper-TGRL environment on the repertoire of circulating MOs, a time course experiment was performed. Chow-fed B6 mice were injected with either P-407 or PBS for a period of 28 days. Two doses of P-407 were tested, namely 5 and 10mg, in separate experiments. The number and frequency of PB MOs and their subsets were analysed using flow cytometry at baseline (day 0) and on day 7, 14, 21, and 28 from starting the injections. In addition to MOs, the numbers and frequency of other PB cells, including T-cells, B-cells, and PMNs, were analysed. For the 5mg P-407 dose, only one time course experiment was performed (n=4, per group). Whereas for the 10mg P-407 dosage, a total of 5 experiments were performed. Three of which were carried up to 28 days of 10mg P-407 injection i.p. thrice weekly while the other two experiments were terminated at 7 and 14 days to enable organ collection at these time points. Details of experimental design are shown in the materials and methods section, Fig-2.1. Thus, the data presented for the 10mg P-407 dose represent pooled data from the 5 different experiments with a minimum number of n=7 per group at each time point. To ensure that P-407 injection induced the expected hyper-TGRL environment, lipid levels were measured at each time point. As shown in the previous chapter, the injection of 5 and 10mg P-407 resulted in a dose-dependent elevation in both TG and CHOL levels (Fig-4.1). The mean high level of TGs achieved by 10mg P-407 was (2768

± 1906 mg/dl, mean \pm SD) compared to a mean level of 74.5 ± 35.4 mg/dl in the PBS-injected group. While the mean TG level in the 5mg P-407 group was 581.3 ± 258.8 mg/dl compared to a mean level of 91.7 ± 12.3 mg/dl in the control group (Fig-4.1A & B). Similar changes were seen in CHOL levels, although less dramatic, with a mean high level of 321.4 ± 131.5 mg/dl and 168.5 ± 33.2 mg/dl in the 10mg and 5mg injected animals respectively, compared to a mean level of 98 ± 20.9 and 99.2 ± 14.6 mg/dl in their corresponding control groups (Fig-4.1C & D).

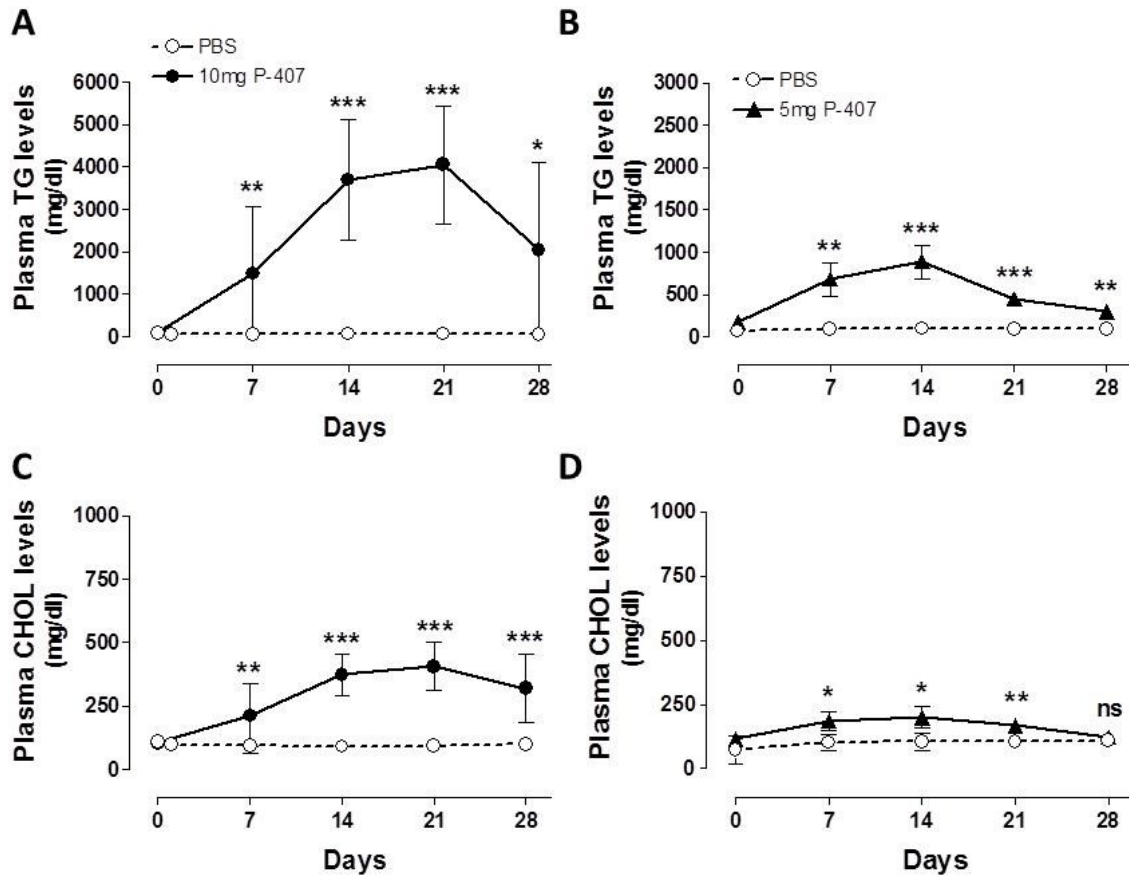


Figure 4.1. Time course of lipid levels upon 10 and 5mg P-407 injection over a period of 28 days.

Non-fasting plasma levels of TGs (A & B) and CHOL (C & D) induced by 10mg and 5mg P-407 injections over a period of 28 days. For the 10mg experiment data represent pooled data from 5 independent experiments with a minimum $n=7$ per group at each time point (details of experimental design are described in materials and methods section, Fig-2.1). For 5mg experiment data represent one experiment ($n=4$ per group). Data are presented as mean \pm SD. P value calculated using unpaired t-test. * $P<0.05$, ** $P<0.01$, *** $P<0.001$, and ns = not significant.

Following the induction of a hyper-TGRL state, I then looked at its effect on PB MOs. Using flow cytometry, MOs can be identified by their low SSC and co-expression of CD115 and CD11b (Sunderkotter et al., 2004) (Fig-4.2A). Regardless of the dose, the total number of MOs showed no sustained difference in the P-407-injected groups when compared to their corresponding controls (Fig-4.2B & C). However, the effect on the percentage of MOs within the total white blood cells (WBCs) was different. The injection of 10mg P-407 resulted in a slight drop in the frequency of MOs towards the end of the 28-day period when compared to the control group (Fig-4.2D). On the other hand the percentage of MOs in the 5mg P-407-injected group showed no differences when compared to their corresponding controls throughout the period of the experiment (Fig-4.2E). As the numbers of MOs in the 10mg P-407 were not significantly different, the drop in the percentage of MOs in this group may reflect a difference in the total WBC count between the groups. In fact, there was a slight, albeit not significant, increase in the total WBC count in the 10mg P-407 group towards the later time points of the experiments (Fig-4.3).

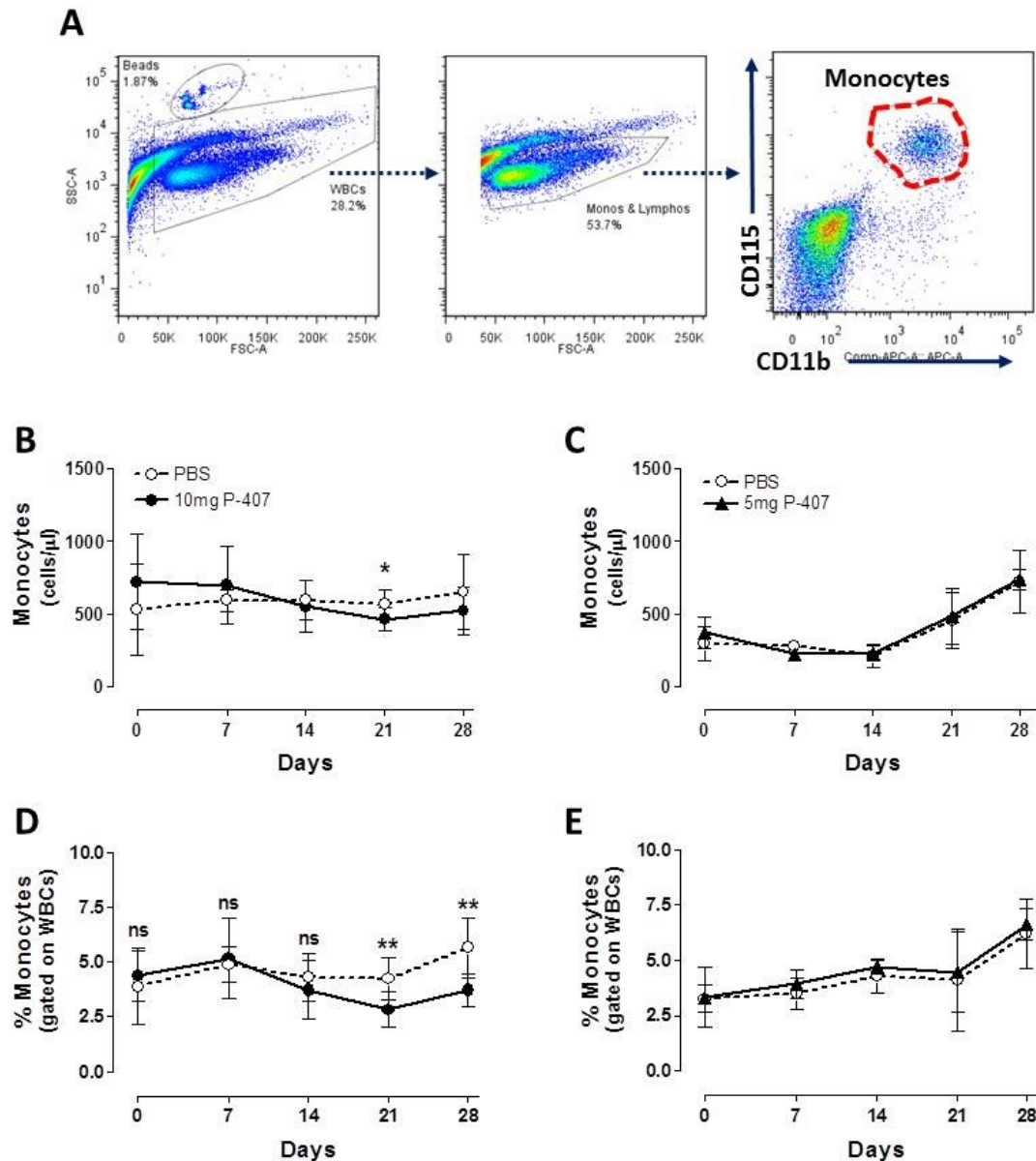


Figure 4.2. Time course of peripheral blood MOs upon 10 and 5mg P-407 injections.

(A) Shows the gating strategy used to identify PB MOs. (B & C) show the absolute MO numbers in response to the i.p. injection of 10 (B) and 5mg (C) P-407 thrice weekly over a period of 28 days. (D & E) show the frequency of MOs in response to 10 (D) and 5mg (E) P-407 injections. For the 10mg P-407 dose, the data represent pooled data from 5 different experiments with a minimum number of $n=7$ for each group at each time point (details of the experimental design are shown in materials and methods section, Fig-2.1). Whereas for the 5mg P-407, the data represent a single experiment ($n=4$, per group). Data are presented as mean \pm SD. P value calculated using unpaired t-test, * $P<0.05$, ** $P<0.01$, and ns=not significant.

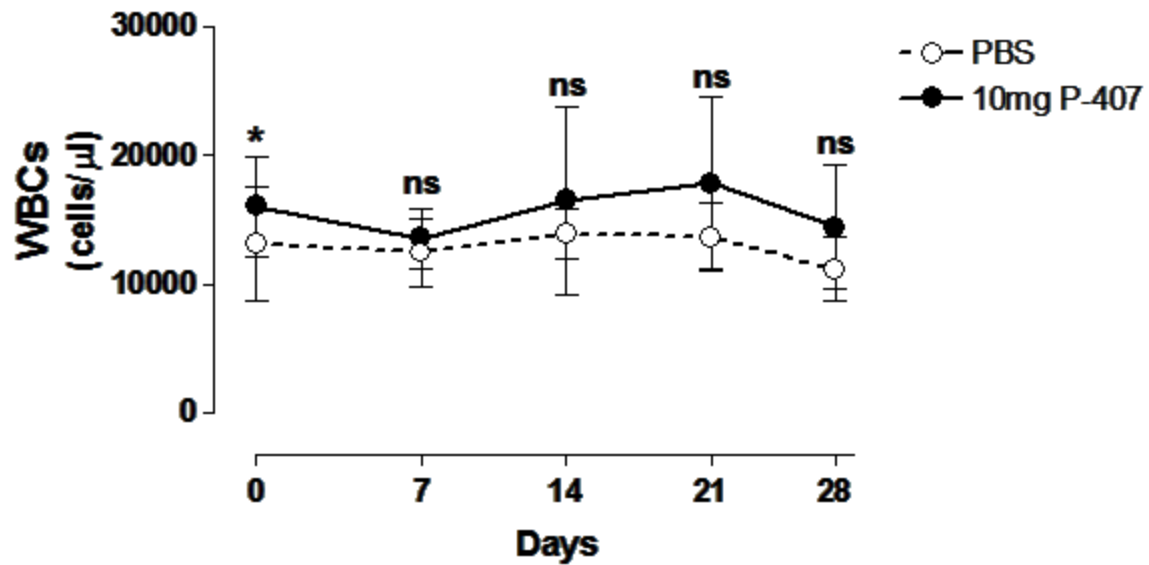


Figure 4.3. The effect of 10mg P-407 injections on the total number of WBCs over a period of 28 days.

Total numbers of WBCs following 28 days of 10mg P-407 injections i.p. thrice weekly against a PBS-injected control group. Data represent pooled data from 5 different experiments with a minimum number of n=7 for each group at each time point (details of the experimental design are shown in materials and methods section, Fig-2.1). Data are presented as mean \pm SD. P value calculated using unpaired t-test. *P<0.05 while ns=not significant.

Although the total MO numbers were not affected by the hyper-TGRL state, I then investigated whether this hyperlipidemic environment could influence MO subpopulations. MO subsets were identified according to their Gr1 surface expression as Gr1^{high} and Gr1^{low} MOs (Geissmann et al., 2003) as shown in Fig-4.4A. As expected PBS injections did not alter the numbers of Gr1^{low} and Gr1^{high} MOs significantly (Fig-4.4A,B & C). Interestingly, the injection of 10mg P-407 resulted in a progressive decline in the numbers the Gr1^{low} MOs from an initial value of 401.5±168 cells/μl (mean ± SD) at day 0 to 122.5 ± 49.3 cells/μl by day 28 (P<0.001, paired t-test) (Fig-4.4B). The numbers of Gr1^{high} MOs, on the other hand, showed an initial increase with 10mg P-407 injection. However, the effect was transient and the numbers of Gr1^{high} MOs returned to values similar to their baseline levels by day 14 (P=0.7926, paired t-test) and continued as such throughout the remaining period of the experiment (Fig-4.4C).

The percentage of MO subsets, expressed as their relative frequencies within total MOs, was skewed towards a preponderance of Gr1^{high} MOs at the expense of Gr1^{low} MOs in the 10mg P-407-injected group (Fig-4.4D & E). This was different from the PBS-injected group that showed an almost equal contribution of the two MO subsets (Fig-4.4D & E). The changes in the numbers and frequencies of MO subsets were observed only with the 10mg P-407 dose and not with the 5mg P-407 dose (Fig-4.5).

With regards to other circulating blood cells, 10mg P-407 injections did not result in consistent changes in the numbers of B- or T-cells (Fig-4.6A & C). The numbers of PMNs, on the other hand, showed a tendency to be slightly increased in the 10mg P-407 group (1388±294.8 cells/μl and 1122±276.8 cells/μl, mean±SD) on days 21 and 28, respectively when compared to their corresponding control values (904.8±256.4 cells/μl

and 831.1 ± 233.1 cells/ μ l, mean \pm SD) ($P=0.0019$ and $P=0.0483$, unpaired t-test, respectively) (Fig-4.6E). With regards to the relative frequencies of these cells within the total WBC pool, there was no sustained difference in the percentages of B-cells and PMNs in the 10mg P-407-injected group when compared to the PBS-injected control (Fig-4.6B & F). Whereas the percentage of T-cells had a tendency to be consistently lower in the 10mg P-407-injected group when compared to controls (Fig-4.6D). Again, the 5mg P-407 dose showed no significant differences in any of these cellular parameters when compared to the PBS-injected control (Fig-4.7).

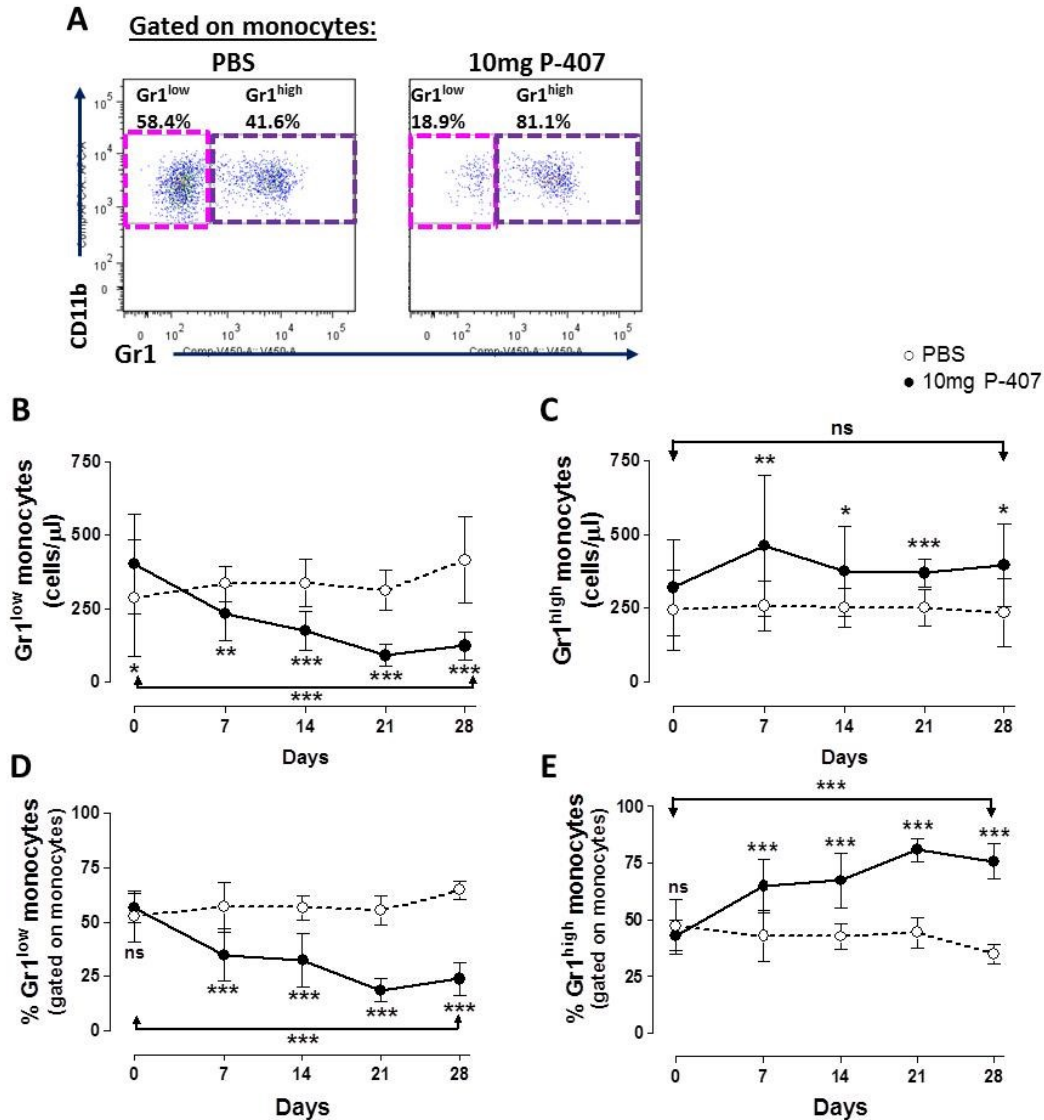


Figure 4.4. The effect of 10mg P-407 injection on MO subsets in the blood.

(A) Representative flow-cytometry plots showing the frequencies of Gr1^{low} and Gr1^{high} MOs in 10mg P-407 and PBS-injected mice after 28 days of P-407 injection. (B & C) Show the changes in MO subset numbers while (D & E) show changes in the frequency of Gr1^{low} and Gr1^{high} MOs, respectively over a period of 28 days of thrice weekly i.p. injection with either 10mg P-407 or PBS. Data are presented as mean \pm SD and represent pooled data from 5 different experiments with a minimum of 7 mice per group at each time point (details of the experimental design are shown in materials and methods section, Fig-2.1). P value shown at each time point indicate comparisons between the two different groups calculated using unpaired t-test. While arrows indicate comparisons between day 0 and day 28 in the 10mg P-407 group using paired t-test. *P<0.05, **P<0.01, ***P<0.001, and ns=not significant.

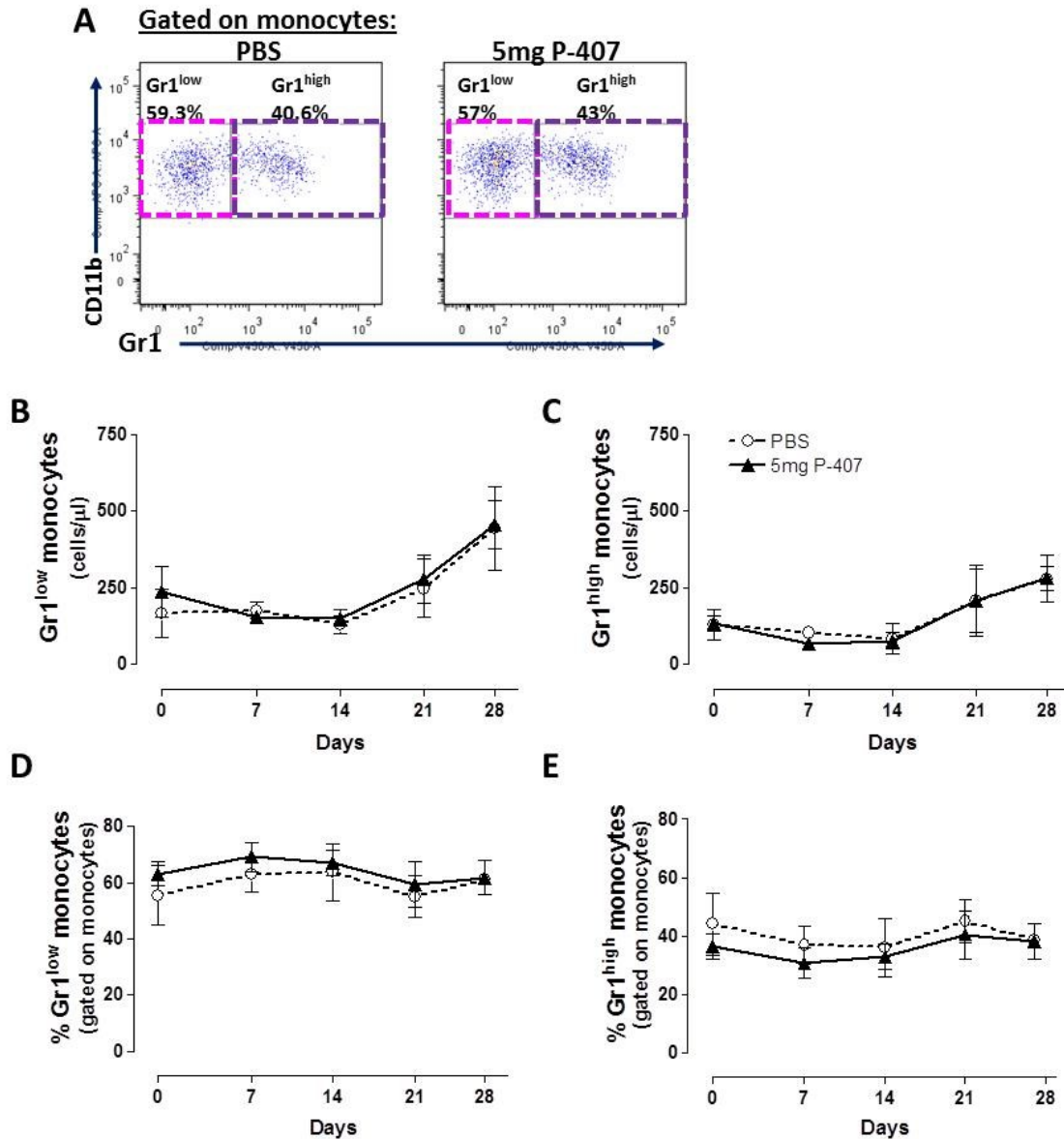


Figure 4.5. The effect of 5mg P-407 injection on MO subsets in the blood.

(A) Representative flow cytometry plots showing the frequencies of Gr1^{low} and Gr1^{high} MOs in 5mg P-407 and PBS-injected mice after 28 days of P-407 injection. (B & C) Show the changes in MO subset numbers while (D & E) show the changes in the frequencies of Gr1^{low} and Gr1^{high} MOs in response to the i.p. injection of either 5mg P-407 or PBS three times a week over a period of 28 days. Data are presented as mean \pm SD, n=4 per group at each time point.

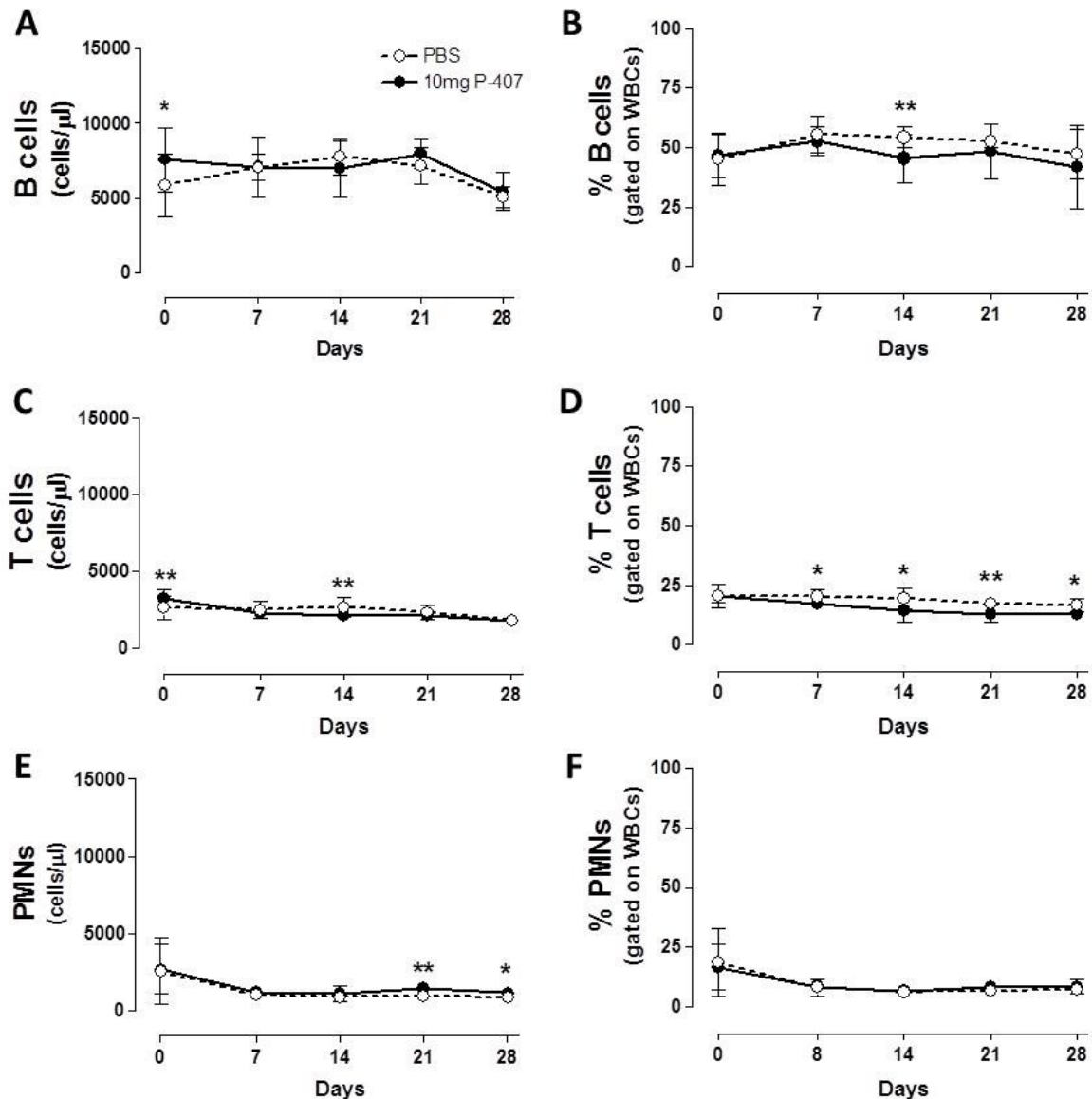


Figure 4.6. The effect of 10mg P-407 injection on the different peripheral blood cells.

PB number and frequency of B-cells (A & B), T-cells (C & D), and PMNs (E & F) in response to either 10mg P-407 or PBS injection i.p. thrice weekly over a period of 28 days. Data are presented as mean \pm SD and represent pooled data from 5 different experiments with a minimum of 7 mice per group at each time point (details of the experimental design are shown in materials and methods section, Fig-2.1). P value was calculated using unpaired t-test comparing between 10mg P-407 and PBS at each time point. *P<0.05, and **P<0.01.

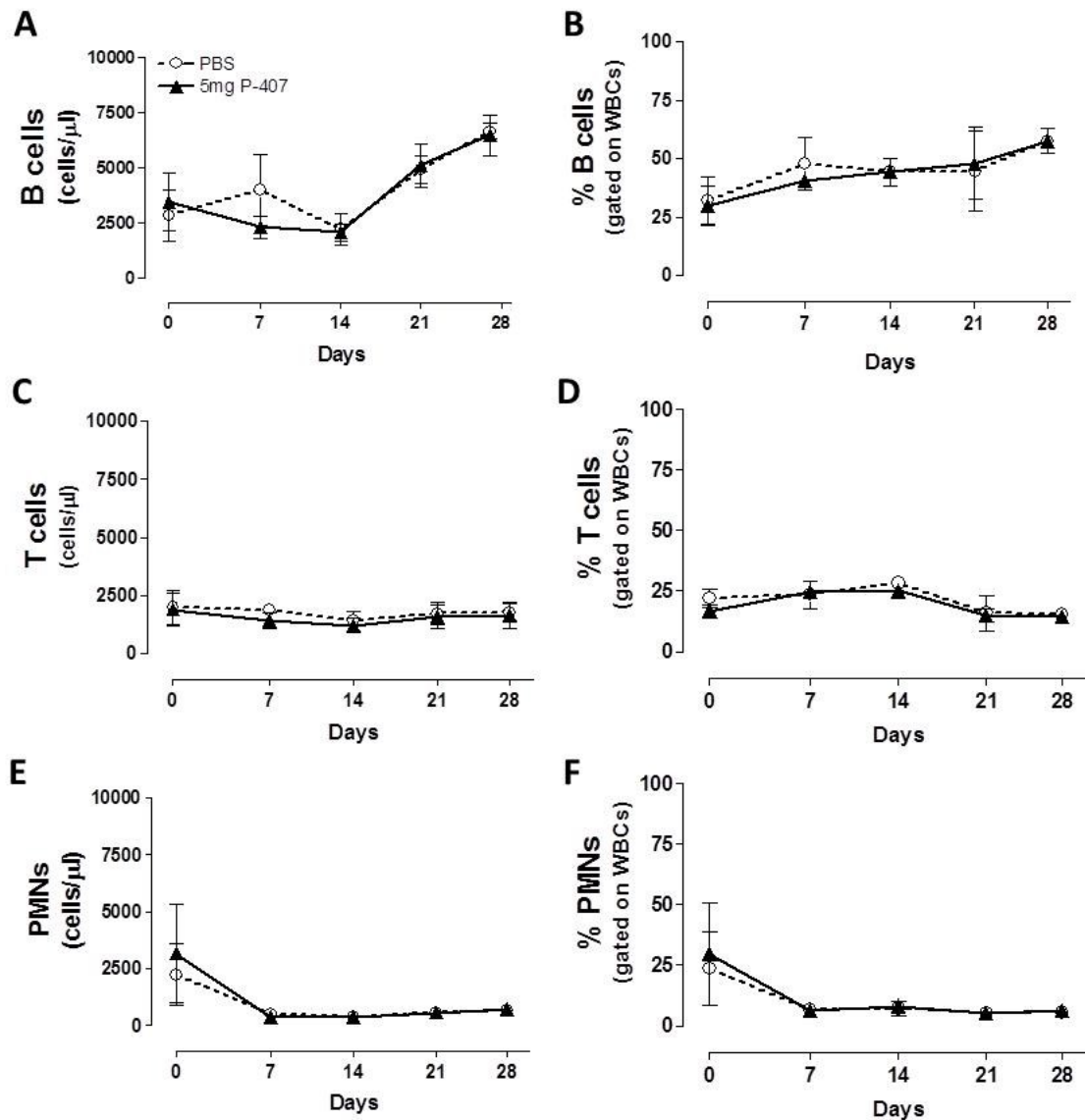


Figure 4.7. The effect of 5mg P-407 injection on the different peripheral blood cells.

PB number and frequency of B-cells (A & B), T-cells (C & D), and PMNs (E & F) in response to either 5mg P-407 or PBS injection i.p. three times a week over a period of 28 days. Data are presented as mean \pm SD (n=4, per group). At each time point the P value, calculated using unpaired t-test, was not significant.

Taken together these findings indicate that the 10mg P-407-induced hyper-TGRL results in a differential effect on MO subsets with a dramatic drop in the numbers of circulating Gr1^{low} MOs with a minimal effect on the numbers of Gr1^{high} MOs, while the total number of MOs remains unaffected. This intriguing result paved the ground for a series of experiments directed towards elucidating the possible explanation behind such an observation. Given that the 5mg P-407 dose had no effect on MO subset distribution it was not used in subsequent experiments and all the following experiments were done using the 10mg dose of P-407 that will be referred to as P-407 throughout the remainder of the chapter.

4.3. The effect of P-407 on the BM production of MO subsets

The BM constitutes the primary site for MO synthesis. The generation of MOs in the BM follows a series of restriction steps in the differentiation potential of HSCs until commitment to MO/MØ lineage ensues. The hyperlipidemic environment of the apoE^{-/-} and Ldlr^{-/-} mouse models has been shown to cause expansion of HSCs in the BM (Murphy et al., 2011), which raised the possibility of an effect for P-407-induced hyper-TGRL on MO precursors in the BM. To determine whether the drop in circulating Gr1^{low} MOs reflected an impaired production of these cells by the BM, chow-fed B6 mice were injected with either 10mg P-407 or PBS i.p. thrice weekly and the BM was analysed at two different time points; namely, after 14 and 28 days of injection (n = 4, per group at each time point). BM analysis included total MOs, their subsets, and the clonotypic MO precursor the MDP. MDPs were identified by their co-expression of CD117 (c-kit) and CD115, while BM MOs were identified by their co-expression of CD115 and CD11b and the absence of CD117 (Fig-4.8A & B). To facilitate the identification of MO subsets in

the BM, two markers were used; Gr1 as well as CD62L (L-selectin). Gr1^{high} MOs were identified as Gr1^{high} CD62L⁺, whereas Gr1^{low} MOs were identified as Gr1^{low} CD62L⁻ (Fig-4.8B). The percentage of MDPs and MOs refers to their frequency in total BM, whereas the percentage of MO subsets refers to their frequency within the MO population.

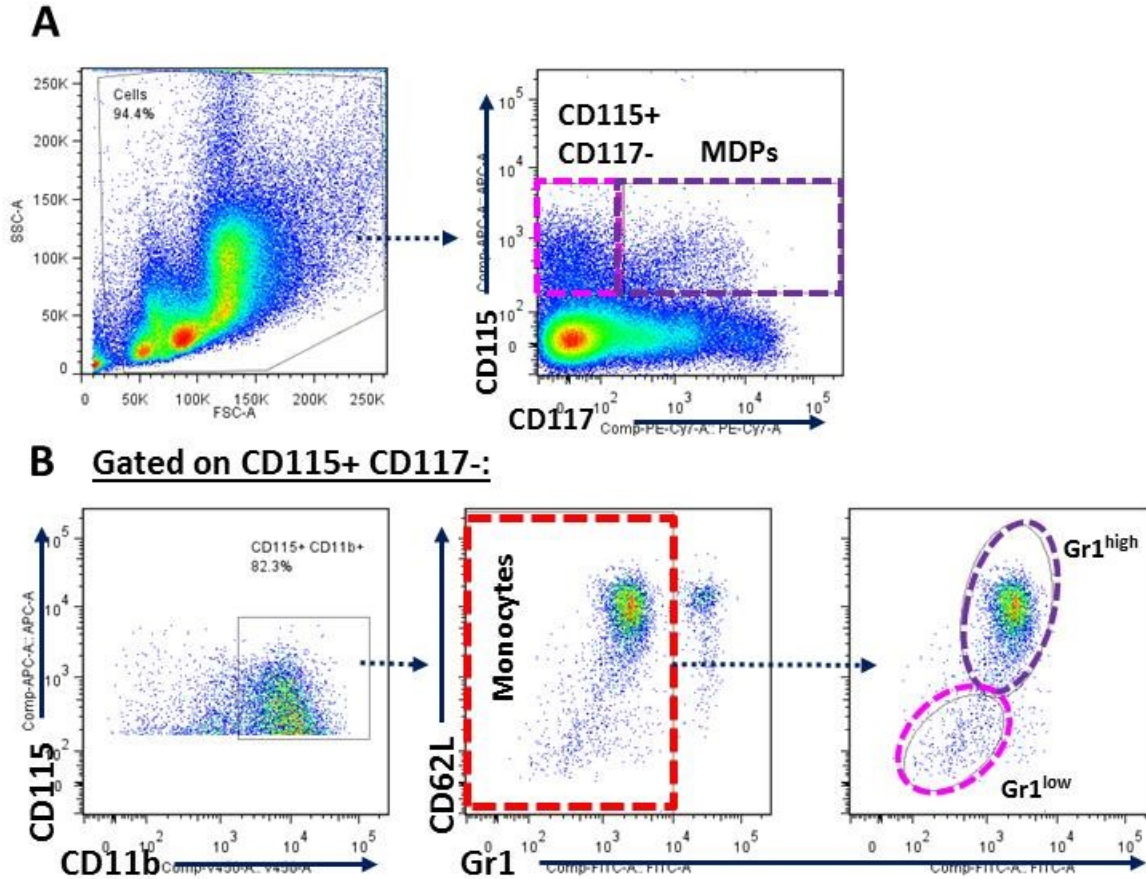


Figure 4.8. Gating strategy used to identify MDPs, mature MOs and their subsets in the BM.

(A) MDPs were identified from the BM cell pool by their co-expression of CD117 (c-kit) and CD115. (B) MOs were identified as the CD115⁺ cells that lacked CD117 but co-expressed CD11b. Using Gr1 to exclude contaminating granulocytes, another gate was applied that excluded a small population that expressed very high levels of Gr1. From the MO population, Gr1^{high} and Gr1^{low} MOs were identified by their double expression or lack of Gr1 and CD62L, respectively.

There was a drop in the percentage of MDPs and MOs in the P-407-injected group when compared to controls. For MDPs, the difference was significant at day 14 ($2.04 \pm 0.21\%$ vs $3 \pm 0.42\%$, mean \pm SD, $P=0.0074$, unpaired t-test) as well as day 28 ($1.92 \pm 0.43\%$ vs $2.87 \pm 0.12\%$, mean \pm SD, $P=0.0055$, unpaired t-test) comparing P-407-injected group with the PBS-injected control, respectively (Fig-4.9A). Whereas for MOs, the difference was significant only at day 14 with the P-407-injected group showing a value of ($3.24 \pm 0.63\%$, mean \pm SD) compared to ($4.54 \pm 0.57\%$, mean \pm SD) in the PBS-injected group ($P=0.0224$, unpaired t-test) (Fig-4.9B). On the other hand, the frequencies of Gr1^{high} and Gr1^{low} MOs in the BM showed no significant difference between the two experimental groups at any time point (Fig-4.9C & D).

Despite the observed drop in the percentages of MDPs and MOs, their total numbers (expressed as cells per leg) were not different at any time point (Fig-4.10A & B). Similarly, there were no significant differences in the numbers of BM Gr1^{high} and Gr1^{low} MOs between the P-407 and the PBS-injected groups at any time point (Fig-4.10C & D). Of note, the total BM cell count exhibited a significant difference between the groups with the P-407-injected group showing a higher BM cell count of ($323.8 \pm 31.2 \times 10^5$, mean \pm SD) compared to the PBS-injected group at day 14 ($227.5 \pm 45.18 \times 10^5$, mean \pm SD) ($P=0.0127$, unpaired t-test), and at day 28 ($431.3 \pm 67.5 \times 10^5$ vs $322.5 \pm 54.2 \times 10^5$, mean \pm SD) ($P=0.0458$, unpaired t-test) (Fig-4.10E).

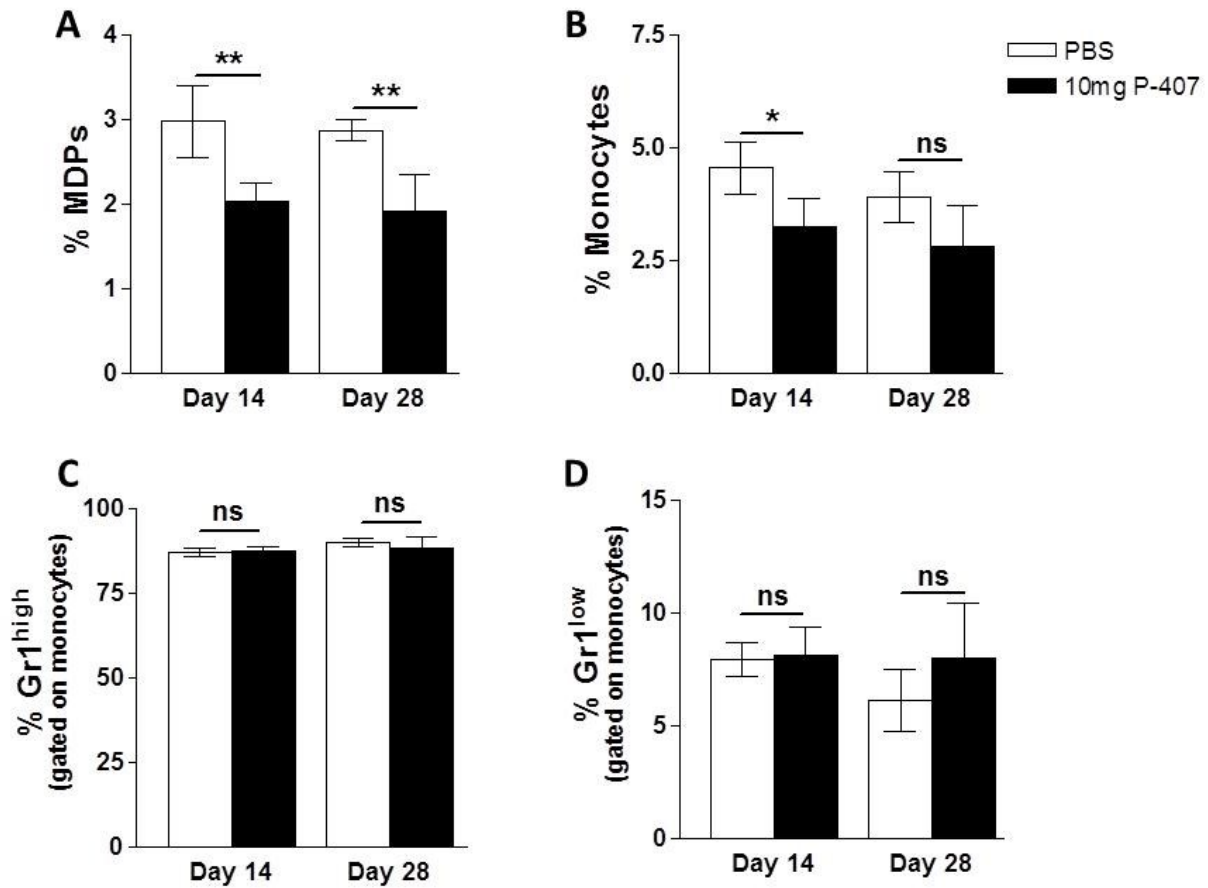


Figure 4.9. The effect of P-407-induced hyper-TGRL environment on the percentages of mature MOs, their subsets, and their precursors in the BM.

Percentage of (A) MDPs, (B) total MOs, (C) Gr1^{high} MOs, and (D) Gr1^{low} MOs after 14 and 28 days of 10mg P-407 injection i.p. three times weekly against PBS-injected controls (n=4, per group at each time point). Data are presented as mean \pm SD. P value calculated using unpaired t-test. *P<0.05, **P<0.01, and ns = not significant.

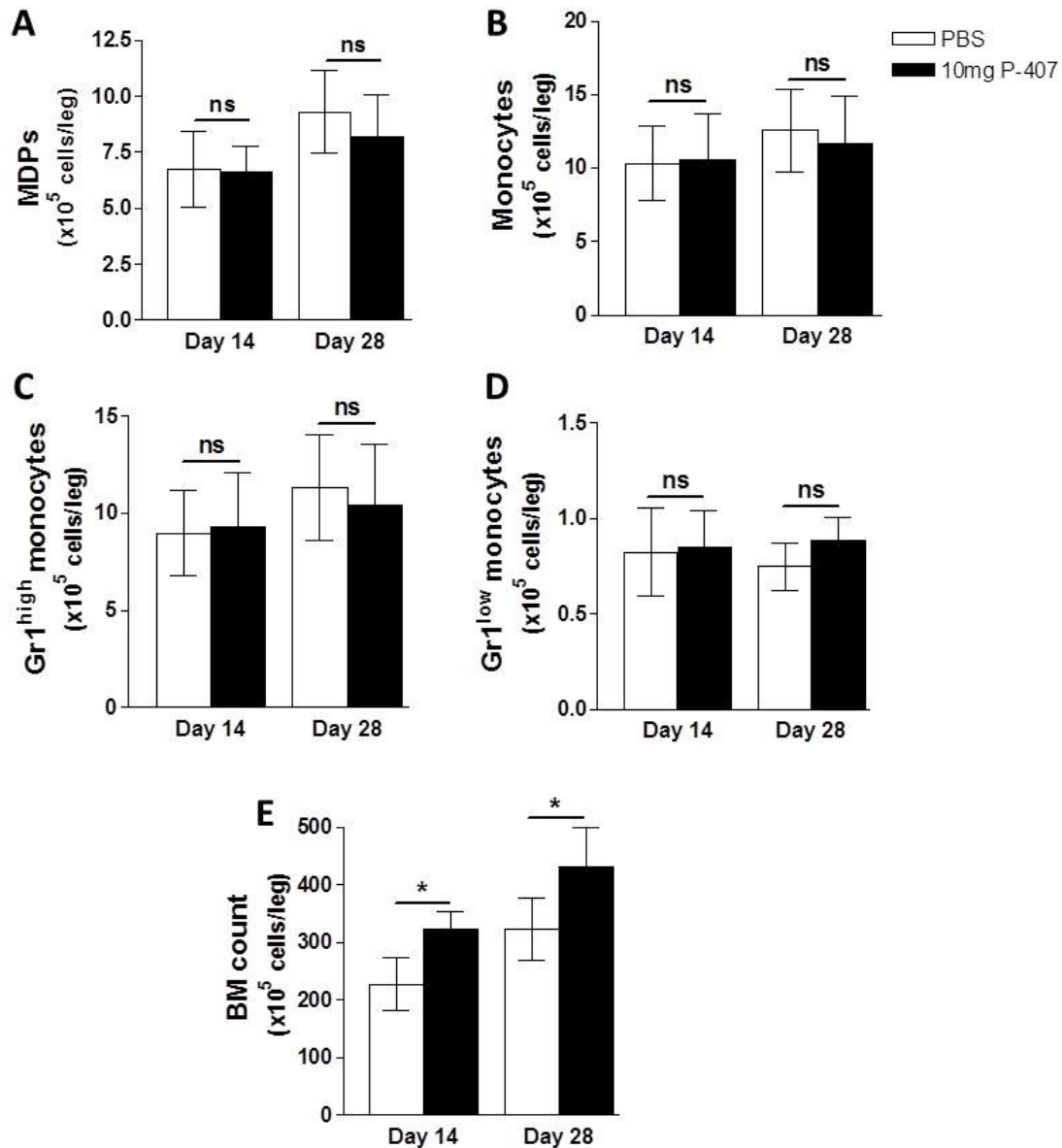


Figure 4.10. The effect of P-407-induced hyper-TGRL environment on the number of MDPs, MOs and their subsets in the BM.

Numbers (expressed as cells/leg) of the different BM populations: (A) MDPs, (B) total MOs, (C) Gr1^{high} MOs, (D) Gr1^{low} MOs, and (E) total BM cell count after 14 and 28 days of 10mg P-407 injection i.p. thrice weekly against a PBS-injected control (n=4, per group at each time point). Data are presented as mean \pm SD. P value calculated using unpaired t-test. *P< 0.05 and ns = not significant.

Despite the similarity in MDP numbers between P-407 and PBS experimental group, the observed drop in their percentage in the P-407 injected group mandated further investigation. In view of the higher total BM count observed in the P-407 group, the drop in MDP percentage could be attributed to an expansion of another cell line within the BM rather than an abnormality in MDPs themselves. To investigate this, I performed another BM experiment aiming to look at progenitors upstream of the MDPs; namely LT-HSCs, CMPs and GMPs. I also included MEPs in the panel since they constitute a large proportion of the BM giving rise to RBCs and platelets. Given that the changes in MDP frequency was observed at both time points i.e. 14 and 28 days post P-407 injection, I chose the latter time point to look for progenitors since any differences would be much more apparent at that time. Ten B6 mice received either 10mg P-407 or PBS (n=5 per group) three times a week for a period of 28 days. At the end of the experiment, the numbers of the aforementioned progenitors in the BM were examined using flow cytometry. Lineage markers used for the exclusion of mature committed cells included CD3, B220, and CD49b which collectively will be denoted as (Lin). I also used a dead/live (D/L) marker to detect dead cells that may arise during the processing of the BM and help in their exclusion. LT-HSCs were identified as live Lin⁻ cells that express CD117 (c-kit) and Sca-1 but lack CD34 expression. MEPs were identified as live Lin⁻ Sca-1⁻ CD117⁺ CD34⁻, whereas CMPs and GMPs were identified together as live Lin⁻ Sca-1⁻ CD117⁺ CD34⁺ (Akashi et al., 2000) (Fig-4.11). Data are expressed as number of cell population per leg.

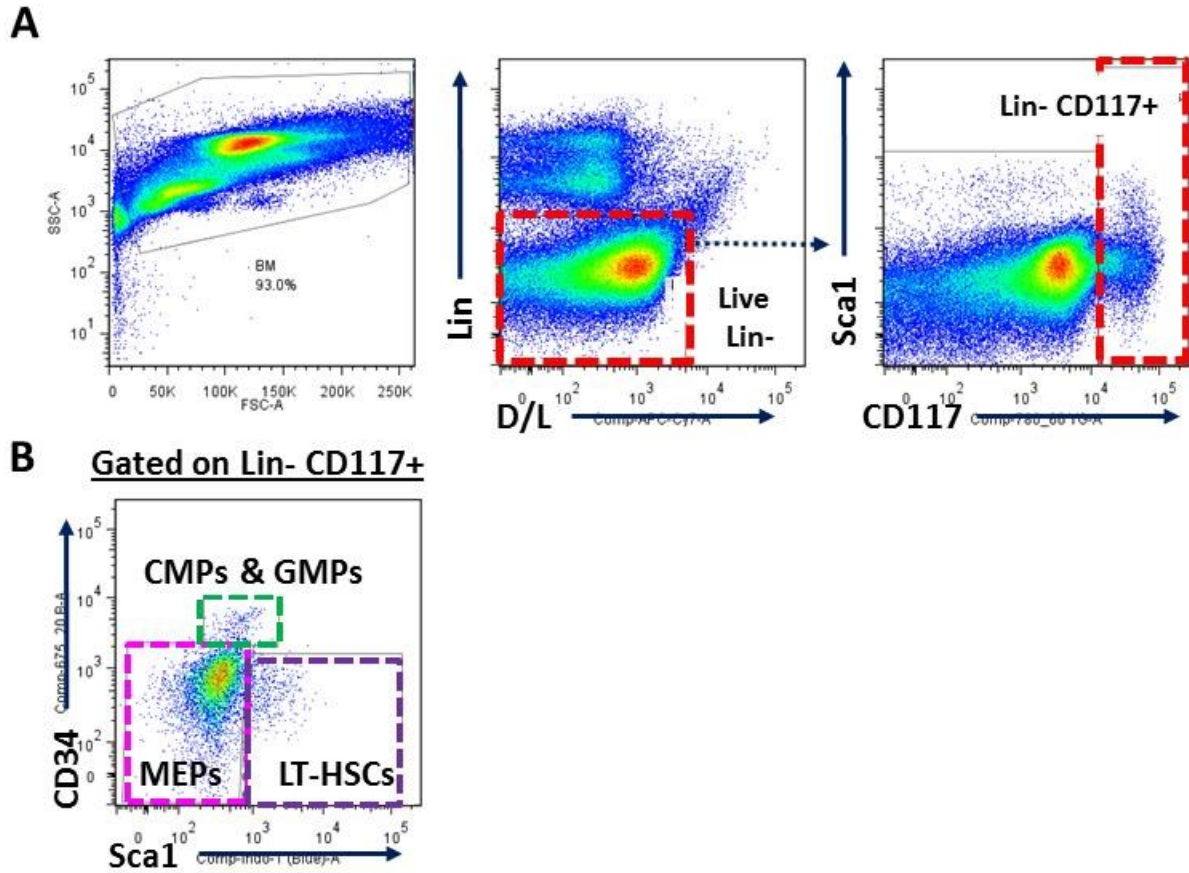


Figure 4.11. Gating strategy for the flow cytometry analysis of early BM progenitors.

(A) After excluding dead cells using D/L marker and lineage committed cells using CD3, B220, and CD49b (Lin⁻), the population expressing CD117 (c-kit) was identified. Within the live Lin⁻ CD117⁺ population (B), the three cell populations were identified by their differential expression of Sca-1 and CD34; LT-HSCs are Sca-1⁺ CD34⁻, MEPs are Sca-1⁻ CD34⁻, while CMPs and GMPs were identified together as Sca-1⁻ CD34⁺.

I observed a significant increase in the numbers of LT-HSCs ($0.043 \pm 0.007 \times 10^6$ cells/leg vs $0.022 \pm 0.005 \times 10^6$ cells/leg, $P=0.0007$, unpaired t-test) and MEPs ($0.52 \pm 0.1 \times 10^6$ cells/leg vs $0.31 \pm 0.045 \times 10^6$ cells/leg, $P=0.0029$, unpaired t-test) in the P-407 injected group when compared to controls, respectively (Fig-4.12A & B). Whereas the group constituting the CMPs and GMPs, the direct precursors of the MDP, showed no significant difference in their numbers between the P-407 ($0.028 \pm 0.01 \times 10^6$ cells/leg) and the PBS ($0.022 \pm 0.01 \times 10^6$ cells/leg) injected groups ($P=0.375$, unpaired t-test) (Fig-4.12C). Taken together the analysis of the BM demonstrated that the drop in circulating Gr1^{low} MOs numbers could not be explained by impaired BM production. Given the controversy surrounding the origins of Gr1^{low} MOs, other possibilities had to be entertained.

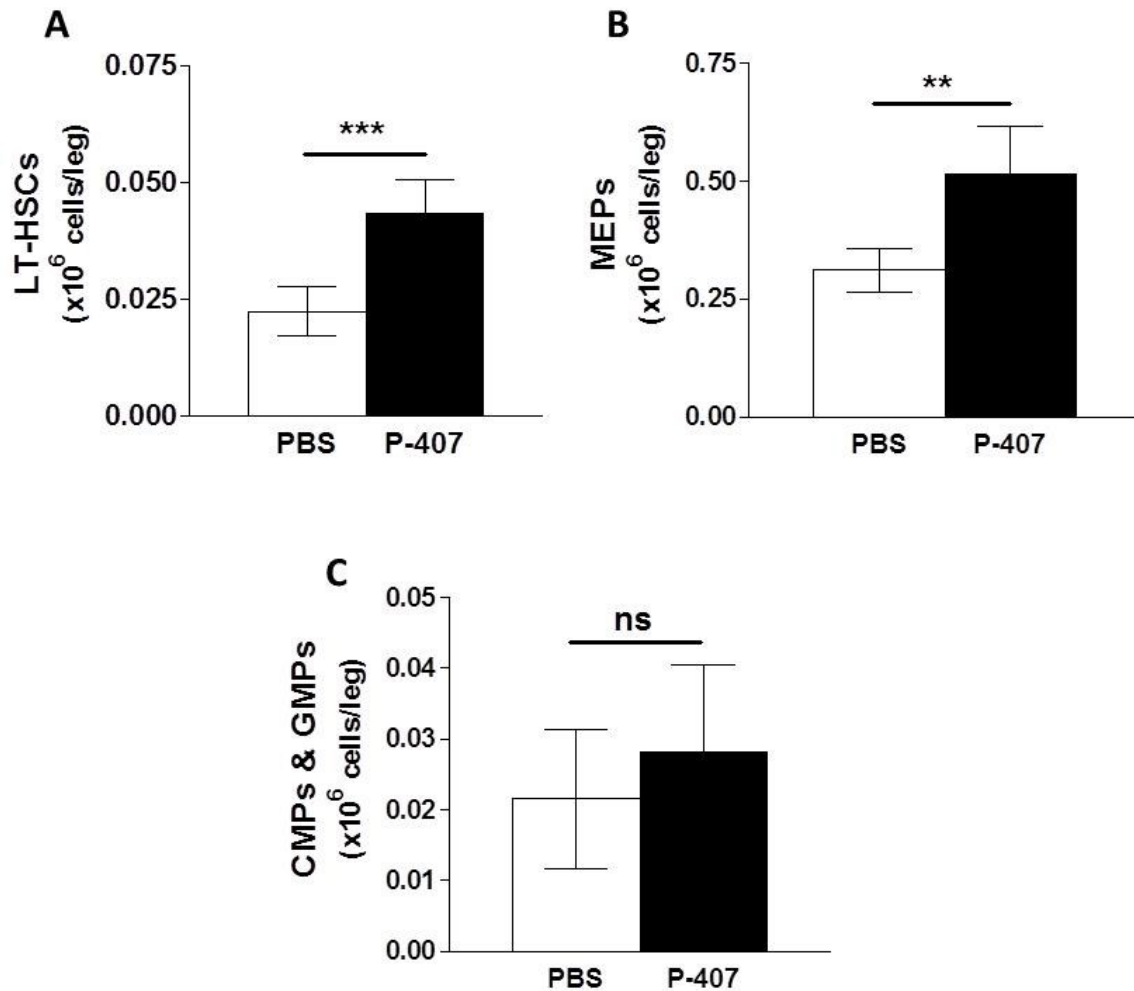


Figure 4.12. Numbers of early BM progenitors after 28 days of P-407 injection.

Numbers of early BM progenitors including; (A) LT-HSCs, (B) MEPs, and (C) CMPs and GMPs in the BM following 28 days of thrice weekly injection of either 10mg P-407 or PBS i.p. (n=5 per group). The number of BM progenitors is expressed as cells/leg. Data expressed as mean \pm SD. P value calculated using unpaired t-test. **P<0.01, ***P<0.001, and ns=not significant.

4.4. The effect of P-407 on the peripheral conversion of MO subsets

Despite the recognition that Gr1^{low} MOs arise from BM precursors, circumstantial evidence points toward their possible derivation from Gr1^{high} MOs in the circulation. It has been proposed that the maturation of Gr1^{high} MOs involves the loss of Gr1 expression and thence their conversion to the Gr1^{low} MOs (Sunderkotter et al., 2004; Yona et al., 2013). With this in mind, I then hypothesized that a hyper-TGRL environment might delay or inhibit this maturation process leading to the observed drop in Gr1^{low} MOs.

To investigate this possibility, I took advantage of a BrdU experiment used by Yona et al (Yona et al., 2013). By tracing BrdU incorporation into the different MO subsets following its administration, Yona et al have demonstrated sequential acquisition of the label into the different subsets. The Gr1/Ly6C^{high} MOs acquired it first followed by the Gr1/Ly6C^{low} subset as the former loses it (Yona et al., 2013). Based on this experimental approach it was hypothesized that should there be a delay in Gr1^{high} > Gr1^{low} conversion, it will be reflected in the kinetics of BrdU acquisition by the different subsets.

To test that, chow-fed B6 mice were injected with either 10mg P-407 or PBS i.p. (n=3, per group) every other day for a period of 5 days. At the day of commencing the injections, the mice were pulsed once with BrdU i.p. (3 doses of 2mg BrdU i.p. administered 3 hours apart). The incorporation of BrdU was tracked over a period of five days following the BrdU pulse (Fig-4.13A). On the first day, the majority of MOs that have acquired BrdU were Gr1^{high} MOs, whereas its incorporation was undetectable in the Gr1^{low} fraction. However, there was a detectable difference in BrdU incorporation into the Gr1^{high} subset between the two experimental groups with P-407 injected group

showing a significantly higher BrdU incorporation into Gr1^{high} subset at day 1 when compared to the PBS injected control (89.8 ± 3.2 % vs 62.8 ± 6.3 %, mean \pm SD, $P=0.0026$, unpaired t-test) (Fig-4.13C). From day 1, the percentage of BrdU⁺ Gr1^{high} MOs started to drop in both groups while still maintaining the difference in BrdU incorporation between the two experimental groups with P-407 injected mice showing a higher (82.1 ± 10.7 %) BrdU⁺ Gr1^{high} MOs when compared the PBS injected control (57.5 ± 4.5 %, mean \pm SD) ($P=0.0212$, unpaired t-test). From there onwards, both groups showed a massive drop in the frequency of BrdU⁺ Gr1^{high} MOs reaching comparable levels of (17.6 ± 2.9 % vs 22 ± 8.8 %, mean \pm SD, $P=0.4612$, unpaired t-test) in P-407 and PBS groups, respectively (Fig-4.13C). Thus, despite the initial difference in BrdU incorporation into the Gr1^{high} MOs between the groups, the kinetics of BrdU loss between the two groups were similar indicating that the hyper-TGRL environment had not altered the half-life of Gr1^{high} subset and thus could not be the explanation for the drop in the Gr1^{low} compartment. On the other hand, a steady increase in the percentage of BrdU⁺ Gr1^{low} MOs was observed from day 1 onwards in the PBS-treated group (Fig-4.13D), confirming the sequential BrdU incorporation into the different MO subsets observed by Yona et al (Yona et al., 2013). However, the kinetic of the BrdU incorporation in the Gr1^{low} fraction differed slightly in the P-407-treated mice and the expected increase at day 5 was not observed (Fig-4.13D), suggesting the possibility of a different steady-state behaviour of this MO compartment under hyper-TGRL conditions.

Taken together, it appears that the drop in PB Gr1^{low} MOs cannot be attributed to a defect in BM production neither does it appear to be due to an impaired conversion of

Gr1^{high}>Gr1^{low} MOs. The failure of Gr1^{low} MOs to show the expected increase at day 5 following BrdU pulsing as seen in the PBS-injected group or even higher, given that the Gr1^{high} MOs showed higher BrdU incorporation in the P-407 group, points toward a different effect of the hyper-TGRL environment on the behaviour of these cells. Gr1^{low} MOs have been assigned a “patrolling” role as they were shown to crawl along the luminal side of the endothelium under steady-state conditions *in vivo* (Auffray et al., 2007). This along with the many reports showing enhanced expression of endothelial adhesion molecules under conditions of hyperlipidemia (Wang et al., 2013), led to the proposition that the drop observed in circulating Gr1^{low} MOs may reflect enhanced margination to the endothelial surface brought about by the rise in circulating TGRLs secondary to P-407 injection. To examine the effect of a hyper-TGRL environment on the crawling of Gr1^{low} MOs, with the aid of GFP reporter mice, the movement of Gr1^{low} MOs was tracked *in vivo* using intravital microscopy. The result of this experiment is presented in the following section.

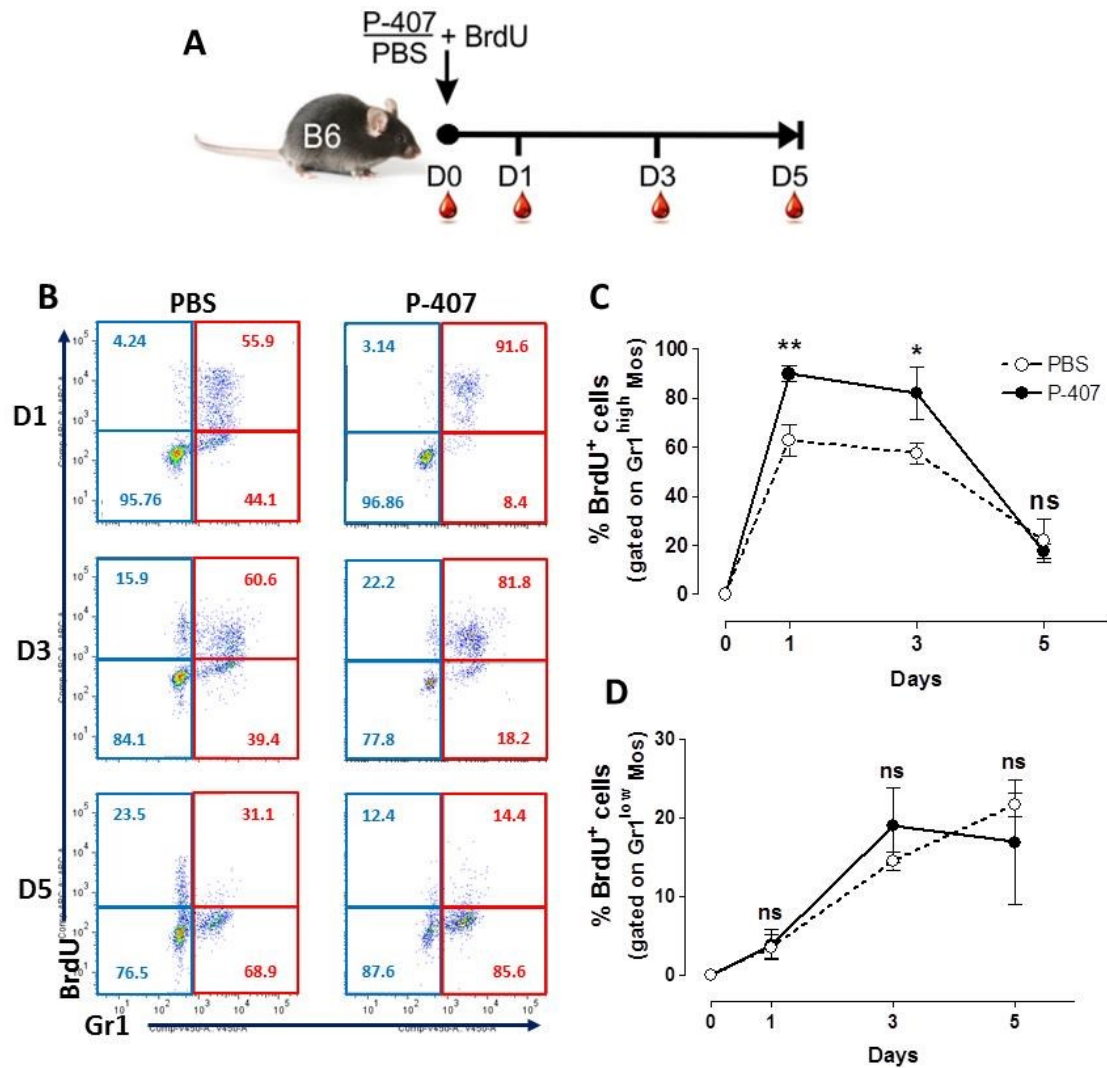


Figure 4.13. The effect of P-407 induced hyper-TGRL environment on BrdU incorporation into the different MO subsets.

A diagrammatic illustration of the BrdU experiment is shown in (A). Representative dot plots (B) showing BrdU incorporation into Gr1^{high} and Gr1^{low} blood MOs over a period of 5 days in mice receiving either PBS or 10mg P-407 i.p. every other day following a single pulse of BrdU administered i.p. in three doses of 2mg, 3 hours apart. Percentages of BrdU incorporation in Gr1^{low} MOs (blue rectangle) and Gr1^{high} monocytes (red rectangle) are indicated. (C & D) Shows BrdU incorporation into the different MO subsets expressed as percentage of BrdU⁺ cells within the gated Gr1^{high} (C) and Gr1^{low} (D) MOs in mice receiving either PBS or 10mg P-407 i.p. every other day (n=3 in each group). Data are expressed as mean \pm SD. Data representative of two independent experiments. P value calculated using unpaired t-test. *P<0.05, **P<0.01, and ns=not significant.

4.5. The effect of P-407-induced hyper-TGRL environment on the behaviour of Gr1^{low} MOs

To investigate whether the P-407-induced hyper-TGRL environment promotes the margination of Gr1^{low} “patrolling” MOs, CX3CR1^{gfp/gfp} reporter mice were used. These mice harbour a GFP reporter at the Cx3cr1 locus and thus have been instrumental in studying the *in vivo* behaviour of the different MO subsets (Geissmann et al., 2003; Jung et al., 2000). Due to their differential expression of CX3CR1, and hence GFP, MO subsets can be identified in CX3CR1^{gfp/gfp} mice as: GFP^{high} (Gr1^{low}) MOs and GFP^{low} (Gr1^{high}) MOs.

The effect of a hyper-TGRL environment on the behaviour of Gr1^{low} MOs was studied by treating CX3CR1^{gfp/gfp} with either PBS or 10mg P-407 i.p. every other day for a period of 7 days. On day 7, the vasculature was visualized using intravital microscopy. The intravital imaging experiment was performed by Dr. Kevin Woollard.

Intravital analysis of the ear dermal vasculature showed that the number of crawling GFP^{high} cells per hour was moderately enhanced in the mice treated with P-407 compared to the PBS-treated counterparts (Fig-4.12A & B). More importantly, a striking accumulation of GFP^{high} cells was noticed extravascularly in the ears of P-407-treated animals compared to the PBS controls (Fig-4.14A). Similar results were observed using CX₃CR1^{gfp/+} mice.

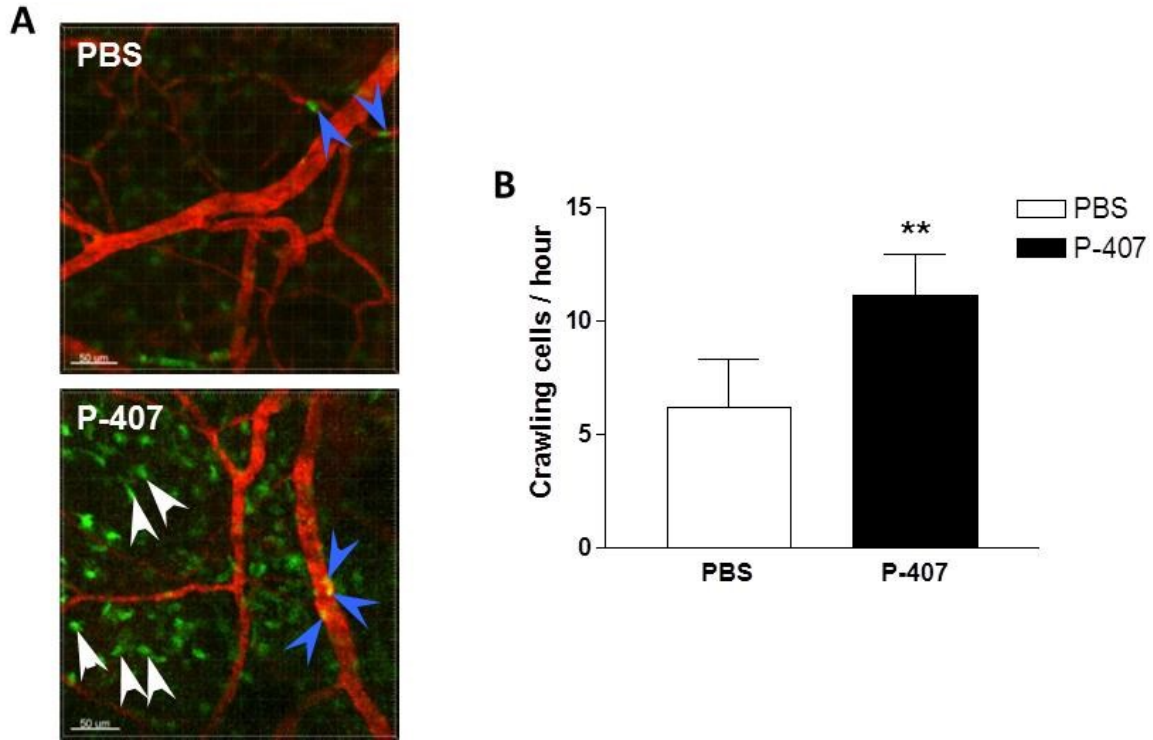


Figure 4.14. The *in vivo* effect of P-407-induced hyper-TGRL on GFP^{high} MO behaviour.

Cx3cr1^{gfp/gfp} mice were treated with PBS or P-407 i.p. every other day for 7 days and ear dermis vasculature imaged by intravital microscopy. (A) Examples of intravascular crawling cells (blue arrow) or tissue cells (white arrow) with PBS or P-407 treatment. (B) Quantitative representation of the number of intravascular crawling cells per hour after each treatment. Data presented as mean ±SD (n=3 per group). P value calculated using Mann-Whitney test. ** P=0.0023 from PBS control. Scale bars = 50μm. Data kindly provided by Dr. K. Woollard.

The enhanced crawling observed for Gr1^{low} MOs over the endothelial surface could be related to changes in surface CD11b expression. CD11b is an adhesion molecule commonly found in complex with CD18 forming the heterodimeric β 2-integrin known as complement receptor 3 (CR3) or Mac-1 (Ross, 2002). It is known to mediate leukocyte adhesion and diapedesis via its interaction with intercellular adhesion molecule-1 and 2 (ICAM-1 and ICAM-2) (Ross, 2002). To investigate its expression by the different subsets, B6 mice were injected i.p. three times weekly with either 10mg P-407 or PBS for a period of 28 days (n=4 per group). At the end of the experiment, PB FACS was performed analysing the MO subset distribution and their surface expression for CD11b. An appropriate isotype control for CD11b was used to enable calculation of the change in mean fluorescence intensity (dMFI) by subtracting background. After 28 days of P-407 injection, Gr1^{low} MOs from mice receiving P-407 expressed higher levels of CD11b when compared to their PBS injected counterparts (P<0.0001, unpaired t-test), whereas no difference in CD11b expression was detected on the Gr1^{high} subset (Fig-4.15).

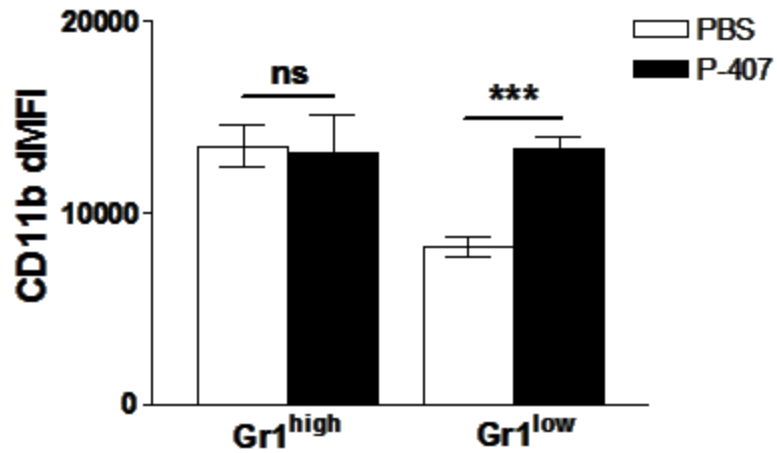


Figure 4.15. CD11b expression on MO subsets after 28 days of P-407 administration.

CD11b surface expression on the different MO subsets expressed as dMFI following 28 days of 10mg P-407 injection i.p. thrice weekly compared to PBS injected control (n=4 per group). Data are expressed as mean \pm SD. P value calculated using unpaired t-test. ***P<0.001, and ns=not significant.

The accumulation of GFP^{high} cells in the dermis of the ear was surprising and the natural question was whether it represents an example of a generalized effect of the P-407-induced hyper-TGRL condition or merely reflects a finding that is confined to the ear. The difficulty in visualizing deep organs using intravital imaging, along with the lack of reliable immunohistological markers for MO staining in tissues prompted the use of other means to address this question. Given that MO extravasation into tissues is associated with their differentiation into MØs, tissue staining for MØs was considered.

Organs including liver, heart, and kidney were collected from B6 mice after 7, 14, and 28 days of either 10mg P-407 or PBS injections i.p. three times weekly and fixed in PLP solution (n=4 per group at each time point, except for the PBS group at day 28 n=3). Five micrometer thick tissue sections were then stained for CD68 (macrosialin), a marker for MØs. The staining was visualised using Olympus microscope with digital camera and analysed using Image Pro Plus software. For the liver and heart, images were taken for 5 different fields at x20 magnification. Brown (CD68) staining was quantified using Image Pro Plus software by selecting a fixed field within the acquired images and calculating its area, followed by calculating the brown stained area within the selected field. This was repeated for 5 different fields per section. The selected field was kept constant by the aid of a grid. Percent brown area per field was then calculated by dividing the measured brown area over the total area of selected field. For each mouse, the average % brown area for the 5 independent fields was calculated to obtain the mean % brown area used here to express my data. A similar method was used for the kidney with few differences. In the kidney, images were taken for 20 glomeruli per section at x40 magnification and the brown area was calculated within the glomerulus.

This was done by drawing around the glomerulus measuring its area followed by calculating the area of brown staining within the selected glomerulus using the same software. Percentage brown glomerular area is then calculated by dividing the measured brown glomerular area over total glomerular area for the selected glomerulus which was repeated for the 20 glomeruli. To obtain the mean % brown glomerular area for each mouse, the average % brown area for the 20 glomeruli was then calculated.

Interestingly, there was a striking gradual accumulation of CD68⁺ cells in the liver, heart, and kidney (Fig-4.16 & 4.17A& B). The accumulation of CD68⁺ cells correlated with the duration of exposure to the hyper-TGRL environment induced by P-407 and, in agreement with the intravital findings, was visible as early as 7 days following P-407 injection (Fig-4.16 & 4.17A & B).

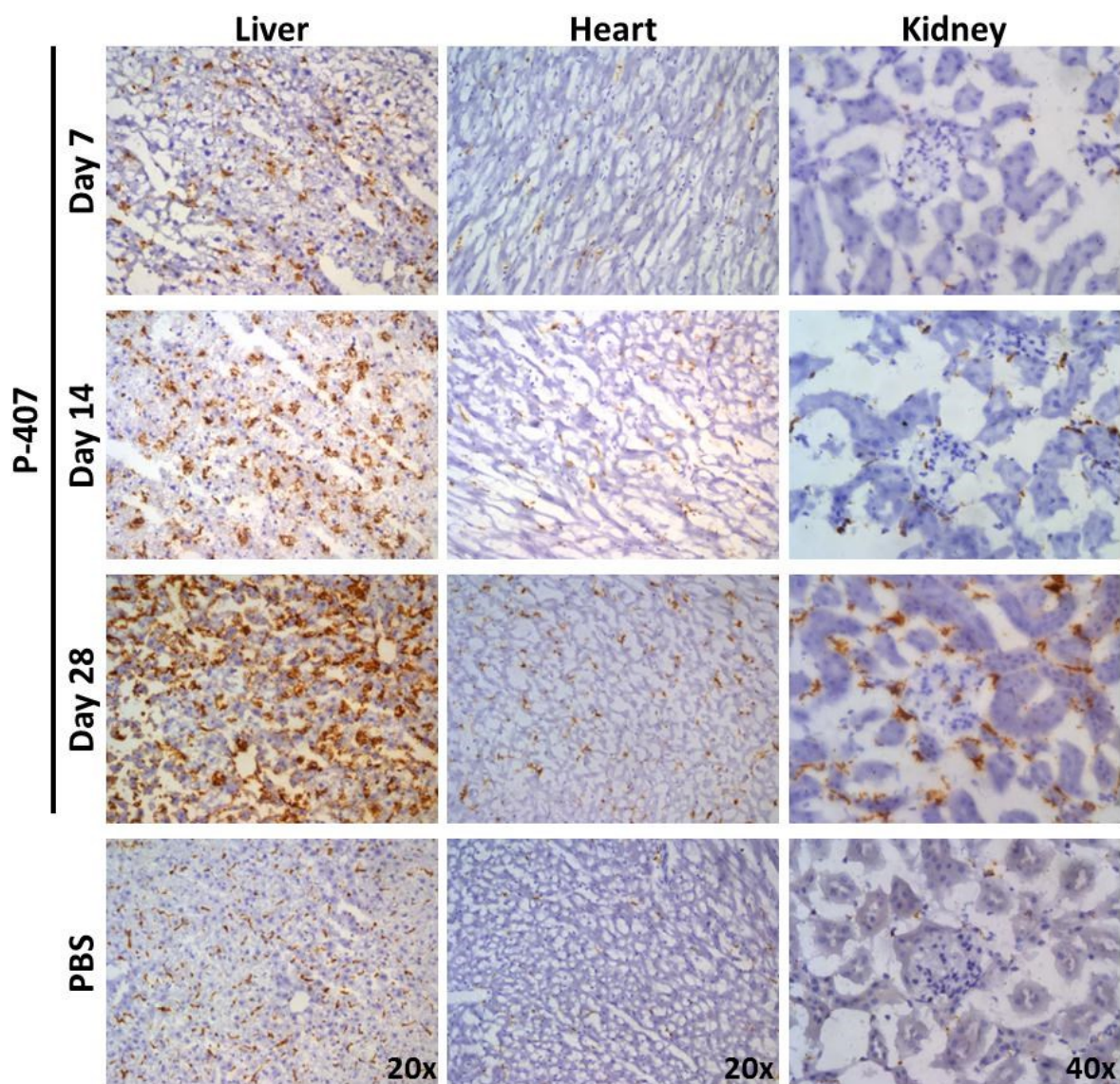


Figure 4.16. CD68-stained sections of liver, heart, and kidney following P-407 injections

Representative photomicrographs of CD68 staining (brown) in liver, heart, and kidney after 7, 14 and 28 days of either 10mg P-407 or PBS administration i.p. three times weekly. The sections show gradual accumulation of CD68⁺ cells in the tissues correlating with the duration of P-407-induced hyper-TGRL state in comparison to sections from PBS-injected control after 28 days of PBS treatment. Magnification as indicated.

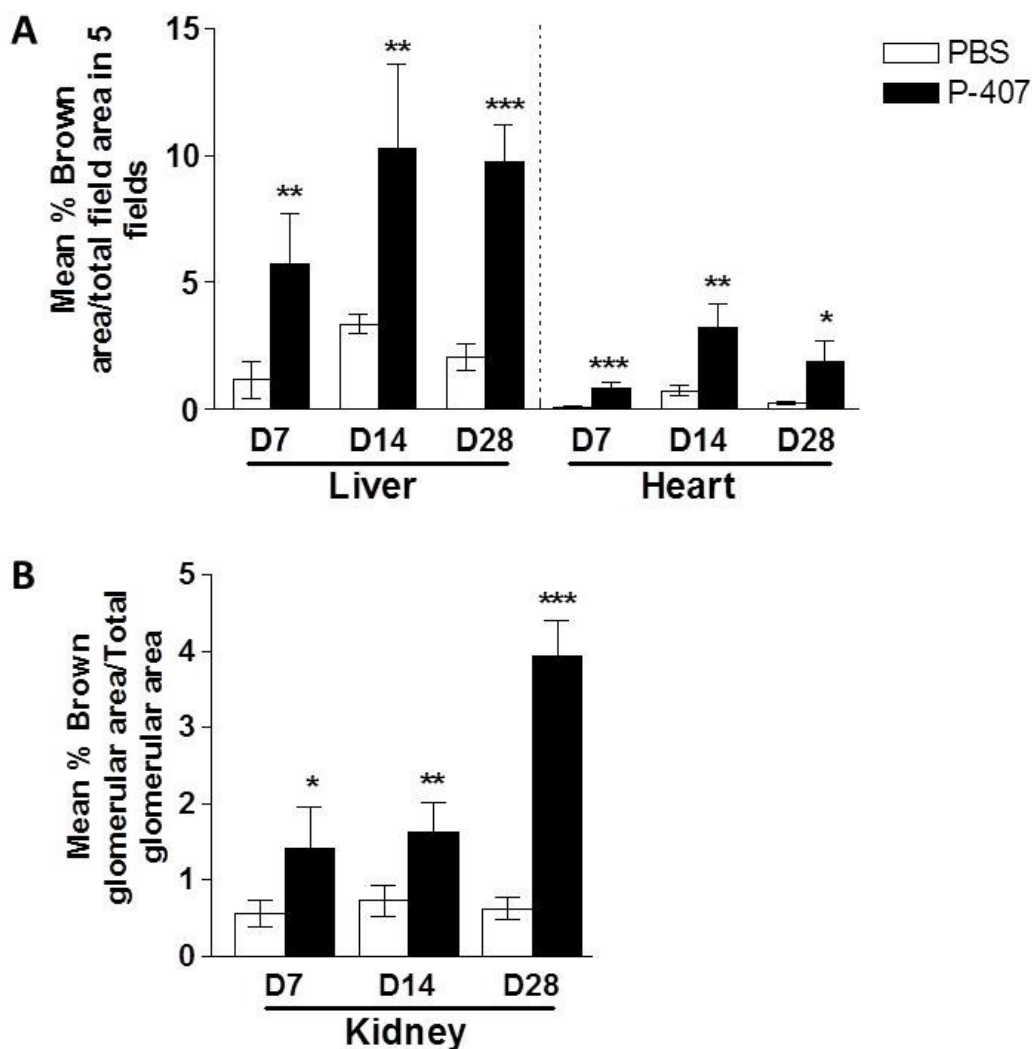


Figure 4.17. Quantitative representation of CD68 staining in the liver, heart, and kidney following P-407 injections.

Quantitative analysis of CD68⁺ cells in specimens as in figure Fig-4.16. For liver and heart data are expressed as mean percentage \pm SD of brown-stained area in a selected field/total field area (5 different fields per section). For the kidney, data represent mean percentage \pm SD of brown-stained glomerular area/total glomerular area for 20 glomeruli per section. Values represent the mean \pm SD of 4 mice per group at each time point, except in the PBS group on day 28 n=3. P value was calculated using unpaired t-test. *P<0.05; **P<0.01, ***P<0.001. Data at day 28 are representative of 3 independent experiments.

The accumulation of CD68⁺ macrophages in the analysed tissues was intriguing. As tempting as it is to attribute such an increase to enhanced MO recruitment, the exclusion of local proliferation of tissue-resident MØs as a possible cause to this observed increase had to be investigated. This deemed necessary especially with accumulating evidence supporting the self-renewal ability of tissue-resident MØs through local proliferation under steady-state conditions (Hashimoto et al., 2013; Robbins et al., 2013). Therefore, to investigate whether the accumulation of CD68⁺ cells in the organs of mice injected with P-407 may reflect enhanced local proliferation, rather than MO extravasation, tissue sections from liver, heart, and kidney were double stained for CD68 and Ki-67, a known proliferation marker, following 4-weeks of either PBS or 10mg P-407 injections (n=5 per group). Splenic sections were used as positive control for Ki-67 staining. Staining was visualized using Leica SP5 confocal microscope with the help of Dr. K. Woollard. I observed an accumulation in CD68⁺ cells similar to that observed using DAB staining, however, I was unable to detect any Ki-67 staining in the tissues of P-407 injected mice (Fig-4.18).

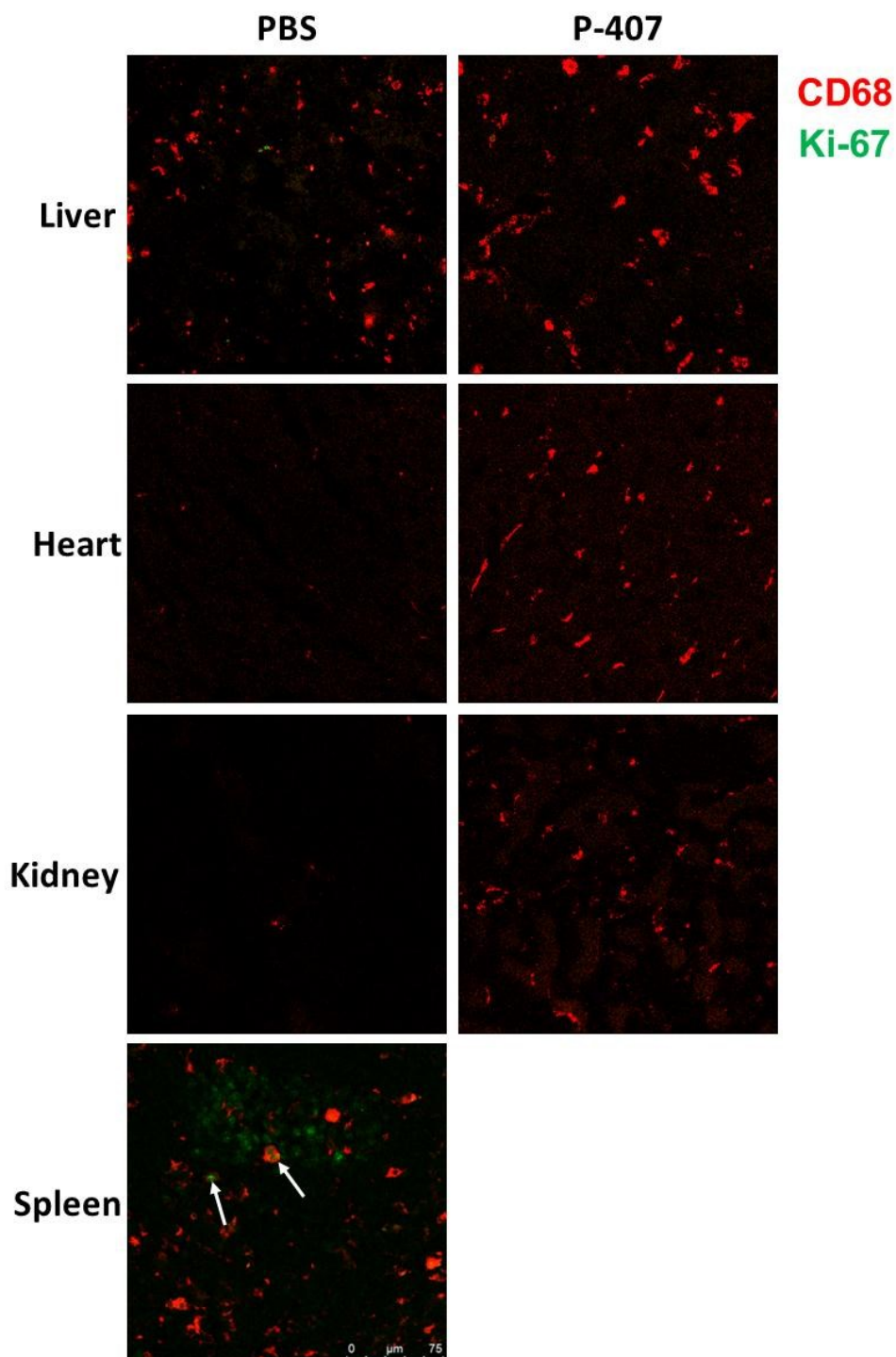


Figure 4.18. Tissue Ki-67 staining after 4 weeks of P-407 injections.

Representative images of Ki-67 (green) and CD68 staining (red) of tissue sections following 28 days of thrice weekly i.p. injections of 10mg P-407 or PBS (n=5 per group). Splenic sections were used as positive controls and Ki-67⁺ cells are indicated with arrows. Scale bar=75μm (shown in spleen).

The absence of Ki-67 staining in the tissues of P-407-injected mice made it less likely to attribute the dramatic accumulation of CD68⁺ cells in these tissues to merely enhanced local MØ proliferation. This along with the observation of enhanced crawling of Gr1^{low} MOs on the endothelial surface under hyper-TGRL conditions induced by P-407 led to the proposition of the possibility of Gr1^{low} MO extravasation as a source of these increased CD68⁺ cells. A notion strongly encouraged by the observation of the extravascular accumulation of GFP^{high} cells in the ears of mice injected with P-407 as seen by intravital imaging.

To investigate whether the hyper-TGRL environment promotes the extravasation of Gr1^{low} MO, bone marrow transplant (BMT) and adoptive transfer experiments were conducted using CX3CR1^{GFP} reporter mice. The results of these experiments are discussed in the following sections.

4.6. The effect of P-407-induced hyper-TGRL environment on the extravasation of Gr1^{low} MOs

To address the possibility of Gr1^{low} MO extravasation under the influence of hyper-TGRL conditions, BMT and adoptive transfer experiments were performed.

In the BMT experiment, six B6 mice were irradiated at 8 Gy using a ¹³⁷Cs c-ray source and reconstituted with 10 million BM cells from Cx3cr1^{gfp/+} mice. BM reconstitution was checked 2 months following BMT by PB analysis. Soon thereafter, 3 mice were culled and organs (liver, heart, kidney and spleen) were examined for GFP⁺ cells to determine baseline tissue appearance before undertaking a P-407 experiment (Fig-4.19A).

To ensure BM reconstitution, PB was analysed using flow cytometry to check for PB cell numbers and frequencies including; B-, T-cells, PMNs, MOs and their subsets. Pooled baseline data from PB analysis of normal B6 mice generated from previous experiments was used as a reference (n=24). Percentages of for B-, T-cells, PMNs and MOs reflected frequencies within total WBCs while MO subset percentage reflect their frequencies within MOs. Generally, the numbers and frequencies of B-, T-cells, PMNs and MOs in PB of BMT mice were comparable to normal baseline levels observed with B6 mice (Fig-4.19B-E). However, PB of BMT mice displayed higher number and frequency of B-cells when compared to reference data while PMNs showed a tendency to be lower in the BMT mice. With regards to MO subsets, GFP⁺ cells were detected in the blood of transplanted mice as shown in (Fig-4.20A & B) and MO subset numbers and frequencies in BMT mice were comparable to those seen for normal B6 mice (Fig-4.20C & D).

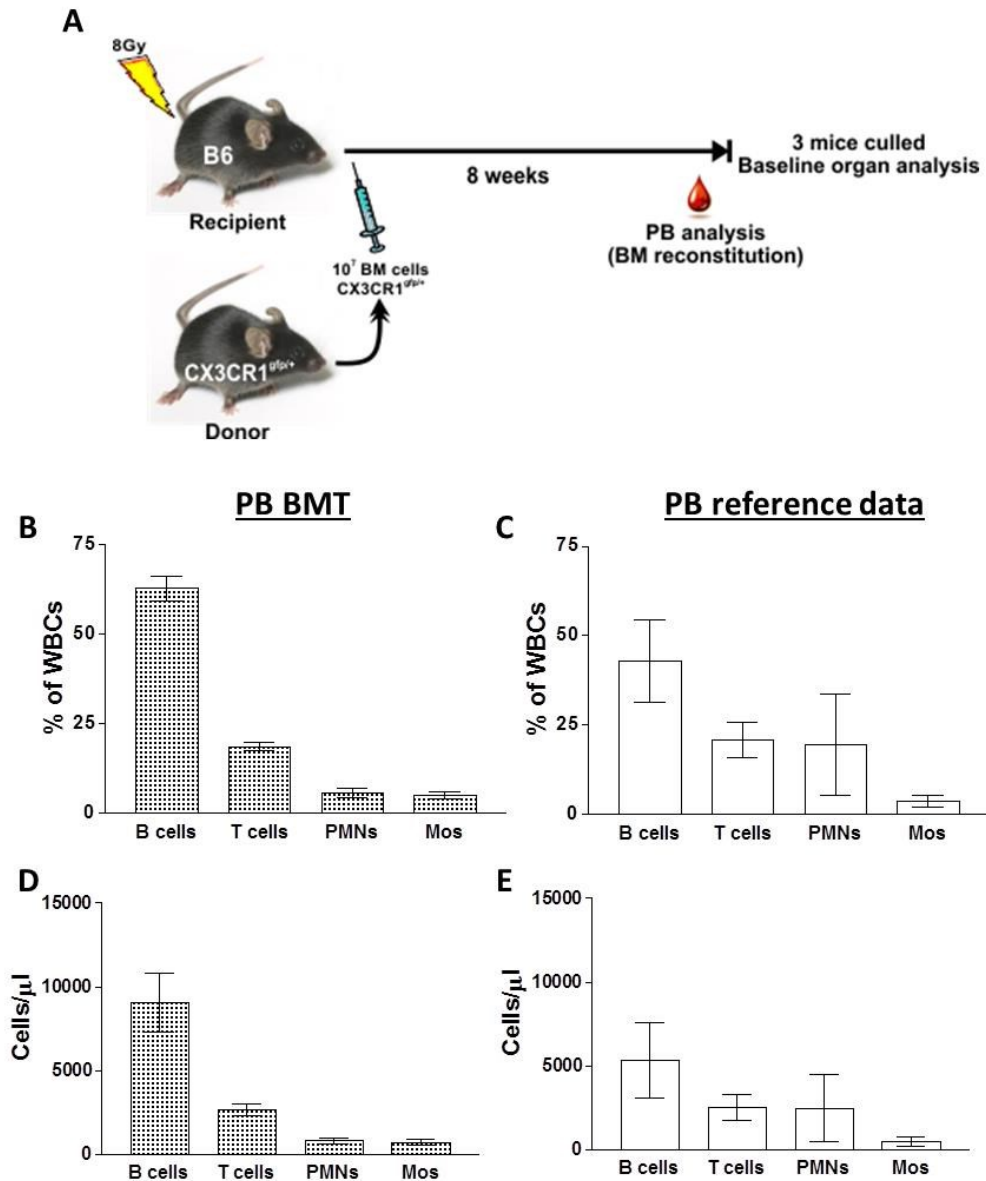


Figure 4.19. BMT experimental plan and PB analysis to check reconstitution.

(A) Graphic representation of BMT experiment. B6 mice were reconstituted with 10^7 BM cells from $Cx3cr1^{gfp/+}$ mice. Two months later, PB flow cytometry analysis was performed to confirm BM reconstitution followed by culling of 3 mice prior to any treatment to check baseline tissue MØs. (B & C) Frequencies of PB B-, T-cells, PMNs, and MOs in BMT mice ($n=6$) (B) compared to pooled baseline PB data of normal B6 mice from previous experiments (C) ($n=24$). (D & E) Numbers of PB B-, T-cells, PMNs, and MOs in BMT mice ($n=6$) (D) compared to pooled baseline PB data of normal B6 mice from previous experiments ($n=24$) (E). Data are presented as mean \pm SD.

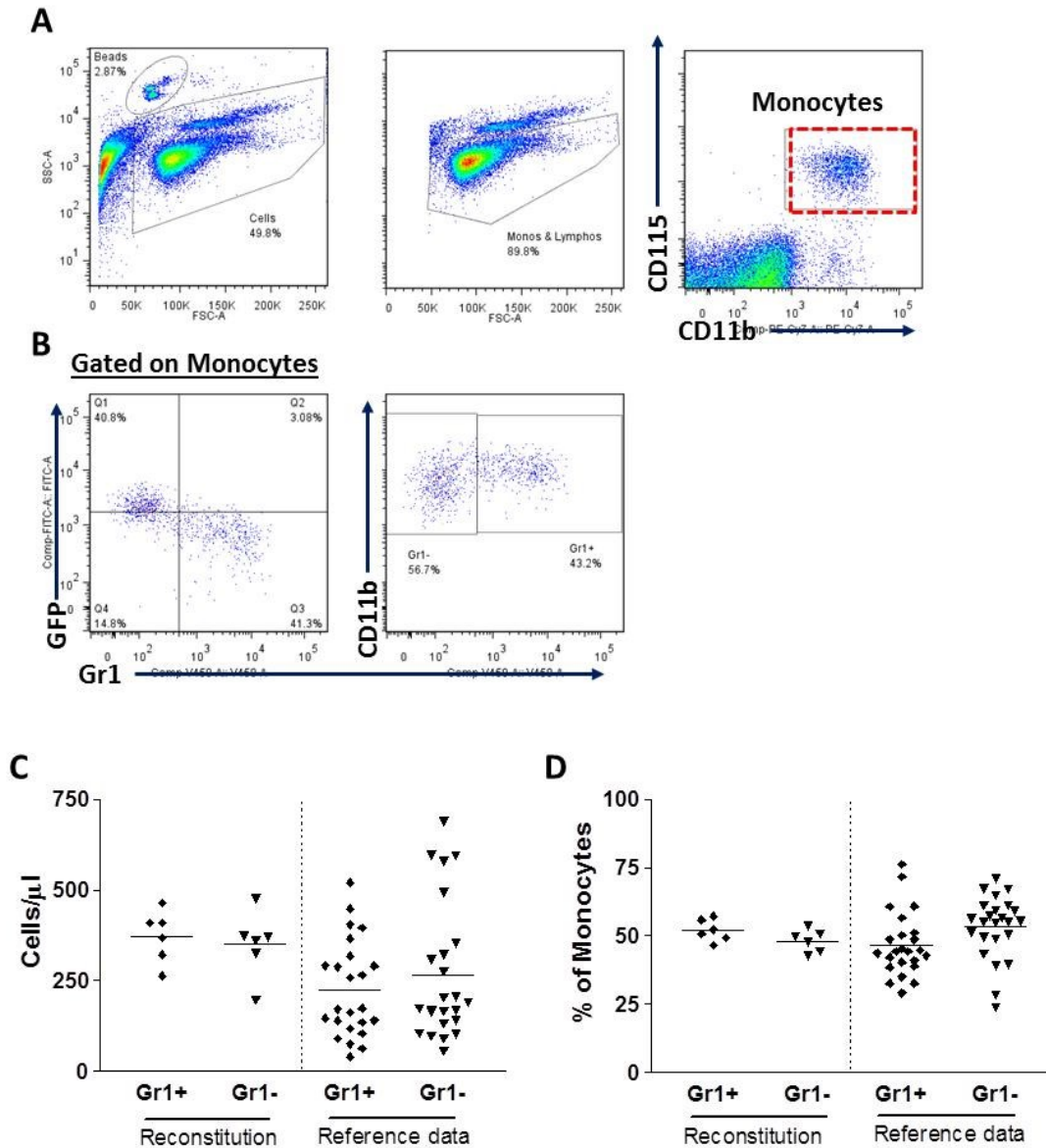


Figure 4.20. Gating and BM reconstitution for MO subsets in BMT mice.

(A) Gating strategy used for MO subset determination. (B) Representative plots from BMT mice showing GFP⁺ MOs in PB of BMT mice. (C & D) Numbers and frequencies, respectively of MO subsets in PB of BMT mice (n=6) along with reference data obtained from pooling baseline data of normal B6 mice of previous experiments (n=24). Horizontal bars represent the mean.

Two months following BMT and before commencing P-407 injections, 3 mice were culled and organs including heart, liver, kidney, and spleen were collected, digested and the cells were analysed using flow cytometry (Fig-4.21). There was a large number of GFP⁺ cells in all the organs prior to any P-407 intervention (Fig-4.21), probably as a result of the damage caused by irradiation and repopulation of tissue resident MØs from BM progenitors (Hashimoto et al., 2013), and thus I abandoned this approach.

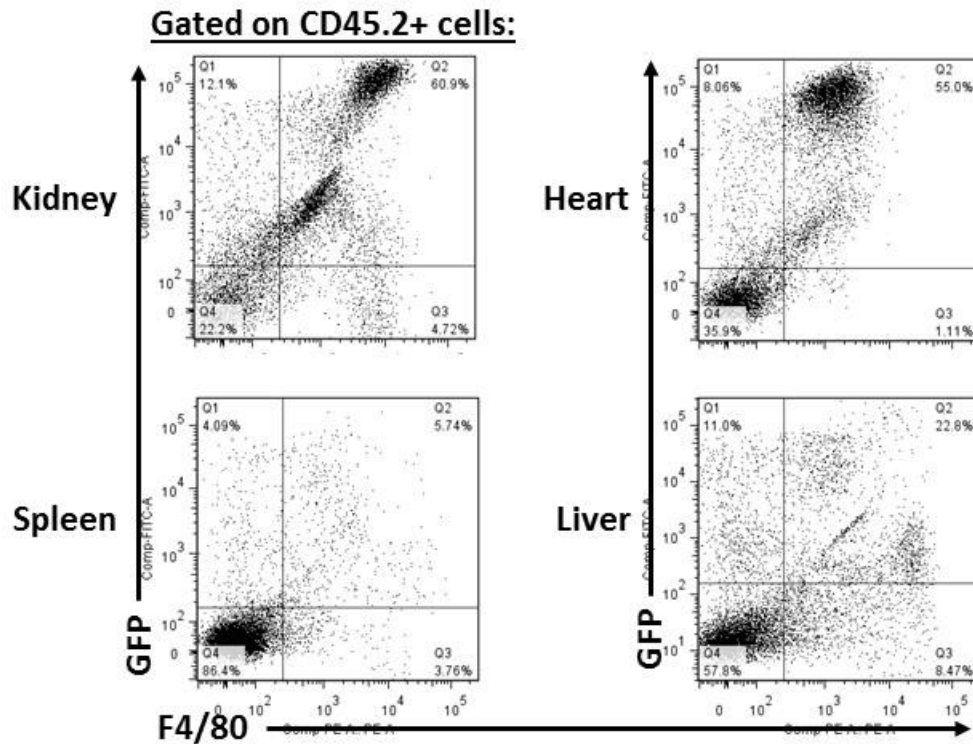


Figure 4.21. Flow cytometric analysis of organs from B6 mice following 2 months of BMT with BM cells from $Cx3cr1^{gfp/+}$.

Flow cytometry analysis of the kidney, heart, spleen and liver obtained from B6 mice transplanted with BM from $Cx3cr1^{gfp/+}$ mice. Tissue MØs were analysed within $CD45.2^+$ cells and were identified as $F4/80^{high}$ cells. Representative dot plots showing $GFP^+ F4/80^+$ cells (gated on $CD45.2^+$ cells).

An adoptive transfer experiment was then used. In this experiment, Gr1^{low}GFP^{high} and Gr1^{high}GFP^{low} blood MOs were sorted from CD45.2 Cx3cr1^{gfp/gfp} mice and 0.1 X 10⁶ cells were injected i.v. into congenic CD45.1 B6 mice that have been treated with either PBS or 10mg P-407 i.p. thrice weekly for a period of 2 weeks (n=4 for the Gr1^{low} GFP^{high} adoptively transferred group and n=3 for the Gr1^{high} GFP^{low} adoptively transferred group). Sixteen hours after the adoptive transfer, the mice were culled, perfused, and organs collected to be analysed by flow cytometry. In addition to organ perfusion, and to exclude any blood contamination during analysis, an anti-CD11b antibody was injected i.v. 15 minutes prior to culling (Fig-4.22A). The adoptive transfer experiment was performed by Dr. Lucie Baudino.

Analysis of the heart, kidney, liver, and spleen of the mice transferred with Gr1^{low}GFP^{high} MOs revealed greater accumulation of the transferred cells in the organs of the P-407-injected group when compared to the PBS-treated controls (Fig-4.22B). The accumulation was more pronounced in the spleen followed by the liver and then the kidney, whereas the heart showed the least impressive accumulation of adoptively transferred Gr1^{low}GFP^{high} cells (Fig-4.23A). On the other hand, recipients of the Gr1^{high}GFP^{low} MOs did not show much accumulation of the transferred cells in any of the organs of the P-407-injected group (Fig-4.22B). In addition, the minimal number of Gr1^{high}GFP^{low} cells retrieved in the P-407-injected group was similar to those retrieved in the PBS-injected group (Fig-4.23B).

Taken together, the drop on Gr1^{low} MOs observed under P-407-induced hyper-TGRL environment is due to their selective recruitment into tissues under such conditions.

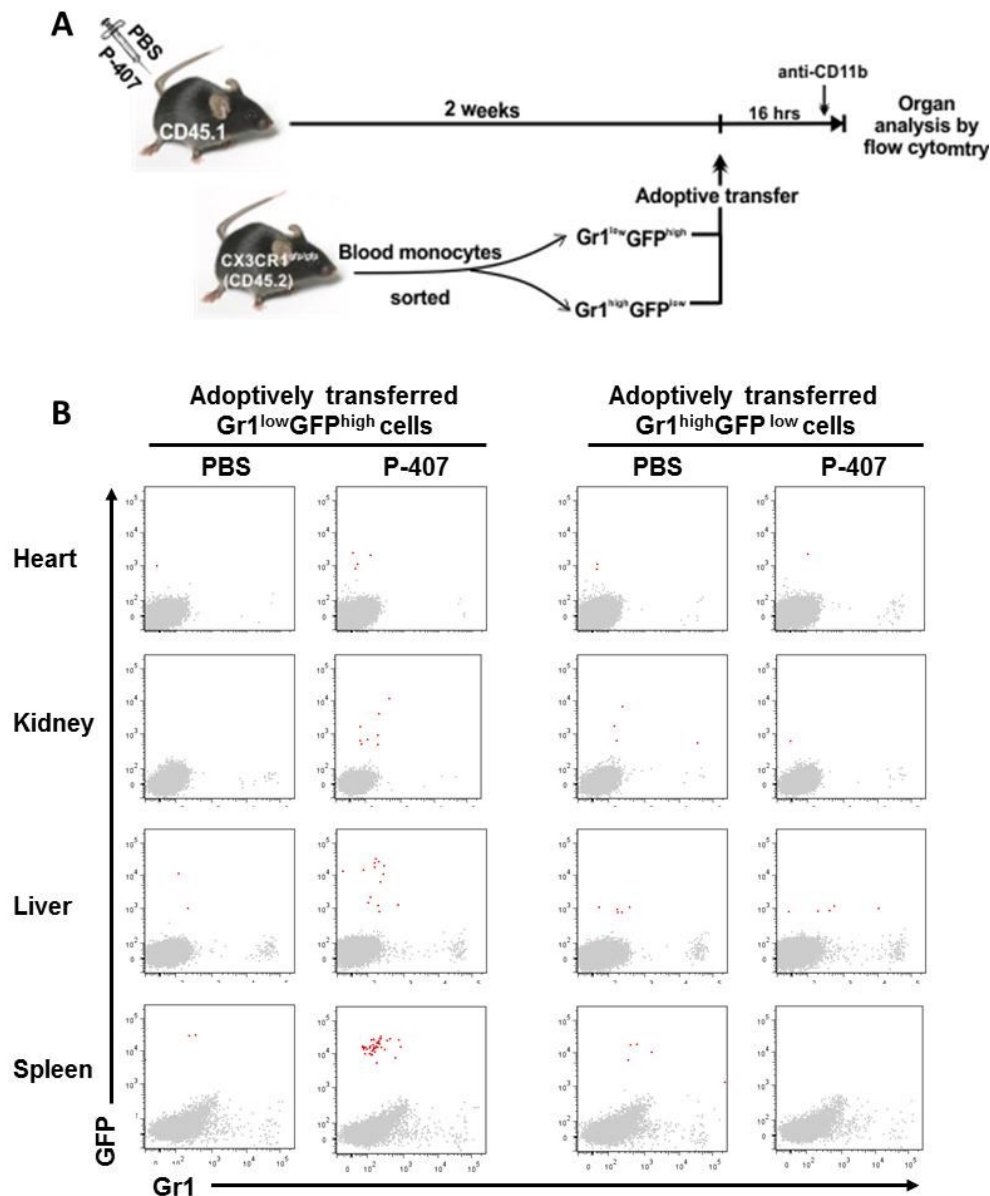


Figure 4.22. Adoptive transfer experiment.

A graphic representation of the adoptive transfer experiment (A), $Gr1^{low}GFP^{high}$ or $Gr1^{high}GFP^{low}$ blood MOs were sorted from $CD45.2\ Cx3cr1^{gfp/gfp}$ mice and 0.1×10^6 injected i.v. into $CD45.1.B6$ mice that have been injected with either 10mg P-407 or PBS i.p. thrice weekly for a period of 2 weeks ($n=4$ for the $Gr1^{low}GFP^{high}$ adoptively transferred group and $n=3$ for the $Gr1^{high}GFP^{low}$ adoptively transferred group). After 16hrs of adoptive transfer, mice were injected with an anti-CD11b antibody ($3\mu g$) to exclude blood contamination. (B) Dot plot overlays displaying total cells (gray) and $CD45.2^{+}CD11b^{-}GFP^{+}$ cells (red). Experiment done by Dr. Lucie Baudino.

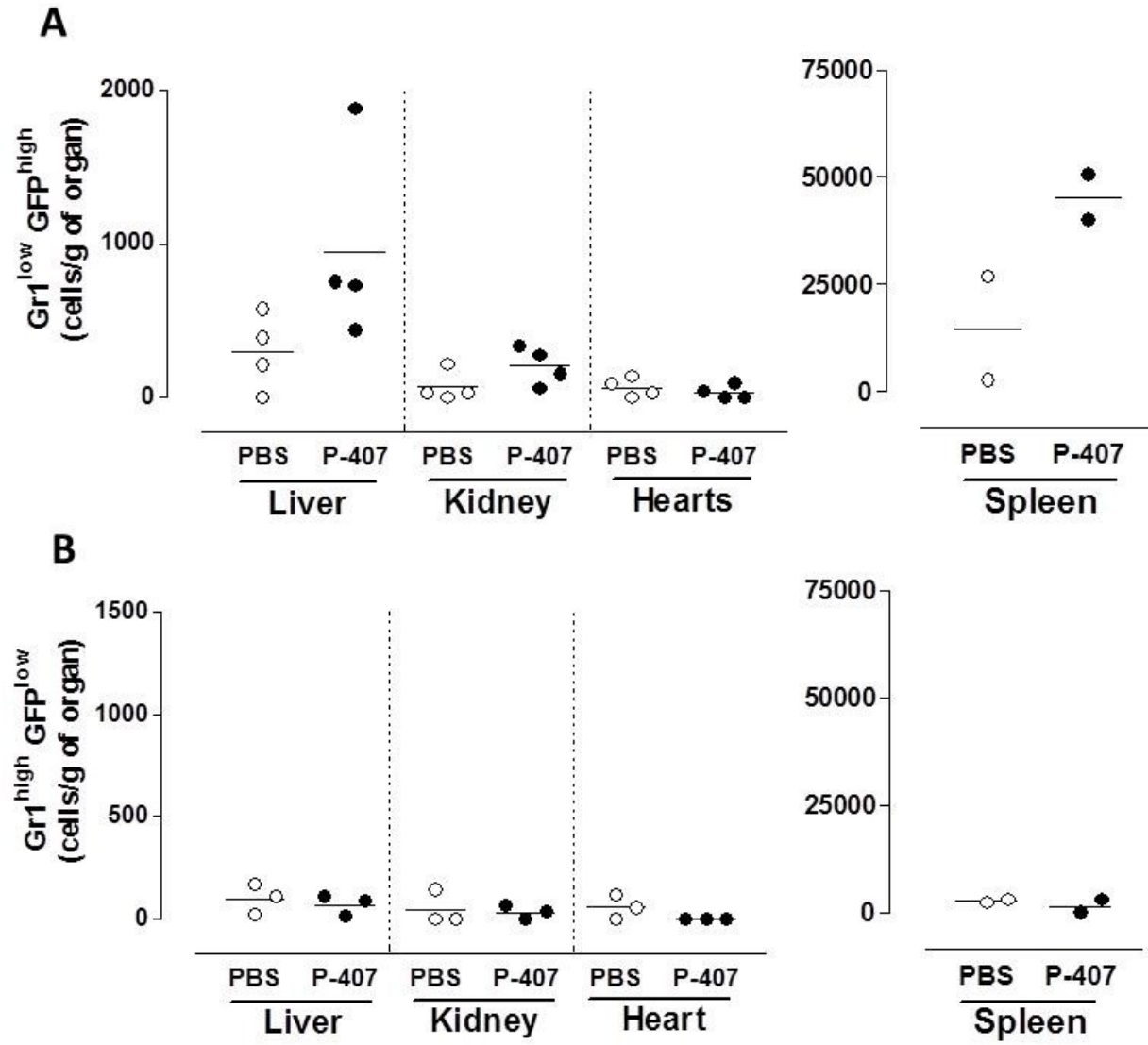


Figure 4.23. Quantitative analysis of the adoptively transferred cells.

Quantitative representation of Fig-4.22B. (A) Numbers of adoptively transferred Gr1^{low}GFP^{high} MOs in the liver, kidney, heart, and spleen expressed as cells/g of organ and analysed by flow cytometry (n=4). (B) Numbers of adoptively transferred Gr1^{high}GFP^{low} MOs in the same organs expressed as cells/g of organ and analysed by flow cytometry (n=3). The spleen data of two Gr1^{low} GFP^{high} adoptively transferred mice and one Gr1^{high} GFP^{low} adoptively transferred mouse are not available. Data are representative of two independent experiments and presented as mean \pm SD. Data kindly provided by Dr. Lucie Baudino.

4.7. Conclusion

The observations outlined in this chapter demonstrate that a hyper-TGRL environment affects the mononuclear phagocytic system in various ways:

- The induction of a hyper-TGRL state alters the distribution of MO subsets in the blood as evidenced by the dramatic drop seen in circulating Gr1^{low} MOs with minimal effect on the Gr1^{high} counterparts.
- The changes observed in the blood are mirrored by a massive accumulation of CD68⁺ MØs in the tissues.
- The lack of Ki-67⁺ staining in the CD68⁺ tissues makes local tissue proliferation an unlikely explanation for this accumulation.
- The observation of enhanced margination of GFP^{high} Gr1^{low} cells on intravital microscopy along with the accumulation of adoptively transferred GFP^{high} Gr1^{low} cells in the organs of P-407-treated animals make extravasation of the Gr1^{low} MOs a reasonable explanation for the enhanced accumulation of CD68⁺ MØs in the tissues of hypertriglyceridemic animals.

4.8. Discussion

In this chapter I describe a distinctive effect of hyper-TGRL environment on the behaviour of MO subsets. Although the numbers of total MOs in the blood did not change significantly following the induction of a hyper-TGRL state, there was a progressive sharp drop in the levels of Gr1^{low} MOs with minimal change in the Gr1^{high} MOs (Fig-4.2 & 4.4). This is extremely different from the Gr1^{high}/Ly6C^{high}-driven monocytoysis observed with the apoE^{-/-} murine model of atherosclerosis (Murphy et al., 2011; Swirski et al., 2007). It is worth noting that the apoE^{-/-} model have been shown to

exhibit systemic inflammation which may explain the preferential expansion of the Gr1^{high}/Ly6C^{high} subset known for its pro-inflammatory functions (Lohmann et al., 2009; Nahrendorf et al., 2007; Serbina et al., 2008). The Gr1^{low} MOs seemed the most susceptible to the effects of a hyper-TGRL environment, since most of the other PB cellular parameters failed to show consistent or sustained changes over the period of P-407 induced hypertriglyceridemia. Nevertheless, circulating levels of PMNs did show a slight increase after three weeks of P-407 injection which may indicate some effect of the hyper-TGRL environment on this cellular subset (Fig-4.6E). The drop in circulating Gr1^{low} levels could not be explained by defective BM synthesis since the numbers BM MOs as well as their progenitors namely MDPs, CMPs and GMPs were not affected in the P-407 injected mice when compared to controls (Fig-4.10 & 4.12C). There was, however, a significant decrease in the frequency of MDPs in the BM of P-407 injected mice (Fig-4.9A). In view of the similarity in MDP numbers between the two groups, this drop is most likely due to an expansion of other cellular components within the BM which was confirmed with the observation of higher levels of MEPs and LT-HSCs in the P-407 injected mice (Fig-4.12A & B). BM synthesis is not the only source for Gr1^{low} MOs as they were shown to derive peripherally from Gr1^{high} MOs as the latter loses its Gr1 expression (Sunderkotter et al., 2004; Yona et al., 2013). Inhibition of Gr1^{high} MOs conversion has been suggested as a cause behind the observed Gr1^{high}/Ly6C^{high} monocytosis seen in HF-fed apoE^{-/-} mouse model (Swirski et al., 2007). However, the P-407-induced hyper-TGRL model does not seem to have a similar effect on Gr1^{high}>Gr1^{low} conversion since the kinetics of BrdU label loss from this subset was not delayed and was very much in line with its loss from Gr1^{high} MOs in the PBS group (Fig-

4.13C). The similarity in BrdU loss from the Gr1^{high} subset occurred despite the initial higher incorporation of BrdU into Gr1^{high} cells in the P-407, which further emphasises that the P-407-induced hyper-TGRL state did not alter the half-life of Gr1^{high} cells in the blood (Fig-4.13C). On the other hand, the kinetics of BrdU acquisition by the Gr1^{low} subset carried some interesting observations. The undetectable BrdU incorporation into Gr1^{low} MOs at day 1 was followed by a steady rise in BrdU⁺ Gr1^{low} MOs over the 5 day period in the PBS injected group, whereas the increase in BrdU⁺ Gr1^{low} MOs in the P-407 injected group failed to match the rise seen in their PBS counterparts suggesting different kinetics for this cellular subset under the influence of P-407-induced hyper-TGRL state (Fig-4.13D). This is especially true in view of the higher BrdU⁺ incorporation into the Gr1^{high} subset observed in P-407 injected mice which, along with the undisturbed conversion, should result in a higher level of BrdU⁺ Gr1^{low} MOs in the P-407 group towards the end of the 5 day period. The halted rise in BrdU⁺ Gr1^{low} MOs in the P-407 injected group suggested loss of these cells from the circulating pool. Gr1^{low} Mo have been recognised to constitutively crawl along the luminal side of the endothelium (Auffray et al., 2007), this along with reported effects of hyperlipidemia on the expression of ICAM-1 and ICAM-2 by endothelial cells (Botham and Wheeler-Jones, 2013) suggested enhanced margination of these cells under the influence of high TGRL levels as a cause for the lower BrdU⁺ Gr1^{low} MOs seen in P-407 injected group. In fact, intravital imaging of CX₃CR1^{gfp/gfp} reporter mice showed enhanced crawling of Gr1^{low} on the endothelial surface of P-407 injected mice (Fig-4.14). Surprisingly, it also revealed massive accumulation of GFP^{high} cells around in the tissue surrounding the vasculature of the ear which may indicate their recruitment into tissues under the influence of a

hyper-TGRL environment (Fig-4.14A). MO recruitment into tissues is associated with their conversion into MØ, and thus staining for MØs using the MØ marker CD68 was used to investigate the occurrence of a similar effect on other tissues. The liver, kidney and heart showed a progressive accumulation of CD68⁺ cells which correlated with the duration of treatment (Fig-4.16 & 4.17). The accumulation of CD68⁺ cells could not be attributed to enhanced local proliferation since double staining with Ki-67 failed to show Ki-67 positive staining in the same tissues (Fig-4.18). Collectively, the absence of defective generation of Gr1^{low} MOs along with their enhanced margination and the accumulation of non-dividing CD68⁺ cells in the tissues were all pointing toward the recruitment of Gr1^{low} MOs into the tissues of P-407 injected animals as a cause for the observed drop in their circulating levels. To answer this I initially resorted to a BMT experiment, however, this approach was complicated by the massive accumulation of GFP⁺ cells in the tissues of B6 irradiated mice before the commencement of any treatment (Fig-4.21). Although tissue resident MØs are capable of sustaining themselves with minimal input from circulating MOs, in the advent of inflammation MOs can readily be recruited into the tissues to replenish the resident population, which could be the case here following whole body irradiation (Hashimoto et al., 2013; Ossetrova et al., 2014). This massive accumulation of GFP⁺ cells would hamper the identification of any P-407 induced effect and thus this approach was abandoned. Adoptive transfer experiments were then used as an alternative approach as they avoid the induction of a generalised inflammatory state and also allowed for the study of the behaviour of both subsets independently under P-407-induced hyper-TGRL environment. Adoptively transferred GFP^{high} Gr1^{low} MOs showed more accumulation in the organs of P-407

injected animals when compared to controls (Fig-4.22). The accumulation was much more pronounced in the spleen, liver, and kidney whereas no difference was detected in the heart (Fig-23A). This pattern is similar to that observed for CD68⁺ cells which also showed a more pronounced accumulation in the liver followed by the kidney and lastly the heart indicating that different kinetics govern the recruitment for each organs (Fig-4.16 & 4.17). It is also worth noting, that the tissues were collected 16 hrs following adoptive transfer which might not be enough to visualise accumulation of these cells into the heart given its milder phenotype. On the other hand, the adoptive transfer of GFP^{low} Gr1^{high} cells resulted in minimal recruitment into the tissues which was not different from that detected in the control group (Fig-4.23B). Taken together, the P-407-induced hyper-TGRL state seems to alter the behaviour of Gr1^{low} MOs with minimal effect on Gr1^{high} subset resulting in their enhanced margination and preferential recruitment into tissues causing a decrease in their circulating levels.

Despite the extensive changes in the mononuclear phagocytic system, the P-407-treated animals remained healthy and showed no evidence of end organ damage throughout the experimental period. These observations raised the question of what role these CD68⁺ macrophages play in the tissues. Is their presence in the tissues under high TGRL conditions completely harmless, or do they put organs under the risk of developing more damage should a secondary inflammatory insult occur? The next chapter deals with experiments aimed at addressing the pathologic significance of the hyper-TGRL driven changes in mononuclear phagocytic cells.

CHAPTER 5- THE EFFECT OF P-407-INDUCED HYPER-TGRL ENVIRONMENT IN PRIMING THE KIDNEY FOR RENAL INJURY

5.1. Introduction:

Lipids are fundamental components of living organisms and play important metabolic as well as structural roles. However, excessive lipid accumulation in tissues can lead to deleterious effects and cell injury. The question remains as to whether lipid accumulation is harmful by itself or whether their excessive presence renders organs more susceptible to the injurious effects of a secondary inflammatory insult (Bobulescu, 2010; Ruan et al., 2009).

The intriguing accumulation of MØs under high-TGRL conditions described in the previous chapter along with the derangement seen in the distribution of circulating MO subsets revived that question. Despite the healthy appearance of the P407-treated mice, could the changes in MOs and MØs put them at greater risk of organ damage should an inflammatory stimulus or event ensue? In other words, do these changes prime organs for injury in the event of a secondary inflammatory stimulus?

In an attempt to address this question, the kidney was chosen as the target for the secondary inflammatory insult following a period of induced hyper-TGRL state. In humans, renal dysfunction occurs in a variety of conditions associated with hypertriglyceridemia, including primary lipid disorders, the nephrotic syndrome, and diabetes mellitus (Bobulescu, 2010; Hung et al., 2013). Whether lipid accumulation in these conditions mediates renal injury or whether it is merely the consequence of the renal impairment is yet to be determined. The difficulty in interpreting these data stems

from the fact that the hypertriglyceridemia observed in these settings occur as part of a more complex metabolic derangement, and the exact contribution of high TG levels to the general picture becomes difficult to dissect (Grundy, 1998; Sarwar et al., 2007).

In this chapter, I tried to experimentally determine the effect of a hyper-TGRL environment on the renal response to an inflammatory insult. This was addressed by inducing renal inflammation, namely IC-mediated renal disease, in mice that had been rendered hyperlipidemic for a certain period of time. The following sections describe the results of these experiments.

5.2. The effect of 10mg P-407 induced hyper-TGRL environment on IC-mediated renal disease

A total of 21 B6 mice were divided into two groups: P-407-injected group (n=10) and a PBS-injected control (n=11). The mice, being maintained on regular chow diet, were injected with either 10mg P-407 or PBS i.p. every other day. Access to food and water was allowed *ad libitum*. Ten days after the commencement of the P-407 or PBS injections, the mice were immunized i.p. with sheep immunoglobulin IgG in CFA. Five days later a single i.v. injection of NTS was administered. A schematic representation of the experimental design is shown in Fig-5.1A. The dose of NTS has been previously optimised to induce glomerular inflammation without thrombosis at day 10-14 in WT B6 mice. The mice were sacrificed two weeks following the injection of NTS. One day prior to sacrifice, the mice were placed in individual metabolic cages for 24 hours to enable collection of urine. They were sacrificed the following day and kidneys were collected. Blood was collected at three points; before starting the P-407 or PBS injections

(baseline-day 0), before injection of the NTS (pre-NTS-day 14), and at the end of the experiment (final-day 28) (Fig-5.1A).

As expected, the injection of 10mg P-407 resulted in an increase in plasma TG levels from a mean value of 73.13 ± 13.63 mg/dl (mean \pm SD) at day 0 to an average of 6497 ± 2400 mg/dl, prior to NTS injection (Fig-5.1B). A much more modest increase was seen in plasma CHOL levels, from an average of 81.64 ± 4.909 mg/dl (mean \pm SD) at day 0 to 911.5 ± 241.2 mg/dl prior to NTS injection (Fig-5.1C). Over the course of the experiment, one mouse died in the P-407 group six days following NTS injection, whereas no deaths occurred in the PBS-injected controls. This mouse was excluded from subsequent analyses.

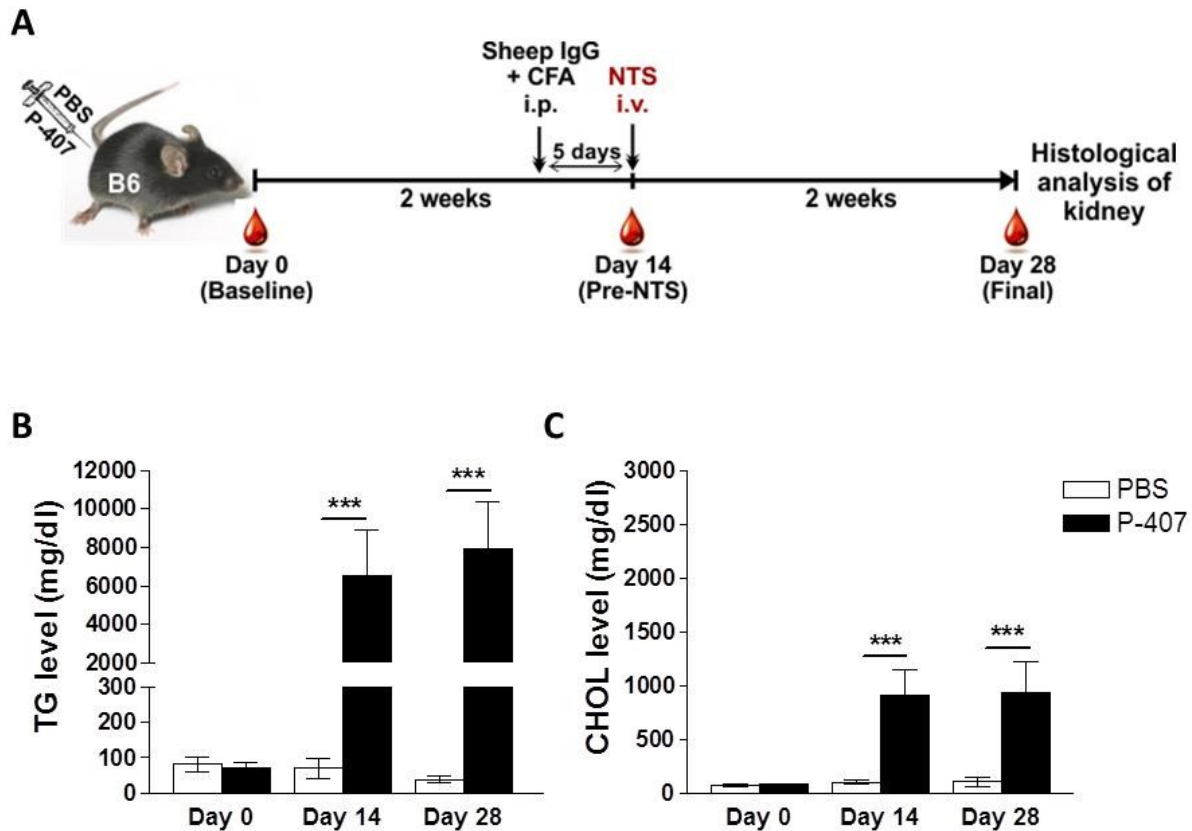


Figure 5.1. The aNTN model under P-407-induced hyper-TGRL conditions.

(A) A schematic representation of the experimental design: a hyper-TGRL state was induced by 10mg P-407 injection i.p. every other day and maintained throughout the 28 day-period of the experiment. A PBS-injected group served as normolipidemic controls. Fourteen days following the generation of a hyperlipidemic state, aNTN was induced by the i.v. administration of NTS in mice that had been immunized 5 days earlier with sheep IgG in CFA. After the injection of NTS, the mice were followed over a period of 2 weeks for signs of renal impairment including hematuria and proteinuria using serial urine dipstick analyses. Blood was collected at three time points; before any intervention (baseline-day 0), before injecting NTS (pre-NTS-day 14), and at the end of the experiment (final-day 28). The bar graphs represent non-fasting plasma TG levels (B) and CHOL levels (C) measured at the three time points (n=9 for the P-407 group and n=11 for PBS group). Data are presented as mean \pm SD. P value calculated using unpaired t-test. ***P<0.001.

5.2.1. Renal functional parameters

Following the induction of aNTN, the mice were monitored closely for the development of hematuria and proteinuria by serial urine dipstick analysis. The degree of proteinuria and hematuria was measured using a graded system: in ascending order of severity: 0, trace, grade 1, 2, and 3. Mice in the P-407-injected group started to show hematuria and proteinuria of grade 2 or more as early as 2 days following NTS injection (Fig-5.2A & B). In addition to the early development of hematuria and proteinuria, the percentage of mice developing hematuria and proteinuria of grade 2 or more was higher in the P-407-injected group when compared to controls throughout the period of the experiment (Fig-5.2). With regards to hematuria, the difference between the two experimental groups was statistically significant at all the time points (Fig-5.2A). Proteinuria, on the other hand, showed a statistically significant difference only during the early stages of aNTN, i.e. days 2 and 4 following NTS injection (Fig-5.2B).

At the end point (day 28) more mice developed hematuria in the P-407-injected group when compared to the PBS-injected controls ($P=0.0269$, Mann-Whitney test) (Fig-5.3A). Although proteinuria tended to be worse in the P-407-injected group, it was not statistically significant when compared to the control group ($P=0.1260$, Mann-Whitney test) (Fig-5.3B).

Analysis of the 24hr urinary albumin excretion was consistent with the proteinuria data and showed no statistically significant difference between the two experimental groups (Fig-5.3C). Plasma urea levels, however, were significantly higher in the hyper-TGRL mice when compared to the normolipidemic controls at the end point ($P=0.0038$, unpaired t-test). Of note, after the induction of aNTN only the P-407-treated animals developed uremia ($P=0.0492$, paired t-test) (Fig-5.3D).

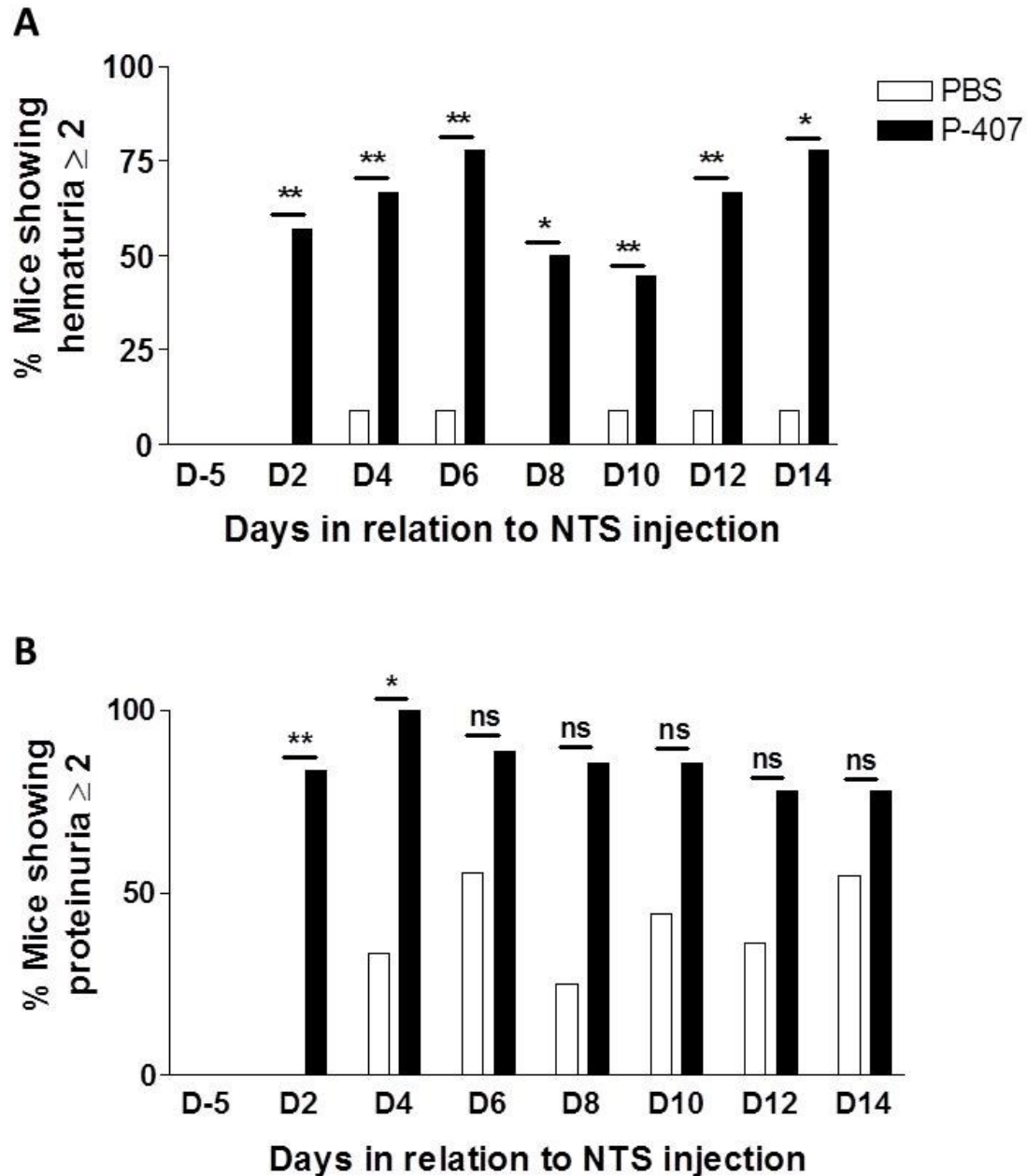


Figure 5.2. Percentages of mice developing hematuria and proteinuria following aNTN.

The figure depicts the percentage of chow-fed B6 mice developing (A) hematuria and (B) proteinuria of 2 or more on spot urine dipstick examination in the period following NTS injection in mice that have been subjected to a hyper-TGRL state (P-407) 2 weeks prior to NTS injection. The hyper-TGRL state was achieved by injecting 10mg P-407 i.p. every other day over the entire period of the experiment, i.e. 28 days (n=9) (Fig-5.1A) with PBS-injected mice serving as the normolipidemic controls (n=11). P value was calculated using Mann-Whitney test. * $P < 0.05$; ** $P < 0.01$, and ns = not significant.

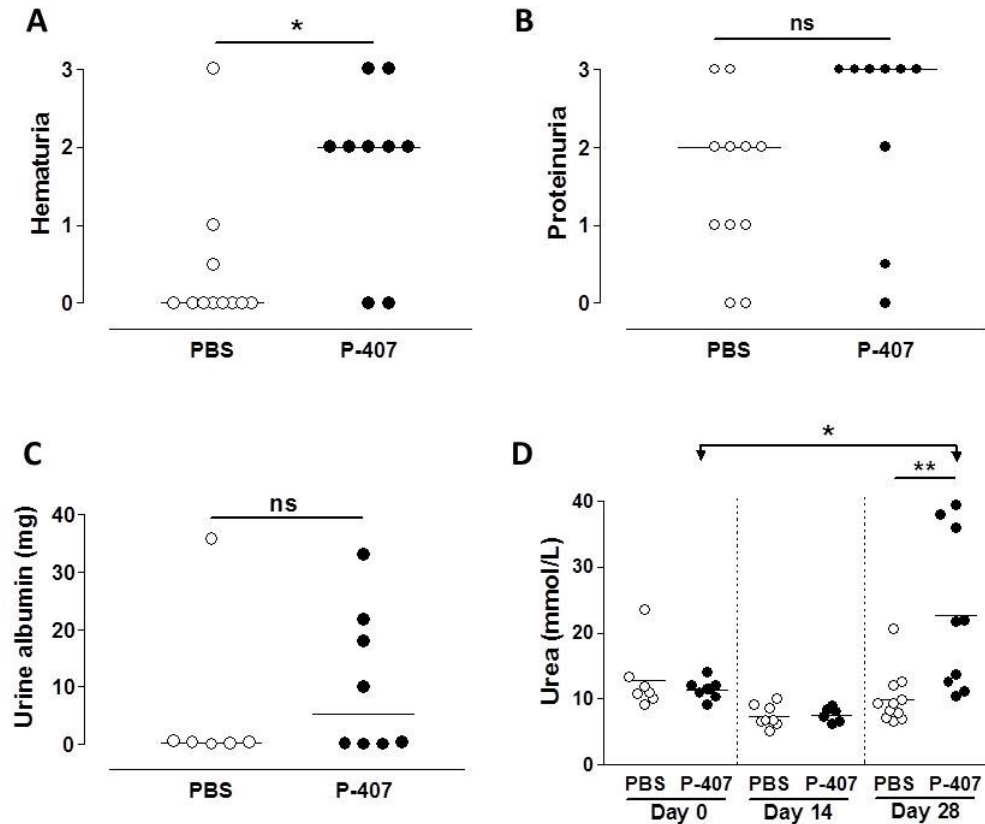


Figure 5.3. Renal functional parameters after aNTN.

Renal parameters assessed after 14 days of following NTS injection in chow-fed B6 mice that have been rendered hyperlipidemic for two weeks prior to NTS injection (Fig-5.1A). Hyperlipidemia was induced by injecting 10mg P-407 i.p. (n=9) every other day over the period of the experiment with PBS-injected mice serving as normolipidemic controls (n=11) (A) and (B) show hematuria and proteinuria, respectively, assessed using urinary dipsticks at the end of the experiment. (C) Represents 24hr urinary albumin excretion (mg) at the end of the experiment. Due to technical reasons not all the mice could be housed in the metabolic cages. For hematuria, proteinuria, and urinary albumin excretion, horizontal bars represent median value, P value was calculated using Mann-Whitney test with $*P < 0.05$ and ns = not significant. (D) Plasma urea levels (mmol/L) measured at baseline (day 0), before NTS injection (day 14), and at the end of the experiment (day 28). The urea data are not available for 4 and 3 mice at day 0 and 14, respectively from the PBS group and from one and 3 mice, respectively in the P-407 group at the same time points). Horizontal bars represent the mean. P value calculated using unpaired t-test when comparing between P-407 and PBS-injected groups, and paired t-test when comparing between day 0 and day 28 for the P-407-injected group. $*P < 0.05$; $**P < 0.01$.

5.2.2. Renal histology

Kidneys were collected at the end of the experiment and processed for PAS as well as CD68 staining. PAS-stained renal sections were graded on the basis of glomerular cellularity as follows: grade 0, normal; grade 1, segmental hypercellularity in 10–25% of the glomeruli; grade 2, hypercellularity involving >50% of the glomerular tuft in 25–50% of glomeruli; grade 3, hypercellularity involving >50% of the glomerular tuft in 50–75% of glomeruli; grade 4, glomerular hypercellularity in >75% or crescents in >25% of glomeruli. The grading was done in a blinded fashion (Prof. H.T. Cook). PAS-stained renal tissues of hyper-TGRL-induced mice exhibited more glomerular cellularity when compared to the PBS-injected controls ($P=0.0173$, Mann-Whitney test) (Fig-5.4A&B). Similarly, CD68 staining revealed massive accumulation of CD68⁺ cells both inside the glomeruli as well as in the interstitium of the kidneys of P-407-induced hyper-TGRL mice when compared to controls ($P<0.001$, unpaired t-test) (Fig-5.4 A&C). The CD68 staining of the kidneys of nephritic mice was compared with CD68 staining of kidneys collected from B6 mice that have been injected with either 10mg P-407 or PBS for the same period of time, i.e. 28 days but without the induction of aNTN ($n=5$ for PBS group, and $n=7$ for P-407 group). The extent of CD68⁺ cell accumulation in the kidney following aNTN was much more pronounced than that seen following 28 days of P-407-induced hyper-TGRL state alone in the absence of aNTN (Fig-5.5).

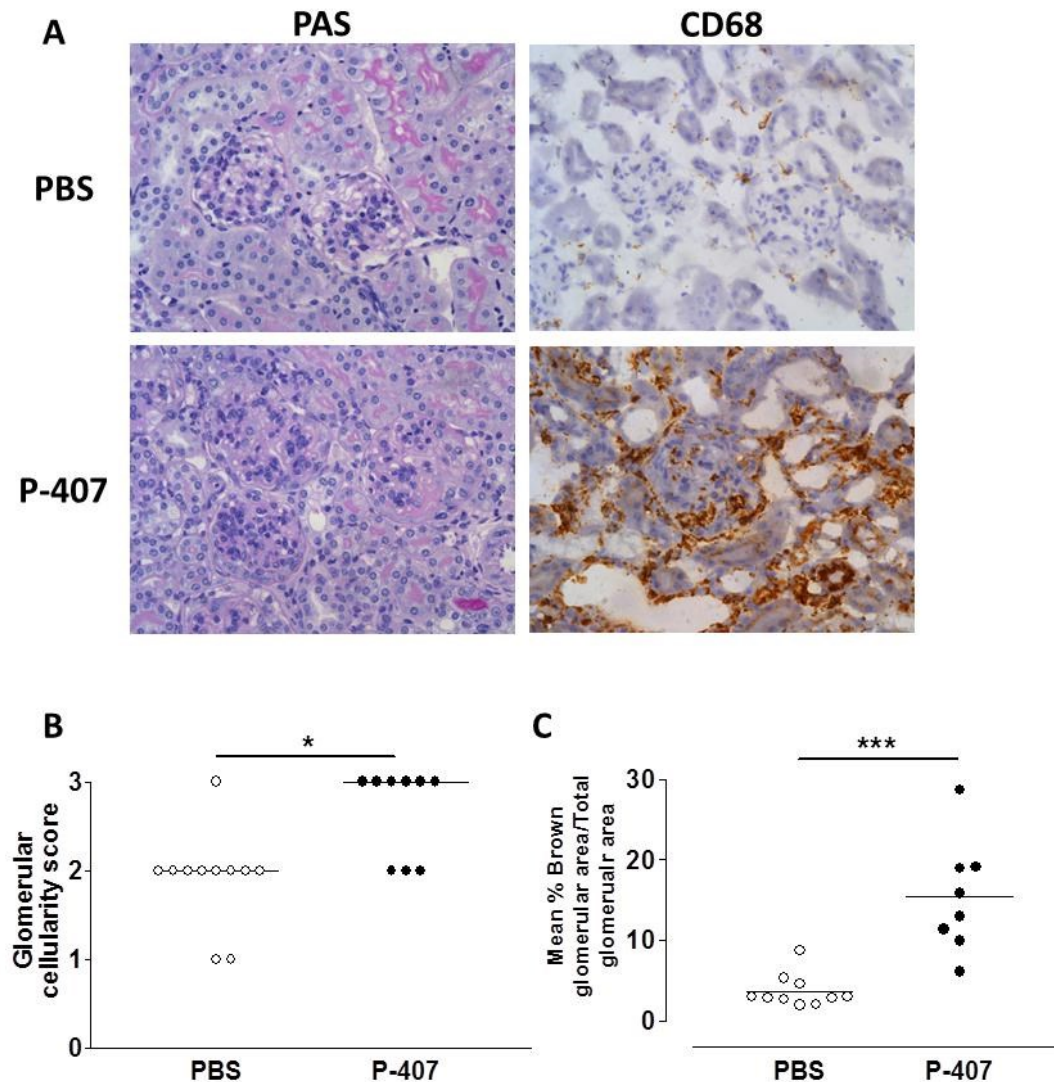


Figure 5.4. Histological evaluation of renal tissue after aNTN.

(A) Representative sections of PAS- and CD68-stained renal sections assessed after 14 days of NTS injection in chow-fed B6 mice that have been injected with either 10mg P-407 (n=9) or PBS (n=11) i.p. every other day for 2 weeks prior to NTS injection (Fig-5.1A). (B) Glomerular cellularity score of PAS-stained kidney tissue shown in (A) assessed in a blinded fashion (Prof. H. T. Cook). Horizontal bars represent the median. P value calculated using Mann-Whitney test. *P<0.05. (C) Quantitative analysis of CD68⁺ cells (brown) staining in (A), due to technical reasons one mouse is missing from each group. Data are expressed as mean percentage of brown glomerular area over total glomerular for 10 glomeruli per section. Horizontal bars represent the mean. P value calculated using unpaired t-test. ***P<0.001.

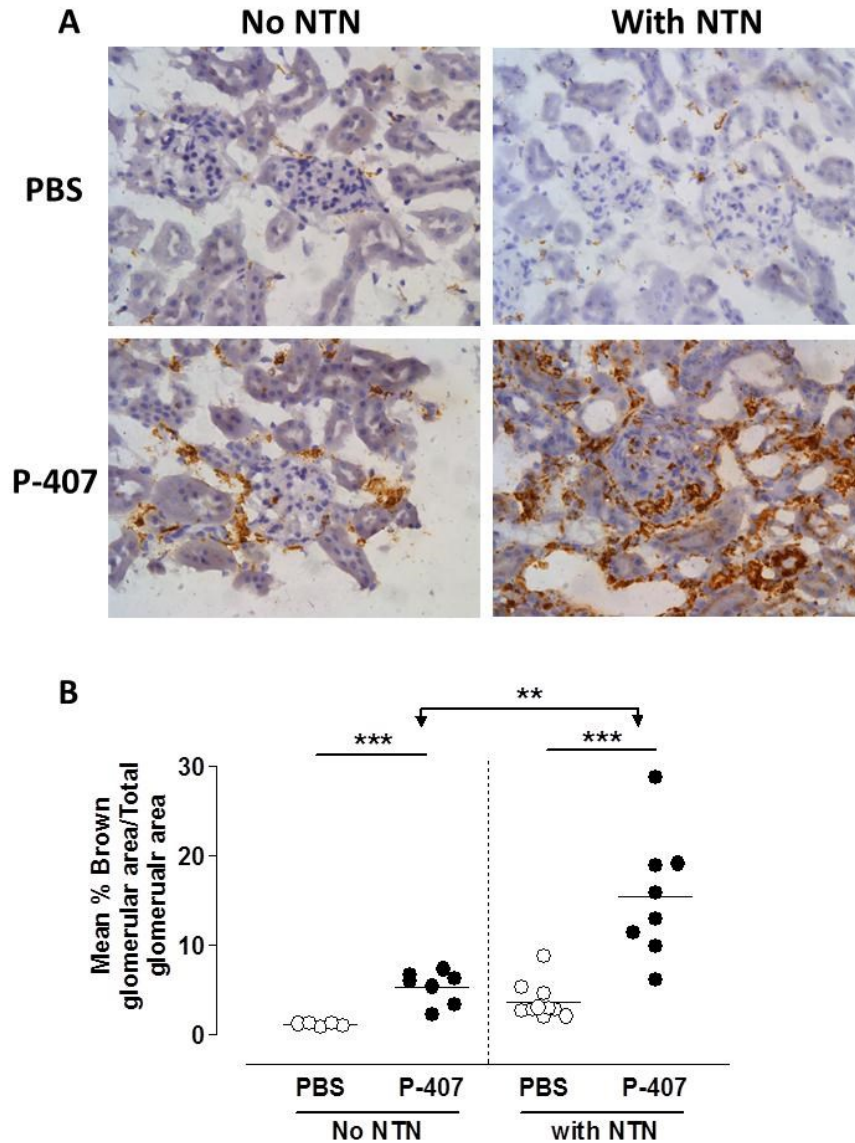


Figure 5.5. Comparison of CD68 staining in the absence or presence of aNTN.

CD68-stained renal sections from the experiment shown in Fig-5.4 were compared to CD68-stained renal sections from the kidneys of chow-fed B6 mice that have been treated with either 10mg P-407 (n=7) or PBS (n=5) i.p. every other day for a period of 28 days without the induction of aNTN. Representative CD68-stained renal sections after 28 days of P-407-induced hyper-TGRL environment with or without NTN are shown in (A). (B) Quantitative analysis of CD68⁺ cells (brown) in (A). Data are expressed as mean percentage of brown glomerular area over total glomerular for 10 glomeruli per section. Due to technical reasons one mouse is missing from each group in the NTN groups. Horizontal bars represent the mean. P value calculated using unpaired t-test. **P<0.01 and ***P<0.001.

As complement plays an important role in the pathogenesis of IC-mediated renal disease and since its activation is known to trigger MØ recruitment, it has become important to delineate whether the hyper-TGRL environment have triggered complement activation which in turn enhanced MØ recruitment resulting in aggravated tissue damage.

5.2.3. Glomerular C3 and IgG deposition

To assess whether the increased MØ accumulation in 10mg P-407-treated mice was due to enhanced complement activation triggered by the hyper-TGRL environment, kidney sections were stained for glomerular C3 and IgG deposition at the end point (day 28) of the aNTN experiment (Fig-5.6A) and the amount quantified using an Olympus fluorescent microscope with digital camera and captured images were analysed using Image-Pro Plus software. Ten glomeruli were examined per section with the mean fluorescence intensity expressed in arbitrary fluorescence units (AFU). Surprisingly, the mean glomerular C3 and IgG fluorescence was significantly lower in 10mg P-407-injected mice when compared to PBS-injected controls ($P=0.0039$ and $P=0.0079$, respectively, Mann-Whitney test) (Fig-5.6B&C).

In contrast to glomerular C3 staining, plasma C3 levels were not different between the two experimental groups at any of the time points (Fig-5.7). The pattern of plasma C3 fluctuation over the 28-day period of the experiment was also similar between the two groups. Both the P-407 as well as the PBS-injected mice displayed an increase in the circulating levels of C3 from a baseline level (day 0) of 273.8 ± 109.5 and 193.3 ± 109.9 $\mu\text{g/ml}$ (mean \pm SD), respectively to a level of 518.3 ± 235.9 and 603.5 ± 158 $\mu\text{g/ml}$ at day 14. By day 28, the plasma levels of C3 show a slight drop from their level at day 14

reaching 421.5 ± 200 and 416.5 ± 119.2 $\mu\text{g/ml}$ in the P-407 and PBS-injected groups, respectively (Fig-5.7).

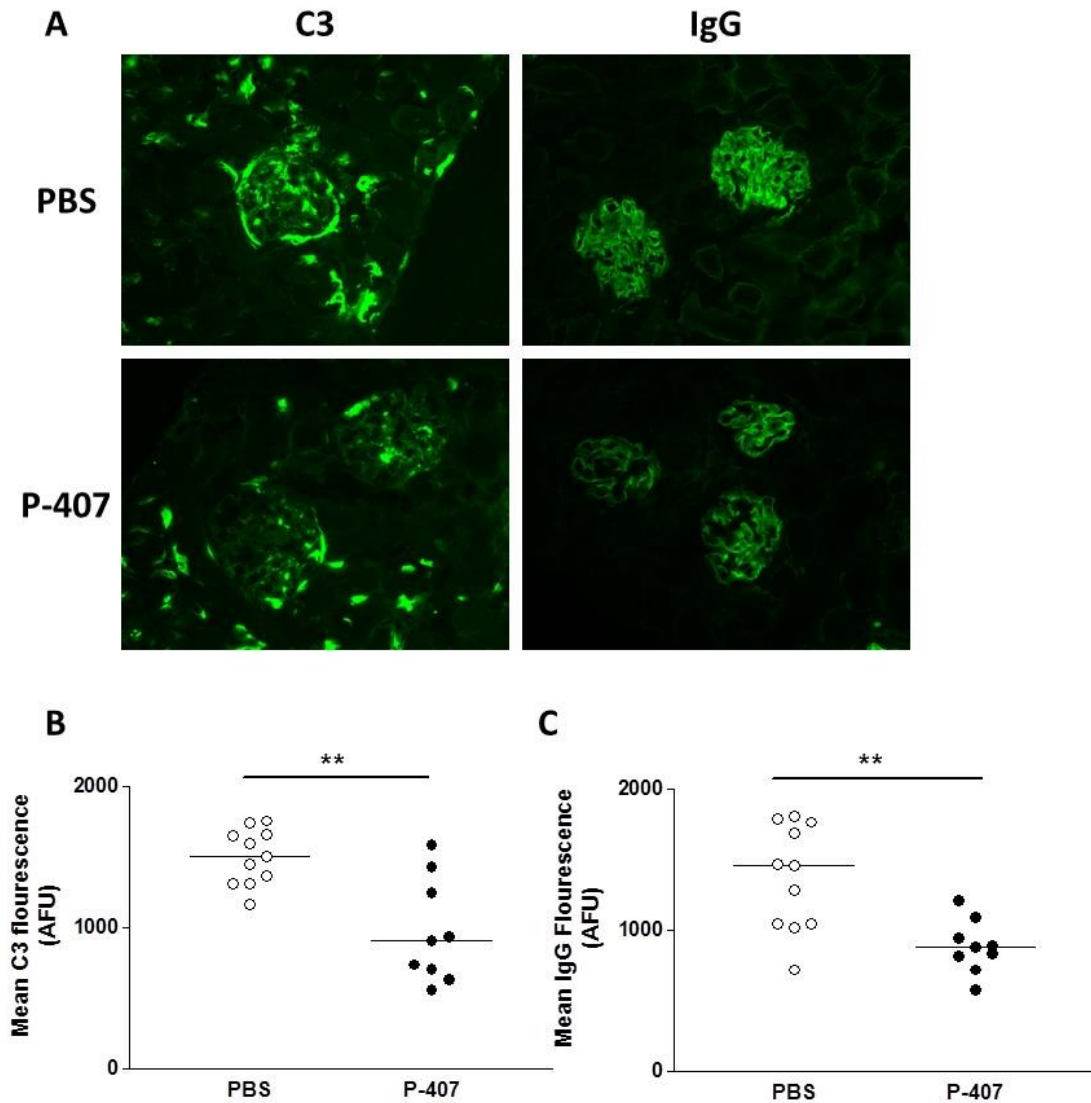


Figure 5.6. Glomerular C3 and IgG deposition.

Glomerular C3 and IgG staining assessed in the kidneys of chow-fed B6 mice after 14 days of NTS injection following a 2-week period of either 10mg P-407 (n=9) or PBS (n=11) injection i.p. every other day (Fig-5.1A). (A) Representative images of fluorescent glomerular C3 and IgG staining in 10mg P-407- vs PBS-injected mice (x40 magnification). (B) Quantification of glomerular C3 (B) and glomerular IgG (c) staining shown in (A). Quantification of C3 and IgG glomerular staining represents the mean fluorescent signal expressed as arbitrary fluorescence units (AFU) of either C3 or IgG in 10 glomeruli per section. Horizontal bars represent the median. P value calculated using Mann-Whitney test. **P<0.01.

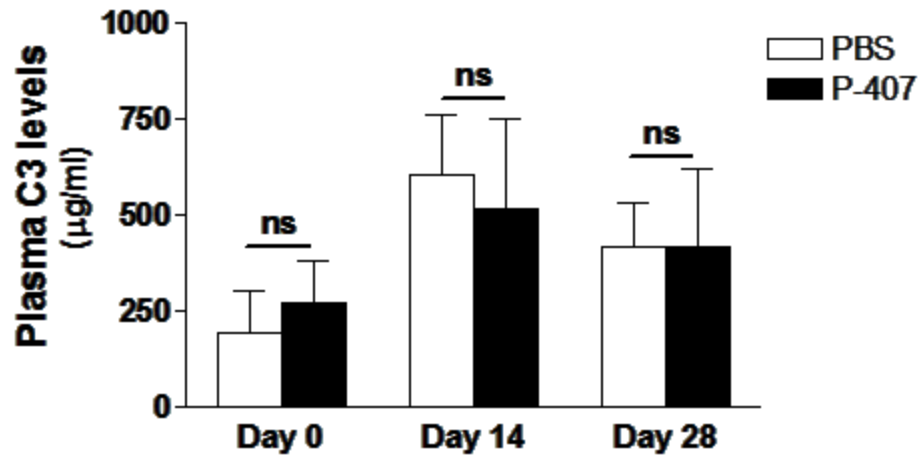


Figure 5.7. Plasma C3 levels along the course of aNTN.

Circulating plasma C3 levels expressed as µg/ml assessed in chow-fed B6 mice that underwent the experimental protocol shown in Fig-5.1A. Circulating plasma C3 levels were measured in both, the 10mg P-407- (n=9) and PBS-injected (n=11) mice at three different time points over the 28-day period of the experiment (Fig-5.1A). Day 0 corresponds to baseline data before any intervention. Day 14 represent bleeding before the NTS injection and 5 days following immunization with sheep IgG. Day 28 corresponds to the final bleeding after 14 days of aNTN induction. Data are presented as mean \pm SD. P value calculated using unpaired t-test, ns=not significant.

The above findings were reproduced in a 2nd aNTN experiment using the same experimental design. B6 mice were injected with either 10mg P-407 (n=10) or PBS (n=10) for 2 weeks before inducing aNTN as done previously. Two weeks following NTS injection the mice were sacrificed and kidneys were collected. Blood was collected at three points; before starting the P-407 or PBS injections (baseline-day 0), before injection of the NTS (pre-NTS-day 14), and at the end of the experiment (final-day 28) (Fig-5.1A). One mouse died in the 10mg P-407 group and was excluded from analysis. The only difference between this experiment and the previous one is the frequency of injections, the P-407/PBS injections were administered 72 hourly instead of 48 hourly as done in the previous experiment.

As demonstrated previously, the 10mg P-407 injection increased the plasma levels of both TG (1341 ± 1732 mg/dl) and CHOL (606.3 ± 92.98 mg/dl) at day 14, prior to NTS injection, compared to their levels in the PBS injected controls (118.8 ± 19.1 mg/dl and 79.77 ± 15.99 , mean \pm SD), respectively (Fig-5.8). Following NTS injection, mice in the P-407 group developed hematuria of grade 2 or more as early as day 2 following the injection of the NTS, whereas the PBS injected control showed no hematuria all through the experimental period (Fig-5.9A). The P-407 group also showed higher proteinuria levels at the end point when compared to the PBS injected controls ($P=0.0434$, Mann-Whitney test) (Fig-5.9B). Plasma urea levels although showed a significant difference in the P-407 group when compared to PBS controls at the end point, this level was not different in comparison to its baseline level (day 0) (Fig-5.9C). Histologic examination of PAS-stained kidney tissue was done in a blinded fashion (Prof. H. T. Cook) and was scored on the presence of glomerular cellularity from least to worst. P-407 injected mice

exhibited worse glomerular cellularity when compared to the PBS injected controls (P=0.0004, Mann-Whitney test) (Fig-5.9D).

Taken together, a hyper-TGRL environment appears to have detrimental effects on IC-mediated renal injury manifested by accelerated development of hematuria and enhanced glomerular cellularity along with MØ accumulation in the kidneys of hyper-TGRL mice.

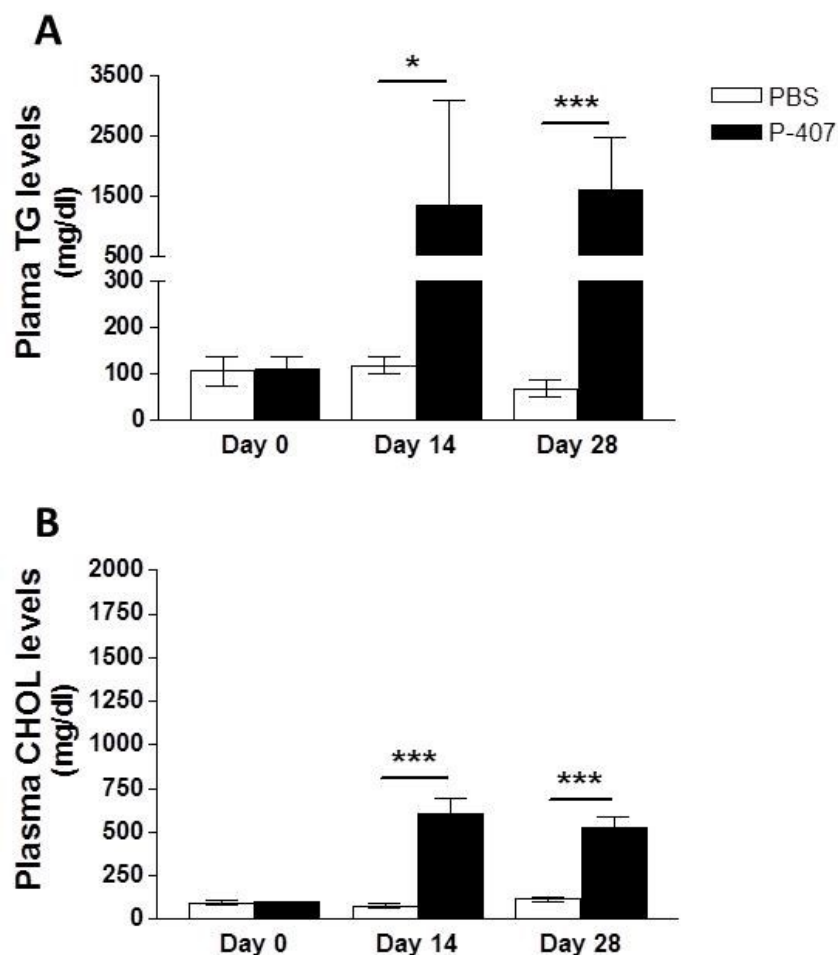


Figure 5.8. Plasma lipid levels of the 2nd NTN experiment using 10mg P-407.

Non-fasting plasma levels of TGs (A) and CHOL (B) of the 2nd NTN experiment done following the same experimental protocol shown in Fig-5.1A with 10mg P-407 and PBS being administered i.p. every 72 hours rather than the 48-hourly regimen used in Fig-5.1 through to Fig-5.7. Shortly, chow-fed B6 mice are injected with either 10mg P-407 (n=9) or PBS (n=10) i.p. 72-hourly for 14 days followed by the induction of aNTN. The mice are then monitored for another 14 days following NTS injection after which the animals are culled. Throughout the 28-day period of the experiment, the mice are bled at the three time points; at baseline and before the commencement of any intervention (day 0), after 14 days of 10mg P-407/PBS injections and before the administration of NTS (day 14), and at the end of the experiment (day 28) corresponding to 14 days following NTS injection. Data presented as mean \pm SD. P value calculated using unpaired t-test. *P<0.05 and ***P<0.001.

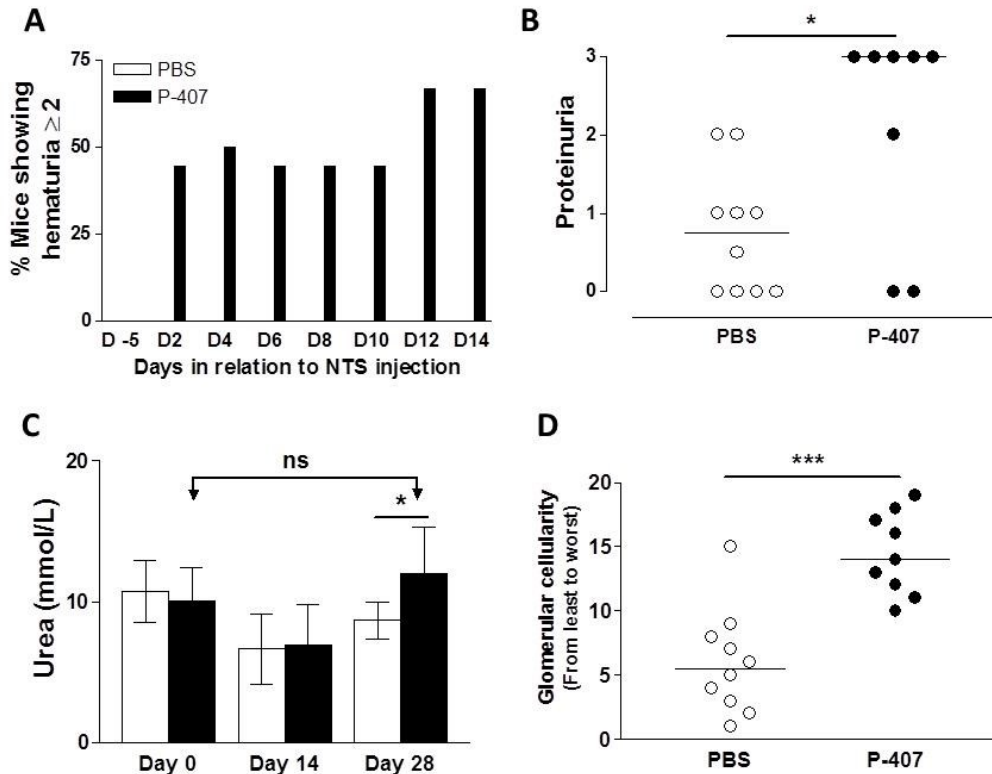


Figure 5.9. Renal parameters of the 2nd aNTN experiment using 10mg P-407.

Renal parameters of the 2nd aNTN done following the same protocol shown in Fig-5.1A with 10mg P-407 (n=9) and PBS (n=10) injections being administered i.p. every 72 hours (kindly refer to Fig-5.8 for a short description of the experimental design). (A) Shows percentage of mice developing hematuria grade 2 or more measured using urine dipstick analysis before injecting NTS (D-5) and every other day after NTS injection. (B) Proteinuria measured at the end point using urine dipstick analysis (urine dipstick reading for proteinuria was not obtained for one mouse in the P-407 group). (C) Plasma urea levels measured at baseline (day 0), before injecting NTS (day 14), and at the end point (day 28). (D) Glomerular cellularity score assessed on PAS-stained kidney sections in a blinded fashion and scored sequentially according to glomerular cellularity from least to worst. n=10 for PBS group and n=9 for P-407 group except when otherwise indicated. For urea levels data represent mean \pm SD and P value calculated using unpaired t-test when comparing between different groups or paired t-test when comparing the levels of the same group at different time points. For proteinuria and glomerular cellularity, horizontal bars represent the median and P value calculated using Mann-Whitney test. *P<0.05, ***P<0.001 and ns=not significant.

5.3. The effect of a milder hyper-TGRL environment on IC-mediated renal injury

From the above findings, it became clear that the hyper-TGRL environment induced by 10mg P-407 injection aggravated IC-mediated renal damage with accelerated development of hematuria, greater proteinuria and glomerular cellularity along with the enhanced accumulation of CD68⁺ cells in the kidney which could not be attributed to enhanced complement activation. The 10mg dose of P-407 induced marked hypertriglyceridemia and so I next examined if a milder hypertriglyceridemic and hyper-TGRL environment would exacerbate IC-mediated renal injury.

To test this, I induced aNTN using exactly the same protocol used previously (Fig-5.1A) in B6 mice that have received either 5mg P-407 (n=8) or PBS (n=9) every 48 hours for a period of 2 weeks prior to NTS injection. Following the administration of NTS, the mice were followed for the development of signs of renal damage including hematuria and proteinuria using urine dipstick analysis every other day for a period of two weeks. Plasma was collected at baseline and before starting any treatment (day 0), 2 weeks following 5mg P-407 and PBS administration and before injecting NTS (day 14), and at the end point which corresponds to 2 weeks following NTS administration (day 28) (Fig-5.1A). Portions of the kidney were collected at day 28 and fixed appropriately for PAS and CD68 staining, or snap frozen in OCT embedding medium for C3 and IgG staining. Fourteen days following the commencement of 5mg P-407 injections and before the induction of aNTN, plasma TG levels increased to a mean level of 3102 ± 688.8 mg/dl in the 5mg P-407 injected group in comparison to a mean level of 123 ± 34.6 mg/dl in the PBS injected controls ($P < 0.0001$, unpaired t-test) (Fig-5.10A). Similarly, CHOL levels showed an increase to a mean level of 377.3 ± 63.3 mg/dl in the 5mg P-407 group

when compared to a mean level of 86.8 ± 24.8 mg/dl in the PBS injected group ($P < 0.0001$, unpaired t-test) (Fig-5.10B).

Urinalysis for hematuria and proteinuria following the induction of aNTN showed that both groups developed grade 2 or more hematuria at a similar time point, i.e. day 4 following NTS injection. Although the percentage of mice showing grade 2 or more hematuria was initially higher in the 5mg P-407 group the difference between the groups was not significant at the end point (Fig-5.11A). With regards to proteinuria, despite the tendency for the 5mg P-407 injected mice to have a higher proteinuria at the end point when compared to the PBS group, the difference was not significant ($P = 0.4418$, Mann-Whitney test) (Fig-5.11B). Similarly, when PAS-stained kidney tissue was examined for glomerular cellularity, no significant difference was detected between the two experimental groups ($P = 0.1304$, Mann-Whitney test) (Fig-5.11C).

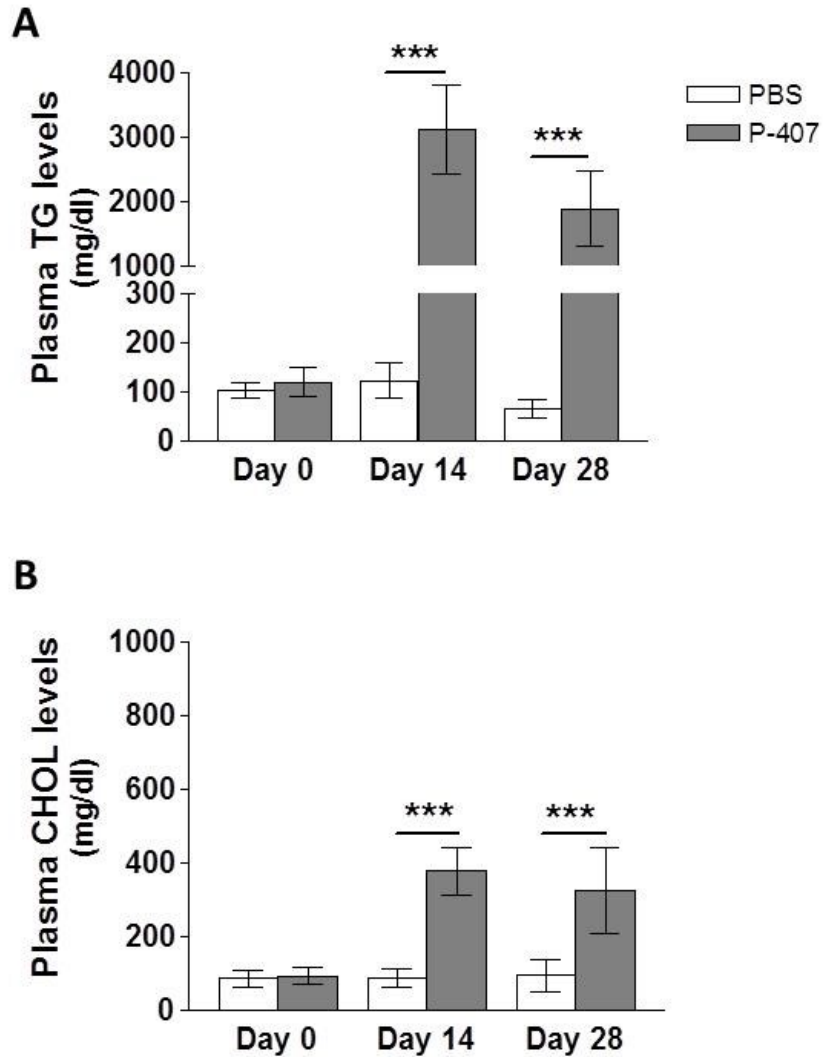


Figure 5.10. Plasma lipid levels in response to 5mg P-407 injection over the aNTN experimental period.

Non-fasting plasma TG (A) and CHOL (B) levels in response to 5mg P-407 (n=8) injection i.p. every 48 hrs over the period of the aNTN experiment against their levels in PBS injected controls (n=9). Day 0 refers to baseline levels before commencing 5mg P-507 and PBS injections, day 14 refers to 14 days following the P-407 and PBS injection but before NTS injection, while day 28 refers to the end point corresponding to 2 weeks following NTS injection. Data are presented as mean \pm SD. P value calculated using unpaired t-test. ***P<0.001.

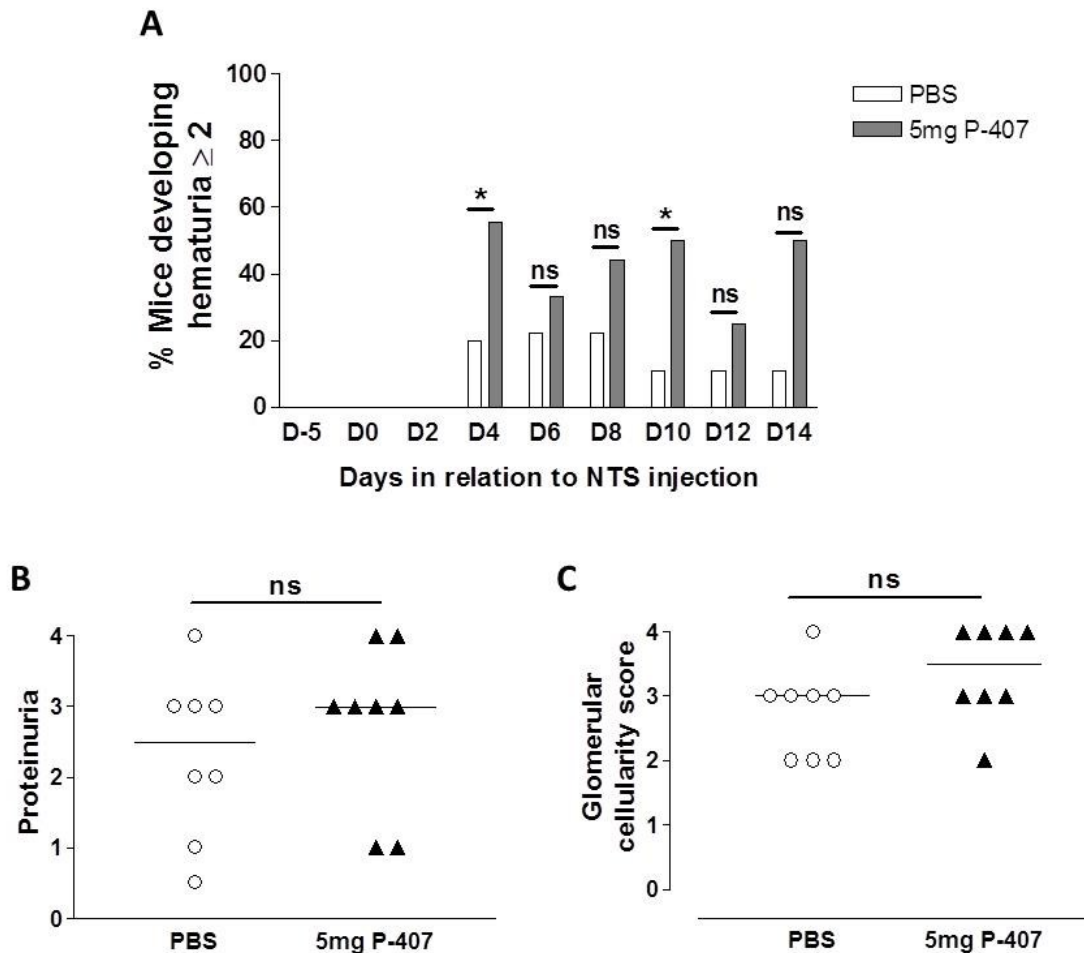


Figure 5.11. Renal parameters following aNTN induction in mice receiving 5mg P-407 against a PBS control.

Renal parameters following aNTN induction in B6 mice that have been receiving either 5mg P-407 (n=8) or PBS (n=9) for 2 weeks prior to NTS injection. Following the injection of NTS, the mice were followed for the development of hematuria/proteinuria using urine dipstick analysis every other day for another 2 weeks (experimental design shown in Fig-5.1A). (A) Shows percentage of mice developing hematuria (grade 2 or more) measured by urine dipstick analysis before injecting NTS (D-5) and every other day after NTS injection. (B) Proteinuria measured at the end point (day 28) using urine dipstick analysis. (C) Glomerular cellularity score assessed on PAS-stained kidney sections by a blinded observer. For proteinuria and glomerular score results were missing from one mouse in the PBS group. Horizontal bars represent the median. P value calculated using Mann-Whitney test. *P<0.05 and ns=not significant.

Despite the lack of differences observed in glomerular cellularity, staining of PLP-fixed kidney tissue for CD68 revealed more accumulation of CD68⁺ cells in the glomeruli and the interstitium of 5mg P-407 injected mice when compared to PBS injected controls (Fig-5.12A). Although the difference in CD68 staining between the two groups was visible, the difference in its quantification was not significant ($P=0.0623$, unpaired t-test) (Fig-5.12B). Glomerular C3 and IgG staining showed a similar pattern to that observed for the 10mg P-407 group, with the 5mg P-407 group showing less C3 and IgG staining in the glomeruli when compared to PBS injected controls ($P=0.0464$ and $P=0.0037$, Mann-Whitney test) (Fig-5.13).

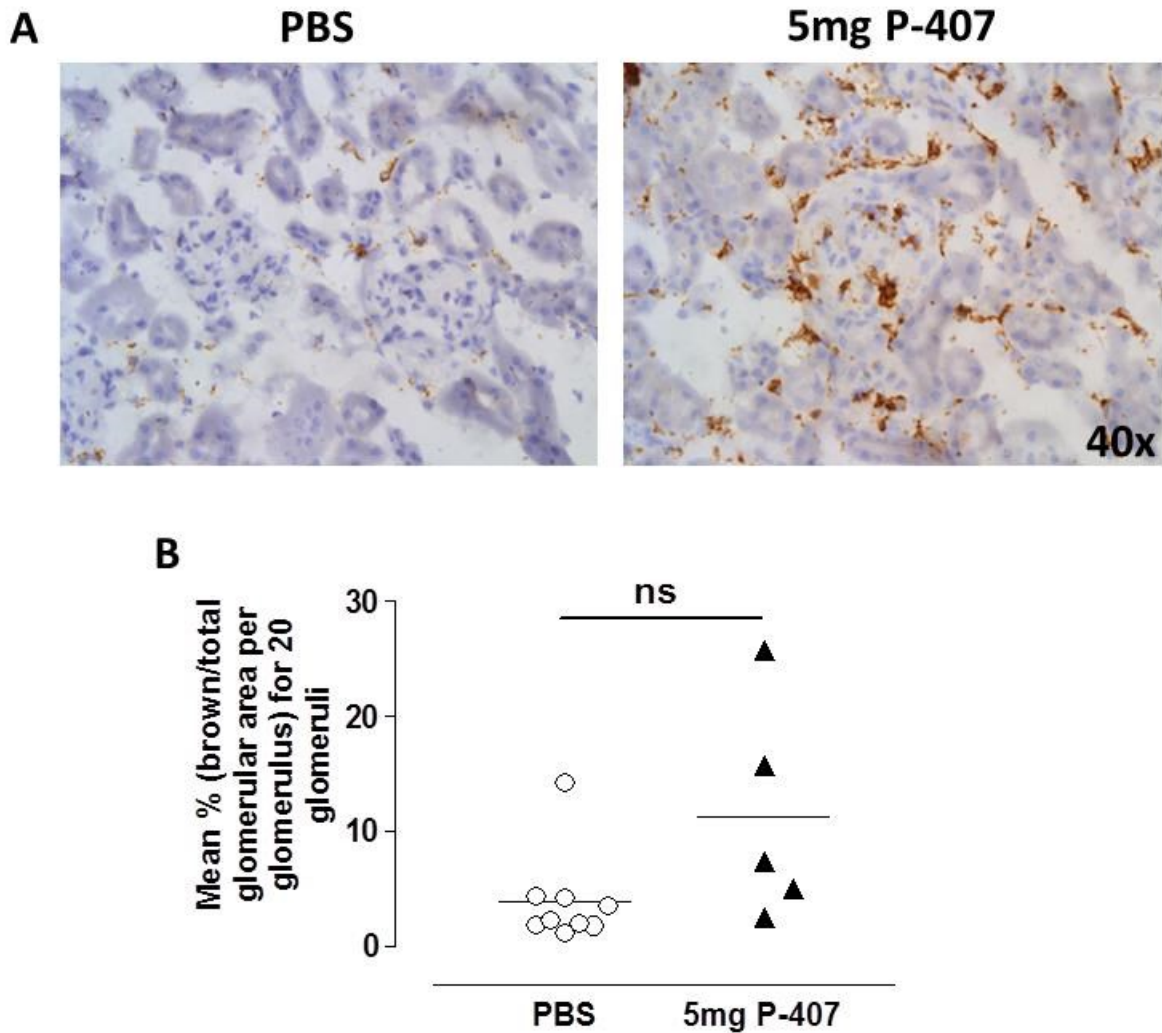


Figure 5.12. CD68 staining of kidney sections following aNTN induction in mice receiving 5mg P-407.

Representative CD68-stained renal sections are shown in (A) after 14 days of NTS injection in mice that have been receiving either 5mg P-407 (n=8) or PBS (n=9) i.p. every 48 hrs for 2 weeks prior to NTS injection and another 2 weeks thereafter (experimental design shown in Fig-5.1A). (B) Quantitative analysis of CD68⁺ cells (brown) in (A). Data are expressed as mean percentage of brown glomerular area over total glomerular for 20 glomeruli per section. Due to technical reasons 3 sections from 5mg P-407 group were not analysed. Horizontal bars represent the mean. P value calculated using unpaired t-test. ns=not significant.

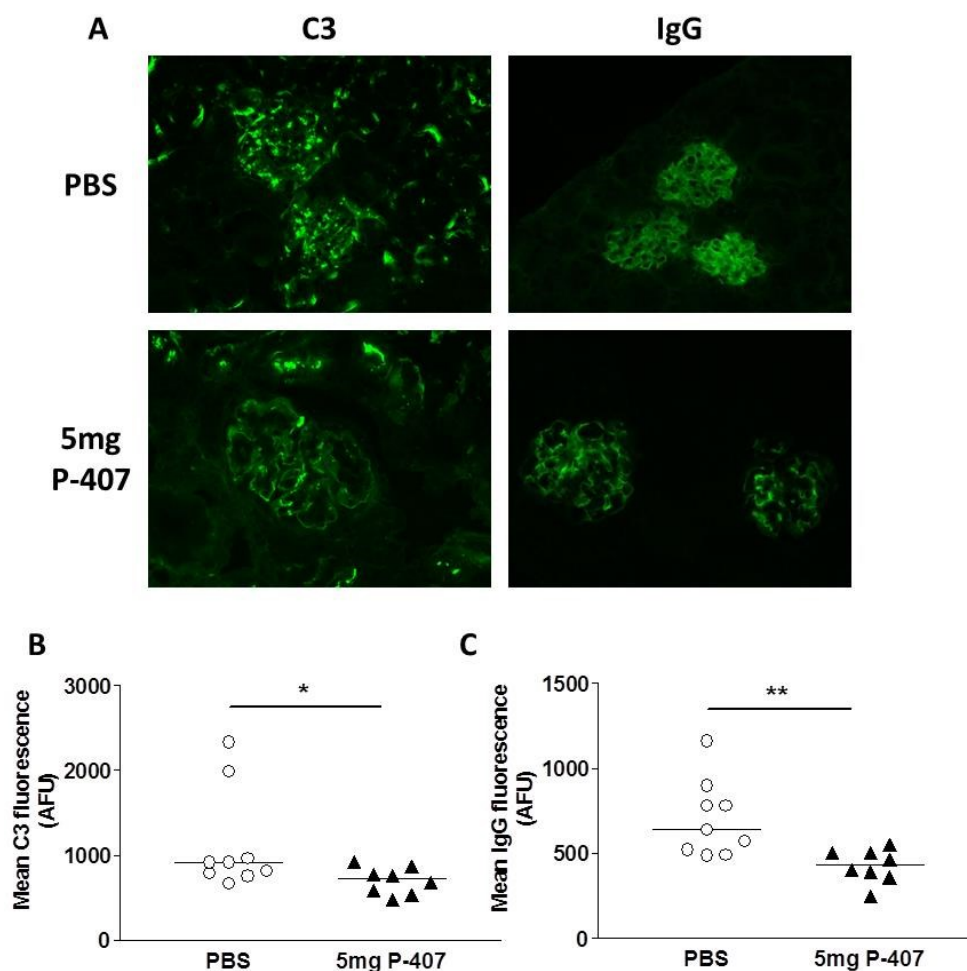


Figure 5.13. Glomerular C3 and IgG staining following the induction of aNTN in mice receiving 5mg P-407.

(A) Representative images of fluorescent glomerular C3 and IgG staining after 14 days of NTS injection in chow-fed B6 mice that have been receiving 5mg P-407 (n=8) or PBS (n=9) i.p. every 48 hrs for 2 weeks prior to NTS injection and another 2 weeks thereafter (experimental design shown in Fig-5.1A) (x40 magnification). (B) Quantification of glomerular C3 (B) and glomerular IgG (C) staining shown in (A). Quantification of C3 and IgG glomerular staining represents the mean fluorescent signal expressed as arbitrary fluorescence units (AFU) of either C3 or IgG in 10 glomeruli per section. Horizontal bars represent the median. P value calculated using Mann-Whitney test. *P<0.05 and **P<0.01.

The consistent observation of lower IgG glomerular staining in the kidneys of P-407 injected mice raised the question as to whether or not the P-407-induced hyper-TGRL environment is interfering with the immune response against the injected sheep IgG in these animals. Based on that, the immune response of P-407 and PBS injected mice against sheep IgG was measured at the end point of the aNTN experiment in mice that received either the 5mg P-407 or PBS. The immune response data is expressed as the sample dilution that corresponds to the OD double that of the blocking buffer used in the assay. There was no difference in the relative amount of mouse anti-sheep IgG generated by both groups after 19 days of sheep IgG injection (Fig-5.14).

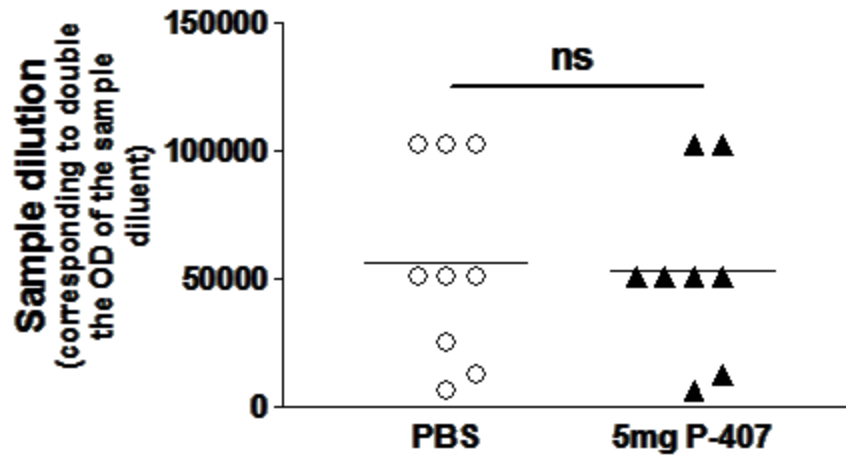


Figure 5.14. Immune response determined at the end point of the aNTN experiment.

The immune response of chow-fed B6 mice that have been treated with either 5mg P-407 (n=8) or PBS (n=9) to sheep IgG immunization. B6 mice were injected with either 5mg P-407 or PBS i.p. every other day for 10 days prior to a single i.p. immunization with sheep IgG in CFA. Five days following i.p. immunization with sheep IgG, NTS was injected i.v. and the mice were followed for a period of 2 weeks for the development of signs of renal injury (Fig-5.1A). The immune response was measured at the end point, i.e. 19 days following the administration of sheep IgG by diluting each sample 12x starting from 1/400. All dilutions were then plated in one row on the 96-well plate with one well on each plate receiving only sample diluent. After reading the plate, the OD equivalent to double the OD of the diluent is marked and the corresponding dilution (titre) is plotted for each sample. Horizontal bars represent the mean. P value calculated using unpaired t-test. ns=not significant.

5.4. Conclusion

P-407-induced hypertriglyceridemic environment and its associated hyper-TGRL state enhanced IC-mediated renal disease as evidenced by earlier development of hematuria and proteinuria along with enhanced glomerular cellularity and CD68⁺ MØ accumulation in the kidneys of P-407 injected mice. The renal damage correlates with the degree of hypertriglyceridemia as the lower TG levels observed with the 5mg P-407 dose and the spaced 10mg P-407 dosing resulted in a milder phenotype.

5.5. Discussion

Renal disease complicates the course of various metabolic and inflammatory conditions where disturbances in TG metabolism are a common occurrence. The contribution of hypertriglyceridemia and the hyper-TGRL environment to the progression of renal disease under such circumstances has not been clearly dissected. This is largely due to the complex metabolic environment associated with such disease states. The results of this study clearly supports a role for hyper-TGRL environment in accelerating Ab-mediated renal injury as evidenced by the earlier onset of hematuria and proteinuria in hypertriglyceridemic mice as well as enhanced glomerular cellularity and marked accumulation of CD68⁺ cells both in the glomerulus as well as the interstitium of the kidney (Fig-5.2,3,& 4). Enhanced glomerular injury secondary to hyperlipidemia has been reported in guinea pigs, mice and rats fed high fat diets with increased development of proteinuria and increased glomerular cellularity (Al-Shebeb et al., 1988; Joles et al., 2000; Kelley and Izui, 1983). In all of these models, CHOL-rich diet was used resulting mainly in elevations in plasma CHOL levels with minimal effects on TGs (Al-Shebeb et al., 1988; Joles et al., 2000; Kelley and Izui, 1983). The P-407-induced

hyper-TGRL environment provided evidence that not only hypercholesterolemia but also hypertriglyceridemia is pathogenic to the kidney. In addition, the hyper-TGRL environment induced by P-407 bears great resemblance to the lipid profile seen under metabolic and inflammatory conditions, making it a useful model for delineating the effects of such an environment on the progression of renal disease in the absence of other confounding effects.

The enhanced glomerular injury seen in the presence of the P-407-induced hyper-TGRL state is largely mediated through MØ accumulation which showed massive accumulation following aNTN than in its absence (Fig-5.5). MØ accumulation in the kidney has been reported in other hypercholesterolemic models where they are thought to contribute to clearance of deposited lipids in the tissue of those animals (Joles et al., 2000). Thus it is reasonable to hypothesise that the initial MØ recruitment induced by the hyper-TGRL environment might have primed the kidney for more renal damage in the presence of Ab-mediated glomerular injury triggering the release of more inflammatory mediators promoting more MØ accumulation resulting in the aggravation of glomerular damage.

The enhanced MØ accumulation under hyper-TGRL environment could not be attributed to enhanced complement activation since glomerular C3 staining did not show increased deposition in the kidneys of P-407-injected mice (Fig-5.8 & 13). On the contrary, there was less deposition of glomerular C3 in the kidneys of P-407 injected mice when compared to PBS injected controls regardless of the P-407 dose used (Fig-5.8 & 13). The difference in glomerular C3 deposition could not be explained by a difference in plasma C3 levels since its levels were comparable between the P-407 and

PBS injected groups (Fig-5.9). There was, however, a demonstrable increase in plasma C3 levels in both groups seen at day 14 followed by a decline back to baseline levels by day 28 (Fig-5.9). The increase seen in plasma C3 levels at day 14 occurred 5 days following the injection of sheep IgG emulsified in CFA. CFA is an immune adjuvant composed of inactivated mycobacterial antigen emulsified in oil. I considered that administration of CFA could induce an acute phase response, which, since C3 is an acute phase reactant, could then explain the observed increase in C3 levels at that time point (Fig-5.9). Importantly, both groups showed similar levels and pattern of plasma C3 changes and thus the difference in glomerular C3 could not be attributed to differences in plasma C3 levels (Fig-5.9).

Given that complement activation occurs in response to interaction with the deposited antibodies (Nangaku and Couser, 2005; Unanue and Dixon, 1964), it was then hypothesised that the lower C3 may reflect lower IgG deposition into the glomeruli of P-407 injected mice. Staining for glomerular mouse IgG showed a similar pattern to that observed with glomerular C3 staining with lower glomerular IgG deposition in the kidneys of P-407 injected mice (Fig-5.8 & 13). These results were consistent regardless of the dose used, and indicated the possibility of an impaired immune response in the P-407 injected animals resulting in less IgG deposition in the glomerulus. However, this does not appear to be the case since plasma levels of mouse anti-sheep IgG measured at the end of the aNTN experiment were not different between the groups (Fig-5.14). The decreased glomerular IgG staining may be attributed to either their enhanced clearance by the accumulated CD68⁺ MØ seen in P-407 injected animals making them unavailable to be recognised by the staining antibody or C3, or to the presence of other

material such as lipids which may interfere with the deposition of ICs. However, further investigations are needed to confirm these propositions. These findings are different from those reported in a combined SLE and atherosclerosis murine model, Sle16.Ldlr^{-/-}. In the Sle16.Ldlr^{-/-} mouse, HF feeding resulted in enhanced IC-mediated renal inflammation by increasing glomerular complement deposition. These mice are characterised by a systemic autoimmune response different from the targeted IC-induced renal injury induced by the aNTN model. In addition, HF-fed Sle16.Ldlr^{-/-} mice exhibited higher anti-dsDNA and anti-ssDNA along with enhanced T- and B-cell activity when compared to HF-fed Sle16 only mice indicating a heightened immune response in these mice inciting a different pathologic process. Additionally, these mice are at risk of developing anti-oxidised LDL (anti-ox-LDL) which may deposit in the glomeruli causing complement activation. Although the occurrence of anti-ox-LDL antibodies cannot be excluded in the P-407 model, its induction is unlikely given that I have avoided the use of models characterised by a generalised state of auto-immunity.

Notably, the degree of renal damage seems to be dose dependent with a milder phenotype observed with the use of 5mg P-407 (Fig-5.11). This may carry therapeutic potential entailing more vigorous treatment of dyslipidemia that accompanies inflammatory conditions such as SLE.

Taken together, my data demonstrate that a hyper-TGRL environment enhanced IC-mediated renal damage. The damage correlated with the level of TGs and TGRL and is largely mediated through enhanced MØ accumulation. However, given that most of these exciting observations were seen using P-407, and despite its safety profile, I could not rule out that my findings might be mediated through an unidentified P-407 action. To

exclude a P-407-dependent effect outside of its role in inducing hyperlipidemia, I wanted to determine if I could replicate my findings in another model of hyperlipidemia. The next chapter describes the phenotype of IC-mediated renal disease in a P-407-independent model of hyperlipidemia.

CHAPTER 6- EFFECTS OF DIET-INDUCED HYPERLIPIDEMIA IN LDLR-DEFICIENT MICE ON MONOCYTES AND RENAL DAMAGE

6.1. Introduction:

The evidence presented in the previous chapters on the effect of a hyper-TGRL environment on MO distribution and the demonstration of enhanced inflammatory organ damage under such conditions was intriguing and at the same time fascinating. The use of P-407 as the means of inducing the hyper-TGRL environment was, however, a potential concern. Despite its safety and lack of inflammatory side effects, the question remains as to whether the observed effects are due to the hyperlipidemic environment *per se* or are the product of, as yet, unknown properties of the compound itself. The ideal way around such a problem is to induce a similar hyperlipidemic environment using diet instead. Although HF diet models have been widely used in the field of atherosclerosis, they are tailored towards inducing a hypercholesterolemic rather than hypertriglyceridemic state. In rats, many investigators have tried inducing hypertriglyceridemia by feeding high sugar diet, i.e. high-fructose or high-glucose diets (Choi et al., 2014; Jeon et al., 2013). These models induce changes similar to those observed in the MS including change in glucose which may complicate the picture even more. It is thus difficult to induce pure hypertriglyceridemia by diet alone. In addition, mice are known to be resistant to atherosclerosis and a rise in the circulating lipid levels cannot be achieved by diet alone (Jawien et al., 2004). Most of the models used depend on diet alteration in genetically modified mice, e.g. apoE^{-/-} and Ldlr^{-/-} mice, in which the genetic defect accentuates the effect of diet on circulating lipid levels.

In view of difficulties surrounding the induction of dyslipidemic conditions in WT mice by diet, I elected to use the $Ldlr^{-/-}$ mouse strain to assess the validity of the results observed with P-407. These mice develop a diet-induced hyperlipidemia and, although the lipoprotein profile is characterized mainly by an elevation in LDL, HF diet can induce a moderate elevation in VLDL (Ishibashi et al., 1993), making it a plausible alternative to P-407.

This chapter describes the results obtained using the $Ldlr^{-/-}$ animals.

6.2. The effect of $Ldlr^{-/-}$ diet-induced hyperlipidemia on peripheral blood MOs and tissue MØs

To assess the effects of $Ldlr^{-/-}$ diet-induced hyperlipidemia on PB MOs and tissue MØs, ten $Ldlr^{-/-}$ mice on the B6 background were used. Before the start of any dietary intervention, the mice were bled for baseline lipid levels. They were then divided into two groups; those receiving the HF diet ($Ldlr^{-/-}$ HF) (n=5) and those receiving the control LF diet ($Ldlr^{-/-}$ LF) (n=5). The mice were allowed free access to food and water *ad libitum*. Animals were maintained on their specific diets for a period of 50 days after which they were culled and kidneys collected for PAS and CD68 staining. At the end point, blood was also collected for plasma lipid measurement and MO determination and kidneys were harvested and fixed in PLP for CD68 staining.

After 50 days of specified diet, $Ldlr^{-/-}$ mice receiving HF diet displayed higher levels of plasma TGs (545.9 ± 337.7 , mean \pm SD) when compared to their baseline levels (210.3 ± 31.8 mg/dl) and the levels observed in the $Ldlr^{-/-}$ LF group at the same time point (243.4 ± 116.6 mg/dl). However, the observed increase was not statistically significant (Fig-6.1A). Plasma CHOL levels, on the other hand, showed a significant increase from

a baseline value of 227.9 ± 29.7 and 257.1 ± 32.8 mg/dl to a final value of 474.8 ± 145.8 and 956.1 ± 109.4 mg/dl in the Ldlr^{-/-} LF and the Ldlr^{-/-} HF group, respectively (P=0.0286 and P<0.0001, paired t-test). Although the LF-fed Ldlr^{-/-} mice have also shown an increase in their plasma cholesterol levels, the increase was much higher in the Ldlr^{-/-} HF group (P=0.0004, unpaired t-test) (Fig-6.1B).

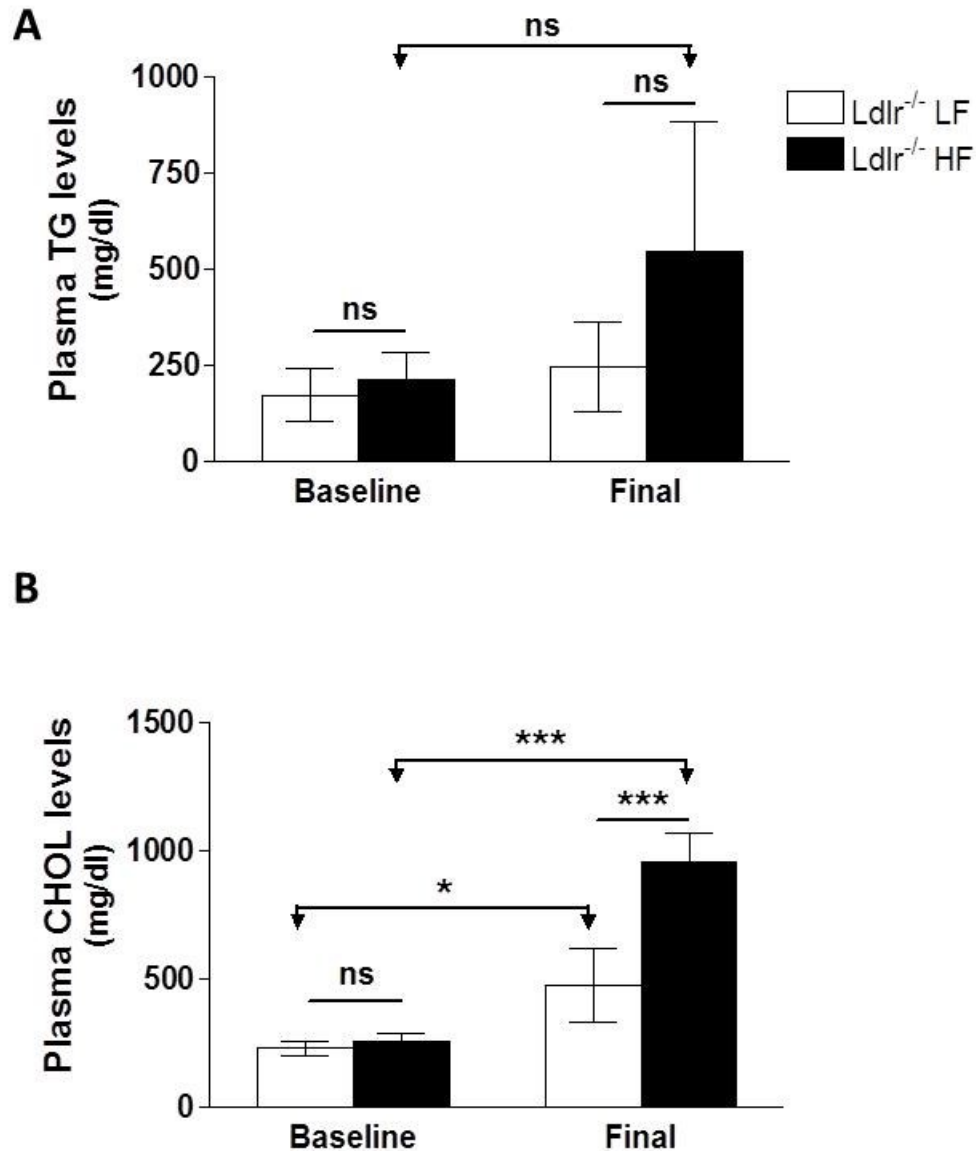


Figure 6.1. Changes in plasma lipid levels in $Ldlr^{-/-}$ mice in response to HF or LF diets.

Changes in non-fasting plasma TG (A) and CHOL levels (B) following 50 days of LF (n=5) vs HF (n=5) diet in $Ldlr^{-/-}$ mice. Data are presented as mean \pm SD. P value was calculated using paired t-test when comparing between baseline and final levels of the same group and unpaired t-test when comparing different groups at the same time point. *P<0.05, ***P<0.001, and ns=not significant.

6.2.1. Changes in peripheral blood MOs and tissue MØs in $Ldlr^{-/-}$ mice following diet modification

The consumption of modified diet for 50 days did not significantly alter the total MO count in the $Ldlr^{-/-}$ HF group when compared to their $Ldlr^{-/-}$ LF counterparts (Fig-6.2A). However, when looking at the distribution of the two MO subsets, there was a significant drop in the numbers of $Gr1^{low}$ ($Ly6C^{low}$) MOs in the $Ldlr^{-/-}$ HF group compared to the $Ldlr^{-/-}$ LF controls (Fig-6.2B). The number of the $Gr1^{high}$ ($Ly6C^{high}$) MOs, on the other hand, showed no difference between the two experimental groups (Fig-6.2B). The observed changes in the numbers of MO subsets affected their frequency within the monocytic pool dominated by the $Gr1^{high}$ ($Ly6C^{high}$) MOs at the expense of their $Gr1^{low}$ ($Ly6C^{low}$) counterparts (Fig-6.2C).

The kidneys of the $Ldlr^{-/-}$ mice were examined for the presence of MØs following 50 days of diet modification. Using CD68 staining as a MØ marker, the $Ldlr^{-/-}$ HF mice showed more accumulation of $CD68^{+}$ cells when compared to the $Ldlr^{-/-}$ LF group. However, the difference was not significant ($P=0.0768$, unpaired t-test) (Fig-6.3).

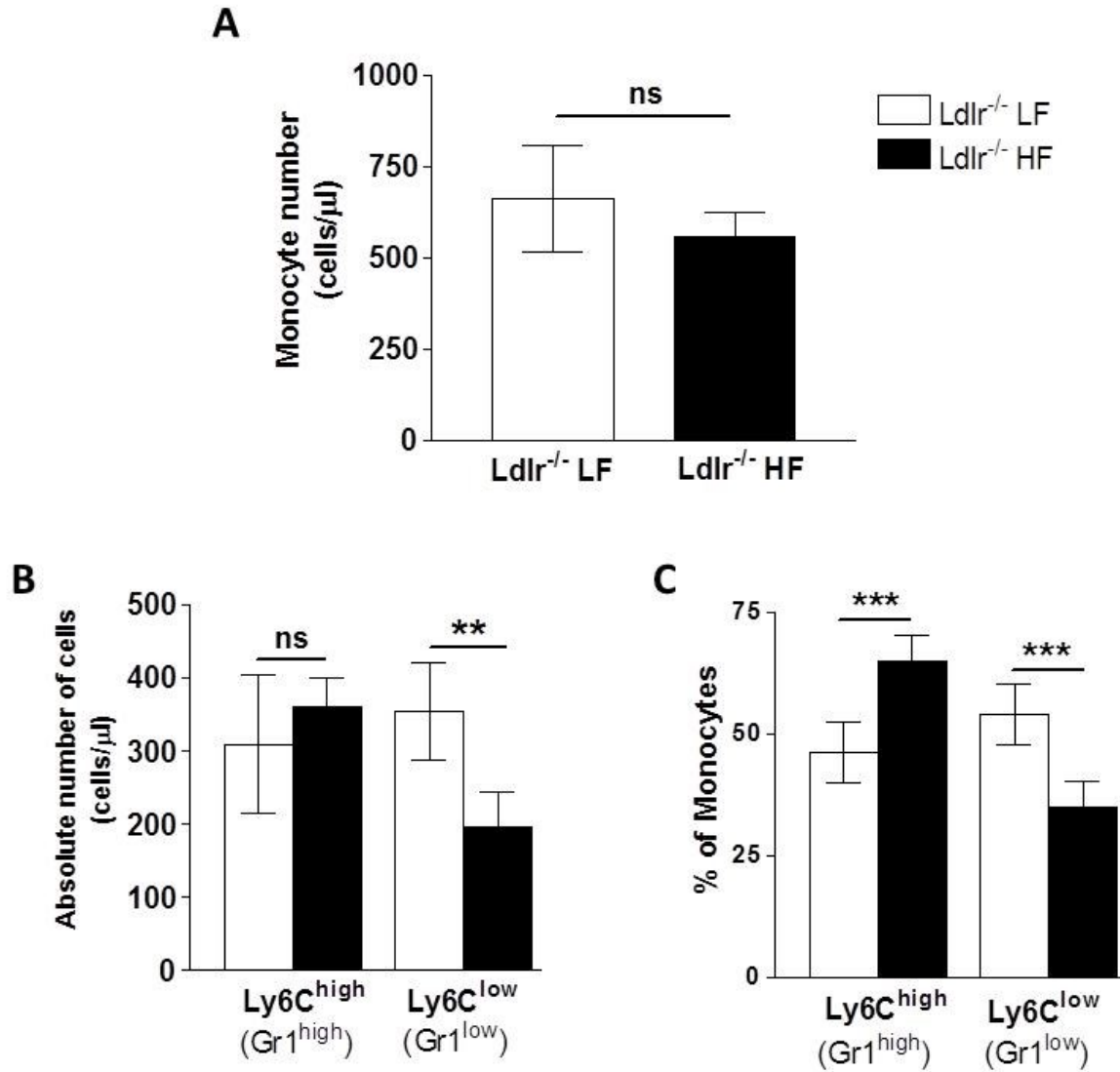


Figure 6.2. Numbers of peripheral blood MOs and their subsets in Ldlr^{-/-} mice fed either HF or LF diets.

Circulating blood MOs (cells/ μ l) (A) and MO subsets (B) in Ldlr^{-/-} mice after 50 days of feeding either HF (n=5) or LF (n=5) diet. (C) Percentage of Gr1^{high} and Gr1^{low} MOs within the total MO pool. Data are presented as mean \pm SD. P value calculated using unpaired t-test. **P<0.01, ***P<0.001 and ns= not significant. Data are representative of two different experiments.

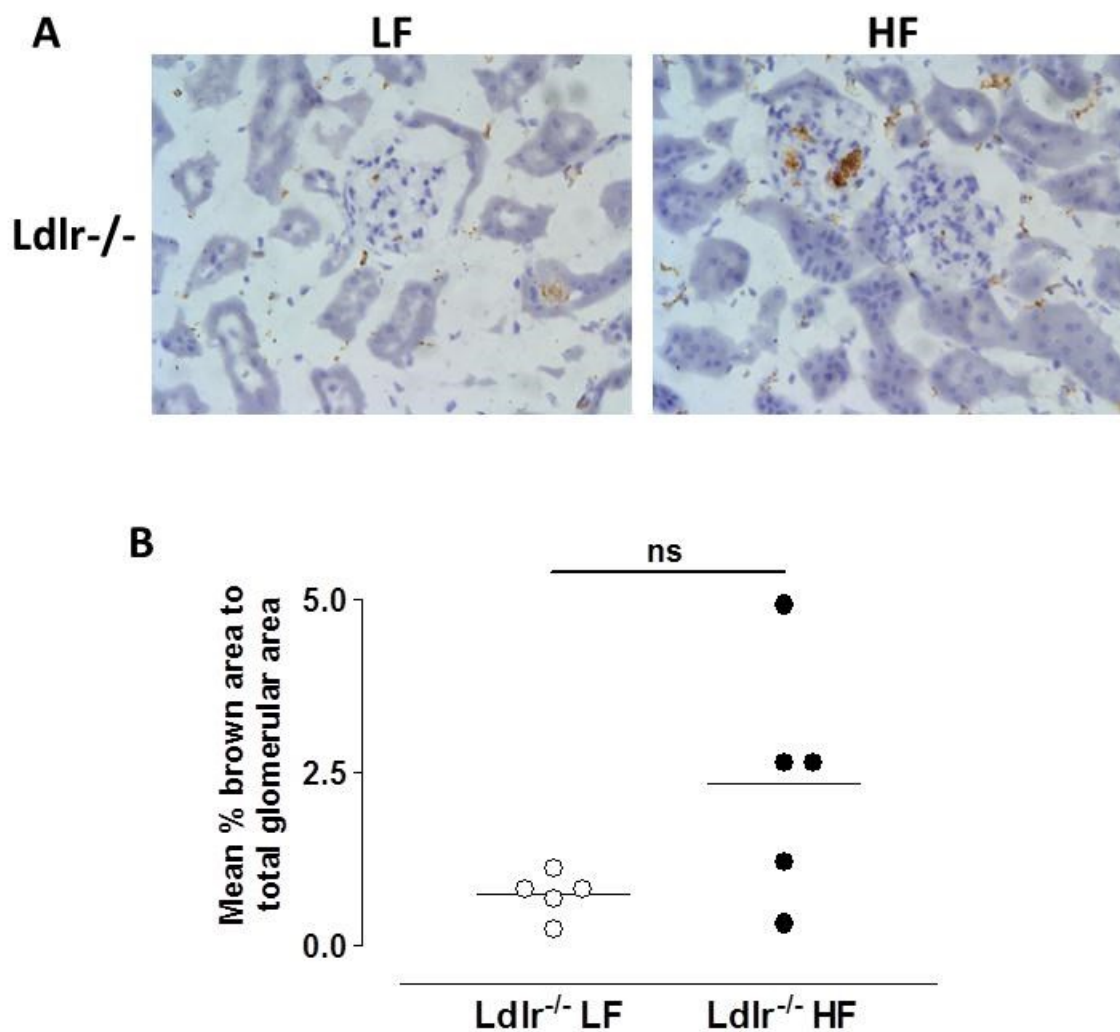


Figure 6.3. CD68-stained kidney tissue of Ldlr^{-/-} mice after 50 days of feeding either HF or LF diet.

(A) Representative sections of CD68-stained (brown colour) kidney sections of Ldlr^{-/-} mice fed either HF (n=5) or LF (n=5) diet for a period of 50 days, magnification x40. (B) Quantitative analysis of CD68⁺ cells (brown) staining in (A). Data are expressed as mean percentage of brown glomerular area over total glomerular for 15 glomeruli per section. Horizontal bars represent the mean. P value calculated using unpaired t-test. **P<0.01 and ***P<0.001.

These data indicated that induction of a dyslipidemic environment using the Ldlr^{-/-} diet-induced model produces changes in peripheral blood MOs that are comparable to those observed using the P-407 model. Histological examination of renal tissue revealed an accumulation of CD68⁺ cells in Ldlr^{-/-} mice fed the HF diet, although less striking than that observed in the P-407 model. Reassured by these data I then assessed whether the induction of a secondary inflammatory stimulus in the form of aNTN would lead to a similar enhancement of renal damage as that observed with the P-407-induced hyper-TGRL state.

6.3. The effect of $Ldlr^{-/-}$ diet-induced hyperlipidemia on renal damage following aNTN

To test whether the hyperlipidemic environment of the $Ldlr^{-/-}$ mice would result in enhanced renal damage following an insult, the aNTN experiment described in chapter-5 was repeated in these mice.

Twenty-one $Ldlr^{-/-}$ mice were divided into two groups; one receiving LF diet ($Ldlr^{-/-}$ LF, n=10), and one receiving HF diet ($Ldlr^{-/-}$ HF, n=11). In addition, a group of 20 B6 mice were similarly divided into two groups; one receiving the LF diet (B6 LF, n=10), and another receiving a HF diet (B6 HF, n=10). Access to food and water was allowed *ad libitum*. Ten days following the commencement of their specific diets, the mice were immunized i.p. with sheep IgG in CFA. Five days following immunization, a single i.v. injection of NTS was administered, a schematic representation of the experimental design is shown in (Fig-6.4A). The dose of NTS has been previously optimised to induce glomerular inflammation without thrombosis between days 10 to 14 in WT B6 mice. One mouse died in the $Ldlr^{-/-}$ LF group that was excluded from subsequent analysis.

Over the 2-week period following NTS injection, the mice were closely monitored for the development of signs of renal damage using serial urine dipstick analysis for hematuria and proteinuria. One day prior to sacrifice, they were placed in individual metabolic cages for 24 hours for collection of urine and sacrificed the following day. Over the experimental period, blood was collected at three different points; before starting the special diet (baseline, Day 0), before NTS injection (pre-NTS, Day 14), and at the end of the experiment (final, Day 28) (Fig-6.4A).

6.3.1. Lipid levels

At baseline, the plasma levels of both CHOL and TG were generally higher in the $Ldlr^{-/-}$ when compared to the B6 controls prior to any dietary intervention (Fig-6.4B & C). After commencing the specialized diets, the $Ldlr^{-/-}$ HF group showed a significant increase in their TG levels from a baseline of 110.7 ± 33.5 mg/dl (mean \pm SD) to a level of 450.7 ± 130.8 mg/dl and 298.8 ± 236.9 mg/dl at day 14 and 28, respectively (Fig-6.4B). The levels of TGs at day 14 were much higher in the $Ldlr^{-/-}$ HF group (450.7 ± 130.8 mg/dl) compared to those in the $Ldlr^{-/-}$ LF, B6 HF, and B6 LF groups (160.3 ± 52.5 , 75.1 ± 22.2 and 86.1 ± 10.4 mg/dl, respectively) (Fig-6.4B). A similar pattern was observed at day 28 with the $Ldlr^{-/-}$ HF group showing a TG level of 298.8 ± 236.9 mg/dl compared to a level of 114.8 ± 57.1 , 34.7 ± 11.8 and 41.3 ± 7.5 mg/dl in the $Ldlr^{-/-}$ LF, B6 HF, and B6 LF groups, respectively (Fig-6.4B)..

With regards to CHOL levels, again the $Ldlr^{-/-}$ mice displayed higher levels at baseline before any dietary intervention (Fig-6.4C). After starting the specialized diet, the $Ldlr^{-/-}$ fed HF diet showed significant increase in their CHOL levels from 279.2 ± 28.1 mg/dl to 873 ± 112.9 and 633.8 ± 431.8 mg/dl at day 14 and 28, respectively (Fig-6.4C). These levels were significantly higher than the corresponding CHOL levels in the $Ldlr^{-/-}$ LF, B6 HF, and B6 LF groups at day 14 (338.8 ± 94.9 , 145.3 ± 52.1 and 114.5 ± 13.6 mg/dl, respectively) and at day 28 (346.1 ± 158.9 , 164.5 ± 57.8 and 139 ± 27.2 mg/dl, respectively) (Fig-6.4C).

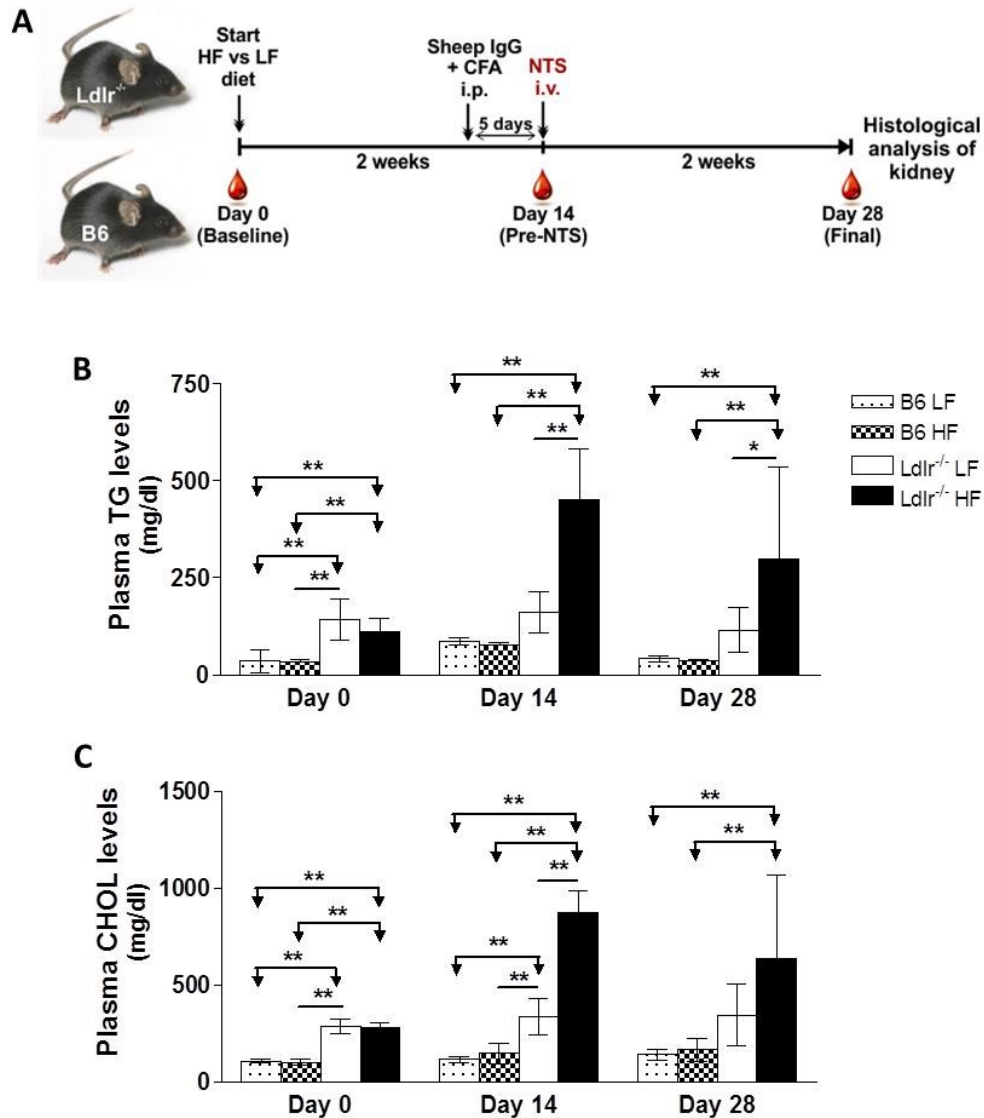


Figure 6.4. Experimental design and lipid levels of the aNTN experiment induced in *Ldlr*^{-/-} and B6 mice fed either HF or LF diets.

(A) Schematic representation of the *Ldlr*^{-/-} aNTN experiment. *Ldlr*^{-/-} and B6 mice were randomly allocated either HF or LF diet. Ten days later, the mice were immunized i.p. with sheep IgG in CFA, followed 5 days later with i.v. NTS injection. Following NTS injection, the mice were monitored for signs of renal damage for a period of 2 weeks after which they were culled (day 28). (B & C) Non-fasting plasma levels of TGs and CHOL respectively. n=10 for B6 LF group, n=10 for B6 HF group, n=9 for *Ldlr*^{-/-} LF group, and n=11 for *Ldlr*^{-/-} HF group. Data are presented as mean \pm SD. P value calculated using ANOVA followed by Bonferroni's Multiple Comparison Test. *P<0.05 and **P<0.01.

6.3.2. Renal functional parameters

Over the 2-week period following the injection of the NTS, the mice were closely monitored for the development of hematuria and proteinuria. At the end point, only a few mice in each group developed a hematuria of grade 2 or more with no significant differences between the experimental groups (Fig-6.5A). Looking at proteinuria (Fig-6.5B), the $Ldlr^{-/-}$ HF group developed more proteinuria when compared to their $Ldlr^{-/-}$ LF counterparts ($P < 0.05$, Kruskal-Wallis test followed by Dunn's Multiple Comparisons). However, the degree of proteinuria seen in the $Ldlr^{-/-}$ HF group was similar to that seen with B6 groups.

With respect to plasma urea levels, with the exception of the B6 HF group, all the other groups showed an elevation in their plasma urea levels following the induction of aNTN when compared to their corresponding baseline levels (Fig-6.5C). However, plasma urea levels remained below 20mmol/L so no animal developed renal failure.

6.3.3. Renal histology

At the end of the experiment, kidney tissue was collected for PAS as well as CD68 staining. PAS-sections were scored in a blinded fashion (Prof. H. T. Cook) as described in the material and method section. Despite the tendency of the $Ldlr^{-/-}$ HF group to show more glomerular cellularity, the overall difference between the groups was not statistically significant ($P=0.1074$, Kruskal-Wallis test). However, when the $Ldlr^{-/-}$ HF group was compared to their $Ldlr^{-/-}$ LF counterparts, the former displayed an enhanced glomerular cellularity ($P=0.0408$, Mann-Whitney test) (Fig-6.6).

On the other hand, CD68 staining revealed marked accumulation of $CD68^{+}$ cells in the $Ldlr^{-/-}$ HF mice when compared to all the other groups (Fig-6.7A). Despite the observed increase in CD68 staining in the $Ldlr^{-/-}$ HF, the difference was only significant when compared with the $Ldlr^{-/-}$ LF group ($P=0.0138$, unpaired t-test) whereas no statistically significant difference was detected in comparison to B6 HF or B6 LF groups (Fig-6.7B).

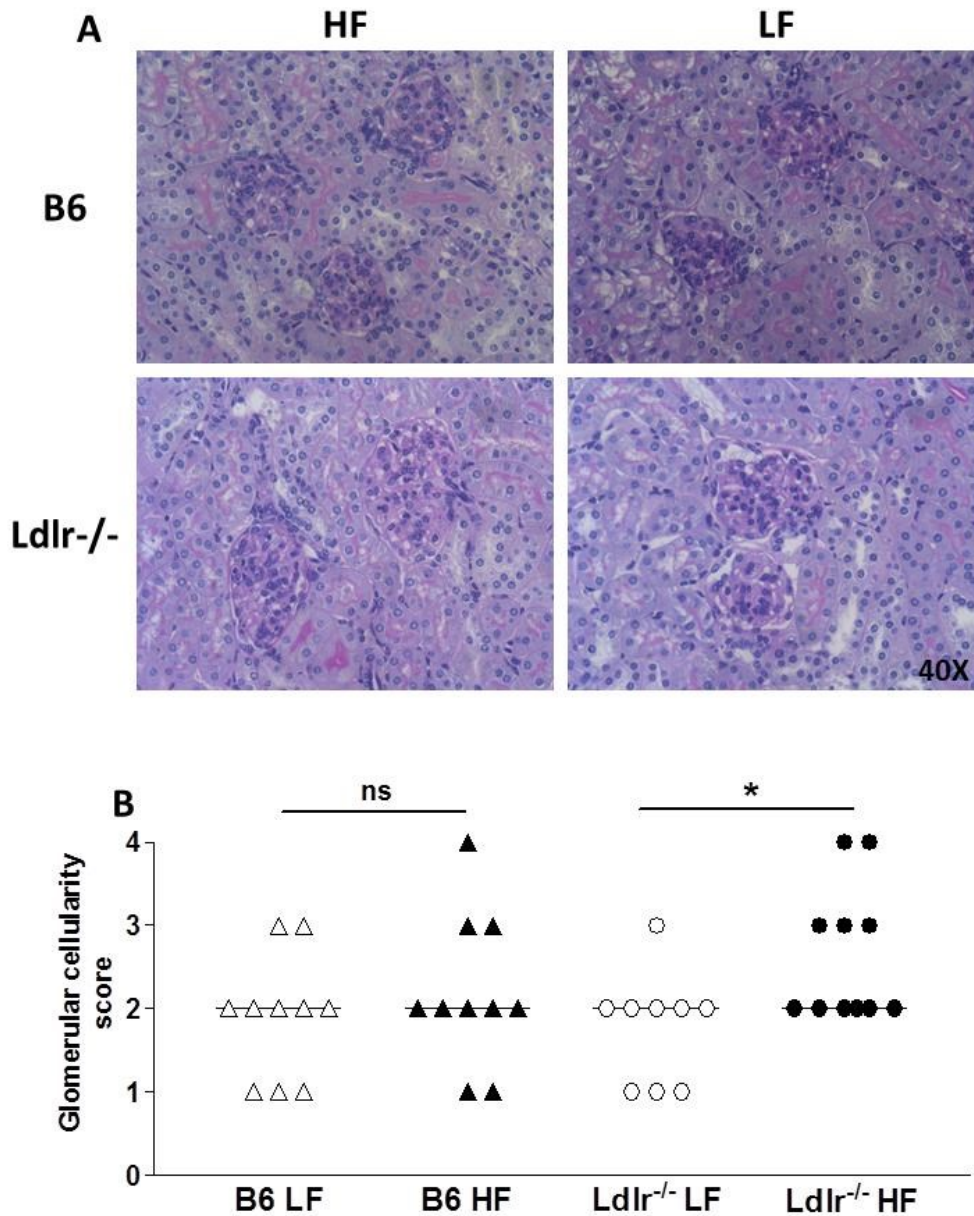


Figure 6.6. Glomerular cellularity score in Ldlr^{-/-} and B6 fed either HF or LF diets following the induction of the aNTN model.

(A) Representative PAS-stained kidney sections of Ldlr^{-/-} and B6 mice fed either HF or LF diets 2 weeks prior to the induction of aNTN (Fig-6.4A). Kidneys were collected 2-weeks following NTS injection (28 days on HF vs LF diet). (n=10 for B6 LF group, n=10 for B6 HF group, n=9 for Ldlr^{-/-} LF group, and n=11 for Ldlr^{-/-} HF group) (B) Blinded assessment of the glomerular cellularity score of PAS-stained kidney tissue shown in (A). Horizontal bars represent the median. P value calculated using Mann-Whitney test between HF and LF-fed mice in each strain. *P<0.05, and ns=not significant.

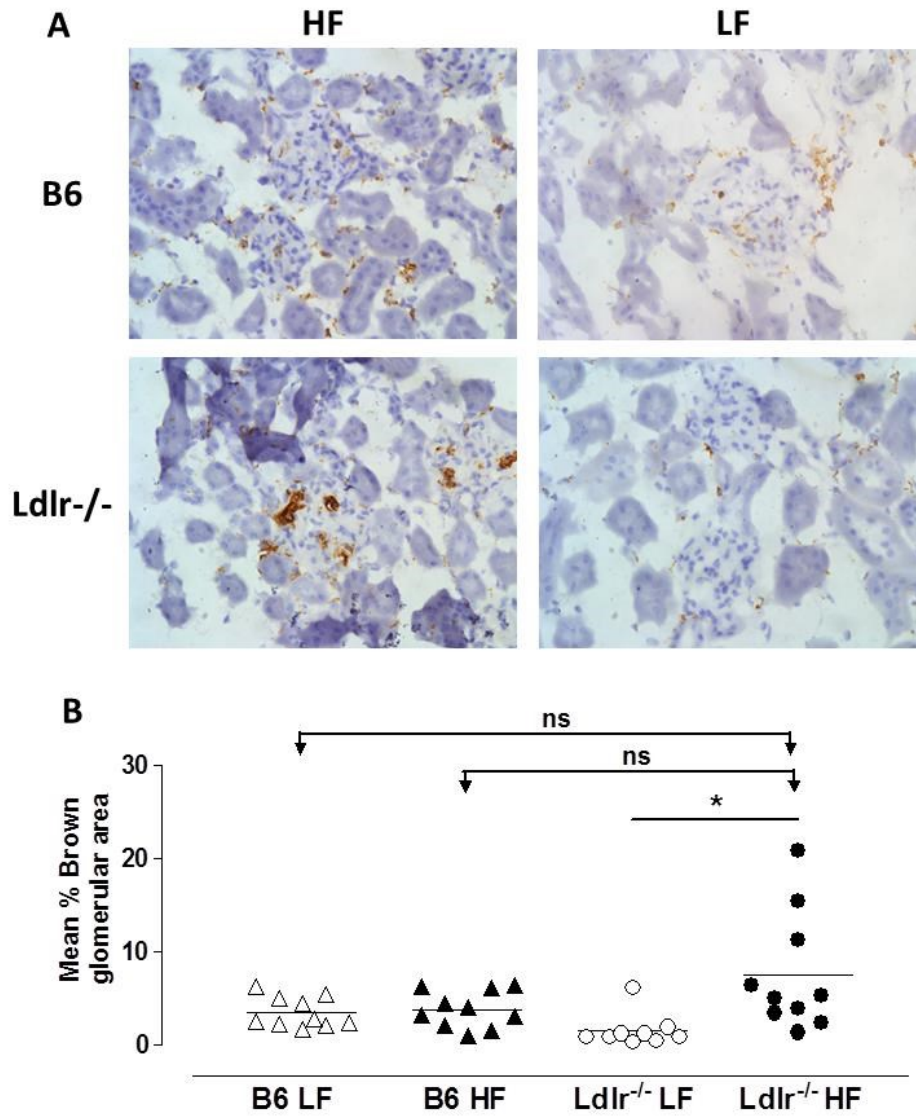


Figure 6.7. CD68-stained kidney tissue following the induction of aNTN in Ldlr^{-/-} and B6 mice fed either HF or LF diets.

(A) Representative CD68 staining of kidney tissue of Ldlr^{-/-} and B6 mice fed either HF or LF diet for 2 weeks prior to aNTN induction (Fig-6.4A). Kidneys were collected 2-weeks following NTS injection (28 days on HF vs LF diet). (n=10 for B6 LF group, n=10 for B6 HF group, n=9 for Ldlr^{-/-} LF group, and n=11 for Ldlr^{-/-} HF group) (B) Quantitative analysis of CD68⁺ cells (brown) staining in (A). CD68 data was not available for one mouse in the Ldlr^{-/-} HF group. Data are expressed as mean percentage of brown glomerular area over total glomerular for 20 glomeruli per section. Horizontal bars represent the mean. P value calculated using unpaired t-test comparing Ldlr^{-/-} HF with Ldlr^{-/-} LF, B6 HF, and B6 LF individually. *P<0.05 and ns=not significant.

As the renal phenotype of the $Ldlr^{-/-}$ HF mice was intriguing, I repeated the aNTN with a group of 16 $Ldlr^{-/-}$ that were divided into; those receiving HF diet ($Ldlr^{-/-}$ HF) (n=8) and those receiving LF diet ($Ldlr^{-/-}$ LF) (n=8). I also included a group of B6 mice that received HF diet only (B6 HF) (n=5). The experiment was conducted using the same experimental protocol described previously (Fig-6.4A).

At the baseline and before diet modification, $Ldlr^{-/-}$ mice had higher TG and CHOL levels when compared to B6 mice (Fig-6.8). Following diet modification, plasma TG and CHOL levels were significantly increased in the $Ldlr^{-/-}$ HF group reaching mean levels of (290.9 ± 76.7 and 893.6 ± 181.5 mg/dl), respectively by day 14 compared to mean levels of (97.4 ± 18.2 and 302.5 ± 28.9 mg/dl) in the $Ldlr^{-/-}$ LF and mean levels of (32.73 ± 3 and 91.69 ± 20.7 mg/dl) in the B6 HF group (Fig-6.8). In addition, plasma CHOL and TG levels were also significantly higher in the $Ldlr^{-/-}$ LF group when compared to B6 HF group at the same time point (day 14) (Fig-6.8). At the end point, plasma CHOL levels were significantly higher in the $Ldlr^{-/-}$ HF group (989.1 ± 328.5 mg/dl, mean \pm SD) when compared to mean levels of (541.4 ± 342.7 and 122.3 ± 27.4 mg/dl) in the $Ldlr^{-/-}$ LF and B6 HF groups, respectively (Fig-6.8B). Whereas plasma TG levels showed a marked drop in both $Ldlr^{-/-}$ groups from their levels at day 14 with great variability in the $Ldlr^{-/-}$ LF group (Fig-6.8A). However, the $Ldlr^{-/-}$ HF group maintained a higher TG level when compared to the B6 HF group (127.2 ± 41.1 vs 55.5 ± 17 mg/dl, mean \pm SD), respectively (Fig-6.8A).

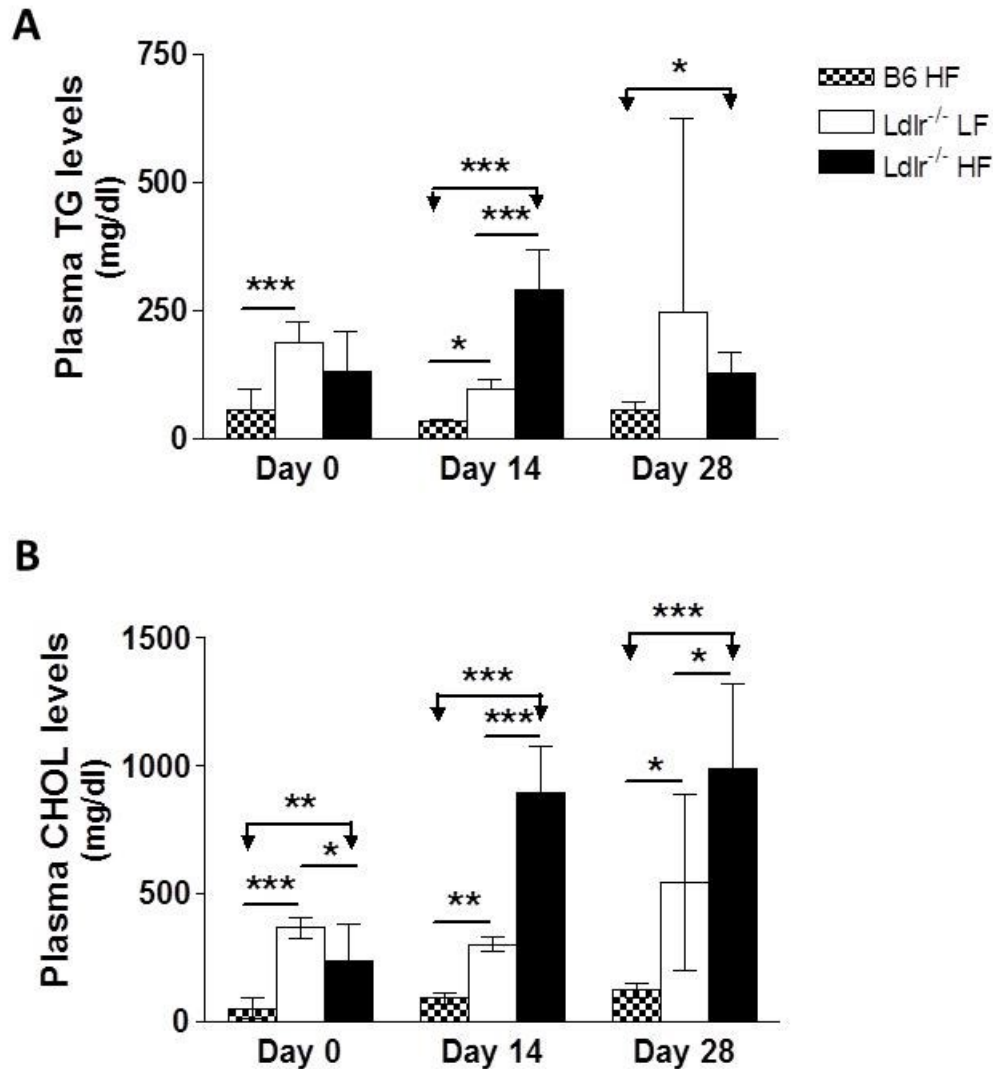


Figure 6.8. Plasma lipid levels in Ldlr^{-/-} mice fed either HF or LF diets over the course of the 2nd aNTN experiment.

Non-fasting plasma levels of TGs (A) and CHOL (B) in Ldlr^{-/-} fed either HF (n=8) or LF (n=8) diets and B6 fed HF diet (n=5) at several time points during the aNTN experiment; before starting the diet (day 0), 2 weeks after starting diet and before injecting NTS (day 14), and 2 weeks following NTS injection (day 28) (Fig-6.4A). Data are presented as mean \pm SD. P value calculated using ANOVA followed by Bonferroni's Multiple Comparison Test. *P<0.05, **P<0.01 and ***P<0.001.

At the end point, none of the groups developed significant hematuria when compared to the others (Fig-6.9A). With regards to proteinuria, although the $Ldlr^{-/-}$ mice had a tendency to show worse proteinuria at day 28, the differences were not significant when compared to the B6 HF group and there was no difference between the $Ldlr^{-/-}$ HF and LF groups (Fig-6.9B). All groups showed a significant increase in urea levels at the end point (day 28) when compared to their baseline levels (day 0) (Fig-6.9C). However, comparison of plasma urea levels at day 28 between the different groups revealed no difference (Fig-6.9C).

Histological examination of PAS-stained kidney tissue showed increased glomerular cellularity in the $Ldlr^{-/-}$ HF group, however, the difference was not significant ($P=0.0696$, Kruskal-Wallis test) (Fig-6.9D), whereas no difference was detected between the $Ldlr^{-/-}$ on the different diets (Fig-6.9D). CD68 staining showed more accumulation of $CD68^{+}$ cells in $Ldlr^{-/-}$ HF group, however, the difference was not statistically significant when compared to the other groups (Fig-6.10).

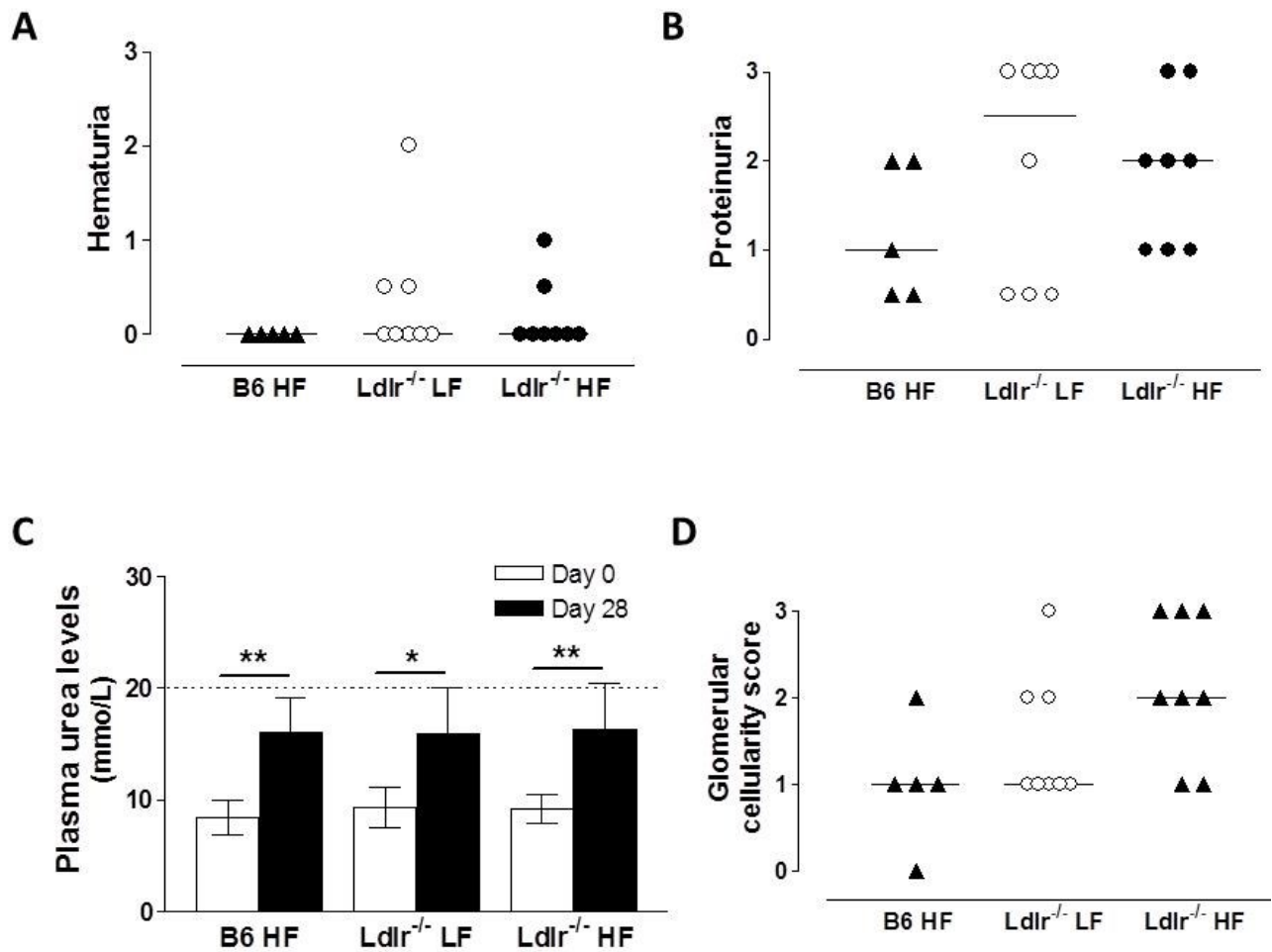


Figure 6.9. Renal functional parameters of HF and LF-fed Ldlr^{-/-} mice following the induction of the 2nd aNTN experiment.

Ldlr^{-/-} were placed either on HF (n=8) or LF (n=8) diet for 2 weeks prior to the i.v. injection of NTS. Following NTS injection, the mice were monitored for signs of renal damage for another 2 weeks (Fig-6.4A). A group of HF-fed B6 mice (n=5) were included as controls. (A & B) Show urinary hematuria and proteinuria, respectively, assessed by urine dipstick examination 2 weeks following NTS injection (day 28). For hematuria and proteinuria, horizontal bars represent the median. (C) Plasma urea levels measured at baseline (day 0) and at the end point (day 28) for each group. Urea level is presented as mean \pm SD. P value calculated using paired t-test comparing levels at day 0 and day 28 for each of the groups. (D) Glomerular cellularity score assessed for PAS-stained kidney tissue in a blinded fashion. Horizontal bars represent the median. P value calculated using Kruskal-Wallis test and was not significant. *P<0.05 and **P<0.01.

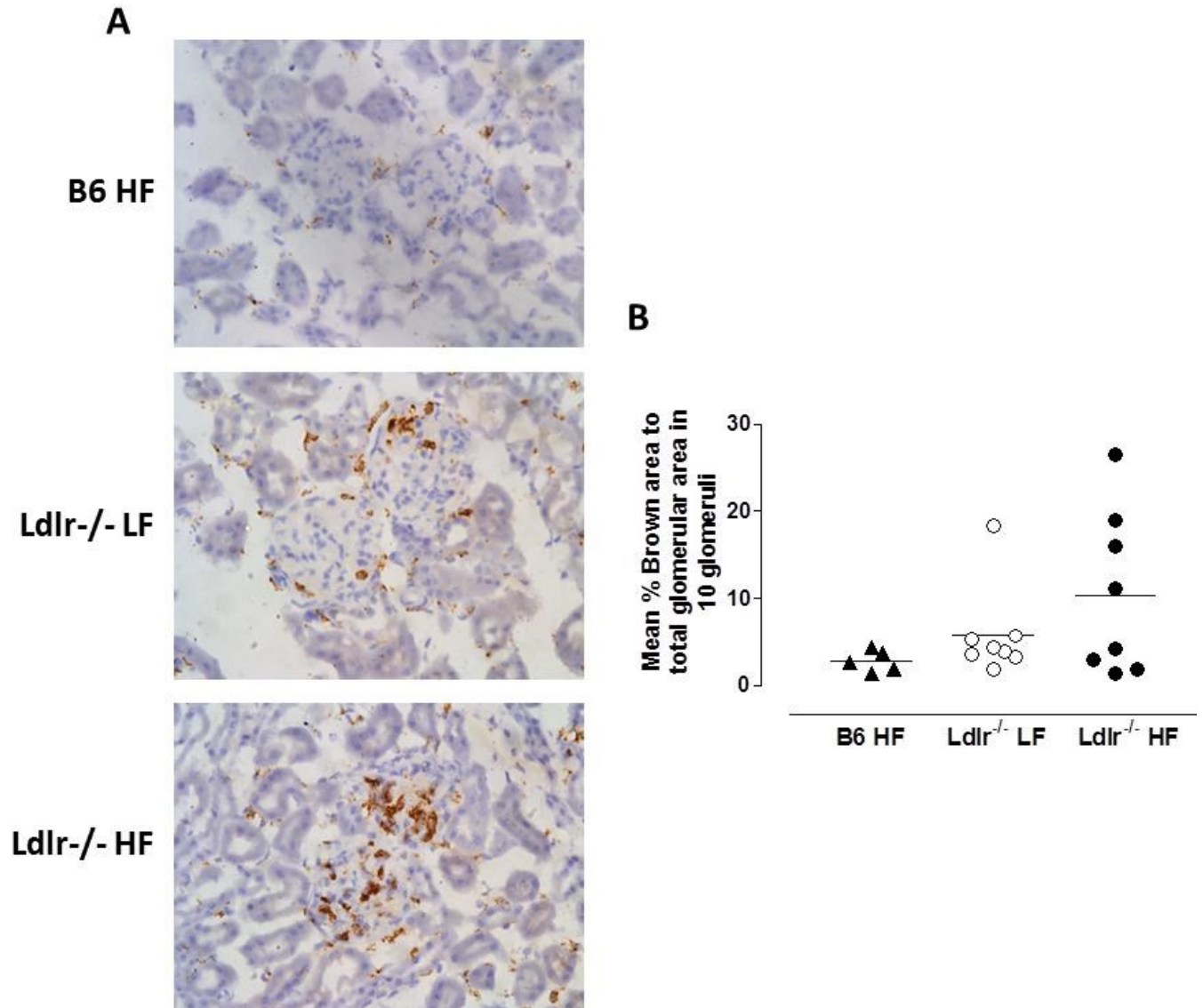


Figure 6.10. CD68 staining of kidney tissue from Ldlr^{-/-} mice fed either HF or LF diet following the induction of aNTN.

(A) Representative CD68 staining of kidney tissue of Ldlr^{-/-} fed HF (n=8) or LF (n=8) diets against B6 mice fed HF diet (n=5) for 2 weeks prior to NTS injection and for another 2 weeks thereafter. Kidneys were collected 2-weeks following NTS injection (i.e. after 28 days of HF vs LF feeding) (Fig-6.4A). (B) Quantitative analysis of CD68⁺ cells (brown) staining in (A). Data are expressed as mean percentage of brown glomerular area over total glomerular for 10 glomeruli per section. Horizontal bars represent the mean.

6.4. Conclusions

- The $Ldlr^{-/-}$ diet-induced hyperlipidemia brings about a drop in circulating $Gr1^{low}$ MOs along with enhanced $CD68^{+}$ MØs accumulation in the tissues of HF-fed $Ldlr^{-/-}$ mice in a manner similar, yet less intense, to that observed in the P-407-induced hyper-TGRL model.
- The changes observed following HF feeding in the $Ldlr^{-/-}$ model enhances IC-mediated renal damage in a manner analogous to that observed with P-407 induced hypertriglyceridemia, yet the renal injury is much milder.

6.5. Discussion

In this chapter, I corroborate the results obtained using the P-407 hyper-TGRL model by demonstrating the occurrence of similar, yet less intense changes in PB MOs and tissue MØs using the $Ldlr^{-/-}$ diet-induced hyperlipidemia model. HF-fed $Ldlr^{-/-}$ mice exhibit a drop in circulating numbers of $Gr1^{low}$ MOs associated with an accumulation of $CD68^{+}$ MØ in the kidneys of HF-fed $Ldlr^{-/-}$ mice (Figs-6.2 & 6.3). Moreover, these changes put the kidneys at greater risk for developing renal damage in the presence of an inflammatory stimulus as evident by the tendency for HF-fed $Ldlr^{-/-}$ mice to show higher glomerular cellularity and more $CD68^{+}$ MØ accumulation in the kidneys following IC-mediated renal injury which was significant in the first aNTN experiment (Figs-6.6 and 6.7, respectively) but failed to reach statistical significance in the second aNTN experiment (Fig-6.9, and 6.10).

The changes observed in PB MOs and tissue MØs using P-407-induced hypertriglyceridemia are fascinating, however, there has always been the pressing

question as to whether the observed effects are due to the hyperlipidemic environment *per se* or are the product of an, as yet, unknown properties of the compound itself. To address that, I elected to use the diet-induced $Ldlr^{-/-}$ model. Although this model is characterised largely by hypercholesterolemia and LDL accumulation, loss of the LDLR causes accumulation of VLDL remnant particles as well causing a rise in TGRL levels making it a plausible alternative.

HF feeding of $Ldlr^{-/-}$ mice causes a drop in the circulating levels of $Gr1^{low}$ MOs without altering total MO numbers or those of the $Gr1^{high}$ subset (Fig-6.2). These results are different from the reported monocytosis observed in HF-fed $Ldlr^{-/-}$ mice. The lack of monocytosis in the current experimental design may be attributed to the short duration of diet administration, i.e. 50 days compared to the usual 20 week diet duration necessary for the induction of atherosclerosis. In fact, one study has demonstrated monocytosis after 20 weeks of HF feeding which was not apparent at 10 weeks of HF feeding (Murphy et al., 2011). HF feeding is also associated with an increase in $CD68^{+}$ cells in kidney glomeruli (Fig-6.3), which is in line with a previous report showing $M\phi$ accumulation in the kidneys of rats fed high CHOL diet (Joles et al., 2000). Moreover, the changes brought about in the $Ldlr^{-/-}$ model by HF feeding put the kidneys at greater risk for developing renal damage in response to IC-mediated renal disease as evident by the increase in $CD68^{+}$ cell accumulation in the kidneys of HF-fed $Ldlr^{-/-}$ mice along with their enhanced glomerular cellularity which was significant in one experiment but failed to reach statistical significance in the other (Figs-6.6, 6.7, 6.9, and 6.10). These findings are comparable to what have been observed with the P-407-induced hyper-TGRL model, however, in view of the renal functional parameters, the phenotype is

much milder compared to the P-407 model. Given the equivalent CHOL levels between HF-fed $Ldlr^{-/-}$ mice and those of 10mg P-407-injected mice (Figs-6.1 & 5.1), it seems reasonable to attribute the milder phenotype observed in HF-fed $Ldlr^{-/-}$ mice to the lower levels of TGs and TGRLs induced in the $Ldlr^{-/-}$ model in comparison to the P-407 hyper-TGRL model.

Collectively, diet-induced hyperlipidemia of the $Ldlr^{-/-}$ model brings about changes in PB $Gr1^{low}$ MOs and tissue MØs that are, although less intense, analogous to those observed using the P-407 hyper-TGRL model, lending further proof to the validity of the results obtained using the P-407 model.

CHAPTER 7- DISCUSSION

In this study I report a peculiar effect for Hypertriglyceridemia and a hyper-TGRL environment on the behaviour of the Gr1^{low} MOs taking advantage of the non-inflammatory P-407 model. Under hyper-TGRL conditions, Gr1^{low} MOs show enhanced migration into surrounding tissues resulting in a progressive drop in their circulating levels along with striking tissue accumulation of CD68⁺ MØs. Moreover, the changes brought about by the hyper-TGRL environment put organs under greater risk of injury in the event of an inflammatory stimulus providing direct evidence for the role of hypertriglyceridemia in enhancing end organ damage.

Hypertriglyceridemia and a hyper-TGRL state pose a great threat to today's modern society. The growing epidemic of obesity and T2D promoted by sedentary lifestyle and fatty diet has contributed to the increased burden of hypertriglyceridemia and its associated hyper-TGRL state across the globe. The realisation that the pathogenic potential of hypertriglyceridemia may be operating on daily basis is quite alarming (Zilversmit, 1995). Studying the effects of hypertriglyceridemia and a hyper-TGRL state has been hampered by the complexity of the environment in which they commonly occur and lack of suitable animal models. Using the P-407 model, I was able to recapitulate the hyper-TGRL environment seen in secondary as well as primary hypertriglyceridemia in the absence of other confounding factors (Johnston and Waxman, 2008) and an overt inflammatory response (Fig-3.7). However, based on the results presented in Fig-3.7, it would be premature to draw any firm conclusions on the effect of P-407 treatment on cytokine/chemokine production and further investigations will be required.

The favourable location of Gr1^{low} MOs and their constant patrolling behaviour put them at the front line against fluctuating levels of TGRLs, yet the effect of such an environment on the behaviour of MOs in general and Gr1^{low} MOs in particular have been largely unexplored. Under P-407-induced hyper-TGRL conditions, Gr1^{low} MOs show enhanced margination at the endothelial interface with subsequent extravasation into the surrounding tissues accompanied by a striking accumulation of CD68⁺ MØs in the liver, heart and kidneys, which was apparent as early as 1 week following the induced hyper-TGRL state (Figs-4.14-4.17, 4.22 & 4.23). As tempting as it is to attribute tissue CD68⁺ accumulation to enhanced recruitment of Gr1^{low} MOs, several reports have demonstrated that steady state maintenance of tissue MØs is largely dependent on local self-renewal with a minimal contribution from circulating MOs (Hashimoto et al., 2013; Yona et al., 2013). The undetectable Ki-67 staining in the liver, heart and kidney where CD68⁺ are clearly present under hyper-TGRL conditions makes enhanced local MØ proliferation an unlikely explanation for the observed accumulation (Fig-4.18). This together with the clear demonstration of increased accumulation of adoptively transferred Gr1^{low} MOs, and not Gr1^{high} MOs, in the different tissues under hyper-TGRL conditions support Gr1^{low} MOs recruitment as a source for the accumulated CD68⁺ MØs (Figs-4.22 & 4.23). While Gr1^{low} MOs have been largely known for their intravascular patrolling function showing minimal extravasation (Auffray et al., 2007), few reports have demonstrated their ability to migrate under certain conditions where their recruitment was associated with an induction of an anti-inflammatory phenotype with tissue remodelling and reparative functions (Arnold et al., 2007; Nahrendorf et al., 2007). The ideal location of Gr1^{low} MOs and their close proximity to sites of TGRL

hydrolysis, along with their continuous monitoring of the endothelium suggest that the enhanced margination of these cells under hyper-TGRL conditions may be related to, yet unknown, homeostatic functions for Gr1^{low} MOs related to lipid scavenging at the endothelial surface. This is not surprising given the reported higher expression of genes encoding lipid-ligand activated nuclear factor PPAR γ and scavenger receptor CD36 involved in lipid metabolism and uptake, respectively on Gr1^{low}/Ly6C^{low} MOs (Ingersoll et al., 2010). Therefore their migration under the induced hyper-TGRL environment may reflect an extension to this housekeeping role as they clear tissues of their deposited lipids with minimal inflammatory response.

Notably, the changes in Gr1^{low} MOs under hyper-TGRL conditions occur in the absence of any substantial effects on Gr1^{high} MOs or total PB MOs, a condition quite different from that observed in atherosclerosis models. Diet-induced hypercholesterolemia was shown to cause progressive monocytosis largely driven by an increase in Gr1^{high}/Ly6C^{high} MOs which has been shown to invade the atherosclerotic plaque giving rise to lesional M ϕ s (Swirski et al., 2007). Contrary to the non-inflammatory hyper-TGRL environment induced by P-407, atherosclerosis is greatly recognised as a chronic inflammatory disease, more so is the apoE^{-/-} model (Lohmann et al., 2009), which may favour the expansion and recruitment of the Gr1^{high} subset known to respond avidly to such inflammatory cues with their subsequent accumulation into the atherosclerotic plaque.

Gr1^{low} MOs have been shown to derive from BM precursors as well as from the peripheral conversion of Gr1^{high} MOs (Fogg et al., 2006; Geissmann et al., 2010; Sunderkotter et al., 2004; Yona et al., 2013). However, defective BM synthesis of Gr1^{low}

MOs does not explain the drop in the circulating numbers of Gr1^{low} MOs since the numbers of their BM equivalents and their precursors, i.e. the MDPs, remain unchanged under hyper-TGRL conditions (Fig-4.10A-D). Neither is the drop justified by a delay in peripheral Gr1^{high} conversion since the circulating half-life of Gr1^{high} MOs under hyper-TGRL conditions (Fig-4.13) is similar to that observed in normolipidemic mice as well as that reported by Yona et al under steady state conditions (Yona et al., 2013). In the absence of defective Gr1^{low} MO generation along with their clear accumulation in tissues following their adoptive transfer (Fig-4.22 & 4.23), it is justifiable to attribute the drop in PB Gr1^{low} MO numbers to their loss from the circulation as they migrate into tissues under the influence of a hyper-TGRL environment.

While a hyper-TGRL environment has no effect on BM generation of the different MO subsets, the Ly6C^{high} monocytosis observed in the apoE^{-/-} model was associated with a generalised BM expansion of MOs in general and Ly6C^{high} MOs in particular which has been attributed to enhanced HSC proliferation (Murphy et al., 2011; Swirski et al., 2007). Apart from the inflammatory environment accompanying the apoE^{-/-} model, a direct role for apoE in controlling HSC proliferation has been suggested (Murphy et al., 2011), which may have had an additive effect on BM HSC proliferation in this model. Having said that, enhanced HSC proliferation is also seen under the current hyper-TGRL environment (Fig-4.12A). However, it appears to be directed towards the production of cell lines other than MOs as evident by the increase in MEPs (Fig-4.12B), the precursors of RBCs and platelets, and PMNs (Fig-4.6E). The increase in PMN production was evident by their higher PB numbers (Fig-4.6E) as well as the tendency for the CMP and GMP populations to be slightly higher under hyper-TGRL conditions

(Fig-4.12C). An increase in circulating PMNs and platelets have been reported in human subjects following pp lipemia, intriguingly, in these subjects the total MO count remained unchanged, however, MO subsets were not investigated (van Oostrom et al., 2004). These findings are intriguing, as cross talk between platelets and MOs is well-documented in the literature (May et al., 2007). Moreover, platelets are thought to support MO recruitment across the endothelium (May et al., 2007). In view of MEP expansion, it would be reasonable to speculate a role for platelets in Gr1^{low} MO recruitment under hyper-TGRL conditions, however, further investigations are needed to address this possibility.

The increase in Gr1^{low} MOs margination and recruitment under the influence of hyper-TGRL environment is accompanied by enhanced expression of CD11b on their surface, a change that is not observed on Gr1^{high} MOs (Fig-4.15). Enhanced CD11b expression on MOs has also been reported in human subjects following pp lipemia (van Oostrom et al., 2004). CD11b, along with CD18, forms part of Mac-1 complex, an integrin that mediates leukocyte adhesion by interacting with ICAM-1 and ICAM-2 on the endothelial surface (Ross, 2002; Sumagin et al., 2010). Although the crawling behaviour of Gr1^{low} MOs is largely dependent on LFA-1 (CD11a/CD18) under steady state conditions (Auffray et al., 2007), MOs were shown to switch from primarily LFA-1-mediated crawling to Mac-1-dependent crawling under conditions of endothelial stimulation (Sumagin et al., 2010). Postprandial lipoproteins were shown to enhance expression of ICAMs on human aortic endothelial cells (HAECs) (Marschang et al., 2006). Taken together, the enhanced expression of CD11b on Gr1^{low} MOs under conditions of hypertriglyceridemia may mediate their enhanced margination to the endothelial surface

and probably their migration, however, further investigations are needed to confirm the role of CD11b in the current model.

Hypertriglyceridemia and a hyper-TGRL environment complicate the course of various immunologic and non-immunologic diseases where ESRD is a common occurrence such as T2D, the MS as well as SLE (Carvalho et al., 2008; Grundy, 1998). Moreover, renal disease itself may bring about abnormalities in lipid and lipoprotein metabolism which may perpetuate the underlying renal damage (Keane, 2000; Ruan et al., 2009). Despite these associations, a clear role for a hyper-TGRL environment in enhancing renal injury has not been fully investigated. Importantly, my study demonstrates a role for a hyper-TGRL environment in enhancing the kidney's susceptibility for renal damage in the event of an inflammatory condition, evidenced by the earlier onset of hematuria and proteinuria, increased glomerular cellularity and the massive accumulation of CD68⁺ MØs in the kidneys following IC-mediated renal injury in the presence of a hyper-TGRL state (Fig-5.2 & 5.4). These results are in accordance with those reported by other investigators showing increased proteinuria and glomerular cellularity in guinea pigs, rats, and mice fed a high CHOL diet (Al-Shebeb et al., 1988; Joles et al., 2000; Kelley and Izui, 1983) with some documenting increased MØ accumulation in the kidneys as well in response to high CHOL feeding (Joles et al., 2000). Most of these studies, however, concentrated on the role of hypercholesterolemia on renal injury with only a few addressing the effects of hypertriglyceridemia such as the report of increased proteinuria and glomerular cellularity in hypertriglyceridemic obese Zucker rats (Kamanna and Kirschenbaum, 1993). Therefore, this study lends further support to the detrimental effects of hypertriglyceridemia and its associated atherogenic lipid profile in

aggravating inflammatory renal injury. These findings carry great implications in the clinical setting warranting more aggressive treatment of the hypertriglyceridemia accompanying diabetes, the MS, SLE and many other conditions where such an intervention may halt or delay the development of ESRD. This is especially true in view of the milder renal affliction observed under the moderate hyper-TGRL state induced using a lower P-407 dose indicating that renal injury may correlate with the levels of TGRLs in the circulation.

The findings obtained with the P-407 hyper-TGRL model were corroborated using another hyperlipidemia model namely, the diet-induced *Ldlr*^{-/-} model. Although the *Ldlr*^{-/-} model has been largely recognised to cause hypercholesterolemia with an increase in LDL, loss of the LDLR results in the accumulation of VLDL remnant particles leading to elevated levels of these TGRL particles as well making it a useful alternative (Teupser et al., 2003). HF feeding of the *Ldlr*^{-/-} model brings about a drop in circulating Gr1^{low} MOs and an increase CD68⁺ MØ in the kidneys, analogous to those observed with the P-407 model (Fig-6.2 & 6.3). Moreover, these changes occur without alteration in total MO or Gr1^{high} MO numbers as seen in the P-407 model. While monocytosis is a well-documented feature of the *Ldlr*^{-/-} model, it usually occurs following a longer period of HF diet feeding, >10 weeks, which is much longer than the period used in this study, i.e. 50 days (Murphy et al., 2011). More importantly, the changes in PB MOs and tissue MØs induced in HF-fed *Ldlr*^{-/-} mice subject kidneys to greater risk of renal damage in response to an inflammatory stimulus as evident by enhanced CD68⁺ cell infiltration and the higher glomerular cellularity observed in these mice (Figs-6.6, 6.7, 6.9, & 6.10). However, in view of the renal functional parameters the phenotype is much milder than

that observed in the P-407 hyper-TGRL model (Figs-6.5 & 6.9A-C vs Figs-5.2, 5.3 & 5.9A-C). Given the similarity in CHOL levels between the HF-fed *Ldlr*^{-/-} mice and 10mg P-407 injected mice (Figs-6.1B & 5.1C), the milder phenotype may reflect the lower circulating levels of TGRLs induced by the former in comparison to the latter model.

These observations draw our attention to the effects that a hyper-TGRL environment can have on the behaviour of Gr1^{low} MOs, enriching our understanding of the role played by these cells in homeostasis. Moreover, they underscore the detrimental role of such an environment on end-organ injury secondary to an inflammatory insult, posing a great threat to the well-being of the organism. This conclusion is based on congruent results obtained with two different models of hyperlipidemia. Despite the differences in the type and degree of hyperlipidemia induced between the two models, the consistency of the results adds validity to its implication and opens more doors for research in this area.

CHAPTER 8- CONCLUSION

This study underscores the detrimental effects of hypertriglyceridemia and a hyper-TGRL environment as it instigate changes in PB MOs and tissue MØs that pose a threat to the well-being of the organism especially in the presence of secondary inflammatory damage. The changes brought about by the hyper-TGRL environment can be summarised as follows;

- A hyper-TGRL environment has a great influence on the behaviour of Gr1^{low} MOs by promoting their margination at the endothelial interface and their extravasation into the tissues causing a drop in their circulating levels with enhanced accumulation of CD68⁺ MØs in various organs.
- The changes brought about by the hyper-TGRL environment prime kidneys for enhanced damage in the presence of an inflammatory condition.

While pp lipemia may be amenable to life style changes, the hyper-TGRL state accompanying other metabolic and inflammatory states may not be as responsive. This study emphasises the importance of early detection and aggressive treatment of hypertriglyceridemia occurring in conjunction with other conditions as it may carry a favourable impact on end organ damage especially the kidneys under such conditions.

CHAPTER 9- FUTURE WORK

- I would like to extend the observations to humans and investigate whether similar mechanisms operate under the influence of pp lipemia. This will be interesting and challenging. Despite the similarities reported between human and mouse MO subsets, they are not identical. Whereas the Gr1^{high} murine MO subset has been recognized for its inflammatory phenotype, it is the human CD16⁺ MOs, the equivalents to murine Gr1^{low} MO subset that share a similar pro-inflammatory profile. It would be interesting to see how pp lipemia would affect the different MO subsets in humans. After all, an innocent fatty indulgence once a week may not be innocent at all. If I am to pursue this, I would induce a pp hyper-TGRL state in human subjects through ingestion of a well-defined fatty meal and start by analysing PB MOs and their subset in response to this challenge. In addition, MOs can be isolated from the blood of subjects that have ingested the fatty meal and their behavior can be studied in vitro.
- I would also like to explore the role of CD11b in the migration of Gr1^{low} MOs under hyper-TGRL conditions. The role of CD11b can be investigated in animal models by inducing a P-407 hyper-TGRL environment in CD11b^{-/-} mice and analyse how loss of CD11b affects the observed phenotype. Delineating the role of CD11b under such circumstances may carry great therapeutic potential and help identify targeted therapies against such a phenomenon.

References

- Abe, T., Sasaki, M., Nakajima, H., Ogita, M., Naitou, H., Nagase, A., Taguchi, K., Miyazaki, S., 1990. Evaluation of pluronic F127 as a base for gradual release of anti-cancer drug. *Gan To Kagaku Ryoho. Cancer & Chemotherapy* 17, 1546-1550.
- Adiels, M., Olofsson, S.O., Taskinen, M.R., Boren, J., 2008. Overproduction of very low-density lipoproteins is the hallmark of the dyslipidemia in the metabolic syndrome. *Arteriosclerosis, thrombosis, and vascular biology* 28, 1225-1236.
- Akashi, K., Traver, D., Miyamoto, T., Weissman, I.L., 2000. A clonogenic common myeloid progenitor that gives rise to all myeloid lineages. *Nature* 404, 193-197.
- Akiyama, Y., Stevenson, G.W., Schlick, E., Matsushima, K., Miller, P.J., Stevenson, H.C., 1985. Differential ability of human monocyte subsets to release various cytokines. *Journal of leukocyte biology* 37, 519-530.
- Al-Shebeb, T., Frohlich, J., Magil, A.B., 1988. Glomerular disease in hypercholesterolemic guinea pigs: a pathogenic study. *Kidney International* 33, 498-507.
- Amano, H., Amano, E., Santiago-Raber, M.L., Moll, T., Martinez-Soria, E., Fossati-Jimack, L., Iwamoto, M., Rozzo, S.J., Kotzin, B.L., Izui, S., 2005. Selective expansion of a monocyte subset expressing the CD11c dendritic cell marker in the Yaa model of systemic lupus erythematosus. *Arthritis Rheum* 52, 2790-2798.
- Arnold, L., Henry, A., Poron, F., Baba-Amer, Y., van Rooijen, N., Plonquet, A., Gherardi, R.K., Chazaud, B., 2007. Inflammatory monocytes recruited after skeletal muscle injury switch into antiinflammatory macrophages to support myogenesis. *The Journal of experimental medicine* 204, 1057-1069.
- Assmann, G., Schulte, H., 1992. Relation of high-density lipoprotein cholesterol and triglycerides to incidence of atherosclerotic coronary artery disease (the PROCAM experience). *American Journal of Cardiology* 70, 733-737.
- Assmann, G., Tangelder, M.M., Lange, W.P.J., Schrijver, G., Koene, R.A.P., 1985. Anti-GBM nephritis in the mouse: severe proteinuria in the heterologous phase. *Virchows Arch* 406, 285-300.
- Auffray, C., Fogg, D., Garfa, M., Elain, G., Join-Lambert, O., Kayal, S., Sarnacki, S., Cumano, A., Lauvau, G., Geissmann, F., 2007. Monitoring of blood vessels and tissues by a population of monocytes with patrolling behavior. *Science* 317, 666-670.

Auffray, C., Sieweke, M.H., Geissmann, F., 2009. Blood monocytes: development, heterogeneity, and relationship with dendritic cells. *Annual review of immunology* 27, 669-692.

Belge, K.U., Dayyani, F., Horelt, A., Siedlar, M., Frankenberger, M., Frankenberger, B., Espevik, T., Ziegler-Heitbrock, L., 2002. The Proinflammatory CD14+CD16+DR++ Monocytes Are a Major Source of TNF. *The Journal of Immunology* 168, 3536-3542.

Berglund, L., Brunzell, J.D., Goldberg, A.C., Goldberg, I.J., Sacks, F., Murad, M.H., Stalenhoef, A.F., Endocrine, s., 2012. Evaluation and treatment of hypertriglyceridemia: an Endocrine Society clinical practice guideline. *The Journal of clinical endocrinology and metabolism* 97, 2969-2989.

Bertrand, J.Y., Chi, N.C., Santoso, B., Teng, S., Stainier, D.Y., Traver, D., 2010. Haematopoietic stem cells derive directly from aortic endothelium during development. *Nature* 464, 108-111.

Blonder, J.M., Baireid, L., Fulfs, J.C., Rosenthal, G.J., 1999. Dose-dependent hyperlipidemia in rabbits following administration of poloxamer 407 gel. *Life Sciences* 65, 261-266.

Bobulescu, I.A., 2010. Renal lipid metabolism and lipotoxicity. *Current Opinion in Nephrology and Hypertension* 19, 393-402.

Bogunovic, M., Ginhoux, F., Helft, J., Shang, L., Hashimoto, D., Greter, M., Liu, K., Jakubzick, C., Ingersoll, M.A., Leboeuf, M., Stanley, E.R., Nussenzweig, M., Lira, S.A., Randolph, G.J., Merad, M., 2009. Origin of the lamina propria dendritic cell network. *Immunity* 31, 513-525.

Boisset, J.C., van Cappellen, W., Andrieu-Soler, C., Galjart, N., Dzierzak, E., Robin, C., 2010. In vivo imaging of haematopoietic cells emerging from the mouse aortic endothelium. *Nature* 464, 116-120.

Borba, E.F., Carvalho, J.F., Bonfa, E., 2006. Mechanisms of dyslipoproteinemias in systemic lupus erythematosus. *Clinical & developmental immunology* 13, 203-208.

Boren, J., Matikainen, N., Adiels, M., Taskinen, M.R., 2014. Postprandial hypertriglyceridemia as a coronary risk factor. *Clinica chimica acta; international journal of clinical chemistry* 431, 131-142.

Boring, L., Gosling, J., Clearly, M., Charo, I., 1998. Decreased lesion formation in CCR2-/- mice reveals a role for chemokines in the initiation of atherosclerosis. *Nature* 394, 894-897.

Botham, K.M., Wheeler-Jones, C.P., 2013. Postprandial lipoproteins and the molecular regulation of vascular homeostasis. *Progress in lipid research* 52, 446-464.

Breslow, J.L., 1996. Mouse models of atherogenesis. *Science* 272, 685-688.

Bruce, I.N., 2005. 'Not only...but also': factors that contribute to accelerated atherosclerosis and premature coronary heart disease in systemic lupus erythematosus. *Rheumatology* 44, 1492-1502.

Carroll, L., Voisey, J., van Daal, A., 2004. Mouse models of obesity. *Clinics in dermatology* 22, 345-349.

Carvalho, J.F., Bonfa, E., Borba, E.F., 2008. Systemic lupus erythematosus and "lupus dyslipoproteinemia". *Autoimmunity Reviews* 7, 246-250.

Castelli, W.P., 1986. The triglyceride issue: a view from Framingham. *American Heart Journal* 112, 432-437.

Champe, P.C., Harvey, R.A., Ferrier, D.R., 2005. *Lippincott's Illustrated Reviews: Biochemistry*, 3rd ed. Lippincott Williams & Wilkins, United States of America.

Choi, H.N., Kang, M.J., Lee, S.J., Kim, J.I., 2014. Ameliorative effect of myricetin on insulin resistance in mice fed a high-fat, high-sucrose diet. *Nutrition research and practice* 8, 544-549.

Cochrane, C.G., Unanue, E., Dixon, F.J., 1965. A role of polymorphonuclear leukocytes and complement in nephrotoxic nephritis *The Journal of experimental medicine* 122, 99-116.

Coffee, C.J., 1998. *Metabolism*, 1st ed. Fence Creek Publishing, United States of America.

Cogger, V.C., Hilmer, S.N., Sullivan, D., Muller, M., Fraser, R., Le Couteur, D.G., 2006. Hyperlipidemia and surfactants: the liver sieve is a link. *Atherosclerosis* 189, 273-281.

Combadiere, C., Potteaux, S., Rodero, M., Simon, T., Pezard, A., Esposito, B., Merval, R., Proudfoot, A., Tedgui, A., Mallat, Z., 2008. Combined inhibition of CCL2, CX3CR1, and CCR5 abrogates Ly6C(hi) and Ly6C(lo) monocytosis and almost abolishes atherosclerosis in hypercholesterolemic mice. *Circulation* 117, 1649-1657.

Couser, W.G., Stilmant, M.M., Jermanovich, N.B., 1977. Complement-independent nephrotoxic nephritis in the guinea pig. *Kidney International* 11, 170-180.

Cros, J., Cagnard, N., Woollard, K., Patey, N., Zhang, S.Y., Senechal, B., Puel, A., Biswas, S.K., Moshous, D., Picard, C., Jais, J.P., D'Cruz, D., Casanova, J.L., Trouillet, C., Geissmann, F., 2010. Human CD14dim monocytes patrol and sense nucleic acids and viruses via TLR7 and TLR8 receptors. *Immunity* 33, 375-386.

Davies, L.C., Jenkins, S.J., Allen, J.E., Taylor, P.R., 2013. Tissue-resident macrophages. *Nature immunology* 14, 986-995.

Dixon, F.J., Feldman, J.D., Vazquez, J.J., 1961. Experimental glomerulonephritis: the pathogenesis of a laboratory model resembling the spectrum of human glomerulonephritis. *The Journal of experimental medicine* 113, 899-920.

Dumortier, G., Grossiord, J.L., Agnely, F., Chaumeil, J.C., 2006. A review of poloxamer 407 pharmaceutical and pharmacological characteristics. *Pharmaceutical research* 23, 2709-2728.

Fogg, D.K., Sibon, C., Miled, C., Jung, S., Aucouturier, P., Littman, D.R., Cumano, A., Geissmann, F., 2006. A clonogenic bone marrow progenitor specific for macrophages and dendritic cells. *Science* 311, 83-87.

Frankenberger, M., Sternsdorf, T., Pechumer, H., Pforte, A., Ziegler-Heitbrock, H.W., 1996. Differential cytokine expression in human blood monocyte subpopulations: A polymerase chain reaction analysis. *Blood* 87, 373-377.

Geissmann, F., Jung, S., Littman, D.R., 2003. Blood Monocytes Consist of Two Principal Subsets with Distinct Migratory Properties. *Immunity* 19, 71-82.

Geissmann, F., Manz, M.G., Jung, S., Sieweke, M.H., Merad, M., Ley, K., 2010. Development of monocytes, macrophages, and dendritic cells. *Science* 327, 656-661.

Getz, G.S., Reardon, C.A., 2006. Diet and murine atherosclerosis. *Arteriosclerosis, thrombosis, and vascular biology* 26, 242-249.

Getz, G.S., Reardon, C.A., 2012. Animal models of atherosclerosis. *Arteriosclerosis, thrombosis, and vascular biology* 32, 1104-1115.

Ginhoux, F., Greter, M., Leboeuf, M., Nandi, S., See, P., Gokhan, S., Mehler, M.F., Conway, S.J., Guan Ng, L., Stanley, E.R., Samokhvalov, I.M., Merad, M., 2010. Fate mapping analysis reveals that adult microglia derive from primitive macrophages. *Science* 330, 841-845.

Ginhoux, F., Jung, S., 2014. Monocytes and macrophages: developmental pathways and tissue homeostasis. *Nature reviews. Immunology* 14, 392-404.

Ginhoux, F., Merad, M., 2010. Ontogeny and homeostasis of Langerhans cells. *Immunology and cell biology* 88, 387-392.

Golbus, J., McCune, W.J., 1994. Lupus nephritis: classification, prognosis, immunopathogenesis, and treatment. *Rheumatic Diseases Clinics of North America* 20, 213-242.

Goldberg, I.J., Eckel, R.H., McPherson, R., 2011. Triglycerides and heart disease: still a hypothesis? *Arteriosclerosis, thrombosis, and vascular biology* 31, 1716-1725.

Gordon, S., Clarke, S., Greaves, D., Doyle, A., 1995. Molecular immunobiology of macrophages: recent progress. *Current opinion in immunology* 7, 24-33.

Gordon, S., Pluddemann, A., 2013. Tissue macrophage heterogeneity: issues and prospects. *Seminars in immunopathology* 35, 533-540.

Gower, R.M., Wu, H., Foster, G.A., Devaraj, S., Jialal, I., Ballantyne, C.M., Knowlton, A.A., Simon, S.I., 2011. CD11c/CD18 expression is upregulated on blood monocytes during hypertriglyceridemia and enhances adhesion to vascular cell adhesion molecule-1. *Arteriosclerosis, thrombosis, and vascular biology* 31, 160-166.

Grage-Griebenow, E., Flad, H.D., Ernst, M., 2001. Heterogeneity of human periphebral blood monocyte subsets. *Journal of leukocyte biology* 69, 11-20.

Grundey, S.M., 1998. Hypertriglyceridemia, atherogenic dyslipidemia, and the metabolic syndrome. *American Journal of Cardiology* 81, 18B-25B.

Hammer, D.K., Dixon, F.J., 1963. Experimental glomerulonephritis: II. Immunologic events in the pathogenesis of nephrotoxic serum nephritis in the rat. . *The Journal of experimental medicine* 117, 1019-1034.

Hanna, R.N., Carlin, L.M., Hubbeling, H.G., Nackiewicz, D., Green, A.M., Punt, J.A., Geissmann, F., Hedrick, C.C., 2011. The transcription factor NR4A1 (Nur77) controls bone marrow differentiation and the survival of Ly6C- monocytes. *Nature immunology* 12, 778-785.

Hashimoto, D., Chow, A., Noizat, C., Teo, P., Beasley, M.B., Leboeuf, M., Becker, C.D., See, P., Price, J., Lucas, D., Greter, M., Mortha, A., Boyer, S.W., Forsberg, E.C., Tanaka, M., van Rooijen, N., Garcia-Sastre, A., Stanley, E.R., Ginhoux, F., Frenette, P.S., Merad, M., 2013. Tissue-resident macrophages self-maintain locally throughout adult life with minimal contribution from circulating monocytes. *Immunity* 38, 792-804.

Hashimoto, D., Miller, J., Merad, M., 2011. Dendritic cell and macrophage heterogeneity in vivo. *Immunity* 35, 323-335.

Hassing, H.C., Surendran, R.P., Mooij, H.L., Stroes, E.S., Nieuwdorp, M., Dallinga-Thie, G.M., 2012. Pathophysiology of hypertriglyceridemia. *Biochimica et biophysica acta* 1821, 826-832.

Hebert, M.J., Takano, T., Papayianni, A., Rennke, H.G., Minto, A., Salant, D.J., Carroll, M.C., Brady, H.R., 1998. Acute nephrotoxic serum nephritis in complement knockout mice: relative roles of the classical and alternate pathways in neutrophil recruitment and proteinuria. *Nephrol Dial Transplant* 13, 2799-2803.

Hegele, R.A., Ginsberg, H.N., Chapman, M.J., Nordestgaard, B.G., Kuivenhoven, J.A., Aversa, M., Borén, J., Bruckert, E., Catapano, A.L., Descamps, O.S., Hovingh, G.K., Humphries, S.E., Kovanen, P.T., Masana, L., Pajukanta, P., Parhofer, K.G., Raal, F.J., Ray, K.K., Santos, R.D., Stalenhoef, A.F.H., Stroes, E., Taskinen, M.-R., Tybjærg-Hansen, A., Watts, G.F., Wiklund, O., 2014. The polygenic nature of hypertriglyceridaemia: implications for definition, diagnosis, and management. *The Lancet Diabetes & Endocrinology* 2, 655-666.

Hettinger, J., Richards, D.M., Hansson, J., Barra, M.M., Joschko, A.C., Krijgsveld, J., Feuerer, M., 2013. Origin of monocytes and macrophages in a committed progenitor. *Nature immunology* 14, 821-830.

Huang, X.R., Tipping, P.G., Apostolopoulos, J., Oettinger, C., D'Souza, M., Milton, G., 1997. Mechanisms of T cell-induced glomerular injury in anti-glomerular basement membrane (GBM) glomerulonephritis in rats. *Clin Exp Immunol* 109, 134-142.

Hung, C.C., Tsai, J.C., Kuo, H.T., Chang, J.M., Hwang, S.J., Chen, H.C., 2013. Dyslipoproteinemia and impairment of renal function in diabetic kidney disease: an analysis of animal studies, observational studies, and clinical trials. *The review of diabetic studies* : RDS 10, 110-120.

Ingersoll, M.A., Spanbroek, R., Lottaz, C., Gautier, E.L., Frankenberger, M., Hoffmann, R., Lang, R., Haniffa, M., Collin, M., Tacke, F., Habenicht, A.J., Ziegler-Heitbrock, L., Randolph, G.J., 2010. Comparison of gene expression profiles between human and mouse monocyte subsets. *Blood* 115, e10-19.

Ishibashi, S., Brown, M.S., Goldstein, J.L., Gerard, R.D., Hammer, R.E., Herz, J., 1993. Hypercholesterolemia in low density lipoprotein receptor knockout mice and its reversal by adenovirus-mediated gene delivery. *Journal of Clinical Investigation* 92, 883-893.

Iwasaki, H., Akashi, K., 2007a. Hematopoietic developmental pathways: on cellular basis. *Oncogene* 26, 6687-6696.

Iwasaki, H., Akashi, K., 2007b. Myeloid lineage commitment from the hematopoietic stem cell. *Immunity* 26, 726-740.

Jagannathan-Bogdan, M., Zon, L.I., 2013. Hematopoiesis. *Development* 140, 2463-2467.

Jawien, J., Nastalek, P., Korbut, R., 2004. Mouse models of experimental atherosclerosis. *Journal of Physiology and Pharmacology* 55, 503-517.

Jeon, Y.H., Kwak, M.S., Sung, M.H., Kim, S.H., Kim, M.H., Chang, M.J., 2013. High-molecular-weight poly-gamma-glutamate protects against hypertriglyceridemic effects of a high-fructose diet in rat. *Journal of microbiology and biotechnology* 23, 785-793.

Johansen, C.T., Hegele, R.A., 2011. Genetic bases of hypertriglyceridemic phenotypes. *Current opinion in lipidology* 22, 247-253.

Johnston, T.P., 2004. The P-407-induced murine model of dose-controlled hyperlipidemia and atherosclerosis. *Journal of Cardiovascular Pharmacology* 43, 595-606.

Johnston, T.P., 2010. Poloxamer 407 as a general lipase inhibitor: its implications in lipid metabolism and atheroma formation in C57BL/6 mice. *Journal of Pharmacy and Pharmacology* 62, 1807-1812.

Johnston, T.P., Baker, J., Jamal, A., Hall, D., Emeson, E.E., Palmer, W.K., 1999. Potential downregulation of HMG-CoA reductase after prolonged administration of P-407 in C57BL/6 mice. *Journal of Cardiovascular Pharmacology* 34, 831-842.

Johnston, T.P., Baker, J.C., Hall, D., Jamal, S., Palmer, W.K., Emeson, E.E., 2000. Regression of poloxamer 407-induced atherosclerotic lesions in C57BL/6 mice using atorvastatin. *Atherosclerosis* 149, 303-313.

Johnston, T.P., Beris, H., Wout, Z.G., Kennedy, J.L., 1993. Effects on splenic, hepatic, hematological, and growth parameters following high-dose poloxamer 407 administration to rats. *International Journal of Pharmaceutics* 100, 279-284.

Johnston, T.P., Li, Y., Jamal, A.S., Stechschulte, D.J., Dileepan, K.N., 2003. Poloxamer 407-induced atherosclerosis in mice appears to be due to lipid derangements and not due to its direct effects on endothelial cells and macrophages. *Mediators of inflammation* 12, 147-155.

Johnston, T.P., Palmer, W.K., 1993. Mechanism of poloxamer 407-induced hypertriglyceridemia in the rat. *Biochemical Pharmacology* 46, 1037-1042.

Johnston, T.P., Palmer, W.K., 1997. Effect of poloxamer 407 on the activity of microsomal 3-hydroxy-3-methylglutaryl CoA reductase in rats. *Journal of Cardiovascular Pharmacology* 29, 580-585.

Johnston, T.P., Waxman, D.J., 2008. Circulating free fatty acids are increased independently of PPARgamma activity after administration of poloxamer 407 to mice. *Can J Physiol Pharmacol* 86, 643-649.

Joles, J.A., Kunter, U., Janssen, U., Kriz, W., Rabelink, T.J., Koomans, H.A., Floege, J., 2000. Early mechanisms of renal injury in hypercholesterolemic or hypertriglyceridemic rats. *Journal of the American Society of Nephrology* 11, 669-683.

Jung, S., Aliberti, J., Graemmel, P., Sunshine, M.J., Kreutzberg, G.W., Sher, A., Littman, D.R., 2000. Analysis of fractalkine receptor CX₃CR1 function by targeted deletion and green fluorescent protein reporter gene insertion. *Molecular and Cellular Biology* 20, 4106-4114.

Kamanna, V.S., Kirschenbaum, M.A., 1993. Association between very low density lipoproteins and glomerular injury in obese Zucker rats. *American Journal of Nephrology* 13, 53-58.

Kannel, W.B., Vasan, R.S., 2009. Triglycerides as vascular risk factors: new epidemiologic insights. *Current opinion in cardiology* 24, 345-350.

Karpe, F., 1999. Postprandial lipoprotein metabolism and atherosclerosis. *Journal of Internal Medicine* 246, 341-355.

Keane, W., 2000. The role of lipids in renal disease: future challenges. *Kidney International* 57, S27-S31.

Kelley, V.E., Izui, S., 1983. Enriched lipid diet accelerates lupus nephritis in NZBxW mice. *American Journal of Pathology* 111, 288-297.

Kennedy, A.J., Ellacott, K.L., King, V.L., Hasty, A.H., 2010. Mouse models of the metabolic syndrome. *Disease models & mechanisms* 3, 156-166.

Kissa, K., Herbomel, P., 2010. Blood stem cells emerge from aortic endothelium by a novel type of cell transition. *Nature* 464, 112-115.

Kondo, M., Weissman, I.L., Akashi, K., 1997. Identification of clonogenic common lymphoid progenitors in mouse bone marrow. *Cell* 91, 661-672.

Korolenko, T.A., Tuzikov, F.V., Johnston, T.P., Tuzikova, N.A., Kisarova, Y.A., Zhanaeva, S.Y., Alexeenko, T.V., Zhukova, N.A., Brak, I.V., Spiridonov, V.K., Filjushina, E.E., Cherkanova, M.S., Monoszon, A.A., 2012. The influence of repeated administration of poloxamer 407 on serum lipoproteins and protease activity in mouse liver and heart. *Canadian Journal of Physiology and Pharmacology* 90, 1456-1468.

Krauss, R.M., 1998. Atherogenicity of triglyceride-rich lipoproteins. *American Journal of Cardiology* 81, 13B-17B.

Lamarche, B., Uffelman, K.D., Carpentier, A., Cohn, J.S., Steiner, G., Barrett, P.H., Lewis, G.F., 1999. Triglyceride enrichment of HDL enhances in vivo metabolic clearance of HDL apo A-I in healthy men. *J Clin Invest* 103, 1191-1199.

Lange, K., Slobody, L., Graige, F., Ogur, G., Oberman, J., LoCasto, F., 1951. Serum complement in acute glomerulonephritis and the nephrotic syndrome. *Pediatrics* 8, 814-820.

Leon, C., Wasan, K.M., Sachs-Barrable, K., Johnston, T.P., 2006. Acute P-407 administration to mice causes hypercholesterolemia by inducing cholesterolgenesis and down-regulating low-density lipoprotein receptor expression. *Pharmaceutical research* 23, 1597-1607.

Lewis, M.J., Malik, T.H., Fossati-Jimack, L., Carassiti, D., Cook, H.T., Haskard, D.O., Botto, M., 2012. Distinct roles for complement in glomerulonephritis and atherosclerosis revealed in mice with a combination of lupus and hyperlipidemia. *Arthritis Rheum* 64, 2707-2718.

Li, C., Palmer, W.K., Johnston, T.P., 1996. Disposition of poloxamer 407 in rats following a single intraperitoneal injection assessed using a simplified colorimetric assay. *Journal of Pharmaceutical and Biomedical Analysis* 14, 659-665.

Li, Y., He, P.-P., Zhang, D.-W., Zheng, X.-L., Cayabyab, F.S., Yin, W.-D., Tang, C.-K., 2014. Lipoprotein lipase: From gene to atherosclerosis. *Atherosclerosis* 237, 597-608.

Liao, F., Andalibi, A., deBeer, F.C., Fogelman, A.M., Lusis, A.J., 1993. Genetic control of inflammatory gene induction and NF-kappa B-like transcription factor activation in response to an atherogenic diet in mice. *J Clin Invest* 91, 2572-2579.

Lindberg, L.H., Rosenberg, L.T., 1968. Nephrotoxic serum nephritis in mice with a genetic deficiency in complement. *Journal of immunology* 100, 34-38.

Loginova, V.M., Tuzikov, F.V., Tuzikova, N.A., Korolenko, T.A., 2013. Comparative characteristics of lipemia models induced by injections of triton WR-1339 and poloxamer 407 in mice. *Bulletin of Experimental Biology and Medicine* 155, 284-287.

Lohmann, C., Schafer, N., von Lukowicz, T., Sokrates Stein, M.A., Boren, J., Rutti, S., Wahli, W., Donath, M.Y., Luscher, T.F., Matter, C.M., 2009. Atherosclerotic mice exhibit systemic inflammation in periaortic and visceral adipose tissue, liver, and pancreatic islets. *Atherosclerosis* 207, 360-367.

Lu, D., Willard, D., Patel, I.R., Kadwell, S., Overton, L., Kost, T., Luther, M., Chen, W., Woychik, R.P., Wilkison, W.O., Cone, R.D., 1994. Agouti protein is an antagonist of the melanocyte-stimulating-hormone receptor. *Nature* 371, 799-802.

Manzi, S., Meilahn, E.N., Rairie, J.E., Conte, C.G., Medsger, T.A., Jansen-McWilliams, L., D'Agostino, R.B., Kuller, L.H., 1997. Age-specific incidence rates of myocardial infarction and angina in women with systemic lupus erythematosus: comparison with the Framingham study. *American Journal of Epidemiology* 145, 408-415.

Marschang, P., Gotsch, C., Kirchmair, R., Kaser, S., Kahler, C.M., Patsch, J.R., 2006. Postprandial, but not postabsorptive low-density lipoproteins increase the expression of intercellular adhesion molecule-1 in human aortic endothelial cells. *Atherosclerosis* 186, 101-106.

Masugi, M., Sato, Y., 1934. Über die allergische Gewebsreaktion der Niere. *Virchows Archiv für pathologische Anatomie und Physiologie und für klinische Medizin* 293, 615-664.

May, A.E., Langer, H., Seizer, P., Bigalke, B., Lindemann, S., Gawaz, M., 2007. Platelet-leukocyte interactions in inflammation and atherothrombosis. *Seminars in thrombosis and hemostasis* 33, 123-127.

Merkel, M., Velez-Carrasco, W., Hudgins, L.C., Breslow, J.L., 2001. Compared with saturated fatty acids, dietary monounsaturated fatty acids and carbohydrates increase atherosclerosis and VLDL cholesterol levels in LDL receptor-deficient, but not apolipoprotein E-deficient, mice. *Proceedings of the National Academy of Sciences of the United States of America* 98, 13294-13299.

Moore, K.J., Tabas, I., 2011. Macrophages in the pathogenesis of atherosclerosis. *Cell* 145, 341-355.

Mosser, D.M., Edwards, J.P., 2008. Exploring the full spectrum of macrophage activation. *Nature reviews. Immunology* 8, 958-969.

Murphy, A.J., Akhtari, M., Tolani, S., Pagler, T., Bijl, N., Kuo, C.L., Wang, M., Sanson, M., Abramowicz, S., Welch, C., Bochem, A.E., Kuivenhoven, J.A., Yvan-Charvet, L., Tall, A.R., 2011. ApoE regulates hematopoietic stem cell proliferation, monocytosis, and monocyte accumulation in atherosclerotic lesions in mice. *J Clin Invest* 121, 4138-4149.

Murray, R.K., Granner, D.K., Mayes, P.A., Rodwell, V.W., 2003. *Harper's Illustrated Biochemistry*, 26th ed. Lange Medical Books/McGraw-Hill, United States of America.

Nagai, H., Takizawa, T., Nishiyori, T., Koda, A., 1982. Experimental glomerulonephritis in mice as a model for immunopharmacological studies. *Japanese Journal of Pharmacology* 32, 1117-1124.

Nahrendorf, M., Swirski, F.K., Aikawa, E., Stangenberg, L., Wurdinger, T., Figueiredo, J.L., Libby, P., Weissleder, R., Pittet, M.J., 2007. The healing myocardium sequentially mobilizes two monocyte subsets with divergent and complementary functions. *The Journal of experimental medicine* 204, 3037-3047.

Naish, P.F., Thomson, N.M., Simpson, I.J., Peters, D.K., 1975. The role of polymorphonuclear leucocytes in the autologous phase of nephrotoxic nephritis *Clin Exp Immunol* 22, 102-111.

Nangaku, M., Couser, W.G., 2005. Mechanisms of immune-deposit formation and the mediation of immune renal injury. *Clinical and experimental nephrology* 9, 183-191.

Napolitano, M., Botham, K.M., Bravo, E., 2013. Postprandial human triglyceride-rich lipoproteins increase chemoattractant protein secretion in human macrophages. *Cytokine* 63, 18-26.

Ohashi, R., Mu, H., Wang, X., Yao, Q., Chen, C., 2005. Reverse cholesterol transport and cholesterol efflux in atherosclerosis. *QJM : monthly journal of the Association of Physicians* 98, 845-856.

Orkin, S.H., Zon, L.I., 2002. Hematopoiesis and stem cells: plasticity versus developmental heterogeneity. *Nature immunology* 3, 323-328.

Orkin, S.H., Zon, L.I., 2008. Hematopoiesis: an evolving paradigm for stem cell biology. *Cell* 132, 631-644.

Ossetrova, N.I., Condliffe, D.P., Ney, P.H., Krasnopolsky, K., Hieber, K.P., Rahman, A., Sandgren, D.J., 2014. Early-response biomarkers for assessment of radiation exposure in a mouse total-body irradiation model. *Health physics* 106, 772-786.

Otten, M.A., Groeneveld, T.W., Flierman, R., Rastaldi, M.P., Trouw, L.A., Faber-Krol, M.C., Visser, A., Essers, M.C., Claassens, J., Verbeek, J.S., van Kooten, C., Roos, A., Daha, M.R., 2009. Both complement and IgG fc receptors are required for development of attenuated antiglomerular basement membrane nephritis in mice. *Journal of immunology* 183, 3980-3988.

Palframan, R.T., Jung, S., Cheng, G., Weninger, W., Luo, Y., Dorf, M., Littman, D.R., Rollins, B.J., Zeerink, H., Rot, A., von Andrian, U.H., 2001. Inflammatory chemokine transport and presentation in HEV: a remote control mechanism for monocyte recruitment to lymph nodes in inflamed tissues. *The Journal of experimental medicine* 194, 1361-1373.

Palmer, W.K., Emeson, E.E., Johnston, T.P., 1997. The poloxamer 407-induced hyperlipidemic atherogenic animal model. *Medicine and Science in Sports and Exercise* 29, 1416-1421.

Palmer, W.K., Emeson, E.E., Johnston, T.P., 1998. Poloxamer 407-induced atherogenesis in the C57BL/6 mouse. *Atherosclerosis* 136, 115-123.

Passlick, B., Flieger, D., Ziegler-Heitbrock, H.W.L., 1989. Identification and characterization of a novel monocyte subpopulation in human blood. *Blood* 74, 2527-2534.

Patsch, J.R., Miesenbock, G., Hopferwieser, T., Muhlberger, V., Knapp, E., Dunn, J.K., Gotto, A.M., Patsch, W., 1992. Relation of triglyceride metabolism and coronary artery disease. Studies in the postprandial state. *Arteriosclerosis, thrombosis, and vascular biology* 12, 1336-1345.

Pickering, M.C., Cook, H.T., Warren, J., Bygrave, A.E., Moss, J., Walport, M.J., Botto, M., 2002. Uncontrolled C3 activation causes membranoproliferative glomerulonephritis in mice deficient in complement factor H. *Nature genetics* 31, 424-428.

Ramasamy, I., 2013. Recent advances in physiological lipoprotein metabolism. *Clinical chemistry and laboratory medicine : CCLM / FESCC*, 1-33.

Ribalta, J., Vallve, J.C., Girona, J., Masana, L., 2003. Apolipoprotein and apolipoprotein receptor genes, blood lipids and disease. *Current opinion in clinical nutrition and metabolic care* 6, 177-187.

Rieger, M.A., Schroeder, T., 2012. Hematopoiesis. *Cold Spring Harbor perspectives in biology* 4.

- Robbins, C.S., Hilgendorf, I., Weber, G.F., Theurl, I., Iwamoto, Y., Figueiredo, J.L., Gorbato, R., Sukhova, G.K., Gerhardt, L.M., Smyth, D., Zavitz, C.C., Shikatani, E.A., Parsons, M., van Rooijen, N., Lin, H.Y., Husain, M., Libby, P., Nahrendorf, M., Weissleder, R., Swirski, F.K., 2013. Local proliferation dominates lesional macrophage accumulation in atherosclerosis. *Nature medicine* 19, 1166-1172.
- Robson, M.G., Cook, H.T., Botto, M., Taylor, P.R., Busso, N., Salvi, R., Pusey, C.D., Walport, M.J., Davies, K.A., 2001. Accelerated Nephrotoxic Nephritis Is Exacerbated in C1q-Deficient Mice. *The Journal of Immunology* 166, 6820-6828.
- Robson, M.G., Cook, H.T., Pusey, C.D., Walport, M.J., Davies, K.A., 2003. Antibody-mediated glomerulonephritis in mice: the role of endotoxin, complement and genetic background. *Clin Exp Immunol* 133, 326-333.
- Rosenson, R.S., Brewer, H.B., Jr., Davidson, W.S., Fayad, Z.A., Fuster, V., Goldstein, J., Hellerstein, M., Jiang, X.C., Phillips, M.C., Rader, D.J., Remaley, A.T., Rothblat, G.H., Tall, A.R., Yvan-Charvet, L., 2012. Cholesterol efflux and atheroprotection: advancing the concept of reverse cholesterol transport. *Circulation* 125, 1905-1919.
- Ross, G.D., 2002. Role of the lectin domain of Mac-1/CR3 (CD11b/CD18) in regulating intercellular adhesion. *Immunologic research* 25, 219-227.
- Ruan, X.Z., Varghese, Z., Moorhead, J.F., 2009. An update on the lipid nephrotoxicity hypothesis. *Nature reviews. Nephrology* 5, 713-721.
- Rubin, L.A., Urowitz, M.B., Gladman, D.D., 1985. Mortality in systemic lupus erythematosus: the bimodal pattern revisited. *Quarterly Journal of Medicine* 216, 87-98.
- Sarwar, N., Danesh, J., Eiriksdottir, G., Sigurdsson, G., Wareham, N., Bingham, S., Boekholdt, S.M., Khaw, K.T., Gudnason, V., 2007. Triglycerides and the risk of coronary heart disease: 10,158 incident cases among 262,525 participants in 29 Western prospective studies. *Circulation* 115, 450-458.
- Savage, D.B., 2009. Mouse models of inherited lipodystrophy. *Disease models & mechanisms* 2, 554-562.
- Schmolka, I.R., 1994. Physical basis for poloxamer interactions. *Annals of the New York Academy of Science* 720, 92-97.
- Schreiner, G.F., Cotran, R.S., Pardo, V., Unanue, E., 1978. A mononuclear cell component in experimental immunological glomerulonephritis *The Journal of experimental medicine* 147, 369-383.

Schrijver, G., Bogman, M.J.J.T., Assmann, K., De Waal, R.M.W., Robben, H.C.M., Van Gasteren, H., Koene, R.A.P., 1990. Anti-GBM nephritis in the mouse: role of granulocytes in the

heterologous phase. *Kidney International* 38, 86-95.

Schulz, C., Gomez Perdiguero, E., Chorro, L., Szabo-Rogers, H., Cagnard, N., Kierdorf, K., Prinz, M., Wu, B., Jacobsen, S.E., Pollard, J.W., Frampton, J., Liu, K.J., Geissmann, F., 2012. A lineage of myeloid cells independent of Myb and hematopoietic stem cells. *Science* 336, 86-90.

Serbina, N.V., Jia, T., Hohl, T.M., Pamer, E.G., 2008. Monocyte-mediated defense against microbial pathogens. *Annual review of immunology* 26, 421-452.

Sieweke, M.H., Allen, J.E., 2013. Beyond stem cells: self-renewal of differentiated macrophages. *Science* 342, 1242974.

Simha, V., Garg, A., 2009. Inherited lipodystrophies and hypertriglyceridemia. *Current opinion in lipidology* 20, 300-308.

Simpson, I.J., Amos, N., Evans, D.J., Thomson, N.M., Peters, D.K., 1975. Guinea-pig nephrotoxic nephritis. I. The role of complement and polymorphonuclear leucocytes and the effect of antibody subclass and fragments in the heterologous phase *Clin Exp Immunol* 19, 499-511.

Singh-Joy, S.D., McLain, V.C., 2008. Safety assessment of poloxamers 101, 105, 108, 122, 123, 124, 181, 182, 183, 184, 185, 188, 212, 215, 217, 231, 234, 235, 237, 238, 282, 284, 288, 331, 333, 334, 335, 338, 401, 402, 403, and 407, poloxamer 105 benzoate, and poloxamer 182 dibenzoate as used in cosmetics. *International Journal of Toxicology* 27, 93-128.

Skrzeczynska-Moncznik, J., Bzowska, M., Loseke, S., Grage-Griebenow, E., Zembala, M., Pryjma, J., 2008. Peripheral blood CD14high CD16+ monocytes are main producers of IL-10. *Scandinavian journal of immunology* 67, 152-159.

Sotos-Prieto, M., Penalvo, J.L., 2013. Genetic variation of apolipoproteins, diet and other environmental interactions; an updated review. *Nutricion hospitalaria* 28, 999-1009.

Stavenow, L., Kjellstrom, T., 1999. Influence of serum triglyceride levels on the risk for myocardial infarction in 12510 middle aged males: interaction with serum cholesterol. *Atherosclerosis* 147, 243-247.

Steiner, G., 1993. Triglyceride-rich lipoproteins and atherosclerosis, from fast to feast. *Annals of Medicine* 25, 431-435.

Stensvold, I., Tverdal, A., Urdal, P., Graff-Iversen, S., 1993. Non-fasting serum triglyceride concentration and mortality from coronary artery disease and any cause in middle aged Norwegian women. *BMJ* 307, 1318-1322.

Strauss-Ayali, D., Conrad, S.M., Mosser, D.M., 2007. Monocyte subpopulations and their differentiation patterns during infection. *Journal of leukocyte biology* 82, 244-252.

Strickland, D.K., Gonias, S.L., Argraves, S.A., 2002. Diverse roles for the LDL receptor family. *TRENDS in Endocrinology and Metabolism* 13, 66-74.

Sumagin, R., Prizant, H., Lomakina, E., Waugh, R.E., Sarelius, I.H., 2010. LFA-1 and Mac-1 define characteristically different intraluminal crawling and emigration patterns for monocytes and neutrophils in situ. *Journal of immunology* 185, 7057-7066.

Sunderkotter, C., Nikolic, T., Dillon, M.J., van Rooijen, N., Stehling, M., Drevets, D.A., Leenen, P.J., 2004. Subpopulations of mouse monocytes differ in maturation stage and inflammatory response. *The Journal of Immunology* 172, 4410-4417.

Swirski, F.K., Hilgendorf, I., Robbins, C.S., 2014. From proliferation to proliferation: monocyte lineage comes full circle. *Seminars in immunopathology* 36, 137-148.

Swirski, F.K., Libby, P., Aikawa, E., Alcaide, P., Luscinskas, F.W., Weissleder, R., Pittet, M.J., 2007. Ly-6Chi monocytes dominate hypercholesterolemia-associated monocytosis and give rise to macrophages in atheromata. *J Clin Invest* 117, 195-205.

Swirski, F.K., Weissleder, R., Pittet, M.J., 2009. Heterogeneous in vivo behavior of monocyte subsets in atherosclerosis. *Arteriosclerosis, thrombosis, and vascular biology* 29, 1424-1432.

Sylvestre, D.L., Ravetch, J.V., 1994. Fc receptors initiate the Arthus reaction: redefining the inflammatory cascade. *Science* 265, 1095-1098.

Tamoutounour, S., Guilliams, M., Montanana Sanchis, F., Liu, H., Terhorst, D., Malosse, C., Pollet, E., Ardouin, L., Luche, H., Sanchez, C., Dalod, M., Malissen, B., Henri, S., 2013. Origins and functional specialization of macrophages and of conventional and monocyte-derived dendritic cells in mouse skin. *Immunity* 39, 925-938.

Taranta, A., Badalamenti, G., Cooper, N.S., 1963. Role of complement in nephrotoxic nephritis. *Nature* 4904, 373-375.

Tarzi, R.M., Cook, H.T., 2003. Role of Fc γ Receptors in Glomerulonephritis. *Nephron Experimental Nephrology* 95, e7-e12.

Tarzi, R.M., Davies, K.A., Claassens, J.W.C., Verbeek, J.S., Walport, M.J., Cook, H.T., 2003. Both Fc γ Receptor I and Fc γ Receptor III Mediate Disease in Accelerated Nephrotoxic Nephritis. *The American Journal of Pathology* 162, 1677-1683.

Tarzi, R.M., Davies, K.A., Robson, M.G., Fossati-Jimack, L., Saito, T., Walport, M.J., Cook, H.T., 2002. Nephrotoxic nephritis is mediated by Fc gamma receptors on circulating leukocytes and not intrinsic renal cells. *Kidney International* 62, 2087-2096.

Tatami, R., Mabuchi, H., Ueda, K., Ueda, R., Haba, T., Kametani, T., Ito, S., Koizumi, J., Ohta, M., Miyamoto, S., Nakayama, A., Kanaya, H., Oiwake, H., Genda, A., Takeda, R., 1981. Intermediate-density lipoprotein and cholesterol-rich very low density lipoprotein in angiographically determined coronary artery disease. *Circulation* 64, 1174-1184.

Tauber, A.I., 2003. Metchnikoff and the phagocytosis theory. *Nature Reviews. Molecular Cell Biology* 4, 897-901.

Teupser, D., Persky, A.D., Breslow, J.L., 2003. Induction of atherosclerosis by low-fat, semisynthetic diets in LDL receptor-deficient C57BL/6J and FVB/NJ mice: comparison of lesions of the aortic root, brachiocephalic artery, and whole aorta (en face measurement). *Arteriosclerosis, thrombosis, and vascular biology* 23, 1907-1913.

Thomson, N.M., Naish, P.F., Simpson, I.J., Peters, D.K., 1976. The role of C3 in the autologous phase of nephrotoxic nephritis. *Clin Exp Immunol* 24, 464-473.

Ting, H.J., Stice, J.P., Schaff, U.Y., Hui, D.Y., Rutledge, J.C., Knowlton, A.A., Passerini, A.G., Simon, S.I., 2007. Triglyceride-rich lipoproteins prime aortic endothelium for an enhanced inflammatory response to tumor necrosis factor-alpha. *Circulation research* 100, 381-390.

Tisseverasinghe, A., Lim, S., Greenwood, C., Urowitz, M., Gladman, D., Fortin, P.R., 2006. Association between serum total cholesterol level and renal outcome in systemic lupus erythematosus. *Arthritis Rheum* 54, 2211-2219.

Tsou, C.L., Peters, W., Si, Y., Slaymaker, S., Aslanian, A.M., Weisberg, S.P., Mack, M., Charo, I.F., 2007. Critical roles for CCR2 and MCP-3 in monocyte mobilization from bone marrow and recruitment to inflammatory sites. *J Clin Invest* 117, 902-909.

Tugal, D., Liao, X., Jain, M.K., 2013. Transcriptional control of macrophage polarization. *Arteriosclerosis, thrombosis, and vascular biology* 33, 1135-1144.

Tulenko, T.N., Sumner, A.E., 2002. The physiology of lipoproteins. *Journal of nuclear cardiology : official publication of the American Society of Nuclear Cardiology* 9, 638-649.

Unanue, E., Dixon, F.J., 1964. Experimental glomerulonephritis: IV. Participation of complement in nephrotoxic nephritis. *The Journal of experimental medicine* 119, 965-982.

Unanue, E., Dixon, F.J., 1965. Experimental glomerulonephritis: VI. The autologous phase of nephrotoxic serum nephritis *The Journal of experimental medicine*, 715-725.

Unanue, E., Mardiney, M.R.J., Dixon, F.J., 1967. Nephrotoxic serum nephritis in complement intact and deficient mice. *Journal of immunology* 98, 609-617.

van Furth, R., Cohn, Z.A., Hirsch, J.G., Humphrey, J.H., Spector, W.G., Langevoort, H.L., 1972. The mononuclear phagocyte system: a new classification of macrophages, monocytes, and their precursor cells. *Bulletin of the World Health Organization* 46, 845-852.

van Oostrom, A.J., Rabelink, T.J., Verseyden, C., Sijmonsma, T.P., Plokker, H.W., De Jaegere, P.P., Cabezas, M.C., 2004. Activation of leukocytes by postprandial lipemia in healthy volunteers. *Atherosclerosis* 177, 175-182.

Varol, C., Landsman, L., Fogg, D.K., Greenshtein, L., Gildor, B., Margalit, R., Kalchenko, V., Geissmann, F., Jung, S., 2007. Monocytes give rise to mucosal, but not splenic, conventional dendritic cells. *The Journal of experimental medicine* 204, 171-180.

Varol, C., Vallon-Eberhard, A., Elinav, E., Aychek, T., Shapira, Y., Luche, H., Fehling, H.J., Hardt, W.D., Shakhar, G., Jung, S., 2009. Intestinal lamina propria dendritic cell subsets have different origin and functions. *Immunity* 31, 502-512.

Veniant, M.M., Sullivan, M.A., Kim, S.K., Ambroziak, P., Chu, A., Wilson, M.D., Hellerstein, M., Rudel, L.L., Walzem, R.L., Young, S.G., 2000. Defining the atherogenicity of large and small lipoproteins containing apolipoprotein B100. *Journal of Clinical Investigation* 106, 1501-1510.

Veniant, M.M., Withycombe, S., Young, S.G., 2001. Lipoprotein Size and Atherosclerosis Susceptibility in Apoe^{-/-} and Ldlr^{-/-} Mice. *Arteriosclerosis, thrombosis, and vascular biology* 21, 1567-1570.

Vogt, A., Kochem, H.G., 1961. Immediate and delayed nephrotoxic nephritis in rats *Am J Pathol* XXXIX, 379-390.

Von Eckardstein, A., Nofer, J.-R., Assmann, G., 2001. High density lipoprotein and atherosclerosis: Role of cholesterol efflux and reverse cholesterol transport. *Arteriosclerosis, thrombosis, and vascular biology* 21, 13-27.

Wade, N.S., Major, A.S., 2011. The problem of accelerated atherosclerosis in systemic lupus erythematosus: insights into a complex co-morbidity. *Thrombosis and haemostasis* 106, 849-857.

Wang, Y.I., Bettaieb, A., Sun, C., DeVerse, J.S., Radecke, C.E., Mathew, S., Edwards, C.M., Haj, F.G., Passerini, A.G., Simon, S.I., 2013. Triglyceride-rich lipoprotein modulates endothelial vascular cell adhesion molecule (VCAM)-1 expression via differential regulation of endoplasmic reticulum stress. *PloS one* 8, e78322.

Wang, Y.I., Schulze, J., Raymond, N., Tomita, T., Tam, K., Simon, S.I., Passerini, A.G., 2011. Endothelial inflammation correlates with subject triglycerides and waist size after a high-fat meal. *American journal of physiology. Heart and circulatory physiology* 300, H784-791.

Weber, C., Belge, K.U., von Hundelshausen, P., Draude, G., Steppich, B., Mack, M., Frankenberger, M., Weber, K., Ziegler-Heitbrock, H.W., 2000. Differential chemokine receptor expression and function in human monocyte subpopulations. *Journal of leukocyte biology* 67, 699-704.

Wong, K.L., Yeap, W.H., Tai, J.J., Ong, S.M., Dang, T.M., Wong, S.C., 2012. The three human monocyte subsets: implications for health and disease. *Immunologic research* 53, 41-57.

Wout, Z.G., Pec, E.A., Maggiore, J.A., Williams, R.H., Palicharla, P., Johnston, T.P., 1992. Poloxamer 407-mediated changes in plasma cholesterol and triglycerides following intraperitoneal injection to rats. *Journal of Parental Science and Technology* 46, 192-200.

Wynn, T.A., Chawla, A., Pollard, J.W., 2013. Macrophage biology in development, homeostasis and disease. *Nature* 496, 445-455.

Yona, S., Jung, S., 2010. Monocytes: subsets, origins, fates and functions. *Current opinion in hematology* 17, 53-59.

Yona, S., Kim, K.W., Wolf, Y., Mildner, A., Varol, D., Breker, M., Strauss-Ayali, D., Viukov, S., Guilliams, M., Misharin, A., Hume, D.A., Perlman, H., Malissen, B., Zelzer, E., Jung, S., 2013. Fate mapping reveals origins and dynamics of monocytes and tissue macrophages under homeostasis. *Immunity* 38, 79-91.

Young, S.G., Zechner, R., 2013. Biochemistry and pathophysiology of intravascular and intracellular lipolysis. *Genes & development* 27, 459-484.

Yusuf, S., Hawken, S., Ôunpuu, S., Dans, T., Avezum, A., Lanas, F., McQueen, M., Budaj, A., Pais, P., Varigos, J., Lisheng, L., 2004. Effect of potentially modifiable risk factors associated with myocardial infarction in 52 countries (the INTERHEART study): case-control study. *The Lancet* 364, 937-952.

Ziegler-Heitbrock, H.W., Fingerle, G., Strobel, M., Schraut, W., Stelter, F., Schutt, C., Passlick, B., Pforte, A., 1993. The novel subset of CD14/CD16 blood monocytes exhibit features of tissue macrophages. *The European Journal of Immunology* 23, 2053-2058.

Ziegler-Heitbrock, L., 2007. The CD14⁺ CD16⁺ blood monocytes: their role in infection and inflammation. *Journal of leukocyte biology* 81, 584-592.

Ziegler-Heitbrock, L., 2014. Reprint of: Monocyte subsets in man and other species. *Cell Immunol.*

Zilversmit, D.B., 1995. Atherogenic nature of triglycerides, postprandial lipemia, and triglyceride-rich remnant lipoproteins. *Clinical Chemistry* 41, 153-158.